

UNIVERSIDAD POLITÉCNICA DE VALENCIA

NUCLEAR AND CHEMICAL ENGINEERING DEPARTMENT



**UNIVERSIDAD
POLITECNICA
DE VALENCIA**

**A THEORETICAL INVESTIGATION OF
AEROSOL RETENTION WITHIN THE SECONDARY SIDE
OF A STEAM GENERATOR UNDER A
SGTR SEVERE ACCIDENT SEQUENCE IN A PWR
NUCLEAR POWER PLANT**

Ph. D. Thesis

Presented by:

Claudia López del Prá

Supervisors:

Dr. Luis Enrique Herranz

Dr. José Luis Muñoz-Cobo

**A THEORETICAL INVESTIGATION OF
AEROSOL RETENTION WITHIN THE
SECONDARY SIDE OF A STEAM GENERATOR
UNDER A
SGTR SEVERE ACCIDENT SEQUENCE
IN A PWR NUCLEAR POWER PLANT**

by

Claudia López del Prá

Licenciada en Ciencias Matemáticas

por la Universidad Autónoma de Madrid

Submitted to the Department of Nuclear and Chemical Engineering in
partial fulfilment of the requirements for the degree of

DOCTOR of PHILOSOPHY

at the

Polytechnic University of Valencia

July 2011

Certified by Dr. Luis Enrique Herranz. Thesis supervisor

Certified by Dr. José Luis Muñoz-Cobo. Thesis supervisor

*To my parents
Pepe and Lea*

Acknowledgements

I owe my gratitude to my team leader and thesis supervisor, Luis Enrique Herranz for making this PhD possible. He devised this thesis and gave me the chance to carry it out. His ability to understand whatever is amazing. I feel grateful because I enjoyed his capacity of generating ideas, his passion and his encouragement to continue. His sharp criticism knocked down the work many times and, although it was hard sometimes, it eventually let me to rebuild the work with better foundations. Someone who knows him told me once that where everybody was just seeing grains of sand, he could construct a castle, and this thesis is an example of it. I thank you Luis Enrique for the time and thoughts shared.

I also want to express my gratitude to Jose Luis Muñoz-Cobo for his supervision. He gave me the first chance to start this long way at the UPV, and I thank him for this. I also want to thank Alberto Escrivá for his support and assistance during this time.

I want to express my gratitude to Salih Güntay and his team, Detlef, Hauke, John, Bernd, Steffen, Terttalissa for their contributions, support and kindness; especially during the months I stayed at the PSI, and an especial word of thanks to Abdel Dehbi for his guidance in the CFD world.

To all the people of ARTIST and ARTIST II projects, in particular to Dana Powers for his comments and encouragement at ARTIST's meetings.

I want also to thank my colleagues of the Unit of Nuclear Safety Research of CIEMAT, Javier and Rosario for their experimental insights. In particular to those that I count on as friends, Paco, Joan and Mónica for their support, encouragement and the nice moments, and also to Paco Álvarez our colleague from CIEMAT.

I want to thank my parents; they have always given me unquestioned support, guidance and love. My father, José López Jiménez, has been engaged with the earliest motivation for this thesis, our talks about physics when I was a teenager were the seeds that I am growing today.

Finally, I want to thank the CIEMAT for giving me the opportunity of performing this PhD thesis, and the Spanish Nuclear Safety Council for the financial support of the project ARTIST, in particular to Fernando Robledo for his interest.

ABSTRACT

Severe accident Steam Generator Tube Rupture (SGTR) sequences are identified as major contributors to risk of Pressurized Water Reactors (PWR). Their relevance lies in the potential radioactive release from reactor coolant system to the environment. The radioactive particles can be partially retained over the surfaces they find along the path from the reactor coolant system, in particular within the secondary side of the steam generator, even in the absence of water. Lack of knowledge on the source term attenuation capability of the steam generator has avoided its consideration in probabilistic safety studies and severe accident management guidelines. As a consequence, the steam generator filtering capability is not usually taken into account either in the probabilistic risk assessment of nuclear safety or in the severe accident management guidelines.

This thesis is a contribution to the technical understanding and quantification of the natural processes mitigating the consequences of SGTR accidents. It describes the main activities and results of a theoretical program focused on modeling the aerosol retention in the break stage of the secondary side of a dry steam generator. The model developed, called ARI3SG, is a semi-empirical, Lagrangian model based on the filter-concept approach. It is built to compute retention efficiency according to dominant aerosol phenomena and gas fluid-dynamics underneath. Fluid dynamics have been analyzed through thorough 3D simulations with the FLUENT 6.2 code, which were validated against ad-hoc experimental data.

The model performance has been assessed through a verification process that has demonstrated its robust and sound behavior. Predictability was also assessed by comparing its estimates to open data and by analyzing the effect of associated uncertainties. Data-model comparison has been shown to be satisfactory and highlight the potential use of an ARI3SG-like formulation in system codes. Through a random sampling of the input variables of the model (i.e., inlet velocity and aerosol size and density), a theoretical correlation has been derived as a function of the Stokes and particle Reynolds non-dimensional numbers. As the average relative deviation with respect to ARI3SG is less than 7%, the correlation provides a useful way of implementing ARI3SG within severe accident system codes, like ASTEC and/or MELCOR.

The work performed in this thesis is framed in the CIEMAT contribution to the ARTIST and ARTIST II projects (2003-2010) which were supported by the Spanish Nuclear Regulatory Commission (CSN).

SINOPSIS

Las secuencias de accidente con rotura de tubos en el generador de vapor (secuencias SGTR) están consideradas como contribuyentes del riesgo en reactores de agua a presión. Su relevancia radica en la potencial liberación de aerosoles radioactivos al medio ambiente en caso de accidente severo. Sin embargo, dichas partículas podrían quedar retenidas parcial o totalmente sobre las superficies del generador de vapor, incluso en condiciones extremas de ausencia de agua en el generador de vapor. La carencia de conocimiento en cuanto a la capacidad de retención de término fuente de este componente ha eludido su consideración en los estudios probabilistas de seguridad y en las guías de gestión de accidente severo.

Esta tesis es una contribución a la comprensión y cuantificación de los procesos naturales de mitigación que tienen lugar dentro del generador de vapor como consecuencia de los accidentes SGTR. La principal actividad llevada a cabo ha sido el desarrollo de un modelo teórico que calcula la capacidad de retención de aerosoles en la etapa de rotura de un generador de vapor seco. El modelo, llamado ARI3SG, está basado en una aproximación de filtro y tiene una naturaleza semi-empírica. En él se tienen en cuenta tanto la dinámica de aerosoles como la hidrodinámica de aerosoles que tiene lugar dentro del generador de vapor en este tipo de escenarios. Para esto último, se han llevado a cabo una serie de simulaciones con el código tridimensional FLUENT 6.2, que han sido validadas con datos experimentales.

El comportamiento del modelo ha sido evaluado en profundidad: primero, a través de un proceso de verificación con el que se ha visto que es robusto. Segundo, a través de un proceso de validación frente a los datos experimentales disponibles. Tercero, a través del estudio del efecto de las incertidumbres del escenario y del modelo sobre los resultados.

La comparación frente a los datos experimentales ha sido satisfactoria y muestra la viabilidad del uso de formulaciones como la de ARI3SG en códigos de sistema. A través de un muestreo aleatorio de las variables de entrada del modelo (velocidad, tamaño y densidad del aerosol) se ha derivado una correlación teórica en función de números adimensionales (Stk y Re_p), que difiere del modelo en menos de un 7%. A través de ella se puede implementar de forma sencilla el modelo ARI3SG en códigos de accidente severo como MELCOR o ASTEC.

El trabajo realizado para esta tesis se ha llevado a cabo en la unidad de investigación en seguridad nuclear del CIEMAT como parte de los proyectos internacionales ARTIST y ARTIST II, que han estado subvencionados por el Consejo de Seguridad Nuclear.

SINOPSI

Les seqüències d'accident amb trencament de tubs en el generador de vapor (seqüències SGTR) estan considerades com a contribuents del risc en reactors d'aigua a pressió. La seva rellevància es troba en el potencial alliberament d'aerosols radioactius al medi ambient en cas d'accident sever. No obstant això, aquestes partícules podrien quedar retingudes parcialment o totalment sobre les superfícies del generador de vapor, fins i tot en condicions extremes d'absència d'aigua al generador de vapor. La manca de coneixement pel que fa a la capacitat de retenció del terme font d'aquest component ha eludit la seva consideració en els estudis probabilistes de seguretat i en les guies de gestió d'accident sever.

Aquesta tesi és una contribució a la comprensió dels processos naturals de mitigació que tenen lloc dins del generador de vapor com a conseqüència dels accidents SGTR. La principal activitat duta a terme ha estat el desenvolupament d'un model teòric que calcula la capacitat de retenció d'aerosols en l'etapa de ruptura d'un generador de vapor sec. El model, anomenat ARI3SG, està basat en una aproximació de filtre i té una naturalesa semi-empírica. En ell es tenen en compte tant l'aerodinàmica com la hidrodinàmica d'aerosols que té lloc dins del generador de vapor en aquest tipus d'escenaris. Per això últim, s'han dut a terme una sèrie de simulacions amb el codi tridimensional FLUENT 6.2, que han estat validades amb dades experimentals.

El comportament del model ha estat avaluat en profunditat: primer, a través d'un procés de verificació amb el que s'ha vist que robust. Segon, a través d'un procés de validació en front a les dades experimentals disponibles. Tercer, degut a l'aproximació de filtre s'ha realitzat un estudi de l'efecte de les incerteses sobre el model.

La comparació amb les dades experimentals ha estat satisfactòria i mostra la viabilitat de l'ús de formulacions com la d'ARI3SG en codis de sistema. A través d'un mostreig aleatori de les variables d'entrada del model (velocitat, mida i densitat de l'aerosol) s'ha derivat una correlació teòrica en funció de nombres adimensionals (Stk i Re_p), que difereix del model en menys d'un 7%. A través d'ella es pot implementar de forma senzilla el model ARI3SG en codis d'accident sever com MELCOR o ASTEC.

Aquesta tesi s'ha dut a terme a la unitat de recerca en seguretat nuclear del CIEMAT com a part dels projectes internacionals ARTIST i ARTIST II, que han estat subvencionats pel Consejo de Seguridad Nuclear.

CONTENTS

LIST OF FIGURES	XIV
LIST OF TABLES	XVI
1. INTRODUCTION	1
1.1. PRESSURIZED WATER REACTOR AND STEAM GENERATOR	1
1.2. THE SGTR SEVERE ACCIDENT SCENARIO	4
1.3. BACKGROUND AND FRAME OF THE WORK	7
1.4. THESIS SETTING OUT: MOTIVATION, OBJECTIVES	11
2. DEVELOPMENT OF FLUID FLOW MODELING	13
2.1. COMPUTATIONAL TOOL AND MODELING PERFORMED	14
2.1.1. <i>The FLUENT code</i>	14
2.1.2. <i>Development of the geometry and grid</i>	16
2.1.3. <i>Hypothesis and boundary conditions performed</i>	19
2.1.4. <i>Assessment of numerics and mesh quality</i>	20
2.1.5. <i>Validation of the simulations</i>	23
2.2. AERODYNAMIC RESULTS OF THE SIMULATIONS.....	28
2.2.1. <i>Guillotine breach analysis</i>	28
2.2.2. <i>Fish-mouth breach analysis</i>	32
2.3. DEVELOPMENT OF ONE-DIMENSIONAL CONCEPTUAL MODEL.....	37
2.3.1. <i>Characterization of the guillotine breach jet</i>	38
2.3.2. <i>Characterization of the fish-mouth breach jet</i>	41
2.3.3. <i>Guillotine and fish-mouth closing results</i>	43
2.4. CONCLUSIONS OF FLUID FLOW MODELING	45
3. DEVELOPMENT OF THE AEROSOL MODELING	47
3.1. HYPOTHESES AND APPROXIMATIONS PERFORMED	49
3.1.1. <i>The filter approach applied to the scenario</i>	49
3.1.2. <i>The single tube efficiency applied to the scenario</i>	52
3.1.3. <i>The aerodynamic characterization performed</i>	54
3.1.4. <i>Development of the jet penetration</i>	55
3.2. DEVELOPMENT OF THE FUNDAMENTAL EQUATIONS	55
3.2.1. <i>Size dependence</i>	56
3.2.2. <i>Assessment of phenomena relevance</i>	56
3.2.3. <i>Deposition</i>	58
3.2.3.1. <i>Turbulent deposition</i>	58
3.2.3.2. <i>Inertial impaction</i>	62
3.2.4. <i>Resuspension</i>	64
3.3. DEVELOPMENT OF ARICODE	67
3.3.1. <i>ARI3SG structure</i>	68
3.3.2. <i>Input description</i>	71
3.3.3. <i>Output description</i>	71
3.4. VERIFICATION OF THE ARI3SG MODEL	72

3.5. VALIDATION OF THE ARI3SG MODEL	73
3.5.1. <i>Experimental Set-up</i>	73
3.5.2. <i>Database</i>	75
3.5.3. <i>Hypotheses and approximations performed</i>	76
3.5.4. <i>Results obtained</i>	77
3.5.4.1. TiO ₂ simulations	78
3.5.4.2. SiO ₂ simulations	82
3.6. UNCERTAINTY ANALYSES PERFORMED TO ARI3SG	85
3.6.1. <i>Model uncertainty applied to ARI3SG</i>	85
3.6.2. <i>Input parameters uncertainty applied to ARI3SG</i>	89
3.6.3. <i>Sensitivity analysis performed</i>	95
3.6.4. <i>Total uncertainty performed</i>	97
3.7. DERIVED CORRELATION OF ARI3SG	98
3.8. CONCLUSIONS OF THE AEROSOL MODELING	102
4. CONCLUSIONS AND FINAL REMARKS	105
4.1. CONCLUSIONS AND FINAL REMARKS ON FLUID FLOW MODELING	105
4.2. CONCLUSIONS AND FINAL REMARKS ON AEROSOL MODELING	106
4.3. MODELING DRAWBACKS AND FUTURE WORK	107
5. PUBLISHED PAPERS	109
5.1. INTERNATIONAL JOURNALS	109
5.2. NATIONAL JOURNALS	110
5.3. INTERNATIONAL CONFERENCES	110
5.4. NATIONAL CONFERENCES	111
6. NOMENCLATURE	113
7. REFERENCES	117
 APPENDIXES	
A. PRELIMINARY HYDRODYNAMIC SIMULATIONS	A-1
A.1. SIMPLIFIED BUNDLE	A-1
A.1.1. AERODYNAMIC RESULTS	A-2
A.1.2. DISCUSSION OF AEROSOL EXPERIMENTS	A-5
A.2. SUPPORT PLATE AS A POROUS MEDIA	A-7
A.3. PROCEDURE FOR CFD SIMULATIONS	A-9
A.4. INITIAL SIMULATIONS: STANDARD κ - ϵ MODEL	A-13
A.5. TURBULENCE ASSESSMENT: RSM MODEL	A-17
B. POSTPROCESS OF FLUENT FILES	B-1
C. RESUSPENSION	C-1
D. ARI3SG INPUT GENERATION	D-1
D.1. LOGNORMAL PARTICLE DISCRETIZATION	D-1
D.2. SOURCE CODE OF INPUT GENERATION OF ARICODE	D-4
E. INPUT AND OUTPUT FILES OF ARICODE	E-1

E.1. ARICODE INPUT.....	E-1
E.2. ARICODE OUTPUT.....	E-4
E.2.1. OUTBUNDLE.DAT.....	E-4
E.2.2. OUTTUBE.DAT.....	E-5
E.2.3. OUTPSIZE.DAT.....	E-7
E.2.4. OUTTIME.DAT.....	E-13
F. UNCERTAINTY OF THE DIMENSIONLESS AXIAL DEPOSITION VELOCITY AND RESUSPENSION RATE CORRELATIONS.....	F-1
ARICODE.....	ARICODE.f-1
ARI3SG.....	ARI3SG.f-1
ARI3WSC.....	ARI3WSC.f-1

LIST OF FIGURES

Fig. 1.1.1. Flow scheme of a PWR system (Westinghouse).....	2
Fig. 1.1.2. Steam generator (Westinghouse).	3
Fig. 1.3.1. Breach type configuration: guillotine (right), fish-mouth (left).	8
Fig. 1.3.2. SGTR collection efficiency (η) vs inlet gas mass flow rate (Φ).	9
Fig. 1.3.3. Scheme of the research approach.....	10
Fig. 2.1.1. Tube bundle configuration.....	16
Fig. 2.1.2. Horizontal cross-section of the meshed domain (guillotine).....	17
Fig. 2.1.3. Horizontal cross-section of the meshed domain (fish-mouth).	18
Fig. 2.1.4. Vertical velocity profiles (250 kg/h).	22
Fig. 2.1.5. Experimental CAHT configuration.	23
Fig. 2.1.6. PIV and FLUENT velocity fields of guillotine breach simulations.	24
Fig. 2.1.7. Guillotine velocity profiles at 0° , $r/s=1/3$, $1/2$ and $3/4$ (250 kg/h).....	25
Fig. 2.1.8. Guillotine velocity profiles at 0° , $r/s= 1/3$ (left: 150kg/h; right: 75kg/h). .	26
Fig. 2.1.9. Particle deposits and FLUENT prediction.	26
Fig. 2.1.10. Fish-mouth normalized velocity vectors: PIV (left) FLUENT' (right).....	27
Fig. 2.1.11. PIV, Pitot and FLUENT' velocities at 0° , $r/s=1/3$ (75kg/h;fish-mouth)..	28
Fig. 2.2.1. Guillotine velocity magnitude vectors: 250 kg/h (left), 75 kg/h (right).....	30
Fig. 2.2.2. Normalized maximum radial velocity vs tube row position (guillotine).	31
Fig. 2.2.3. Normalized maximum axial velocity vs axial position (guillotine).....	32
Fig. 2.2.4. Vertical view of velocity streamlines (250 kg/h, fish-mouth).....	33
Fig. 2.2.5. Top view of velocities higher than 10 m/s (250 kg/h, fish-mouth).....	34
Fig. 2.2.6. Fish-mouth velocity vectors: 250 kg/h (left), 75 kg/h (right).	35
Fig. 2.2.7. Normalized maximum radial velocity vs radial position (fish-mouth).	36
Fig. 2.2.8. Normalized maximum axial velocity vs axial position (fish-mouth).....	37
Fig. 2.3.1. Fluid development across the bundle.	38
Fig. 2.3.2. Normalized radial velocity vs tube row position (guillotine).	39
Fig. 2.3.3. Normalized radial and axial velocities vs tube row position (guillotine).....	40
Fig. 2.3.4. Normalized axial velocity vs axial position (guillotine).....	41
Fig. 2.3.5. Normalized radial velocity vs tube row position (guillotine,fish-mouth)....	42
Fig. 2.3.6. Normalized axial velocity vs axial position (guillotine,fish-mouth).	43
Fig. 2.3.7. Maximum velocity vs inlet gas mass flow rate (guillotine, fish-mouth).	44

Fig. 3.0.1. Normalized collection efficiency vs inlet gas mass flow rate.....	48
Fig. 3.1.1. Sketch-I of ARI3SG approach.....	50
Fig. 3.1.2. Particle deposits after a PIV experiment and FLUENT velocity vectors..	52
Fig. 3.2.1. Fitting of turbulent deposition.....	60
Fig. 3.2.2. Dimensionless deposition velocity vs dimensionless relaxation time.....	61
Fig. 3.2.3. Fitting of inertial impaction.....	63
Fig. 3.2.4. Experimental data and correlation estimates of inertial impaction.....	63
Fig. 3.2.5. Resuspension rate vs resuspension force.	66
Fig. 3.3.1. ARICODE platform flowchart.	68
Fig. 3.3.2. ARI3SG flowchart.....	70
Fig. 3.5.1. Scheme of the PECA-SGTR facility.....	74
Fig. 3.5.2. Inlet aerosol mass distributions of TiO ₂ simulations ($\rho=1000$ kg/m ³).....	77
Fig. 3.5.3. TiO ₂ SGTR, ARI3SG efficiency vs inlet gas mass flow rate (I).....	78
Fig. 3.5.4. TiO ₂ SGTR, ARI3SG efficiency vs inlet gas mass flow rate (II).....	79
Fig. 3.5.5. TiO ₂ CAAT, ARI3SG efficiency vs inlet gas mass flow rate.....	80
Fig. 3.5.6. TiO ₂ SGTR, CAAT, ARI3SG efficiency vs inlet gas mass flow rate.	82
Fig. 3.5.7. SiO ₂ CAAT, ARI3SG efficiency vs inlet gas mass flow rate (I).....	83
Fig. 3.5.8. SiO ₂ CAAT, ARI3SG efficiency vs inlet gas mass flow rate (II).....	84
Fig. 3.6.1. Model uncertainty of SGTR and CAAT simulations.	89
Fig. 3.6.2. Histogram of SGTR-1 input samplings.....	92
Fig. 3.6.3. Histogram of SGTR-7 input samplings.....	92
Fig. 3.6.4. Histogram of SGTR-1 output computations.....	93
Fig. 3.6.5. Histogram of SGTR-7 output computations.....	93
Fig. 3.6.6. Results of input uncertainty of SGTR simulations.	94
Fig. 3.6.7. Results of input uncertainty of TiO ₂ -CAAT simulations.....	95
Fig. 3.6.8. Sensitivity results of SGTR-1 simulation.....	96
Fig. 3.6.9. Sensitivity results of SGTR-7 simulation.....	96
Fig. 3.6.10. Total uncertainty of SGTR and CAAT simulations.	97
Fig. 3.7.1. ARI3SG results vs Stokes number.....	99
Fig. 3.7.2. Correlation vs ARI3SG collection efficiency.....	101

LIST OF TABLES

Table 1.1.1. Almaraz Unit I, Spanish NPP (cnat, 2010).....	2
Table 1.2.1. Farthest boundary conditions of a faulted SG (Auvinen et al., 2005).....	5
Table 2.1.1. Hypotheses and Boundary Conditions of 3D simulations.	20
Table 2.1.2. Numerical results of guillotine 3D simulations.	21
Table 2.1.3. Numerical results of fish-mouth 3D simulations.....	22
Table 2.2.1. Guillotine 3D simulation results.....	29
Table 2.3.1. Guillotine, fish-mouth 3D simulation results.	44
Table 3.2.1. Estimate of characteristic parameters of depletion mechanisms.	57
Table 3.2.2. Non dimensional numbers for aerosol scrubbing.	58
Table 3.2.3. Correlations of inertial impaction.	64
Table 3.3.1. ARI3SG modules.	68
Table 3.4.1. Verification cases.....	72
Table 3.5.1. SGTR experimental conditions and results (Herranz et al., 2006).	75
Table 3.5.2. CAAT experimental conditions and results(López del Prá et al., 2010c).75	
Table 3.5.3. Manufacturer aerosol specifications.....	76
Table 3.5.4. SGTR experimental outlet aerosol diameter.....	79
Table 3.6.1. ARI3SG fundamental equations and uncertainties.....	86
Table 3.6.2. Uncertainties of correlations within ARI3SG.	88
Table 3.6.3. SGTR, CAAT inlet velocity uncertainty.....	91
Table 3.6.4. Uncertainty ranges of ARI3SG simulations (SGTR, CAAT).....	98
Table 3.7.1. Characteristic SGTR & CAAT tests ranges.....	99

1. INTRODUCTION

Over the last several years there has been a growing interest in accident management measures to enhance defense-in-depth strategies that ensure the safety of nuclear power plants (NPP). In this context, an important threat to public health and safety posed by nuclear power plants are the accidents in pressurized water reactors (PWR) involving steam generator tube ruptures (SGTR). In such accidents, an open pathway from the reactor vessel to the environment could occur and radioactive material could bypass the reactor containment and the engineered safety systems. Much attention has been devoted to accident management measures that would mitigate the consequences of SGTR accidents. Should these measures fail, only natural mitigation processes would attenuate accident consequences. It is important, then, to have an understanding of these natural mitigation processes. This thesis is a contribution to the technical understanding and quantification of the natural processes mitigating the consequences of SGTR accidents. It is focused on the aerosol retention capability of the secondary side of the steam generator (SG), in particular in the region near the tube rupture. The particle and the flow performance are analyzed and encompassed into a model that estimates their depletion over the tube surfaces of the SG.

This section introduces the scenario, the motivations and the frame in which this work has been developed.

1.1. PRESSURIZED WATER REACTOR AND STEAM GENERATOR

Pressurized water reactors are thermal reactors with light water at high pressure and temperature serving as moderator-coolant, and a heterogeneous arrangement of slightly enriched uranium fuel. They rely on indirect cycles to generate electricity, as they require a heat exchanger to produce steam that strikes a turbine which drives a generator producing electricity (Murray, 2001).

Fig. 1.1.1 shows a schematic representation of a three successive separate coolant circuits of a PWR. The initial core thermal energy is transferred to the coolant of the primary circuit. It is maintained at sufficiently high pressure (usually between 13.8 to 17.24 MPa) so that its temperature is below the saturation one (Glasstone and Sesonske, 1963). The heat is transferred to a secondary coolant circuit, by means of a steam

generator which is around 6.8 MPa. The steam generated in the secondary loop strikes the blades of a turbine, condensates and is returned to the steam generator as feedwater. Meanwhile, water of the primary circuit is returned from the steam generator to the core. Depending on the design, the PWR may have from 1 to 4 coolant loops in the primary circuit, each of them with the corresponding steam generator.

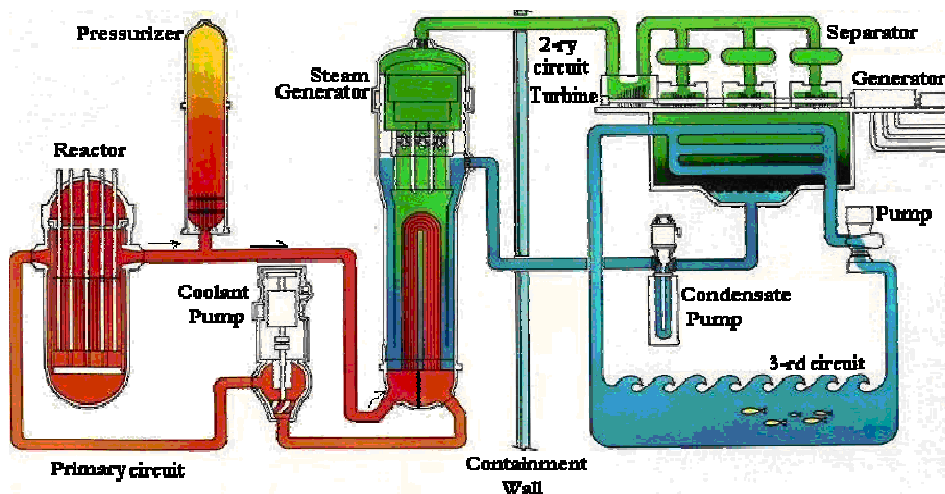


Fig. 1.1.1. Flow scheme of a PWR system (Westinghouse).

Table 1.1.1 collects the nominal conditions of the primary and secondary coolants circuits of the 980 MWe Spanish NPP Almaraz Unit I, which is equipped with three coolant loops.

Table 1.1.1. Almaraz Unit I, Spanish NPP (cnat, 2010).

1 ^{ry} circuit		2 ^{ry} circuit	
Water pressure	15.7 MPa	Vapor pressure	6.8 MPa
Core outlet/ SG inlet T	598 K	SG vapor outlet T	558 K
Core inlet/ SG outlet T	565 K	SG water inlet T	497 K
Flow rate in core	47.8 t/h	Vapor flow rate	1787 t/h

The steam generator is a cylindrical vessel partly filled with water (secondary side), through which many tubes containing the heated water from the reactor pass (primary side)(Murray, 2001). It can measure up to 22 m high and weight as much as $800 \cdot 10^3$ kg (Fig. 1.1.2). Depending on the design, it encloses from 2000 to 5000 inverted U-shaped tubes with diameters around 2 cm. Each of them welded to a thick plate with a hole

for each tube end (called tube sheet) located near the bottom. The tubes are supported with plates at a number of fixed axial locations along the tube bundle. The region between two consecutive support plates is usually called “stage”. The upper region of the vessel contains the feedwater inlet piping and various steam-water separators and dryers (Macdonald et al., 1996).

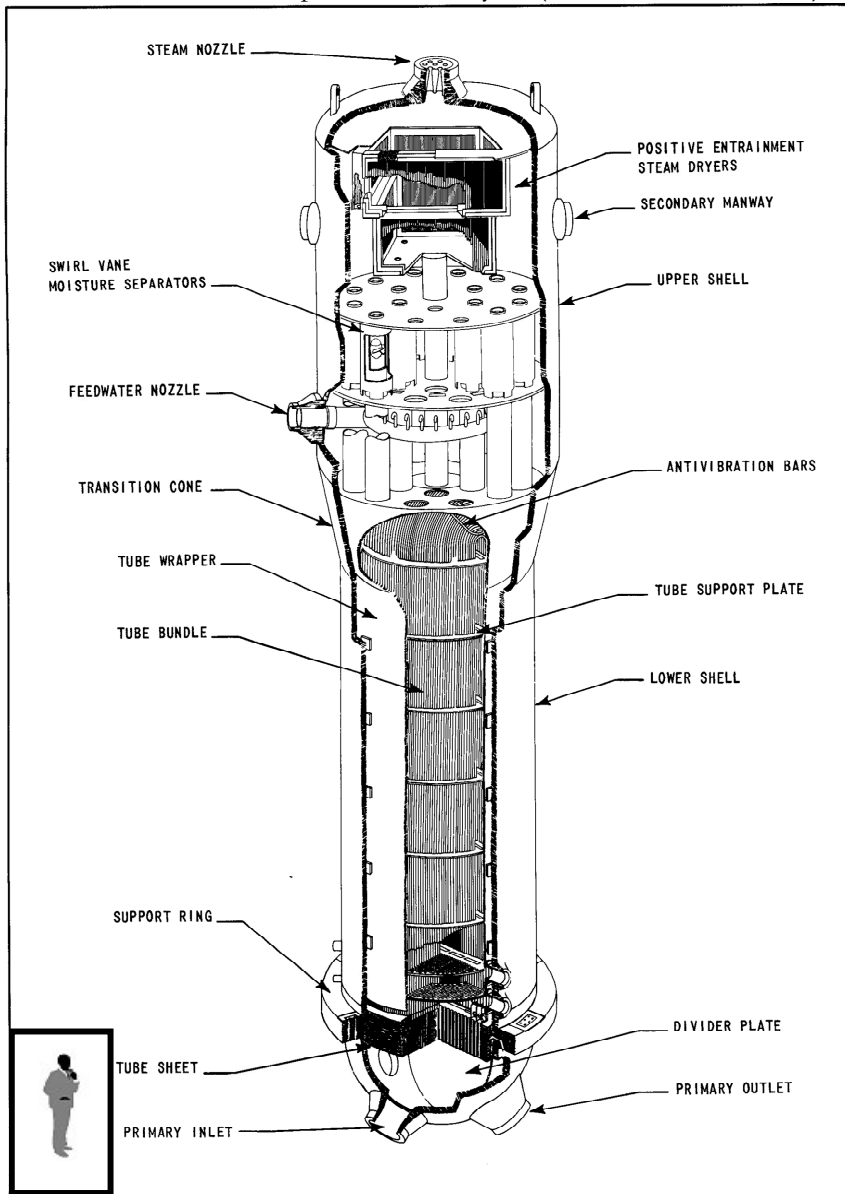


Fig. 1.1.2. Steam generator (Westinghouse).

1.2. THE SGTR SEVERE ACCIDENT SCENARIO

Steam generators are key components for overall plant performance playing a significant role in safety as they constitute the boundary between primary and secondary coolant circuits. For this reason, the integrity of the tubes is essential to prevent any leakage between both sides of the plant. This fact has resulted in design and manufacturing improvements of steam generators as well as new modes of operation. However, a variety of phenomena (stress corrosion cracking of the outside and inside surfaces of the tubing, high-cycle fatigue, loose parts wear, wastage) may degrade the tubes leading to a leak that could result in a SGTR event. These events are handled within design basis accidents (DBA) of western PWR (Macdonald et al., 1996).

NUREG-6365 reported several SGTR events (a total of 10 up to 1996) showing that in all the cases, the plant cope with the accident with no major consequences. However and in spite of being very unlikely, a SGTR accident is risk significant due to the potential for the radionuclides to bypass the reactor's containment building, if another failure in the secondary side pressure boundary occurs (Macdonald et al., 1996; USNRC, 1990).

The SGTR scenario with reactor core melt may have different initiators and progressions. A spontaneous SGTR could be an initiating event of the severe accident; or a severe accident could induce a SGTR by subjecting the tubes to large thermal and pressure loads; or other events like a sudden break in the steam line leading to a rapid depressurization of the secondary system could also induce simultaneous tube ruptures which could give rise to the reactor core melt (USNRC, 1990; Auvinen et al., 2005; Liao and Guentay, 2009; Macdonald et al., 1996). Regarding the bypass sequence, it could result from the SGTR (spontaneous or induced) as it increases the secondary side pressure which is likely to cause relief valves to lift on the secondary side. If these valves fail to reclose, an open pathway from the vessel to the environment can result (USNRC, 1990).

The potential retention within the secondary side of a failed steam generator during a SGTR severe accident sequence was seen as one of the largest uncertainties in the analyses reported in NUREG-1150 (USNRC, 1990). This expert elicitation panel considered that little retention of radionuclides would occur both in the reactor coolant piping and the failed steam generator. They estimated the overall transmission factor from the reactor to the environment to be higher than 75% for all radionuclides considered, and agreed to attribute such a small attenuation to retention in

the primary coolant piping. Consistently, and given present absence of a comprehensive database or specific model for the retention in the secondary side of the failed steam generator, Probabilistic Risk Assessments (PRA) usually give no credit to any potential decontamination within the secondary side of a steam generator (Güntay et al., 2001; Herranz et al, 2006). However, the geometry of the steam generator: tube bank, support plates, separators and dryers provide a large surface area on which fission products may be trapped. The presence of liquid may further augment the retention (Güntay et al., 2004).

The aerosol phenomenology taking place within the SG during these sequences is wide and complex due to the complexity of this component and the wide range of boundary conditions. As an example, Table 1.2.1 collects the maximum values of the conditions of a potential fault SG during the fission product release period of one of the most dominant SGTR accident scenarios of the Swiss Beznau NPP (based on PRA analysis; Auvinen et al., 2005).

Table 1.2.1. Farthest boundary conditions of a faulted SG (Auvinen et al., 2005).

	Primary	Secondary
Pressure (MPa)	3	0.31
Steam temperature (K)	500	500
	Steam	Aerosol
Flow through break (kg/h)	4680	4.25
Time of interest (h)		2.78

Depending on the SG region, the main processes governing aerosol removal when the secondary side is empty of water are the following (Güntay et al., 2000; Allelein et al., 2009). Worth to note that these analyses are ongoing discussions performed within the projects EU-SGTR, ARTIST and ARTIST II that are introduced in the following section:

- Primary side: In-tube. The high velocities expected in this region (several 100 m/s) make turbulent deposition and resuspension the main phenomena in the primary side of the SG. The coupling of deposition/resuspension and the possible fission product condensation in the lower region of the SG (lower plenum) need very detailed and simultaneous treatment that is not yet attempted.
- Secondary side: the “Break stage”. It is the stage between two consecutive support plates where the breach is located. In this region, jet velocities are expected to range from 100 m/s to sonic

levels. Depletion in a single tube was seen to correlate as a function of the Stokes number (Douglas and Ilias, 1988). It is a dimensionless number used to describe the curvilinear motion of a particle. However, the scenario is more complex and retention is expected to depend on the breach shape, particle stickiness, presence of vapors, agglomeration, fragmentation, resuspension, etc. As it will be seen later on, inertial impaction, turbulent deposition and resuspension are the driving mechanisms that determine aerosol depletion.

$$\text{Stk} = C_c \frac{\rho_p \cdot U_g \cdot d_p^2}{18 \cdot \mu_g \cdot d_t} \quad (1.2.1)$$

- Secondary side: the “support plate”. Velocities are expected to decrease considerably with respect to the break point. The passages in the support plate are narrow enough that there exists a potential for inertial impaction on the surface. However, compared to the retention in the break vicinity, the retention at the support plate is low.
- Secondary side: “beyond the break stage”. The flow will be mainly in the vertical direction and little retention by inertial impaction is expected (velocities around 0.2 m/s). However, expected enhanced recirculation in the U-bend region might modify the retention process.
- Separators and dryers. Their complex geometry produces very complex flow patterns and velocities. Inertial impaction, interception and turbulence initiated particle agglomeration are the main processes that could have a role. However, due to the low velocities and the small aerosol size expected, the anticipated removal efficiency is expected to be small.

Other processes like thermophoresis can not be entirely ruled out of the scenario. Likewise, particle-particle and particle-vapor interaction, agglomeration, fragmentation and condensation could have a role. They would change particle population and size distribution. Possible flow recirculation between the outlet of the separator and the riser through the downcomer would additionally enhance the particle removal (Allelein et al., 2009).

For accident management purposes, water injection in the dry secondary side may be an option in order to re-establish heat removal and provide a pool where the incoming aerosols can be scrubbed. According to pool scrubbing studies, main removal mechanisms would happen in the jet

inlet region, where particles would be driven towards the aqueous phase either by diffusiophoresis (in case condensation took place) or by inertial and centrifugal mechanisms (given the high velocities at the breach). Farther in the so called rise region, bubbles containing particles would experience further decontamination, essentially driven by centrifugal forces and flow constraints imposed by support plate (Allelein et al., 2009).

Regarding aerosol characterization during a severe accident, particle size is expected to range from 0.01 to 20 μm . Their size is commonly reported in terms of a lognormal distribution, which agrees with the distribution found in containment during the Phebus-FP experiments (Allelein et al., 2009). These experiments showed that the particles produced consist roughly of 33% structural and nuclear fuel material, 33% control rod material and 33% fission products (Kissane, 2008). However, these particles might not be representative of those encountered during a severe accident SGTR sequence. In this type of sequence, the chemical composition of a prototypical particle is unknown (Sánchez-Velasco et al., 2010).

1.3. BACKGROUND AND FRAME OF THE WORK

In order to investigate source term retention during SGTR sequences arises the EU-SGTR project (2000-2002) of the 5th Framework Program of EURATOM. Its first objective was to generate a comprehensive database on fission product retention in a steam generator. The second one was to verify and develop predictive models to support accident management interventions during steam generator tube rupture sequences (Auvinen et al., 2005). Its natural extension was the ARTIST project (AeRosol Trapping In a Steam Generator, 2003-2007), a seven-phase project that sought to fulfill the database and model development (Güntay et al., 2004). The investigation is presently being continued until the end of 2011 under the frame of a second stage of the ARTIST project, called ARTIST II (Lind et al., 2008).

These projects have demonstrated experimentally that some retention should be expected and that it would be highly dependent upon governing thermal-hydraulic conditions and the location and size of the break (Auvinen et al., 2005; Güntay et al., 2004; Herranz et al., 2006). Particularly, the presence of water in the secondary side appears to be a key factor (Güntay et al., 2004), since a substantial fraction of particles carried by gas might be scrubbed by the water. This is the reason supporting flooding of the failed steam generator as an accident management measure to minimize the release of fission products from a defective steam generator (Güntay et

al., 2001). However, even if no water is present, gas interaction with internal structures (i.e., tubes, support plates, separator, etc.) could result in some fission products and aerosol retention.

CIEMAT has participated in these projects with the aim to characterize theoretically and experimentally the particle retention in the “break stage” of the SG under “dry” conditions. This scenario is particularly relevant for two main reasons: local particle deposition in that area under “dry” conditions could be seen as the lowest bound of decontamination capability of secondary side; removal of particles entering with carrier gas would change the characteristics of the remaining aerosols that would flow upwards and would be partially retained onto upper structures.

Experimentally, CIEMAT performed the SGTR (Herranz et al., 2006), CAAT (Sánchez-Velasco et al., 2010) and CAHT (Velasco et al., 2008) experimental campaigns at the PECA facility. The rig consisted of a gas supply system, an aerosol generation device, a tube bundle, and a measurement system (i.e., sampling and instrumentation). The tube bundle was a mock-up of the break stage of the secondary side of a steam generator composed of 11x 11 tubes of 1.5 m high. The SGTR and CAAT tests allowed the analysis of the influence of the gas mass flow rate, type of breach (guillotine or fish-mouth; Fig. 1.3.1) and the particle nature on the aerosol retention, whereas the CAHT tests characterized the aerodynamic behavior of the gas across the bundle. It was seen that the aerosol mass retained in the bundle of tubes was lower than a 20% of the total injected mass (Fig. 1.3.2). The efficiency was also found to decrease when increasing the inlet gas mass flow rate ($\Phi \geq 100$ kg/h). Finally, from a quantitative point of view, the influence of the breach type, its orientation and location within the bundle was found to have secondary importance with respect to the flow rate one (Herranz et al., 2006).

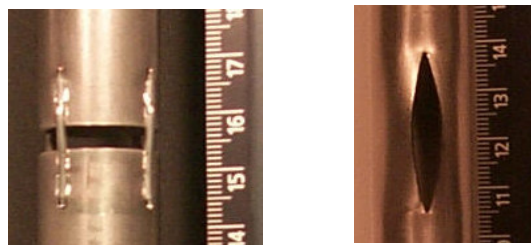


Fig. 1.3.1. Breach type configuration: guillotine (right), fish-mouth (left).

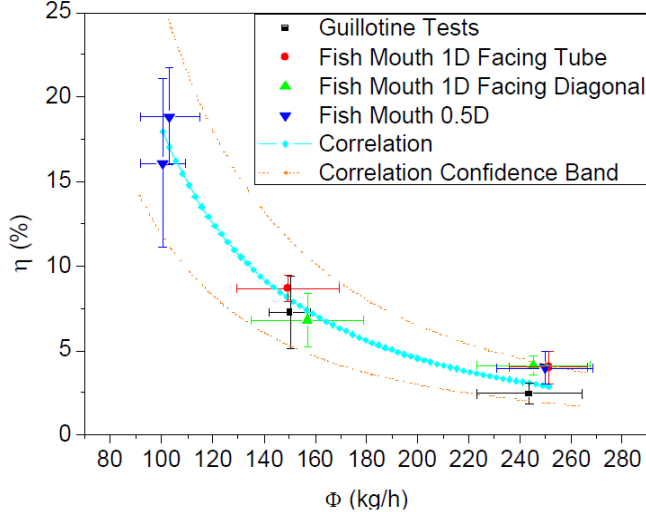


Fig. 1.3.2. SGTR collection efficiency (η) vs inlet gas mass flow rate (Φ).

Theoretically, the ARISG-I model (Herranz et al., 2007) was developed to estimate the aerosol deposition in the near-field of tube breach under dry conditions. ARISG-I was based on ‘filter concept’, which means that aerosol flowing through a bundle of obstacles is submitted to forces that tend to clean up the gas by removing particles onto obstacle surfaces.

Under foreseen SGTR conditions, the major deposition mechanisms in the break stage are turbulent deposition and inertial impaction. Turbulent deposition’s domain extends over a Stokes number (Stk) ranging from 0 up to 0.1. From this upper bound to higher Stokes numbers, inertial impaction becomes dominant. A database to develop individual models for turbulent eddy deposition and inertial impaction was set up based on literature survey (Wong and Johnstone, 1953; Ilias and Douglas, 1989). More than a hundred experimental measurements were compiled and from them, the following expressions for single tube filtration efficiencies were derived:

$$\begin{aligned} & \textit{Turbulent deposition:} \\ \eta_{\text{ST}}^{\text{tbt}} &= 0.438 + 0.0713 \ln(\text{Stk}) \end{aligned} \quad (1.3.1)$$

$$\begin{aligned} & \textit{Inertial impaction:} \\ \eta_{\text{ST}}^{\text{imp}} &= \frac{0.75}{1 + 29.31 \cdot \exp(-3.85 \cdot \text{Stk}^{0.5})} \end{aligned} \quad (1.3.2)$$

Using these expressions, total retention efficiency in the near-field of the tube breach was:

$$\eta_{TB} = 1 - \exp \left\{ - \frac{4 \cdot (s + d_t)^2}{4 \cdot (s + d_t)^2 - \pi \cdot d_t^2} \cdot \left[1 - \prod_{i=1}^{N_t} \left(1 - \frac{d_t}{s + d_t} \cdot \eta_{ST}(i) \right) \right] \right\} \quad (1.3.3)$$

In which N_t is the number of tubes over which deposition is considered (i.e., filtration depth), $\eta_{ST}(i)$ the individual efficiency of a single tube i , d_t the tube diameter and s the minimum distance between tubes.

ARISG-I was a step forward in the modeling of the aerosol retention of the steam generator. However, further development was needed mainly on aspects like: the in-bundle aerodynamic characterization for a more realistic velocity description, and the aerosol dynamics, for a more detailed description of the individual mechanisms responsible for aerosol deposition and/or removal of deposited particles from surfaces. In addition, an extensive validation exercise of the model should also be carried out (SGTR and CAAT data). On these bases, CIEMAT established a research program outlined in Fig. 1.3.3, for the development of a new model, the ARI3SG, which is the final goal of this work.

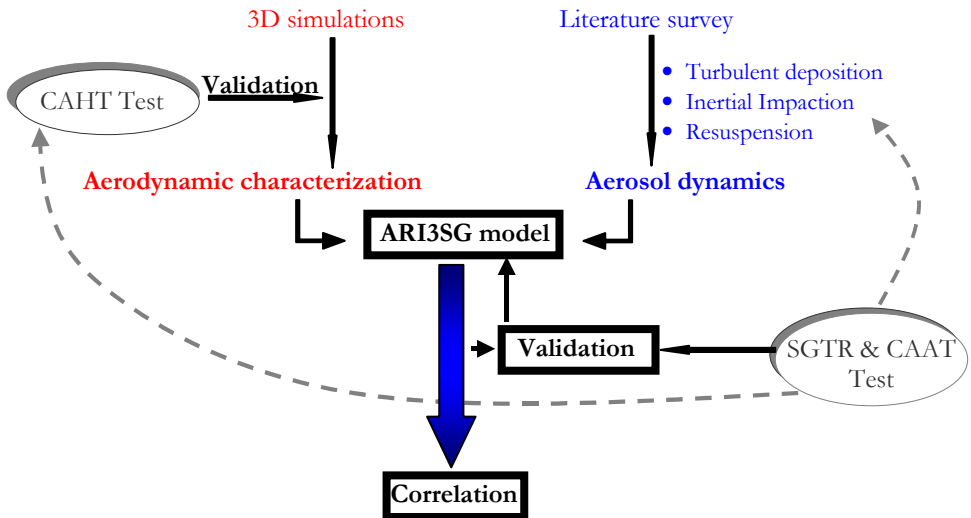


Fig. 1.3.3. Scheme of the research approach.

1.4. THESIS SETTING OUT: MOTIVATION, OBJECTIVES

The motivation of this thesis is to provide a predictive tool for estimating the retention capability of source term in the secondary side of a SG during a severe accident SGTR sequence. The model, hereafter called ARI3SG (Aerosol Retention In the Secondary Side of a Steam Generator) will enable safety codes to assess source term attenuation in severe accident SGTR scenarios. It could influence the results of the PRA level 2 and even change the risk-dominance of this type of sequences if high aerosol retention is found. If this is the case, it could modify accident management guidelines, which currently flood the failed steam generator to minimize the release of fission products from a defective steam generator.

The objective is to develop the ARI3SG model which is step forward in the modeling of the aerosol retention of the steam generator. In order to do so, several specific objectives have been drawn:

- To better estimate the gas hydrodynamics through the bundle (3D simulations).
- To refine specific aerosol models.
- To properly articulate aerosol modeling from the filter approach.
- To allow deposits to resuspend totally or fractionally.
- To build up a platform capable of estimating the retention efficiency on several scenarios.
- To validate the model with the available experimental data.
- To accompany estimates with epistemic and stochastic uncertainties.
- To derive a correlation based on non-dimensional numbers, easy to use in nuclear safety codes.

The scope of the modeling is the “break stage” under “dry” conditions. It appeared as the most unfavorable scenario from the safety point of view, due to the absence of pool scrubbing, with the most potential retention capability, since the break stage is the region where flow velocity reaches the highest values. The resulting retention efficiency could be seen as the

lowest bound of decontamination capability of secondary side of the steam generator.

This thesis is divided in four chapters. The first one introduces the importance the SGTR scenario and the frame in which this work has been developed. The second one is devoted to the modeling of the fluid flow behavior across the bundle of tubes of the SG. This analysis was performed through 3D simulations with the FLUENT 6.2 code. The work consisted first on the generation of the geometry with the subsequent meshing of the secondary side of the bundle of tubes. Two types of breaches were investigated: a guillotine type and a fish-mouth one. Second, the FLUENT case was determined and once the computations had converged, the results were verified through a numerical assessment. The results were validated against the ad-hoc experimental CAHT data obtained in the CIEMAT. Third, the flow behavior across the bundle of tubes was analyzed for both types of breaches, and from the results a 1 dimensional model was derived through theoretical correlations. They provided a better approximation for the velocity fields across the bundle.

The third chapter is devoted to the development of the model for the aerosol retention. It presents the hypothesis, approximations and development of the ARI3SG modeling. They were based on previous version ARISG-I which was thoroughly revised and improved. Depletion mechanisms modeled through experimental correlations were updated with new experimental data (literature survey), and a new model that considers depletion along the direction of the tubes was also introduced. As resuspension was seen to be highly relevant in the scenario, it was implemented in ARI3SG through an existing empirical correlation that was adapted to the scenario. Finally, ARI3SG accommodates the adaptations of the in-bundle velocity profiles derived from previous 3D simulations. The chapter also presents the FORTRAN platform developed to implement ARI3SG, which is capable of estimating the retention efficiency on several scenarios. A sound validation with the available SGTR and CAAT experimental data obtained in the CIEMAT was performed, the code being used as an interpretation tool. In addition, the effect of the associated uncertainties on ARI3SG was analyzed (epistemic and stochastic). This chapter ends with a derived theoretical correlation that encapsulates the aerosol retention efficiency as a function of non-dimensional numbers.

The fourth chapter presents the conclusions of the analysis, the final remarks and further work.

2. DEVELOPMENT OF FLUID FLOW MODELING

In the following section, it will be seen that aerodynamics of the gas carrying particles into the break stage of the secondary side of a “dry” steam generator is of utmost importance to fully understand the potential radioactivity retention in the break stage of a SG. Aerodynamics would determine to some extent particle depletion as in this case it is driven by inertial and turbulent mechanisms. Conversely, phoretic deposition processes were anticipated not to play any role due to the absence of thermal and steam concentration gradients in the scenario (Bakker et al., 2001; Güntay et al., 2002; Güntay et al., 2004).

The aerodynamic scenario of the break stage of a SGTR sequence is complex and specific. Apart from an experimental contribution from Velasco et al. (2008) and Sanchez-Velasco et al. (2007) which has been used to validate this research, no previous aerodynamic investigations were found in the open literature. However, numerical investigations carried out by other authors on scenarios with some similarities were reviewed to support the present research. Most of them pointed out that the turbulence model is a key issue to properly simulate the flow structure and transport phenomena.

Aerodynamics of an impinging jet and a flow across a tube bundle has been widely studied for heat transfer applications (Polat et al., 1989; Craft et al., 1993, Angioletti et al., 2005; Sagot et al., 2008; Meyer, 1994; Rollet-Miet et al., 1999; Benhamadouche and Laurence, 2003; Paul et al., 2008). Most of them analyzed the capability of different turbulence models to simulate a 2D flow configuration. Some of their most relevant outcomes for the present research are summarized next.

Meyer (1994) assessed the limitations and capabilities of the k- ϵ and Reynolds stress models (RSM) applied to the tube bundle problem. He discussed the inadequacy of wall functions and suggested the use of a low Reynolds number (Re) turbulence model (as the k- ω one) at the wall instead of wall laws. In a similar study, Paul et al. (2008) analyzed the performance of k- ω and Shear stress transport (SST) k- ω and found out that these models resulted in mean velocities closer to data in the developing region than other models. Consistently, Angioletti et al. (2005) stated that k- ω SST model provides the most accurate results for impinging jets under turbulent conditions, especially at low Re. This has been reinforced by the last data-predictions comparisons set by Sagot et al. (2008). Possibly, the most complete model survey was conducted by Bardina et al. (1997) who tested four turbulence models of the Reynolds

Average Navier Stokes (RANS) type on a total of ten different flows. All in all, the best model was the $k-\omega$ SST one, particularly capable of capturing boundary layer detachments.

This section explores the aerodynamics of the gas entering the break stage through a guillotine and fish-mouth breaches, by carrying out 3D simulations with $k-\omega$ SST turbulence model and with the FLUENT code. Particular emphasis has been given to the effect of inlet gas mass flow rate (from 75 to 250 kg/h) on gas velocity profiles. In addition, the influence of the breach shape on the jet topology has been analyzed by comparing guillotine results with those obtained from a jet emerging from a fish-mouth breach type. Once predictions are qualified and validated against experimental data (Velasco et al., 2008; Sanchez-Velasco et al., 2007), the 3D velocity profiles have been encapsulated into 1D correlations, whose applicability in the aerosol retention modeling presented in chapter 3 is straightforward as well as its possible use in current nuclear safety codes (i.e. MELCOR, ASTEC).

2.1. COMPUTATIONAL TOOL AND MODELING PERFORMED

2.1.1. The FLUENT code

The code used to investigate the 3D pattern of the gas flow was FLUENT 6.2 (Fluent, 2005). FLUENT is a commercially available CFD (Computational Fluid Dynamic) tool whose formulation and numerics have been profusely validated by a good number of research and industrial teams. Its capabilities in the field of fluid dynamics are at the forefront of the state of the art on this matter. Additionally, it was selected within the ARTIST project as the reference CFD tool, which fostered the scientific exchange among partners.

Once the geometry of the bundle of tubes of the scenario is defined and the domain nodalized with GAMBIT 2.2, Fluent solves the fluid flow by discretizing the conservation equations in each cell by numeric algorithms based on finite volume methods. The set of equations chosen to describe the system was the so called Reynolds Average Navier Stokes equations (RANS, Eq.(2.1.1)-(2.1.3)). The main reason for using RANS approach is the simplicity of the turbulent modeling when compared to other approaches. The scenario under modeling is highly complex and RANS provides robust results of the mean flow by simplifying local turbulent fluctuations, so a compromise between computational effort and results is reached. In addition, RANS modeling is supported by a good

number of researchers who have profusely validated for a good number of applications.

$$\text{Continuity: } \frac{\partial}{\partial x_i} \rho U_i = 0 \quad (2.1.1)$$

$$\text{Momentum: } \frac{\partial}{\partial x_j} \rho U_i U_j = -\frac{\partial}{\partial x_i} P + \frac{\partial}{\partial x_j} (\tau_{ij} - \rho \overline{U'_i U'_j}) + F_i \quad (2.1.2)$$

$$\text{Energy: } \frac{\partial}{\partial x_j} \rho U_i h_s = U_i \frac{\partial}{\partial x_j} \tau_{ij} + \frac{\partial}{\partial x_i} q_i + \phi \quad (2.1.3)$$

Turbulence effects have been simulated by adopting the SST $k-\omega$ model, as recommended by [Menter \(1994\)](#) in the case of flows in which adverse pressure gradients are set (typical in cylinder cross-flow configurations). This model may be understood as an evolution of the $k-\omega$ model, whose accuracy and numerical stability in the inner region of the boundary layer is supplemented with the less demanding $k-\epsilon$ model at the outer region of the boundary layer. A major feature of the SST $k-\omega$ model is the consideration of the main turbulent shear stress transport, which enables to predict adverse pressure gradients. [Bardina et al. \(1997\)](#) extensively tested and validated two-equation eddy viscosity models and showed a better performance of the SST $k-\omega$ model in complex flows with boundary layer separation.

The transport equations (Eq. (2.1.4)) of the turbulent kinetic energy (k) and its specific dissipation (ω) close the previous set of equations (Eq. (2.1.1-2.1.3)) together with the Boussinesq assumption, which makes Reynolds stress tensors ($\overline{U'_i U'_j}$) proportional (μ_t) to the mean velocity gradient (Eq. (2.1.5)):

$$\frac{\partial}{\partial x_i} (\rho \cdot \phi \cdot U_i) = \frac{\partial}{\partial x_j} (\Gamma_\phi \cdot \frac{\partial \phi}{\partial x_j}) + G_\phi - Y_\phi \quad (+D_\omega) \quad (2.1.4)$$

$$-\rho \cdot \overline{U'_i U'_j} = \mu_t \left(\frac{\partial U_i}{\partial x_j} + \frac{\partial U_j}{\partial x_i} \right) - \frac{2}{3} (\rho \cdot k + \mu_t \frac{\partial U_i}{\partial x_i}) \cdot \delta_{ij} \quad (2.1.5)$$

Where ϕ denotes the independent variable (k and/or ω) and G , Y and Γ represent generation, dissipation and effective diffusivity of the given

quantity, respectively. The ω transport equation adds an additional cross diffusion term (D_ω), which arises when merging $k-\omega$ and $k-\epsilon$ formulation. Description of these expressions can be found in literature (Menter, 1994; Bardina et al., 1997; Fluent, 2005).

The whole set of equations are solved by using a segregated implicit solver with a second order discretization scheme.

The overall geometry, hypotheses and boundary conditions used in the modeling of the break stage of a tube with a guillotine and/or a fish-mouth type breaches (Fig. 1.3.1) during a SGTR sequence are presented in the following sections. Both of them share most of these conditions, and the results are compared later on.

2.1.2. Development of the geometry and grid

Preliminary studies demonstrated that most of the jet momentum will occur in the vicinity of the breach (Herranz et al., 2005). This allowed simulating the SG break stage as if it was a square array of 11x11 tubes (0.33 x 0.33 x 1 m), supported by an upper and a lower plate. The bundle of tubes is bounded by vertical walls. The dimensions of the tubes and support plate are identical to those used in a stage of a SG of a nuclear power plant. The tubes are 0.019 m in diameter with a tube-to-tube spacing of 0.008 m (Fig. 2.1.1).

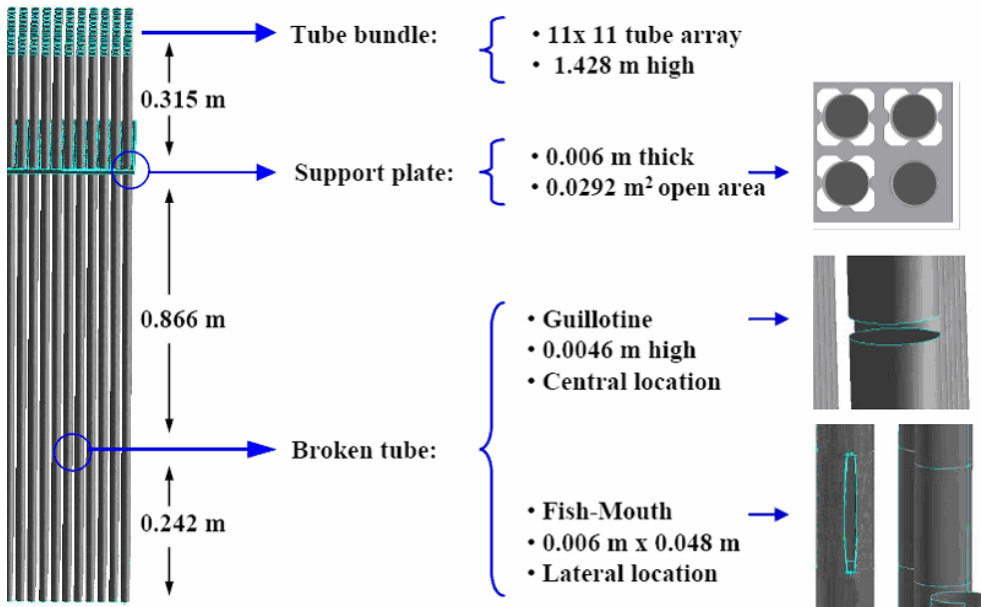


Fig. 2.1.1. Tube bundle configuration.

In the case of the guillotine breach, the broken tube is placed at the centre of the bundle so that the effect of the bounding walls is minimized. Whereas for the fish-mouth breach case, as the jet momentum penetrates further in the bundle, the broken tube is displaced two positions in order to prevent undesirable wall-jet interactions (Fig. 2.1.2 and Fig. 2.1.3). Both breaches whose heights are $h_{\text{guillotine}}=0.005$ m and $h_{\text{fish-mouth}}=0.04$ m are located at 0.25 m from the lower plate.

In both simulations, the flow is injected upward at the base of the broken tube. Since the end of the tube is closed, the flow is forced to exit through the breach and to expand across the bundle. This bundle configuration was identical to the one of the experimental CAHT facility (Velasco et al., 2008; Sanchez-Velasco et al., 2007), whose measurements were used for validation purposes. The facility will be outlined in the validation section later on.

Due to the symmetries and the breaches shape, 1/8 and 1/2 of the original domain was modeled for the guillotine and the fish-mouth cases, respectively. Each volume was meshed with hexahedral cells and a refined grid near the breach was set in order to capture the sharp velocity gradients of the jet shear layers (Fig. 2.1.2 and Fig. 2.1.3).

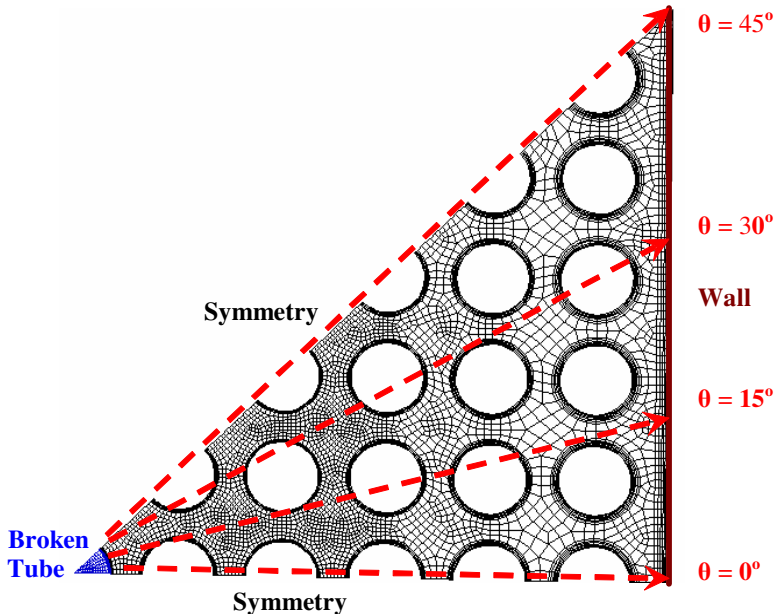


Fig. 2.1.2. Horizontal cross-section of the meshed domain (guillotine).

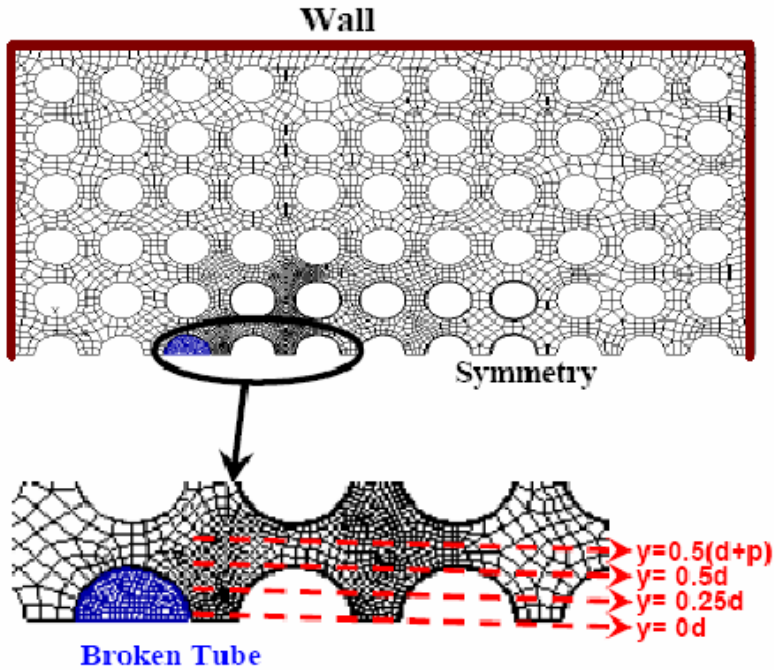


Fig. 2.1.3. Horizontal cross-section of the meshed domain (fish-mouth).

In the guillotine case, two initial grids were defined to assess grid independence: a coarse one of around 0.38 M cells and a fine one of around 1.6 M cells. Both of them were refined in order to describe in more detail boundary layers, which were initially described with more than 10 cells.

In the fish-mouth case, the domain was discretized with a mesh of 1.2 M cells. In one of these cases, grid independence was assessed through a refined version of around 1.29 M cells, since the volume increase and the computational capabilities prevented to define a higher grid density. Such a refinement has a local nature, so that a larger amplification was obtained of the region close to the breach and some tube surfaces capturing the strongest velocity gradients and increasing boundary layer description.

Both meshes were designed according to Best Practices Guidelines (Menter et al., 2002; Mahaffy et al., 2007) so that numerical diffusion was diminished and accuracy and convergence was enhanced by achieving a good quality of the grid (Mahaffy et al., 2007):

√ **Guillotine:**

- Aspect ratios (i.e., ratio between the maximum and minimum averaged edges lengths) are mostly smaller than 50 in regions far from boundary layers (73% of cells). In boundary layers (27%) higher aspect ratios are seen as acceptable.
- Angle and size skewness (i.e., a measure of cells deviation from perfect equilateral cells) are smaller than 0.1 in around 80% of the cells.
- The growing factors (i.e., ratio between the sizes of consecutive cells) used to generate the grid are smaller than 1.4.

√ **Fish-mouth:**

- 87% of the cells have aspect ratios smaller than 50.
- Angle and size skewness are smaller than 0.2 in 70% of the cells.

2.1.3. Hypothesis and boundary conditions performed

Hypothesis and boundary conditions were common to both guillotine and fish-mouth breach simulations; they are described as follows and summarized in Table 2.1.1.

Gas flow modeling required adoption of hypotheses concerning three main aspects:

- Compressibility. The gas flow was considered compressible. Gas mass flow rates in the upper bound of the range explored (75-250 kg/h) yield Mach numbers higher than 0.3, at which point gas density changes appear.
- Steadiness. Boundary conditions were kept constant so that steady state equations were used.
- Turbulence. At the gas mass flow rates explored, the flow is highly turbulent. Inlet and outlet turbulent intensities (TU) need to be defined and were estimated to be 4% and 7.2%, respectively, by (Fluent, 2005):

$$TU = 0.16 \cdot Re_{D_h}^{-1/8} \quad (2.1.6)$$

Where Re denotes the nondimensional gas Reynolds number and D_h correspond to the hydraulic diameter of the inlet tube surface and /or outlet bundle surface.

2. Development of fluid flow modeling

In addition to gas flow assumptions, domain boundaries were defined by:

- A wall, non-slip boundary condition at the tube surfaces, at the lower plate and at the vertical surfaces.
- A symmetry boundary condition at 0° and 45° planes for the guillotine case (Fig. 2.1.2) and at 0° for the fish-mouth one (Fig. 2.1.3), at which flow field is expected to be highly symmetric.
- An absolute pressure condition downstream the upper plate ($1.3 \cdot 10^5$ Pa).

And finally, specific approximations regarding components of the system:

- The upper plate was modeled as a porous medium. The pressure loss coefficient due to the sudden contraction of the cross section of the flow area was empirically estimated to be $k_1 = 3.254$. The pressure drop is then computed as $\Delta P = k_1 \frac{\rho_g U^2}{2}$. Given the small thickness of the plate (0.006 m), viscous losses were neglected.

Table 2.1.1. Hypotheses and Boundary Conditions of 3D simulations.

Breach type		Guillotine	Fish-mouth
Compressibility		√	√
Steadiness		√	√
Turbulence model		SST k- ω	SST k- ω
Inlet	Position	Base of broken tube	Base of broken tube
	Φ	75, 150, 250 kg/h	75, 250 kg/h
	TU	4%	4%
Outlet	Position	Top lid of bundle	Top lid of bundle
	P	$1.3 \cdot 10^5$ Pa	$1.2 \cdot 10^5$ Pa
	TU	7.2%	7.2%
Walls with non-slip condition		Vertical surfaces, tubes, lower plate	Vertical surfaces, tubes, lower plate
Symmetry planes		$\theta=0^\circ, \theta=45^\circ$	$y = 0$
Porous media		Upper support plate	Upper support plate
$\Delta P = k_1 \frac{\rho_g U ^2}{2}$		$k_1 = 3.254$	$k_1 = 3.254$

2.1.4. Assessment of numerics and mesh quality

Two convergence criteria were required for the calculations to be considered satisfactory:

- Low and steady values of scaled residuals ($\leq 10^{-3}$).
- Steadiness of specific variables characterizing gas jet aerodynamics, like mean velocity, turbulent kinetic energy and specific dissipation rate.

Once convergence was met, results were proven to be grid independent (i.e., finer grids do not lead to different predictions). In the case of the guillotine breach, grid independence was explored through the results obtained from several meshes. It is illustrated in Table 2.1.2 through some aerodynamic variables particularly significant for particles deposition on tube surfaces by inertial impaction and/or eddy deposition (i.e., mean wall shear stress, τ_w , and velocities). As observed, the comparison of these values for both Coarse and Fine meshes differ in less than a 10%. In all the cases the y^+ (i.e. non-dimensional wall distance, see Appendix A.4) values reached ensure the good resolution of the flow within the boundary layer. Scaled residuals may be noted to meet the above criterion. In the fish-mouth breach, a refined mesh assessed this analysis for the 250 kg/h case (Table 2.1.3). As observed, differences of wall shear stresses and velocities are less than a 5% and residuals reach previous low values. However, y^+ values exceed the recommended maximum 5 (Fluent, 2005). It must be noticed that these values are an average performed over all surfaces and that they are around 1.5 in the regions near the breach where turbulence is higher.

Table 2.1.2. Numerical results of guillotine 3D simulations.

Case	75 kg/h		150 kg/h		250 kg/h	
	Coarse	Fine	Coarse	Fine	Coarse	Fine
Mesh						
Number of cells	379760	1582905	373334	1582905	431546	1582905
Scaled Residuals	10^{-4}	10^{-3}	10^{-3}	10^{-3}	10^{-4}	10^{-4}
Order of discretization	2 nd					
Mean y^+	1.14	0.47	1.85	1.09	2.63	1.35
Mean τ_w (Pa)	0.05	0.042	0.17	0.164	0.36	0.38
$ U _{\max}$ (m/s)	89	90	160	167	248	250
$ U _{\text{mean, breach}}$ (m/s)	62.41	64.34	116	120.2	170.77	175
$ U _{\text{mean, outlet}}$ (m/s)	0.186	0.208	0.37	0.41	0.63	0.69

2. Development of fluid flow modeling

Table 2.1.3. Numerical results of fish-mouth 3D simulations.

Case:	75 kg/h	250 kg/h	
Number of cells	1200195	1200195	1288633
Scaled Residuals	10^{-5}	10^{-5}	10^{-5}
Order discretization	1 st , 2 nd	1 st , 2 nd	1 st , 2 nd
Mean y^+	11	24	23
Mean τ_w (Pa)	0.07	0.43	0.44
$ U _{\max}$ (m/s)	163	379	369
$ U _{\text{mean, breach}}$ (m/s)	114	248.6	246
$ U _{\text{mean, outlet}}$ (m/s)	0.3	0.68	0.69

Overall, the Fine mesh provided smoother profiles and higher maximum velocities. Fig. 2.1.4 displays velocity profiles along two vertical lines placed at different locations for the guillotine simulation of 250 kg/h. From now on, the layout of the results will be presented in cylindrical coordinates (r , θ , z) whose axial origin is set at the lower part of the breach and the radial one, starts just at the surface of the broken tube (sketch of Fig. 2.1.4). The maximum located at a height close to the breach corresponds to the velocity of the jet emerging from the break into the secondary side. At this location as well as at both sides of the maxima, both meshes provide the same flow behavior. In absolute values, velocity magnitudes agree, deviations being less than 15% at the jet core.

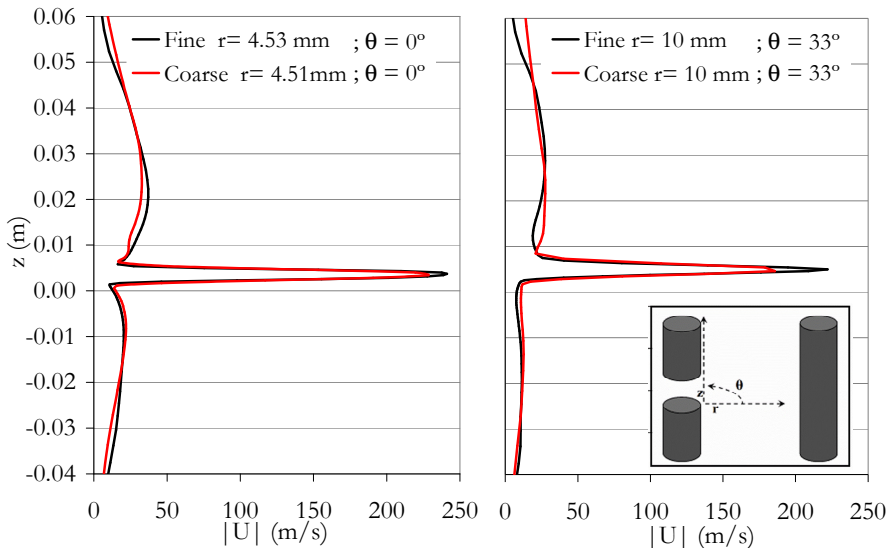


Fig. 2.1.4. Vertical velocity profiles (250 kg/h).

2.1.5. Validation of the simulations

Validation of the simulations was carried out against a data base built-up for this purpose, the so called Cimat Artist Hydrodynamic Tests, CAHT (Herranz et al., 2008; Velasco et al., 2008; Sanchez-Velasco et al., 2007). A mock-up facility consisting of a tube bundle of 11x11 rows was used to simulate the break stage of the SG, whose dimensions were similar to those already described in previous section 2.1.2 (Geometry and grid). The bundle was bounded by a vertical methacrylate structure that permitted the investigation of the jet aerodynamics with optimal optical access. A standard 1660x1200 pixels PIV (Particle Image Velocimetry) cross-correlation CCD camera, a pulsed Nd:Yag laser and two different lenses (28 and 300mm F2.8) were used to record the images obtaining the fluid velocities. Fig. 2.1.5 shows the CAHT experimental facility and a sketch of the region between tubes captured by the camera. Additionally, a Pitot tube was used to characterize specific regions of the fluid domain. Uncertainties in PIV and Pitot tube measurements of the mean velocity field were estimated to be less than 35% and 10%, respectively, within a 95% of confidence level. The inlet tube mass flow rate was varied in the experiments from 75 to 250 kg/h. TiO_2 was used as seeding material.

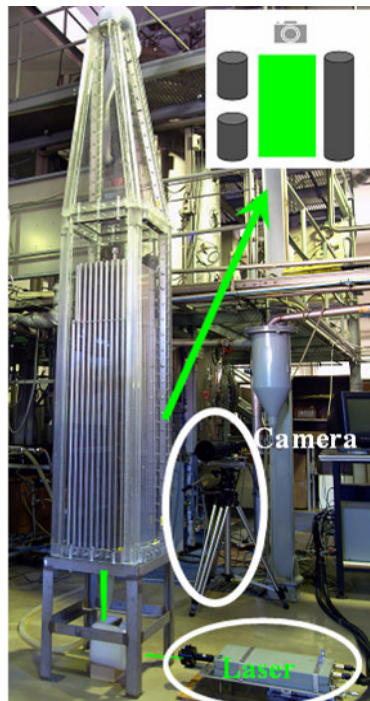


Fig. 2.1.5. Experimental CAHT configuration.

A. Validation of guillotine breach simulations:

Fig. 2.1.6 compares FLUENT predictions obtained in the space between the broken tube and the first neighbor and the equivalent PIV measurements of velocity fields acquired in the CAHT campaign (Herranz et al., 2008; Velasco et al., 2008; Sanchez-Velasco et al., 2007).

FLUENT blank contours mean that velocities in those regions are higher than the range plotted (i.e., up to 52 m/s). Overall the experimental description and the theoretical one are consistent: once impacting the neighbor tube, the gas exiting the breach in form of a jet splits in upwards, downwards and sideways streams (just the two former can be observed in the plot). The jet causes a noticeable entrainment of the fluid around, both at the upper and at the lower region. Nonetheless, again consistently with data, FLUENT anticipates a more substantial suction above than below the jet. This is due to the parabolic trajectory of the jet that promotes a recirculation on the concave region. This trajectory results from the combination of three factors: the initial vertical component of the jet; the presence of tubes, which through the Coanda effect fosters gas motion along tube surfaces; and the gas drift due to the location of gas exit at the top of the facility.

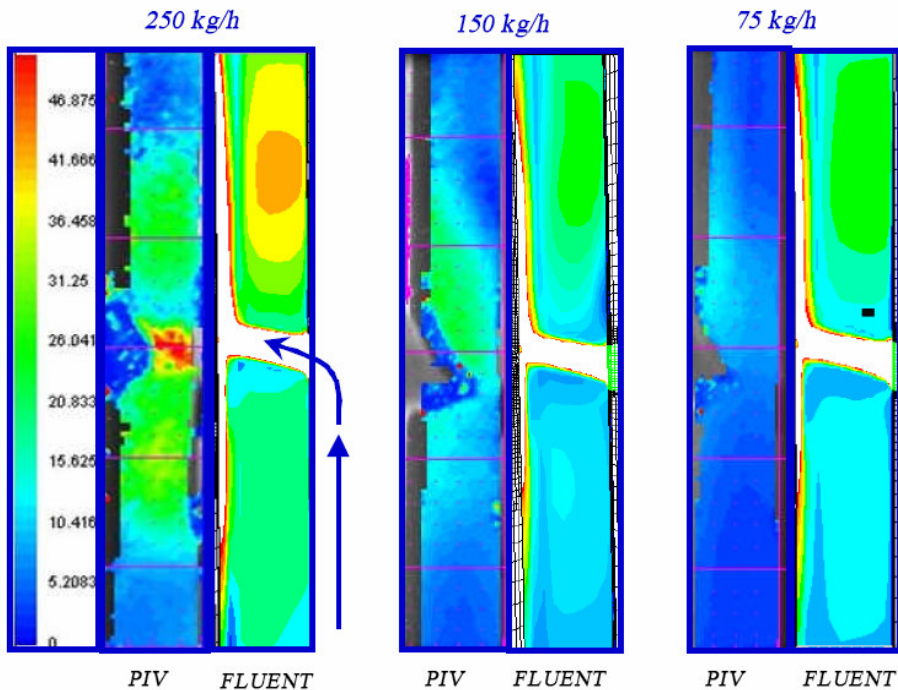


Fig. 2.1.6. PIV and FLUENT velocity fields of guillotine breach simulations.

Given the need of a particle laden gas in the PIV technique, a deposit built up on the surface of the neighbor tube just in front of the breach. As it possibly affected particle trajectories flying towards the tube, no credit was given to PIV measurements in that region. Therefore, complementary Pitot tube data were included in the analysis. They were obtained at $1/3$ of the tube spacing obtained in a free jet configuration. As discussed by Sanchez-Velasco et al. (2007), they provide more reliable velocities in the region of jet core near the breach as PIV measurements in this location suffer from some experimental drawbacks. This comparison is considered meaningful since at such a short distance from the breach, no major effects on velocity magnitude due to the presence of tubes are expected.

Fig. 2.1.7 allows a quantitative comparison between predictions and data along three vertical lines located at $1/3$, $1/2$ and $3/4$ of tubes spacing (s) (see sketch of Fig. 2.1.7) for the case 250 kg/h. FLUENT captured the experimental profile and its accuracy can be considered reasonable. Major deviations found in the core region are around 8% with respect to the Pitot tube readings. A good agreement is also found in the cases of 150 and 75 kg/h (Fig. 2.1.8). As observed, Fluent slightly over predicts PIV measurements in the region above the breach, whereas it underpredicts around 25% Pitot jet core velocities, this could be caused by slight differences in the boundary conditions between the test and simulations. However, predictions are well within the experimental uncertainty band.

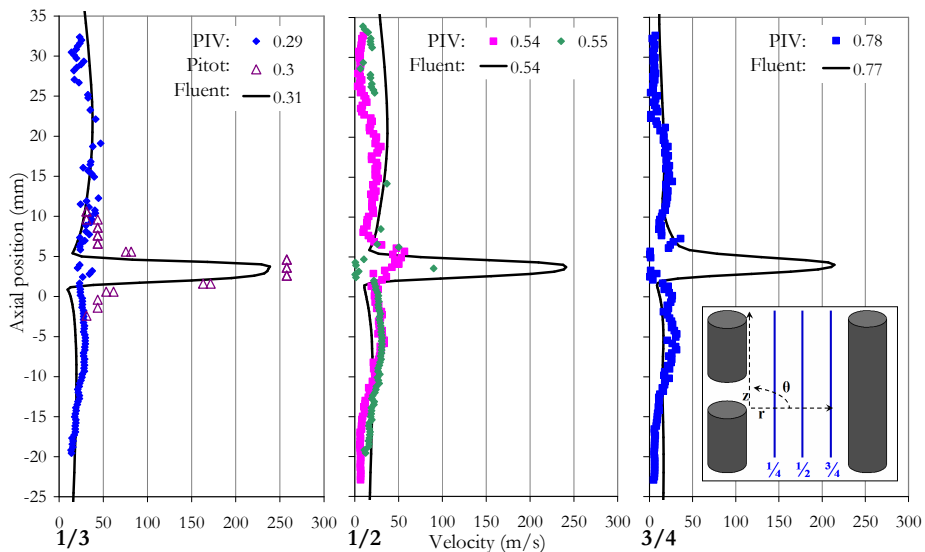


Fig. 2.1.7. Guillotine velocity profiles at 0° , $r/s=1/3$, $1/2$ and $3/4$ (250 kg/h).

2. Development of fluid flow modeling

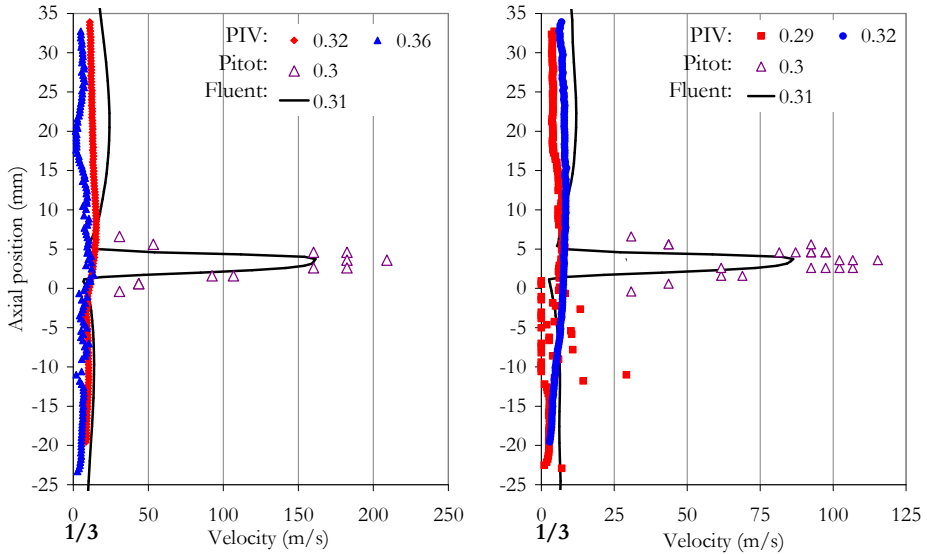


Fig. 2.1.8. Guillotine velocity profiles at 0° , $r/s = 1/3$ (left: 150 kg/h; right: 75 kg/h).

This validation is further supported by indirect comparisons of previous simulations to SGTR aerosol experiments where particle deposit locations were consistent with the gas flow pattern outlined (Appendix A.1). Fig. 2.1.9 shows a sample of these tests. According to FLUENT predictions, particle accumulation on the facing tube might be due to inertial impaction, and “over-the-breach” deposits on the broken tube might be a consequence of the jet suction from the quiescent gas that was forced to flow downwards adjacent to this tube.

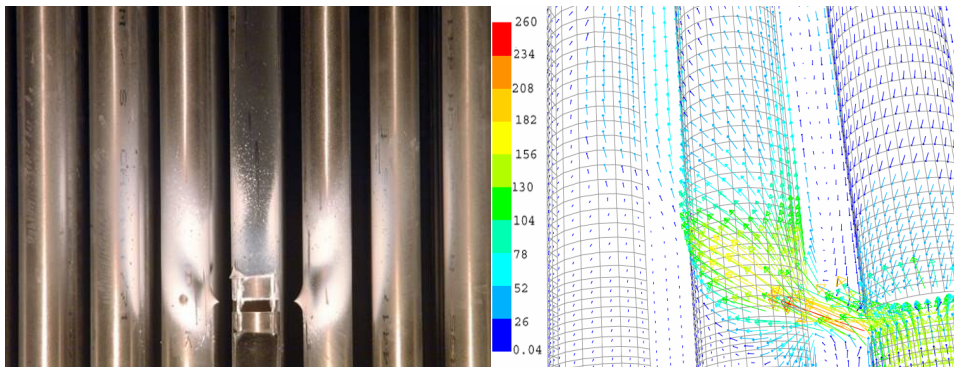


Fig. 2.1.9. Particle deposits and FLUENT prediction.

B. Validation of fish-mouth breach simulations:

Fig. 2.1.10 shows PIV measurements and FLUENT results in the space between the broken tube and its closest neighbor (75 kg/h). Both figures are normalized independently with respect to their individual maximum. Globally, the theoretical and experimental results are consistent: both cases show a quasi top-hat velocity profile, with minor differences. Velocity vectors orientation show a great similarity, except for the lower part of the breach, where PIV data slightly increases with respect to mid and upper regions of the breach. Both experimentally and analytically, the maximum velocities are reached at a radial distance of 3 mm from the breach.

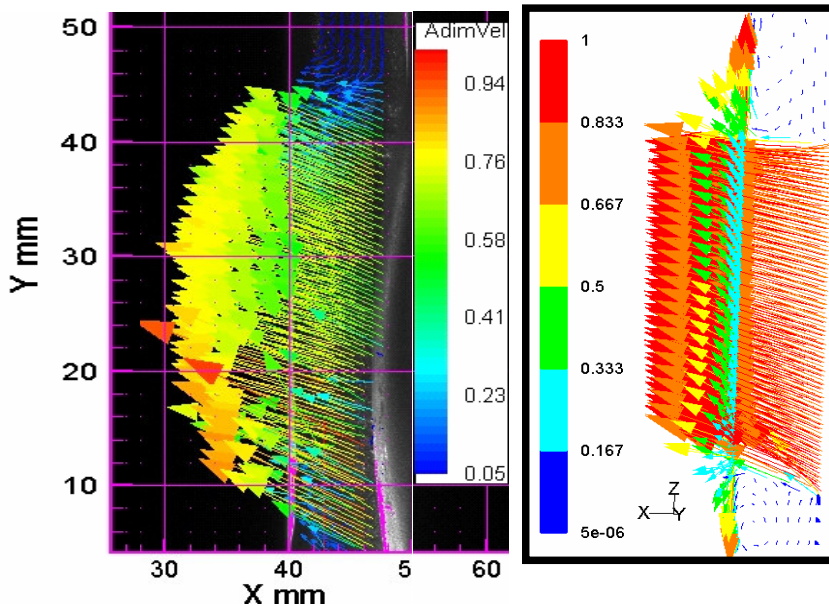


Fig. 2.1.10. Fish-mouth normalized velocity vectors: PIV (left) FLUENT (right).

Fig. 2.1.11 shows vertical profiles of absolute velocities at around 1/3 of the spacing. As observed, simulation estimates and PIV data differ around a 50%, whereas the comparison to Pitot readings shows an outstanding qualitative and quantitative agreement which supports FLUENT consistency.

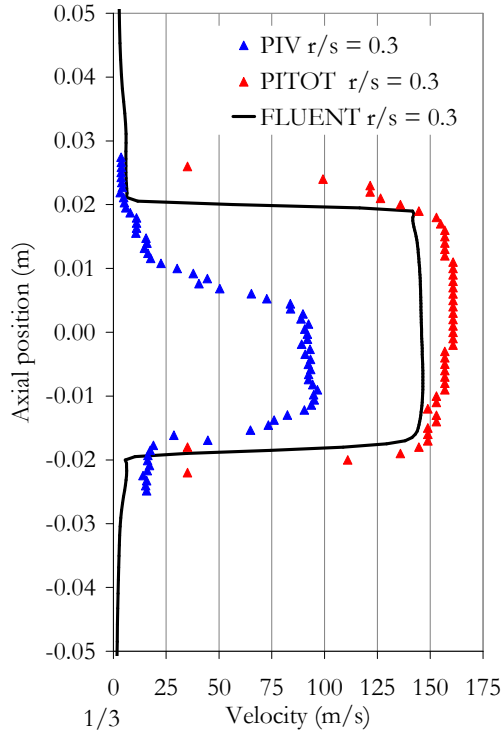


Fig. 2.1.11. PIV, Pitot and FLUENT velocities at 0° , $r/s=1/3$ (75kg/h;fish-mouth).

2.2. AERODYNAMIC RESULTS OF THE SIMULATIONS

The analyses of the simulations were essentially focused on the characterization of the jet entering the bundle from a guillotine and/or a fish-mouth breach configuration. Therefore, this section presents the analysis of each breach shape simulation, describing the flow pattern across the bundle, with particular emphasis on the evolution of radial and axial velocities. Then both resulting jets are compared.

2.2.1. Guillotine breach analysis

Table 2.2.1 gathers some meaningful velocities of the simulations. As noted, jet accelerates as exiting the breach ($|U|_{\max, \text{breach}} < |U|_{\max, \text{bundle}}$) due to the small pressure jump between primary and secondary sides of the system. As experimentally observed, velocities increase linearly with the mass flow rate; so to say, compressible effects do not become significant in the range of mass flow rates analyzed.

Table 2.2.1. Guillotine 3D simulation results.

Mass flow rate (kg/h)	75	150	250
$ \mathbf{U} _{\text{mean, breach}}$ (m/s)	64	120	175
$ \mathbf{U} _{\text{max, breach}}$ (m/s)	71	134	200
$ \mathbf{U} _{\text{max, bundle}}$ (m/s)	90	167	250

Jet evolution across the bundle can be observed in Fig. 2.2.1, which shows the velocity fields at different heights for the 250 kg/h and 75 kg/h cases. Note that in quantitative terms, colors have a different meaning in each plot, since the scales are different. Nonetheless, they show that the initial expansion of the jet is similar, regardless the inlet mass flow rate. However, at a certain height the effect can be noted. Thus, the higher mass flow rate the deeper penetration (the fluid surpasses the 2nd row of tubes for the 250 kg/h case, whereas it barely reaches it for the 75 kg/h case).

The presence of tubes affects the jet trajectory radially and axially. As the jet impinges on tubes two major effects are observed. In the radial direction, jet impingement on the tubes makes it flow along those directions where resistance is minima (fewer obstacles). This effect, more noticeable at high mass flow rates, causes the gas to move preferentially in diagonal directions. In the axial direction, once on the tube surface, a fraction of the jet is driven upwards around the tube, as if it was attached. This behavior may be attributed to the so called Coanda effect (Schlichting and Gersten, 2000; Schuh and Persson, 1964), and it becomes more noticeable as the radial momentum becomes small. The net result is an enhancement of the axial orientation of the jet.

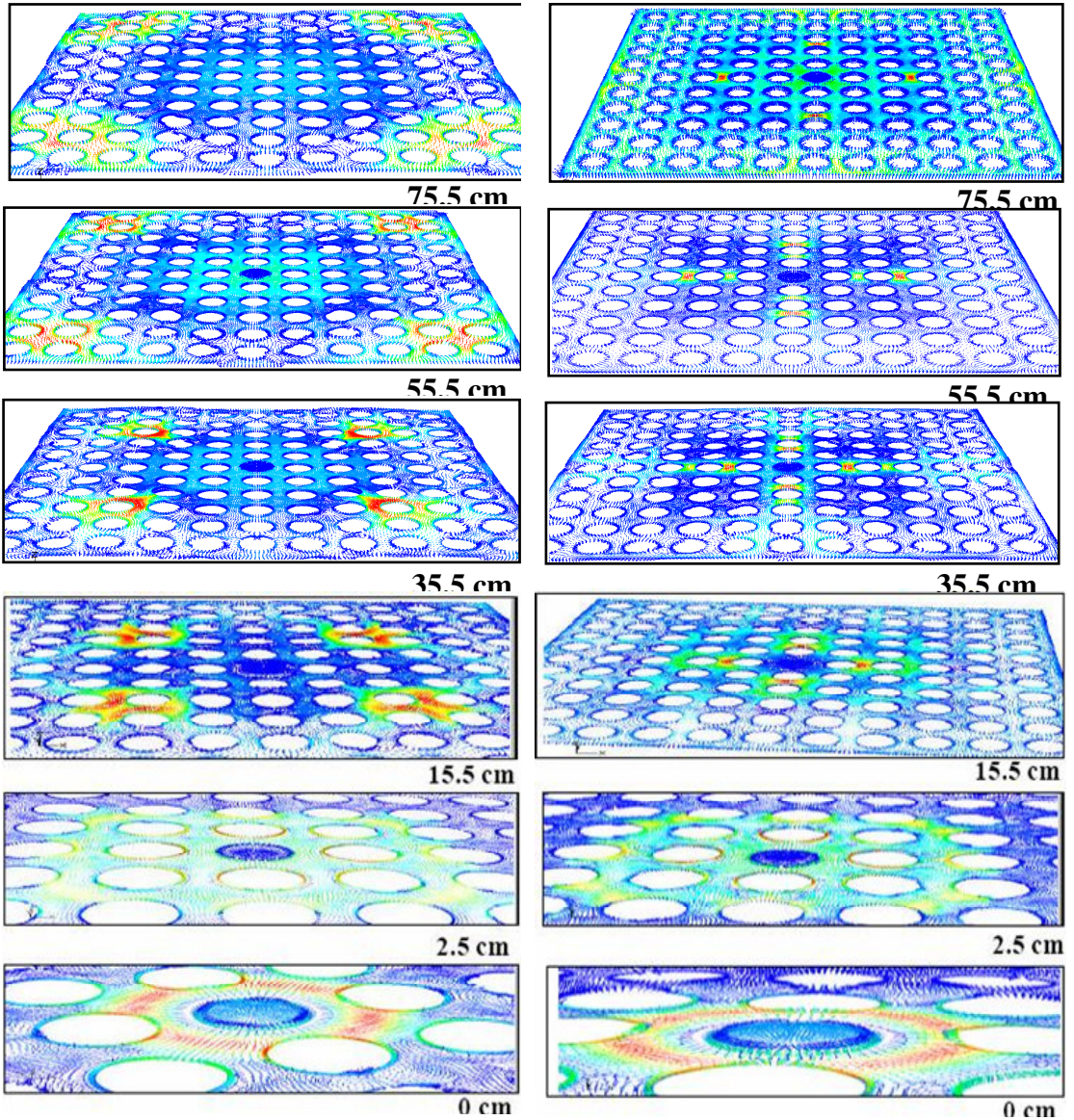


Fig. 2.2.1. Guillotine velocity magnitude vectors: 250 kg/h (left), 75 kg/h (right).

Radial and axial velocity components have been analyzed along four different azimuthal directions (i.e., 0° , 15° , 30° and 45° , Fig. 2.1.2). Fig. 2.2.2 shows the normalized maximum radial velocity as a function of the distance from the breach. The latter is expressed in a dimensionless way by defining a unit length as the distance from the breach to the first tube in

each of the directions analyzed (black vertical lines in the plot representing a tube location). Note that velocity normalizations have been performed independently for each case (250 kg/h and 75 kg/h).

Once radial velocity reaches a maximum at around 1/3 of the first spacing (expansion effect), it decreases monotonously but differently depending on direction. Along 0° and 45° , where the jet impinges the first neighbor tube surface in a nearly cross flow configuration, the profiles are similar: they sharply decrease right at the tube surface to very low values and show a bump in their profiles at the region in-between first and second tubes. Slighter higher velocities may be noted in the diagonal direction (45°).

At directions between 0° and 45° (i.e., 15° and 30°), the jet does not approach the tubes normally but tangentially, which makes their radial velocity evolve in a more continuous way. It is this different behavior between 0° and 45° planes and 15° and 30° the reason for the scattering observed in the second spacing along diagonal directions.

Regardless direction, from the second tube on, normalized radial velocities nearly vanish.

The inlet mass flow rate does not yield any difference in the radial jet behavior. In other words, the decreasing trend of the radial velocity as the jet penetrates across the tube bundle has a generic nature. Of course, as said above, when the natural radial distance is considered, radial reorientation of the jet makes radial velocities hold noticeable values at deeper locations.

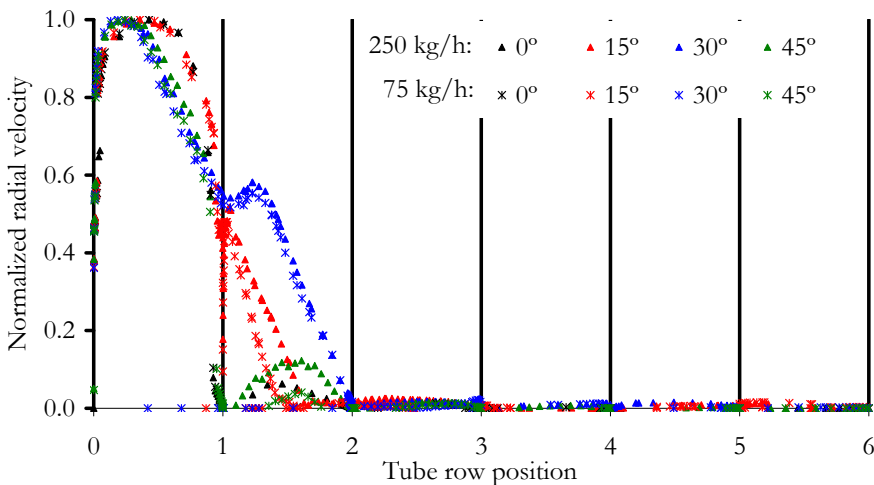


Fig. 2.2.2. Normalized maximum radial velocity vs tube row position (guillotine).

As normalized, axial velocity shows also a flow rate independent, decreasing tendency with distance from the breach (Fig. 2.2.3). The maximum velocities are attained in the first spacing of the 0° direction, as the radial momentum of impacting jet (transformed into the axial) is higher at that location. Anyway, it can be observed that at 10 cm above the breach, velocities have decreased to 10% of the maximum. From then on, velocity keeps on diminishing but with a milder slope.

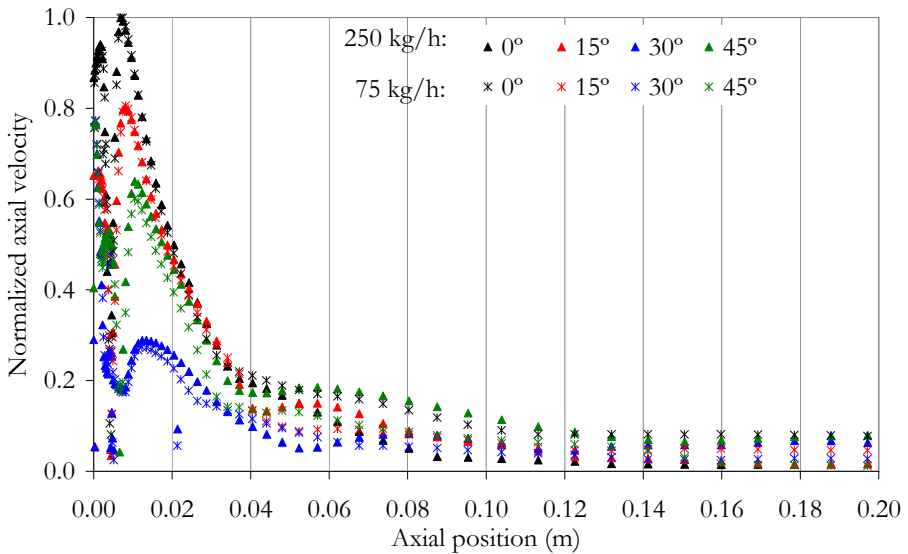


Fig. 2.2.3. Normalized maximum axial velocity vs axial position (guillotine).

Appendix B contains some of the postprocessing fortran files developed for obtaining previous maximum profiles.

2.2.2. Fish-mouth breach analysis

The jet emerging from a fish-mouth breach and flowing across the bundle can be observed in Fig. 2.2.4, Fig. 2.2.5 and Fig. 2.2.6 (250 kg/h). The gas coming out from the breach has a substantially dominant radial velocity component (Fig. 2.2.4). The remaining axial component at the bottom of the breach is practically inexistent at the top. This local orientation makes the lower region of the jet converge to its upper region as it moves into the bundle. The presence of tubes reinforces this effect due to the loss of radial momentum and enhancement of vertical motion

caused by the Coanda effect. The final result is narrowing of jet front as it moves into the bundle.

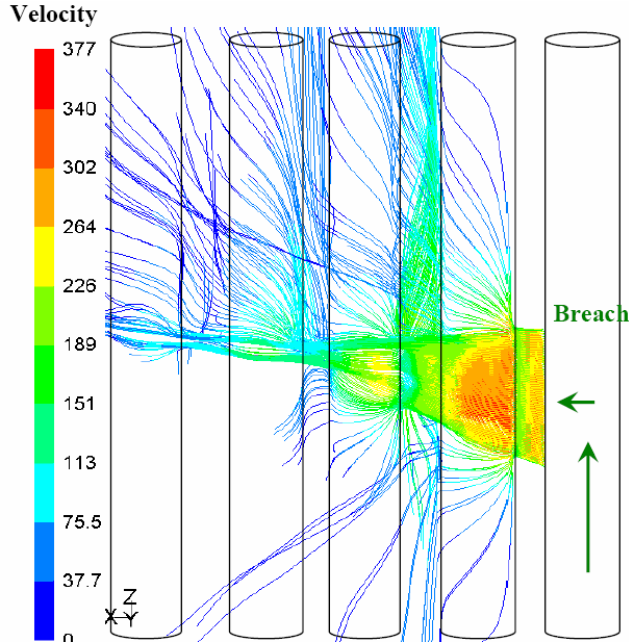


Fig. 2.2.4. Vertical view of velocity streamlines (250 kg/h, fish-mouth).

As noted, jet spreading is noticeably limited in the azimuthal direction (Fig. 2.2.5). The jet exiting the breach hits almost entirely the facing tube row and expands azimuthally in a pseudo-triangular way. In the axial direction, the main jet stream line draws a quasi-parabolic shape with a high initial radial displacement. Once the jet is intercepted by a tube in the facing row, a fraction is diverted and it moves upwards until eventually escaping through the top lid of the bundle.

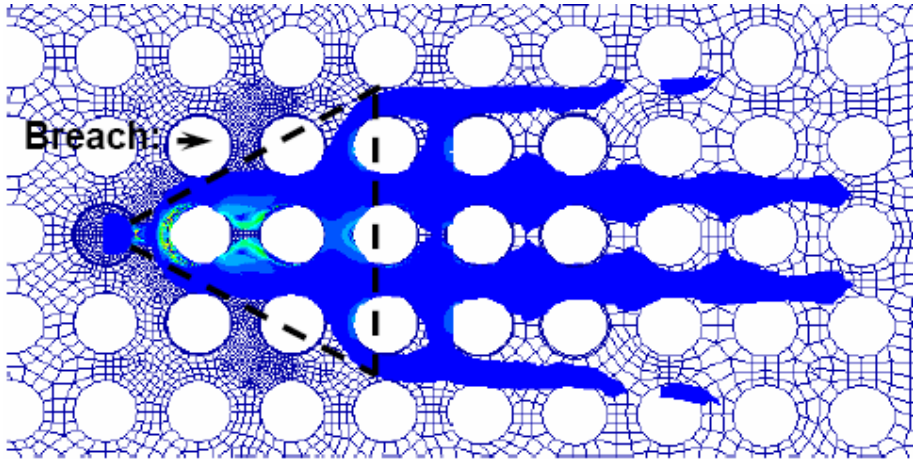


Fig. 2.2.5. Top view of velocities higher than 10 m/s (250 kg/h, fish-mouth).

Fig. 2.2.6 compares velocities at different horizontal cross-sections for the 250 kg/h and 75 kg/h cases. Despite the same colors in the figures, the actual quantitative scales are different. As observed, figures show analogous jet expansions and a noticeable suction from the fluid surrounding the jet.

The main difference arises from the inlet mass flow rate effect. As expected, the higher the mass flow rate the deeper penetration (at 250 kg/h the fluid exceeds the 8th row of tubes, whereas at 75 kg/h it barely reaches the 7th row). In addition, at a height of 1.5 cm both flow rates show the typical wake region in a cross flow configuration at the rear of the tube facing the breach (around 120°-140°). Unlike the 75 kg/h case, at 250 kg/h this high vorticity region is still observed at heights around 5.5 cm, affecting the trajectory of the gas flowing upwards, which shows an axial oscillating profile bounded between the first and the second neighbor tubes.

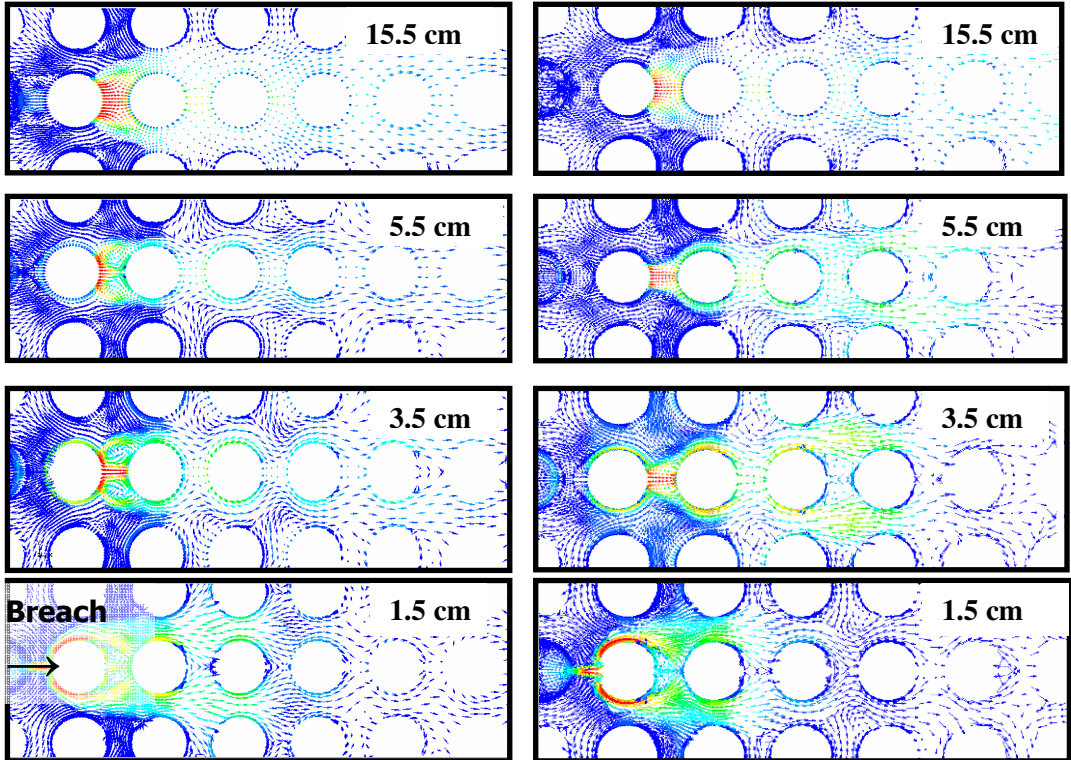


Fig. 2.2.6. Fish-mouth velocity vectors: 250 kg/h (left), 75 kg/h (right).

Contrarily to the guillotine configuration where the jet distributes evenly over the entire azimuthal direction, in the fish-mouth breach such circumferential symmetry vanishes and the jet moves essentially in the r - z plane. Therefore, the flow velocity is analyzed at the plane facing the breach (denoted as $y=0$, Fig. 2.1.3) and at two parallel planes located at a distance of half the tube radius ($y=0.25 \cdot d$) and right in between two parallel tube rows ($y=0.5 \cdot (d+s)$). Fig. 2.2.7 and Fig. 2.2.8 show respectively the normalized radial and axial velocity components (75 kg/h and 250 kg/h) at these planes. Note that normalizations are performed independently for each case.

As in the guillotine case, major radial velocities are reached at $1/3$ of the spacing between the breach and the first neighbor (Fig. 2.2.7). As observed, radial velocity decreases differently depending on the plane. Along $y=0$ and $y=0.25 \cdot d$, where the jet impinges the tubes either perpendicularly or tangentially, profiles display exponential decreases of the in-between tubes maximum velocity along the radial position, similarly to what has been shown in the guillotine configuration. These two decreasing

trends draw a band in which the average jet velocity should be located. In other words, they could be considered upper and lower bounds of jet velocity at each radial position.

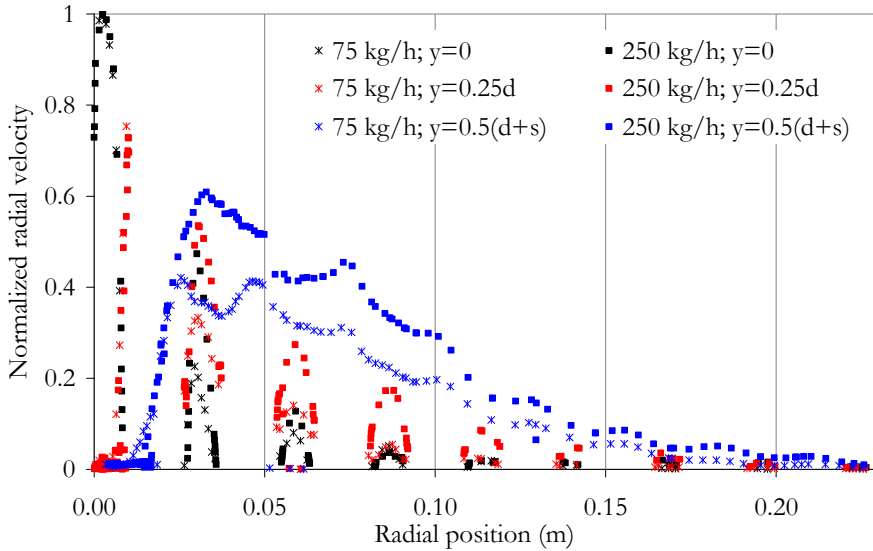


Fig. 2.2.7. Normalized maximum radial velocity vs radial position (fish-mouth).

Along $y=0.5 (d+s)$, where the jet flows freely without obstacles, profile displays higher radial velocities and a milder decrease rate than the previous planes intercepting the facing row of tubes.

As for the effect of mass flow rate, it is noted that radial velocity diminishes differently depending on the plane considered: whereas at $y=0$ both cases tend to the same normalized value after the third row, at planes located at tangential positions or in-between tube rows, convergence needs longer radial distance to happen. Namely, radial velocity convergence among different flow rates is highly enhanced by the momentum decay caused by jet-tube interaction (particularly at those locations at which jet approaches tube surfaces perpendicularly).

Another significant observation from Fig. 2.2.7 is the displacement of the velocity maxima according to the plane. As noted, planes other than $y=0$ reach velocity maxima at longer radial distances. This is a consequence of the jet slot-like shape that restricts the jet width. Those maxima out of the $y=0$ plane in between the broken tube and the first neighbor show the delay of jet suction over the initially quiescent gas.

In the case of normalized axial velocity (Fig. 2.2.8), the maximum velocities are attained in the first spacing of the symmetry plane ($y=0$), as the fraction of radial momentum transformed into axial one is higher at that location. One may note that after 10 cm from the breach, significant differences between mass flow rates vanish. Planes $y=0$ and $y=0.25 \cdot d$ (both intercepting the facing tube) evolve in a similar way, whereas the other plane behaves differently, possibly because of the indirect influence of the jet. Differences noted in the first 10 cm should be attributed to the induced flow of the jet at neighbor locations other than $y=0$.

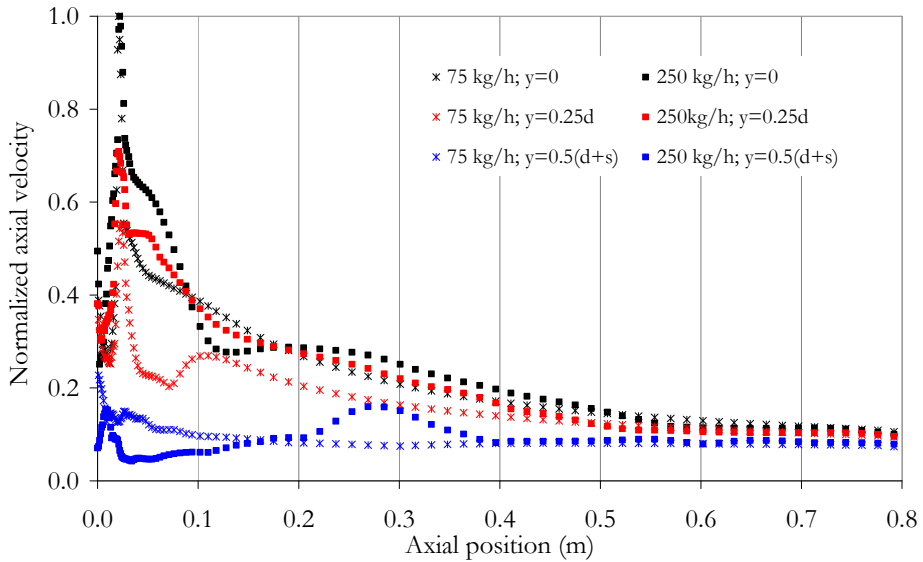


Fig. 2.2.8. Normalized maximum axial velocity vs axial position (fish-mouth).

2.3. DEVELOPMENT OF ONE-DIMENSIONAL CONCEPTUAL MODEL

As discussed in the previous section, the jet evolution across the tube bundle depends on the breach shape, the inlet gas mass flow rate and the azimuthal direction. Nevertheless, it was also demonstrated that observed trends can be said to have a generic applicability. This is of an utmost importance because, in general, actual safety analysis tools do not have 3D simulation capabilities. Therefore, consideration of potential retention of aerosols within the secondary side of a dry steam generator during a SGTR core meltdown sequence, requires forcefully encapsulating all the above 3D

information on jet motion across tube bundle into a 1D approximation of an acceptable accuracy.

2.3.1. Characterization of the guillotine breach jet

The results of the guillotine breach simulations showed that, regardless of flow rate, the jet evolves within the tube bundle following a generic quasi-parabolic pattern with two main stages (Fig. 2.3.1): a radial expansion, where the initially dominant radial velocity sharply decreases to less than 10% of its initial value in no more than 2-3 tubes from the breach; and an axial development, where the jet moves essentially upwards with just a minor displacement in the radial direction (mainly progressing in the direction of “diagonal tubes”). During radial expansion, the jet causes an intense suction from the gas at the concave side of the parabola, establishing a descending stream towards the breach in the space between the broken tube and the first “neighbor ones”. This picture of the jet motion has to be translated into usable equations.

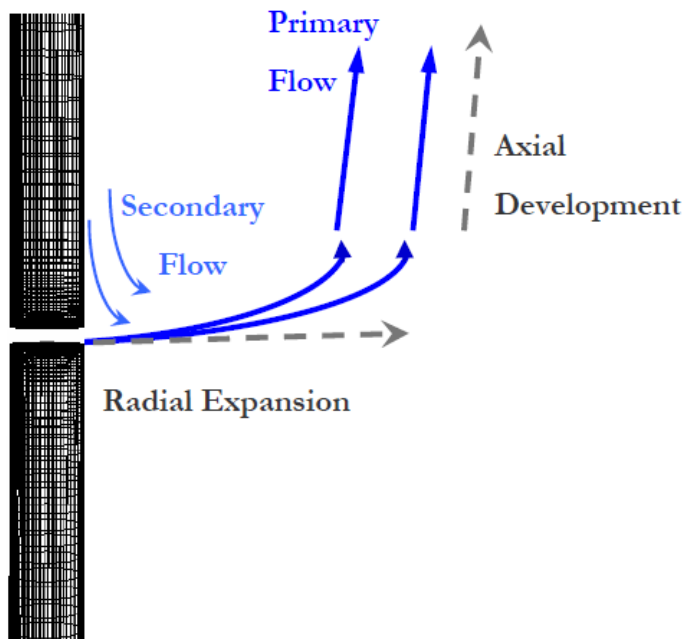


Fig. 2.3.1. Fluid development across the bundle.

A first attempt to approach a 1D concept was carried out by Herranz et al. (2007), who taking into account the studies by Leaver et al. (1998), used an equation for radial velocity (U) depletion across the tube bank according to 1D mass and momentum conservation equation:

$$\rho A_i U_{rd}(i) = \rho A_{i+1} U_{rd}(i+1) \quad (2.3.1)$$

$$\rho A_i U_{rd}^2(i) - \frac{1}{2} C_D \rho A_i U_{rd}^2(i) = \rho A_{i+1} U_{rd}^2(i+1) \quad (2.3.2)$$

where A_i and A_{i+1} are the incoming and outgoing surface areas of a control volume around tube “ i ” respectively, and $U_{rd}(i)$, $U_{rd}(i+1)$ are their corresponding gas velocities. Then, the velocity of the gas jet facing tube “ i ” can be approximated as a function of the inlet velocity in the bank of tubes, U_0 as:

$$U_{rd}(i+1) = \frac{1}{2^i} \cdot U_0 \quad (2.3.3)$$

Fig. 2.3.2 compares estimates with the above equation with an average of the FLUENT maximum radial velocities at 10 different azimuthal planes ($\alpha=0^\circ, 5^\circ, 10^\circ, 15^\circ, 20^\circ, 25^\circ, 30^\circ, 35^\circ, 40^\circ, 45^\circ$). As observed, FLUENT predicts faster velocity depletion possibly due to the 3D phenomena involved in the scenario. A correlation of the FLUENT values results in a potential decay of radial velocity with the tube position ($R^2=0.94$):

$$U_{rd}(i) = \begin{cases} U_0; & i = 1 \\ \frac{5}{4 \cdot i^3} \cdot U_0; & i > 1 \end{cases} \quad (2.3.4)$$

It is worth noting that this equation will result in radial velocities lower than those from Eq. (2.3.3), so that it would provide more conservative estimates of inertial and turbulent deposition mechanisms.

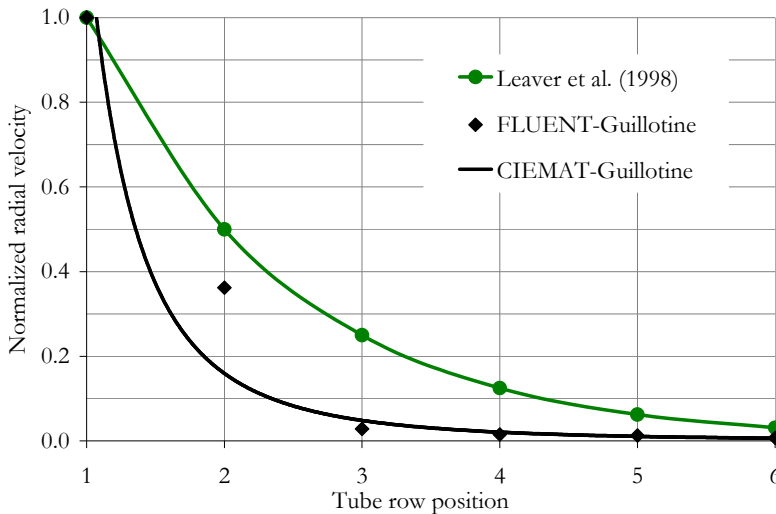


Fig. 2.3.2. Normalized radial velocity vs tube row position (guillotine).

2. Development of fluid flow modeling

Fig. 2.3.3 compares normalized radial and axial velocity decays along the tube row position, where the axial profile has been obtained through the average of FLUENT maximum axial velocities as in previous radial case. The correlation derived is the following:

$$U_{ax}(i) = \frac{4}{5 \cdot i^2} \cdot U_0 \quad (2.3.5)$$

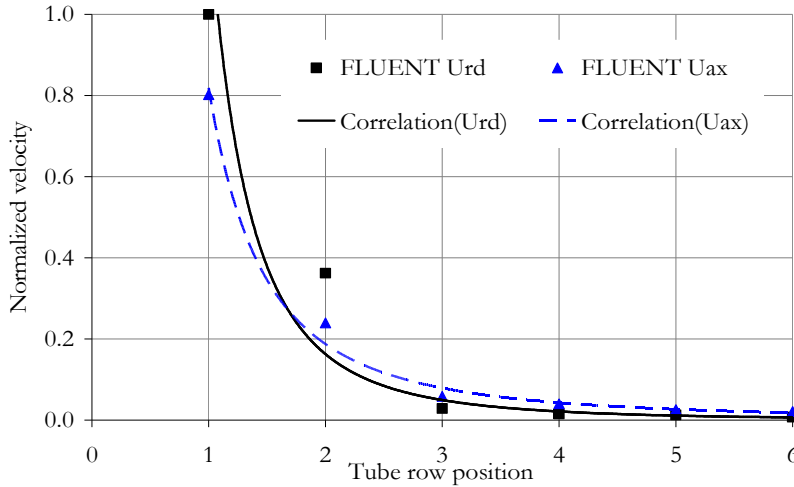


Fig. 2.3.3. Normalized radial and axial velocities vs tube row position (guillotine).

The figure shows that the initial maximum radial velocity is 20% higher than the axial one when facing the first tube of the bundle, whereas from the second tube on, the radial and axial components of gas velocity are similar. In both cases velocities decay fast within the first three tubes due to the high packing of tube bundle and the large momentum surface exchange area of this type of jets.

In addition to the evolution of the jet in the radial direction, data in Fig. 2.2.3, allow for correlating the axial depletion of the normalized axial velocity (U_{ax}) as a function of the axial position z as (Fig. 2.3.4), where $U_{ax,0}$ is the maximum axial velocity reached in the first tube:

$$U_{ax}(z) = \left(\frac{1}{15} + e^{-46z} \right) U_{ax,0} \quad R^2=0.93 \quad (2.3.6)$$

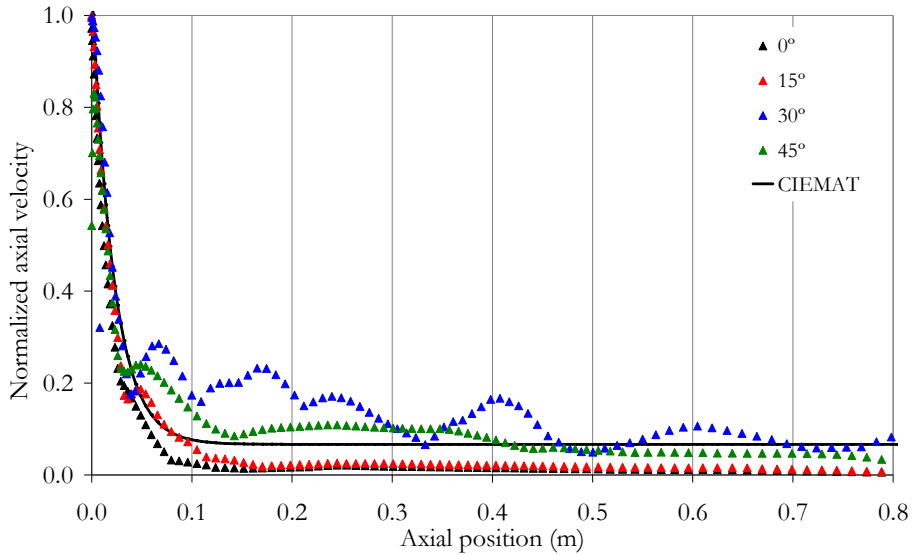


Fig. 2.3.4. Normalized axial velocity vs axial position (guillotine).

In short, at high gas flow rates the radial displacement of the jet during the axial development stage is rather more noticeable than at low flow rates. In addition, at low flow rates axial momentum gets dissipated at a much shorter height than at high flow rates.

2.3.2. Characterization of the fish-mouth breach jet

In the case of a fish-mouth breach, the highly 3D nature of the jet prevents any attempt of this 1D encapsulation. This section intends to characterize the fish-mouth jet in terms of radial and axial velocity components. In addition, comparisons are set to the expressions derived for the 1D guillotine model.

Unlike the guillotine jet, which evolution could be split into two stages, in the fish-mouth case, the radial and axial jet distributions occur at the same time. So to say, during the jet penetration in the bundle, a substantial amount of mass flow rate is diverted upwards between tubes from the first neighbor tube on.

The radial and axial velocity decay trends of the jets generated from both breaches have been compared in the following figures (Fig. 2.3.5 and Fig. 2.3.6). As already mentioned for the fish-mouth case, the lower and the

2. Development of fluid flow modeling

upper bounds of the radial velocity follow an exponential decay with the tube position which have been correlated as follows (Fig. 2.3.5):

$$\text{Lower bound: } U_{rd}(i) = \frac{7}{3} \cdot e^{-5/6i} \cdot U_0 \quad (R^2=0.9) \quad (2.3.7)$$

$$\text{Upper bound: } U_{rd}(i) = (1 - \frac{1}{2} \cdot \ln(i)) \cdot U_0 \quad (R^2=0.99) \quad (2.3.8)$$

The figure also shows that the 1D estimate obtained by [Leaver et al. \(1998\)](#) describes better the radial depletion across a tube bank of a fish-mouth jet than a guillotine one. Most probably it is due to the fact that, in the fish-mouth configuration, the jet flows in the direction of the tubes facing the breach, which is similar to the configuration analyzed by [Leaver et al. \(1998\)](#).

As observed the radial velocity for the guillotine case decays faster than the fish-mouth one. Namely, radial velocities are 5% of the initial one at the third tube for the guillotine case whereas that value is reached around the fifth tube for the fish-mouth one. Therefore, radial penetration is higher for the fish-mouth case than for the guillotine one.

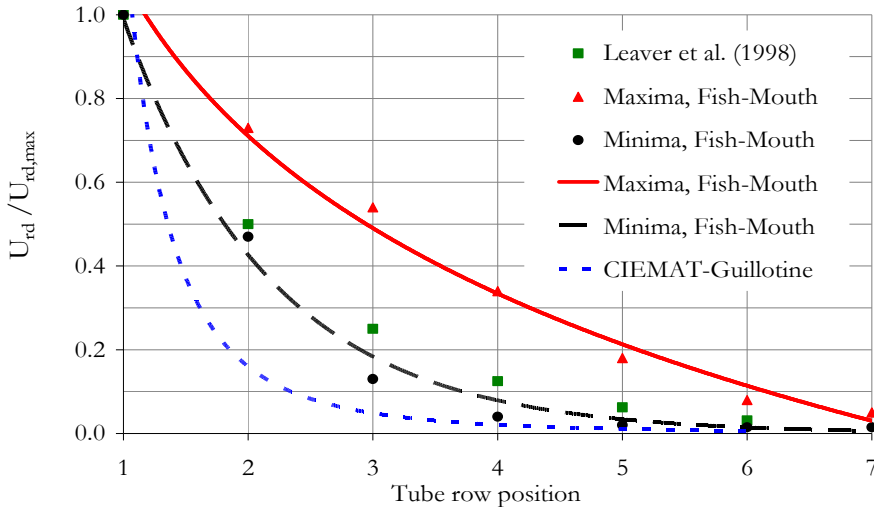


Fig. 2.3.5. Normalized radial velocity vs tube row position (guillotine, fish-mouth).

The axial velocity decay of the fish-mouth case has been described as a function of the axial position (z), with the following potential decay:

$$U_{ax}(z) = \frac{1}{10} \cdot z^{-2/5} \cdot U_0 \quad (R^2=0.88) \quad (2.3.9)$$

Fig. 2.3.6 shows this equation and compares it with Eq. (2.3.6) from the guillotine case. As noted, also in the axial depletion, guillotine case provides a faster decay than fish-mouth. Guillotine axial velocity decreases to a 10% of its initial value at 10 cm above the breach, whereas at that height fish-mouth jet has more than a 25 %.

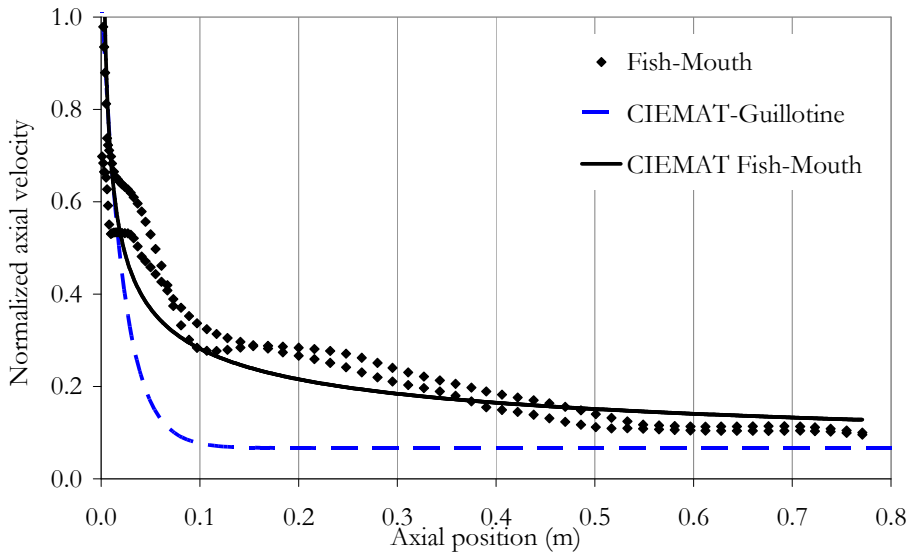


Fig. 2.3.6. Normalized axial velocity vs axial position (guillotine, fish-mouth).

2.3.3. Guillotine and fish-mouth closing results

Previous guillotine fish-mouth comparison is complete with Table 2.3.1 and Fig. 2.3.7, which summarize some meaningful results. Table 2.3.1 shows that at the same initial mass flow rate, jets from fish-mouth breaches reach further radial distances than those from guillotine breaches. Additionally, maximum gas velocities are higher in fish-mouth configurations. This seems to be caused by a smaller exit cross-section whereas the fast velocity decrease of guillotine jets might be a consequence of the large exchange surface area exposed.

2. Development of fluid flow modeling

Table 2.3.1. Guillotine, fish-mouth 3D simulation results.

Mass flow rate	75 (kg/h)		250(kg/h)	
	Guillotine	Fish-mouth	Guillotine	Fish-mouth
Breach type				
$ \mathbf{U} _{\text{mean, breach}}$ (m/s)	64	120	175	249
$ \mathbf{U} _{\text{max, bundle}}$ (m/s)	90	163	250	380
$ \mathbf{U} _{\text{mean, outlet}}$ (m/s)	0.21	0.3	0.69	0.68
Penetration	2 tubes	6 tubes	3 tubes	8 tubes

Fig. 2.3.7 also shows the higher fish-mouth velocities for the same inlet gas mass flow rate. In addition, It includes the experimental Pitot tube readings obtained for both breach configurations (section 2.1.5, [Sanchez-Velasco et al., 2007](#)). In both cases, differences between FLUENT predictions and experimental data go from a 2% to a 20%. In spite of being an indirect comparison because data and predictions belong to different spatial positions, the low discrepancies support the use of the following theoretical correlations relating the inlet gas mass flow rate (Φ) with the maximum velocity (U_0):

$$\text{Guillotine: } U_0 = 0.91 \cdot \Phi + 25 \quad (2.3.10)$$

$$\text{Fish-mouth: } U_0 = 1.22 \cdot \Phi + 84.4 \quad (2.3.11)$$

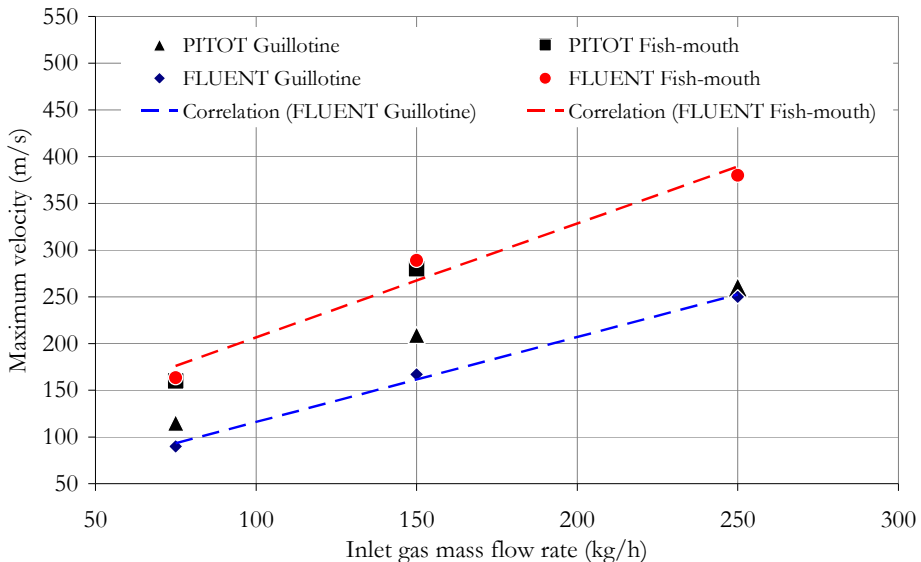


Fig. 2.3.7. Maximum velocity vs inlet gas mass flow rate (guillotine, fish-mouth).

Worth to note that Appendix A contains the preliminary hydrodynamic simulations. They provide further detail on the approximations and modelings performed. In addition, the procedure for performing CFD simulations is summarized, and the initial simulations with examples of grid-dependent, independent and wrong modeling of the turbulence (k- ϵ) are given. Appendix A finishes with a turbulent assessment performed through the comparison of these results with the results obtained by using the Reynolds Stress Model (RSM).

2.4. CONCLUSIONS OF FLUID FLOW MODELING

In the preceding sections, the results from the FLUENT 3D analyses of aerodynamics of a gas jet entering the break stage of a failed and dry steam generator during severe accident SGTR sequences are presented. After qualifying and validating FLUENT predictions, their discussion has provided meaningful insights into the jet behavior across the bundle that can be summarized as follows:

- The guillotine breach provides quite different jet topology when compared to the fish-mouth breach. The former generates an axis-symmetric jet with respect to the broken tube, whereas the latter evolves mainly in the direction facing the breach.
- Dissipation of the initial momentum of the jet in the guillotine configuration is faster than in the fish-mouth one. This could be attributed to the fact that in the guillotine arrangement the surface area of the jet contacting the surrounding gas is much larger than in the fish-mouth one and as a consequence, the momentum exchange is fostered.

Guillotine jet behavior:

- Jet momentum is dissipated in less than 3 tube rows in the range of inlet mass flow rate explored. The higher the inlet mass flow rate, the deeper jet penetration.
- The presence of tubes affects drastically the jet trajectory. Consecutive gas-tube interactions result into a radial reorientation towards the diagonal direction and, once most of radial momentum is lost, they also enhance the axial motion of the jet. Likewise, as experimentally shown, the high packing density of the bundle and the high velocity of the jet make gas, initially stagnant in the secondary side to move into the jet (entrainment).

- Radial and axial velocities decrease exponentially according to theoretical correlations derived.

The analyses and discussion of the guillotine results led to the encapsulation of the 3D description of the jet into a 1-D conceptual model of the flow. The jet evolves within the tube bundle following a pseudo-parabolic pattern that consists of two stages: a radial expansion, where the initially dominant radial velocity sharply decreases to less than 10% in no more than 2-3 tubes from the breach; and an axial development, where the jet moves essentially upwards with minor radial displacement.

Fish-Mouth jet behavior:

- Jet momentum is limited to the direction facing the breach. It is dissipated in less than 8 tube rows in the range of inlet mass flow rate explored. The higher the inlet mass flow rate, the deeper jet penetration.
- The presence of tubes affects the jet trajectory providing an axial reorientation.
- Radial and axial velocities decrease exponentially according to theoretical correlations derived.
- Fish-mouth breaches provide deeper jet penetrations and slower radial and axial velocity decay trends than guillotine breaches.

Even though, the flow in the whole bundle resulting from a fish-mouth breach can not be encapsulated into a 1D model, the fish-mouth jet has been characterized. It develops in a radial expansion, with a high radial component that decreases to 10% in around 5 tubes from the breach; at the same time, it distributes the mass flow rate in a sequence of axial developments at different radial positions.

3. DEVELOPMENT OF THE AEROSOL MODELING

The final goal of the work is to develop a model capable of predicting the retention capability of the break stage of the secondary side of a failed Steam Generator under dry conditions (i.e. either no water is present or water level is below the breach). Once the model is developed and validated, a simple theoretical correlation is derived so that it might be implemented in system severe accident codes, like MELCOR and/or ASTEC.

Modeling of this scenario requires understanding of both gas aerodynamics and aerosol governing mechanisms through the tube bundle. These will be the two main pillars of the ARI3SG (Aerosol Retention in the Secondary Side of a Steam Generator) model, a substantially enlarged and improved version of the first attempt conducted to model these scenarios (Herranz *et al.*, 2007, 2008): the ARISG-I model.

The ARI3SG semi-empirical model is based on the “filter concept”: a particle laden gas flowing through a bundle of obstacles, where it is subjected to forces that tend to clean it up by removing particles onto obstacles surfaces. Its scope is bounded by its target: “dry near field deposition” scenario. In other words:

- The region to model is the stage where the tube breach is located, so that the surface areas available for deposition are those of the tubes around the broken one.
- The region modeled is empty of water and therefore pool scrubbing is dismissed.

Three major improvements upgraded ARI3SG with respect to the previous formulation:

- Deposition phenomena. Axial and radial depositions have been considered. Credited correlations of specific phenomena from the literature have been taken when their applicability has been seen as defensible. In other cases, databases as extensive as possible have been built for cylinder cross-flow configurations and empirical correlations have been derived.
- Resuspension. Comparison of previous ARISG-I estimates with experimental data showed reverse trends with respect to the gas mass flow rate (Fig. 3.0.1). As ARISG-I only accounted for depletion

mechanisms which increase with the velocity; this opposite trend reveals the presence of mechanisms hindering deposition like resuspension, fragmentation and/or particle rebound. A resuspension correlation has been included.

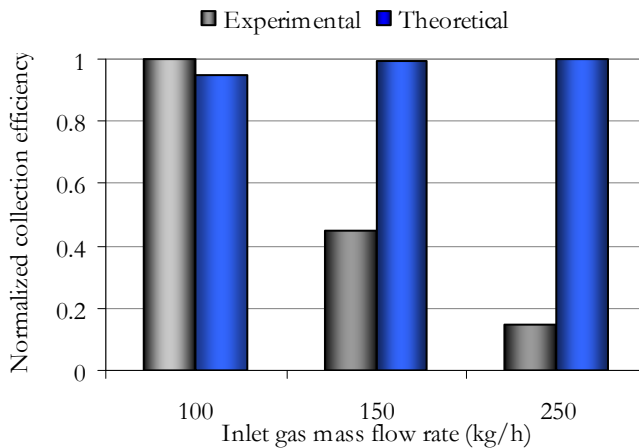


Fig. 3.0.1. Normalized collection efficiency vs inlet gas mass flow rate.

- **Aerodynamics.** ARI3SG accommodates adaptations of in-bundle gas velocity profiles. Radial and axial expressions of velocity decay have been derived from previous 3D aerodynamic simulations (chapter 2, López del Prá et al., 2010a, 2010b) and validated against experimental data (Velasco et al., 2008; Sanchez-Velasco et al., 2007).

In addition, once the experimental campaigns highlighted the huge complexity of the scenario and taking into account the “on-purpose” simple approach of the modeling, it was decided to provide ARI3SG with a supplementary uncertainty analysis. This study considers both model and input uncertainties.

The following two sections describe the bases of the modeling. It starts with the main hypothesis and approximations adopted in order to model the scenario of the bundle of tubes as a filter. It ends with the fundamental equations that model each of the aerosol phenomena taking place in the scenario (deposition and resuspension). The third section shows the implementation of the model in a Fortran code describing input and output decks. The fourth one compares predictions with the experimental data available obtained in the laboratory LASS of CIEMAT within the

international EU-SGTR and ARTIST projects (Herranz et al., 2006; López del Prá et al., 2010c; Sanchez-Velasco et al., 2010). The fifth section describes the procedure and results of the uncertainty analysis performed to the model and the input parameters. The sixth section develops the theoretical correlation that encompasses ARI3SG behavior as a function of non-dimensional numbers. The final equation is derived from a theoretical database of prototypical SGTR conditions. Finally, the last section summarizes the main conclusions of the work.

3.1. HYPOTHESES AND APPROXIMATIONS PERFORMED

3.1.1. The filter approach applied to the scenario

A rigorous theoretical treatment to model aerosol deposition onto tube surfaces would require the solution of Newton's second law for particles in the topology of the scenario. This approach would involve solving the Navier-Stokes equations describing gas flow motion. The complexity of the scenario prevented the derivation of analytical solutions, and even in the simplified case of a single tube facing the aerosol stream, only two extreme situations have been solved: viscous flow and potential flow (Ilias and Douglas, 1989). However, in a real situation the flow field lies in between these options and solutions of Navier-Stokes equations would demand numerical techniques. This approach is presently impractical in the arena of severe accident modeling because it involves a 3D resolution of the flow field during the steam discharge through the breach. Therefore, an integral approach of the particle deposition within tube bundle was adopted.

The model is based on the filter concept adapted to the current scenario. Three major hypotheses have been adopted:

- Gas is seen as a viscous fluid flowing transverse to the tubes. However, the axial motion has been considered when estimating the on-tube deposition and the jet penetration in the tube bundle. Given the tube bundle symmetry, cylindrical coordinates will be used from now on (r, θ, z) ; then, transverse-to-tubes motion is the radial direction and the parallel-to-tubes direction is the axial direction.
- Uniform particle concentration is assumed in the approaching flow.
- Filtration is considered uniform all over any plane perpendicular to incoming gas flow direction. In other words, the major integration variable is the filter depth. As a consequence, the model can be said to be quasi one-dimensional.

3. Development of the aerosol modeling

The relative change of particle mass concentration as the gas moves through the filter is proportional to the fraction of gas carrying particles that would eventually strike the surface (Dorman, 1966),

$$-\frac{dm}{m} = \frac{w \cdot U \cdot L}{Q} \quad (3.1.1)$$

Where w is the width of those gas streamlines (Fig. 3.1.1); Q is the volumetric gas flow rate; U is the average gas velocity through the filter and L is a generic tube length, which can be written as,

$$U = \frac{Q}{(1-\alpha) \cdot A} \quad (3.1.2)$$

$$L = \frac{4 \cdot \alpha}{\pi \cdot d_t^2} \cdot A \cdot dD' \quad (3.1.3)$$

$$\alpha = \frac{\pi}{4} \frac{d_t^2}{(s + d_t)^2} \quad (3.1.4)$$

where α is the fraction of the entire bundle volume occupied by the tubes (i.e., the bundle packing density); A is the cross section area facing the Q flow and dD' is a differential of length in the direction of the flow.

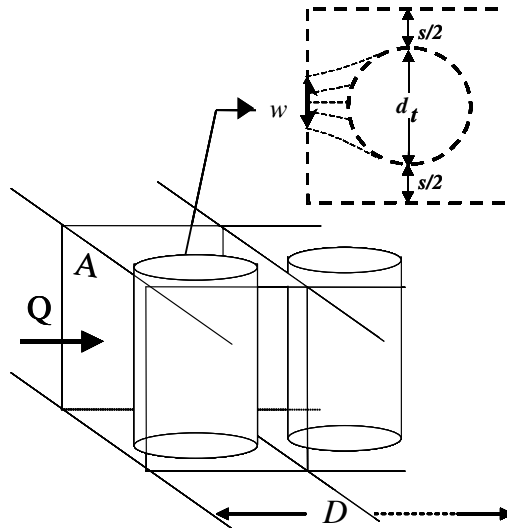


Fig. 3.1.1. Sketch-I of ARI3SG approach.

By substituting Eqs. (3.1.2) and (3.1.3) into Eq. (3.1.1) and integrating along the direction of the flow up to a given filter penetration depth (D), it yields:

$$m = m_{in} \cdot \exp\left(-\frac{4 \cdot \alpha}{1 - \alpha} \cdot \frac{1}{\pi \cdot d_t} \int_0^D \frac{w}{d_t} \cdot dD'\right) \quad (3.1.5)$$

Where the integrand is a generic expression of the single tube efficiency (η_{ST}). By multiplying and dividing by D , the following average of the single tube efficiency is introduced as:

$$\langle \eta_{ST} \rangle = \frac{1}{D} \int_0^D \eta_{ST} \cdot dD' = \frac{1}{N_t} \cdot \frac{\sum_i^{N_t} m_{ret}(i)}{m_0} \quad (3.1.6)$$

where i runs all over the number of tubes (N_t) considered (described in section 3.1.4), $m_{ret}(i)$ is the integral mass retained in tube i and m_0 is the mass facing the surface area projected by the first tube. It is worth to mention that deposition mechanisms due to both radial and axial gas motion have been considered when approximating the average single tube efficiency. Namely, although the gas is assumed to flow in the radial direction, the axial motion has been accounted for in terms of deposition. This way, Eq. (3.1.5) can be rearranged obtaining a generic expression for the tube bundle efficiency ($\eta_{TB} = 1 - \frac{m}{m_{in}}$):

$$\eta_{TB} = 1 - \exp\left\{-\frac{1}{1 - \alpha} \cdot \left[1 - \prod_{i=1}^{N_t} \left(1 - \frac{d_t}{s + d_t} \cdot \eta_{ST}(i)\right)\right]\right\} \quad (3.1.7)$$

Hence, the tube bundle efficiency depends on the product of a geometrical factor accounting for the packing density of the bundle and a function of the individual efficiency of the tubes ($\eta_{ST}(i)$) and the number of tubes available for deposition N_t .

In order to derive Eq. (3.1.7), it was assumed that once the gas undergoes filtration by one tube, particles that still remain suspended mix up. As a consequence, particles concentration becomes uniform before facing the next tube. This treatment is consistent with the enhancement of mixing processes resulting from the high turbulence level foreseen in SGTR sequences, due to high gas velocities and boundary layer separation in the wake region of tubes in a cross-flow-like arrangement as tight as the secondary side of a steam generator.

3.1.2. The single tube efficiency applied to the scenario

Single tube efficiency formulation is based on three major pillars:

- **Radial and axial deposition**

Initially, gas flows in a cross-flow configuration. It implies that particles may be depleted as the jet impinges the tube due to the radial velocity component (η_{rd}). However, as the gas reaches a tube a fraction of it is attached and driven upwards and around the tube (Coanda effect). It means that particles may also be deposited along the tube surface (η_{ax}) as a result of the dominant axial velocity component (Fig. 3.1.2) (Herranz et al., 2008; López del Prá et al., 2010a).

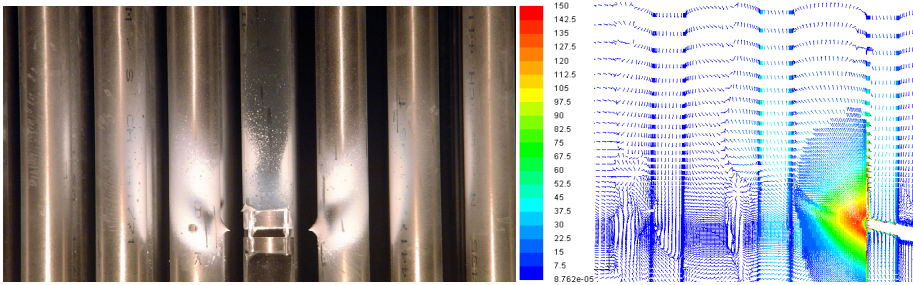


Fig. 3.1.2. Particle deposits after a PIV experiment and FLUENT velocity vectors.

As stated above, single tube efficiency is fed by both radial and axial deposition mechanisms. This consideration requires not double-counting particles undergoing depletion (Hinds, 1999; Chen and Yu, 1993):

$$\eta_{dp}(i) = \eta_{rd}(i) + \eta_{ax}(i) - \eta_{rd}(i) \cdot \eta_{ax}(i) \quad (3.1.8)$$

- **Particle resuspension**

As already mentioned, there are evidences of the presence of deposition inhibiting mechanisms in the scenario. Velocity magnitudes within the bundle are high enough to resuspend some of the previously deposited particles. This effect would cause particles already deposited to get back into the gas or, at least, the partial inhibition of particle deposition (Herranz et al., 2008).

Resuspension efficiency (η_{rs}) is defined as the fraction of mass that resuspend (m_{rs}) with respect to the mass that is already deposited (m_{dp}):

$$\eta_{rs}(i) = \frac{m_{rs}(i)}{m_{dp}(i)} \quad (3.1.9)$$

This way, resuspension is modeled by subtracting the resuspended mass to the previously deposited one, which in terms of efficiencies leads to the following expression:

$$\eta_{ST}(i) = \eta_{dp}(i) \cdot [1 - \eta_{rs}(i)] \quad (3.1.10)$$

- **Time dependence**

Time dependency is mandatory when considering resuspension. On one side, resuspension is dependent on the deposit depth which is a function of time, even under constant boundary conditions. On the other, resuspended particles add up to the mass facing the next tube downstream.

In this case, the process is modeled assuming steady boundary conditions. So to say, the inlet aerosol mass flow rate is assumed to be constant. This way, by splitting the time length of the sequence in “n” successive time-steps of the same length (Δt), the following expression for the collection efficiency is obtained:

$$\eta_{ST}^{(n)}(i) = \frac{m_{dp}^{(n)}(i)}{m_{in}(i, n \cdot \Delta t)} = \frac{m_{dp}^{(n-1)}(i) + m_{dp}(i, \Delta t) - m_{rs}(i, \Delta t)}{n \cdot m_{in}(i, \Delta t)} \quad (3.1.11)$$

Where $m_{dp}^{(n-1)}(i)$ is the mass of the deposit that remains on the tube i after the previous time-step ($n-1$); $m_{dp}(i, \Delta t)$ and $m_{rs}(i, \Delta t)$ are the deposited and resuspended masses in the interval (Δt), respectively.

As will be explained in section 3.2.4 and Appendix C, by maximizing the resuspension efficiency for all the time intervals Δt , the previous equation can be rearranged obtaining:

$$\begin{cases} \eta_{ST}^{(n)}(i) = \frac{n-1}{n} \cdot \eta_{ST}^{(n-1)}(i) \cdot [1 - \eta_{rs}(i)] + \frac{1}{n} \cdot \eta_{dp}(i) \cdot [1 - \eta_{rs}(i)] \\ \eta_{ST}^{(1)}(i) = \eta_{dp}(i) \cdot [1 - \eta_{rs}(i)] \end{cases} \quad (3.1.12)$$

This system gives rise to the single tube efficiency at any given time ($t=n \cdot \Delta t$) or time step (n):

$$\eta_{ST}^{(n)}(i) = \eta_{dp}(i) \cdot [1 - \eta_{rs}(i)] \cdot \frac{1 - [1 - \eta_{rs}(i)]^n}{n \cdot \eta_{rs}(i)} \quad (3.1.13)$$

According to Eq. (3.1.13), the single tube efficiency is the product of a “reference” single tube efficiency at any “ Δt ” ($\eta_{dp} \cdot (1 - \eta_{rs})$) and a decreasing factor with time ($\frac{1 - [1 - \eta_{rs}(i)]^n}{n \cdot \eta_{rs}(i)}$), which accounts for the cumulative effect of the resuspension.

3.1.3. The aerodynamic characterization performed

The applicability of the velocity laws obtained in section 0 for aerosol retention in a fish-mouth configuration is not as straightforward as in a guillotine one (Eq. (2.3.4) to Eq. (2.3.10)). From the aerodynamic descriptions of the jet behavior in guillotine and fish-mouth breach configurations, significant differences are found (Fig. 2.3.5 to Fig. 2.3.7). In particular, both velocity profiles and maximum initial velocities show large discrepancies. In principle, it is foreseeable that they affect aerosol retention. As the gas jet of the fish-mouth configuration, most of the particles will be carried in the direction facing the breach. However, the azimuthal spreading observed in the gas should be also expected concerning particles.

Previous experimental studies showed differences in the deposition patterns but no meaningful discrepancies were found in terms of net deposition (Herranz et al, 2006). This fact, together with the consistency of the guillotine jet symmetry with the adopted filter approach (i.e. uniform particle scrubbing in any plane perpendicular to the jet direction), suggested the adoption of the guillotine profiles in ARI3SG. They are described by Eqs. (2.3.4) and (2.3.5):

$$U_{rd}(i) = \begin{cases} U_0; & i = 1 \\ \frac{5}{4 \cdot i^3} \cdot U_0; & i > 1 \end{cases} \quad (2.3.4)$$

$$U_{ax}(i) = \frac{4}{5 \cdot i^2} \cdot U_0 \quad (2.3.5)$$

3.1.4. Development of the jet penetration

As seen in section 3.1.1, jet penetration is the main variable when applying the filter approach. Here below an approximate method to estimate it from the previous hydrodynamic assessment is derived. By introducing some intermediate variables jet penetration is written in terms of the total number of tubes (N_t) involved in aerosol retention.

The transient time ($t_t(i)$) of a particle in one “tube domain” region (radial length: d_t+s) is:

$$t_t(i) = \frac{(d_t + s)}{U_{rd}(i)} = (d_t + s) \cdot \frac{4 \cdot i^3}{5 \cdot U_0} \quad (3.1.14)$$

The axial length ($L_{ax}(i)$) traveled by the particle in one tube domain region is given by:

$$L_{ax}(i) = U_{ax}(i) \cdot t_t(i) = \left(\frac{4}{5}\right)^2 \cdot i \cdot (d_t + s) \quad (3.1.15)$$

The sum of the axial lengths that the particle can travel before leaving the break stage is the axial distance from the breach to the upper support plate (L_t). This relationship (Eq. (3.1.16)) provides the total number of tubes (N_t) or jet penetration in the bundle (Eq. (3.1.17)):

$$L_t = \sum_{i=1}^{N_t} L_{ax}(i) \quad (3.1.16)$$

$$N_t = \frac{1}{2} \cdot \left[\left(\frac{12.5 \cdot L_t}{d_t + s} + 1 \right)^{0.5} - 1 \right] \quad (3.1.17)$$

3.2. DEVELOPMENT OF THE FUNDAMENTAL EQUATIONS

The previous sections presented some of the major equations of the model through the main model approximations. Here below, those equations will be further developed and their constitutive elements will be introduced. The phenomena considered have been modeled based on either already set correlations or new ones derived from available data in the literature. Before going through, the whole set of ARI3SG equations,

though, some introductory remarks concerning how the model deals with particle size are made.

3.2.1. Size dependence

The particle size dependence of each of the aerosol phenomena is taken into account through a discretized size distribution. The size domain is split in N_{bins} sections giving rise to the following tube-bin deposition efficiency and net tube collection efficiency which are based on Eqs. (3.1.8) and (3.1.13), respectively:

$$\eta_{dp}^{(n)}(i, j) = \sum_k [\eta_{rd}^{(n)} + \eta_{ax}^{(n)} - \eta_{rd}^{(n)} \cdot \eta_{ax}^{(n)}](i, j, k) \quad (3.2.1)$$

$$\eta_{ST}^{(n)}(i) = \sum_{j=1}^{N_{bins}} y(i, j) \cdot \eta_{dp}^{(n)}(i, j) \cdot [1 - \eta_{rs}^{(n)}(i, j)] \cdot \frac{1 - [1 - \eta_{rs}^{(n)}(i, j)]^n}{n \cdot \eta_{rs}^{(n)}(i, j)} \quad (3.2.2)$$

Where n is the time step being calculated, i represents the tube, j is the specific size bin under the analysis, and k stands for each individual process contributing to particle scrubbing from the gas onto the i tube surface area; $y(i, j)$ is the mass fraction of bin j . It must be noted that depletion mechanisms k are assumed to be independent from each other.

3.2.2. Assessment of phenomena relevance

The prevailing boundary conditions of a dry SGTR sequence were investigated by Bakker (2001a, 2001b) and Guntay et al. (2001). Both teams found that no large thermal gradients or steam condensation should be expected in the secondary side of a dry steam generator. As a consequence, neither thermophoresis nor diffusiophoresis are accounted for in the modeling. In addition, most of the aerosol mass was anticipated to be carried by particles big enough ($\geq 10^{-7}$ m) as for Brownian diffusion to be negligible. Thus, the potential removal mechanisms are: inertial impaction, turbulent deposition, settling and interception.

In order to find out which of those mechanisms could be relevant for particle depletion, an assessment of their characteristic parameters was carried out under anticipated SGTR conditions (Table 3.2.1). These parameters are non-dimensional numbers generally defined as the ratio of forces causing particle removal and gas resistance forces opposing to particle motion (Ranz and Wong, 1952). Regarding turbulent deposition, Douglas and Ilias (1988) introduced the product of the turbulent Schmidt number and the square root of gas Reynolds number ($Sc_{tbt} \cdot Re_g^{0.5}$) as the

dimensionless parameter. The estimates of the characteristic parameters of the table correspond to dry-SGTR conditions where the velocities range from 10 to around 300 m/s and the particle sizes from 1 to 10 μm of AMMD (Bakker, 2001a, 2001b; Güntay et al., 2001). Douglas and Ilias (1988) estimated the turbulent diffusion coefficient (ϵ) to be around $1\text{-}2 \cdot 10^{-3} \text{ m}^2/\text{s}$. It is accepted that when the order of magnitude of the characteristic parameter is lower than 10^{-2} , the contribution of that mechanism to retention can be neglected (Ranz and Wong, 1952). Therefore, the estimates obtained indicate that only inertial impaction and turbulent deposition play a significant role in the scenario.

Table 3.2.1. Estimate of characteristic parameters of depletion mechanisms.

	Characteristic parameters	Estimate
Inertial impaction	$\text{Stk} = C_c \frac{\rho_p \cdot U_g \cdot d_p^2}{18 \cdot \mu_g \cdot d_t}$	$> 10^{-2}$
Turbulent deposition	$\text{Sc}_{\text{tbt}} \cdot \text{Re}_g^{0.5} = \frac{(\mu_g \cdot U_g \cdot d_t)^{0.5}}{\rho_g^{0.5} \cdot \epsilon}$	$> 10^{-2}$
Settling	$\frac{U_{\text{TS}}}{U_g} = C_c \frac{\rho_p \cdot d_p^2 \cdot g}{18 \cdot \mu_g \cdot U_g}$	$\sim 10^{-6}$
Interception	$\frac{d_p}{d_t}$	$\sim 10^{-4}$

Both phenomena depend on variables such as particle diameter, tube diameter and gas velocity. Such dependencies may be expressed in terms of a set of non-dimensional numbers: gas Reynolds number (Re_g), particle Reynolds number (Re_p) and Stokes number (Stk). Their ranges in dry-SGTR scenarios are shown in Table 3.2.2 together with those of the experimental databases that are used to develop or assess the model. Most of them do not match entirely the SGTR ranges. In particular, the ranges of the Reynolds number lay below the SGTR one, except for Liu and Agarwal (1974) data. The ranges of Stk and Re_p number overlap the lower bounds of SGTR conditions. However, as will be seen later on, data from different sources will be used as a whole; so that the entire range will well encompass the SGTR one.

3. Development of the aerosol modeling

Table 3.2.2. Non dimensional numbers for aerosol scrubbing.

	Re_g	Stk	Re_p	Re_p^2 / Stk
Dimensionless number	$\frac{\rho_g \cdot U_g \cdot d_t}{\mu_g}$	$C_c \frac{\rho_p \cdot U_g \cdot d_p^2}{18 \cdot \mu_g \cdot d_t}$	$\frac{\rho_g \cdot U_g \cdot d_p}{\mu_g}$	$\frac{18 \cdot \rho_g}{C_c \cdot \rho_p} \cdot Re_g$
SGTR	10^4 - 10^5	0.01-10	0.1-300	100-1000
Turbulent deposition in cross-flow configuration:				
Douglas (1980)	100-8000	0.002-0.07	0.1-0.6	-
Turbulent deposition along a cylinder:				
Liu and Agarwal (1974)	10^4 - $5 \cdot 10^4$	$5.4 \cdot 10^{-3}$ - 5.86	1.09-82	222-1170
Inertial impaction in cross-flow configuration:				
Ranz and Wong (1952)	67-500	0.22-4.6	0.29-8.4	0.38-15
Wong and Johnstone (1953)	13-330	0.087-2.4	0.25-4.4	0.72-8
Wong et al. (1955)	13.7-330	0.1-4.9	0.17-4.2	0.13-4.54
May and Clifford (1967)	165-8500	0.15-15	3-18	-

3.2.3. Deposition

Turbulent deposition and inertial impaction are the driving mechanisms of the aerosol depletion in the scenario. When the particle laden gas flow perpendicular to the bundle of tubes, each phenomenon dominates in a different range of the non-dimensional Stokes number:

- $Stk \leq 0.1$ Turbulent deposition
- $Stk > 0.1$ Inertial impaction

This classification agrees with the analysis of Douglas and Ilias (1988) as well as with numerous authors who claimed that there is a critical Stokes number below which no deposition by inertial impaction occurs (Fuchs, 1964; Ranz and Wong, 1952).

On other side, when the gas flows parallel to the surfaces of the tubes particles may be mainly depleted by turbulent deposition.

3.2.3.1. Turbulent deposition

Turbulent deposition results from the combined action of the turbulent diffusion and the particle inertia. The turbulent eddies induce a velocity to the particle that due to its inertia, coasts through the boundary layer and deposits (Douglas and Ilias, 1988; Wood, 1981). This mechanism also termed as eddy-diffusion or eddy diffusion-impaction has been widely analyzed by different authors being more extensive for parallel than for

perpendicular to the surface flow directions (Table 3.2.2). Douglas and Ilias (1988) showed some experimental measurements of collection efficiency as function of the Stokes number obtained from vertical cylinders in a cross flow configuration (Douglas, 1980). For their part, Sippola and Nazaroff (2002) performed a complete review of the experimental and theoretical investigations of particle deposition for parallel flow in ducts, which are usually reported in the form of the dimensionless deposition velocity and relaxation time.

The ARI3SG models turbulent deposition over the tubes of the secondary side of the steam generator empirically, considering the separate effects of a flow perpendicular to the tube (radial deposition) and a flow parallel to the tube (axial deposition). In the first case an empirical correlation from Douglas (1980) data has been developed. In the second one, due to the lack of data in geometries similar to the SGTR ones, it has been used the experimental correlation of Liu and Agarwal (1974). Given the small particle size compared to tube diameter it has been assumed that the surface curvature has a negligible effect on the deposition velocity.

- **Radial deposition**

Fig. 3.2.1 shows the experimental data of the collection efficiency by turbulent deposition on vertical cylinders in a cross flow configuration obtained at $Stk \leq 0.1$ by Douglas (1980). From these data, the following Eq.(3.2.3) was derived.

$$\eta_{rd}^{tb} (i, j) = 0.438 + 0.071 \cdot \ln(Stk) \quad (3.2.3)$$

The scarcity and scatter of data led to a low linear regression coefficient ($R^2=0.516$) with a standard uncertainty of 0.0566, which means that with a 95% of confidence collection efficiencies would be within the range $\eta_{rd}^{tb} \pm 0.11$. The average relative error of the correlation is around 54%. Further analyses of the uncertainties are given in section 3.6.1.

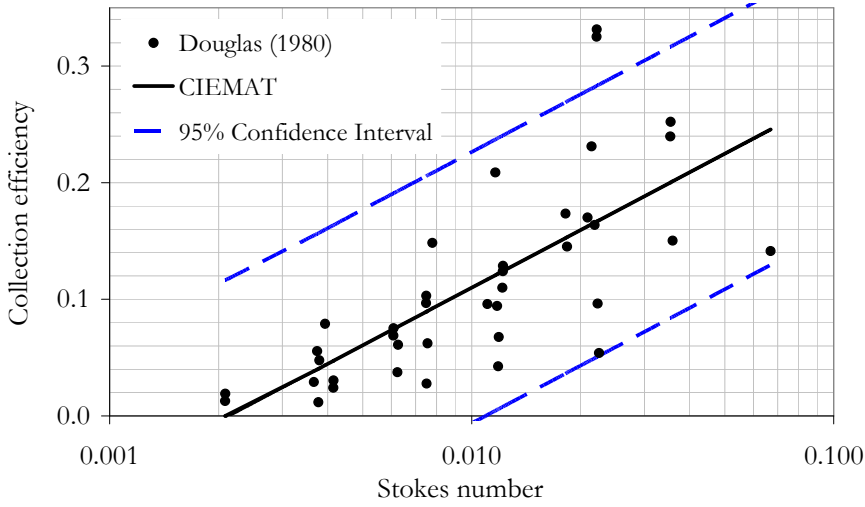


Fig. 3.2.1. Fitting of turbulent deposition.

- **Axial deposition**

The axial collection efficiency of the tube “i” and particle bin size “j” can be written as:

$$\eta_{ax}(i, j) = f(U_{dp}, A_{dp}, A_{crs}) \quad (3.2.4)$$

Where A_{dp} is the tube surface area available for deposition ($A_{dp}(i) = \pi \cdot d_t \cdot L_{ax}(i)$), A_{crs} is the cross section through which the gas flows upwards ($A_{crs} = (d_t + s)^2 - \frac{\pi}{4} \cdot d_t^2$) and U_{dp} is the deposition velocity defined as:

$$U_{dp} = U_{dp}^+ \cdot U^* \quad (3.2.5)$$

Where U^* is the friction velocity, which is obtained as a function of the axial velocity and the friction factor as proposed by Liu and Agarwal (1974) for $Re_g < 10^6$:

$$U^* = \left(\frac{f_w}{2} \right)^{1/2} \cdot U_{ax} \quad (3.2.6)$$

$$f_w = 0.079 \cdot Re_g^{-1/4} \quad (3.2.7)$$

And U_{dp}^+ is the non-dimensional deposition velocity derived by Liu and Agarwal (1974):

$$U_{dp}^+ = \text{Min}(6 \cdot 10^{-4} \cdot \tau_+^2, 0.1) \quad (3.2.8)$$

Where τ^+ is the dimensionless relaxation time:

$$\tau^+ = \frac{\rho_g \cdot (U^*)^2}{\mu_g} \cdot C_c \cdot \frac{\rho_p \cdot d_p^2}{18 \cdot \mu_g} \quad (3.2.9)$$

Fig. 3.2.2 shows Liu and Agarwal (1974) experimental curve of the non-dimensional deposition velocity versus the non-dimensional relaxation time. The figure also includes a 95% of the confidence interval that comes from the standard uncertainties of 0.03 and $0.437 \cdot U^+$ for the high and low non-dimensional relaxations times, respectively. It implies around an 85% of increase/decrease of the correlation. The average relative errors of the correlation are around a 20% and 30% for the high and low non-dimensional relaxation times, respectively. As already mentioned, further analysis of the uncertainties are given in section 3.6.1.

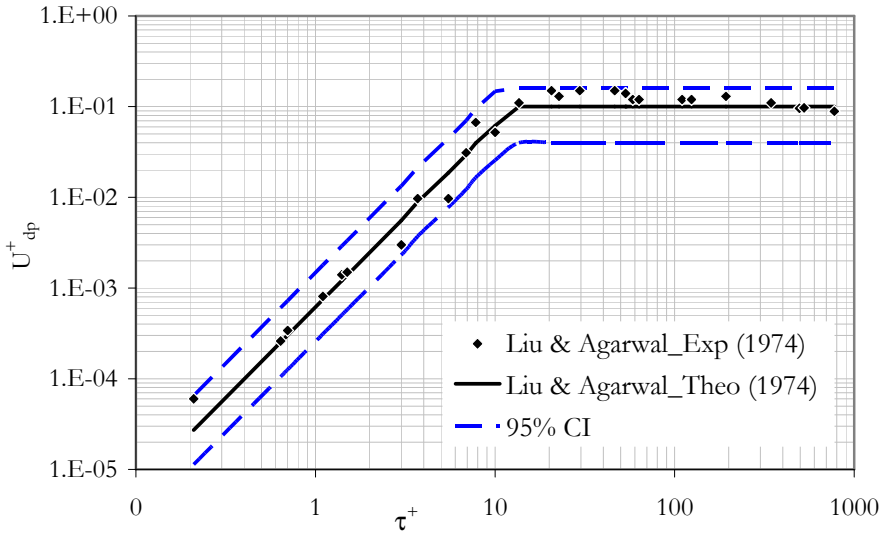


Fig. 3.2.2. Dimensionless deposition velocity vs dimensionless relaxation time.

Finally, the axial collection efficiency of tube “i” and particle bin size “j” is:

$$\eta_{ax}(i, j) = 1 - \exp\left(\frac{U_{dp}^+(i, j) \cdot U^* \cdot A_{dp}(i)}{U_{ax}(i) \cdot A_{crs}}\right) \quad (3.2.10)$$

3.2.3.2. Inertial impaction

At Stokes numbers higher than 0.1 inertial impaction governs aerosol deposition. Regardless of target geometry and boundary conditions, inertial impaction draws an S-shape when plotted versus Stokes number (Fuchs, 1964). Previous version of ARI3SG already proposed a sigmoidal equation for the collection efficiency (Herranz et al., 2007). It was based on the analyses of the available data and compared to other authors' correlations (Table 3.2.3). Current analyses extend this database to around 280 experimental points (Table 3.2.2) from which an improved correlation was obtained:

$$\eta_{rd}^{imp}(i, j) = \frac{1}{1 + 4.87 \cdot 10^{-5} \cdot e^{10 \cdot Stk^{-1/8}}} \quad (3.2.11)$$

This equation is plotted in Fig. 3.2.3 together with previous ARISG-I correlation and the experimental data versus the Stokes number. As observed, both correlations describe the S-shape with similar slopes at medium Stokes numbers (0.4-2). However, at low Stokes number the new modeling describes better experimental results than the previous one, providing lower collection efficiencies. Whereas at high Stokes numbers, the ARI3SG correlation provides higher collection efficiencies, with 1.0 as the upper asymptotic value, ARISG-I is fitted to 0.75 as an asymptote. This upper limit was an indirect way to account for particle resuspension. Such an approximation is needless in ARI3SG since resuspension is explicitly considered.

The regression coefficient R^2 of the current equation (Eq. (3.2.11)) is 0.91. The standard uncertainty is around 0.07, so that 95% of the confidence interval is $\eta_{rd}^{imp} \pm 0.14$. In this case, the average relative error of the correlation with respect to the experimental data is around a 24% which is deemed acceptable, given the own data scattering.

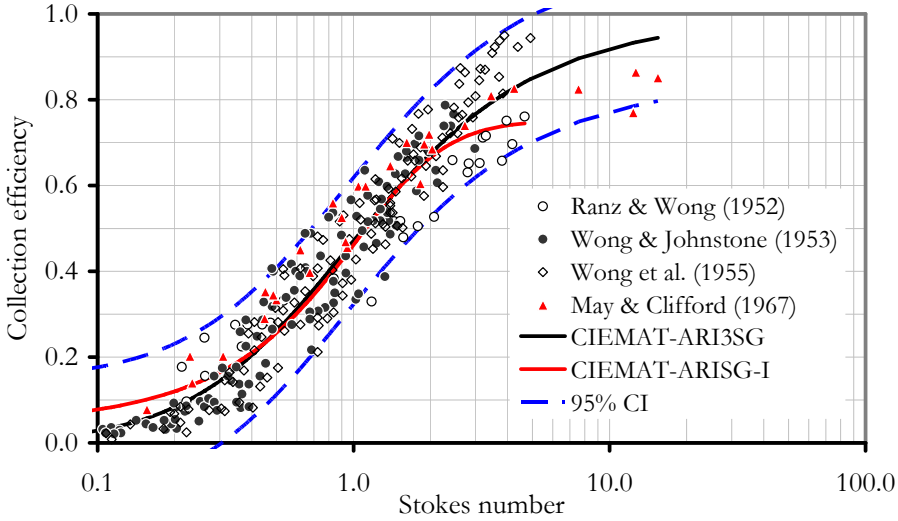


Fig. 3.2.3. Fitting of inertial impaction.

To verify Eq. (3.2.11) performance, Fig. 3.2.4 compares it with other theoretical correlations that stemmed from the resolution of the Navier-Stokes equations based on different approximations and numerical techniques (Wessel and Righi, 1988; Ilias and Douglas, 1989; Zhu et al., 2000). All those equations are gathered in Table 3.2.3 together with its validity range. As observed, Ilias's correlation shows the best agreement with the experimental data. It is worth to note that estimates from Eq. (3.2.11) are very similar to those from Ilias. Nevertheless, the advantage of Eq. (3.2.11) is the simplicity with respect to Ilias', as it relies on just two numerical parameters when Ilias' correlation uses six.

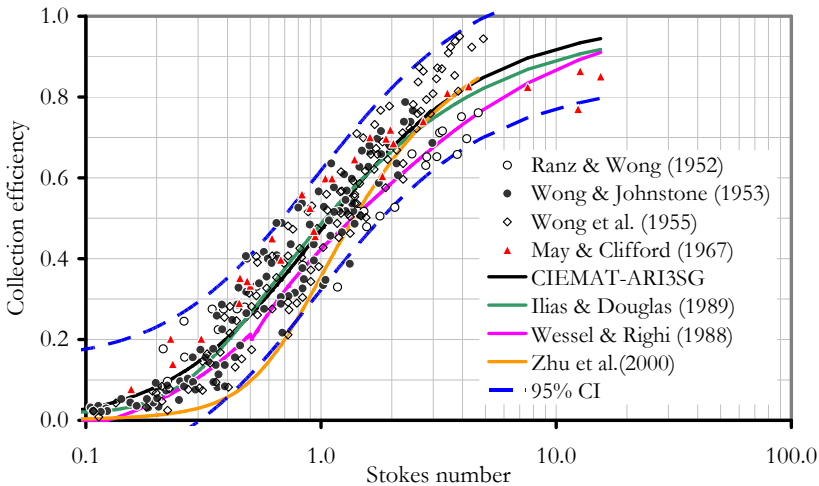


Fig. 3.2.4. Experimental data and correlation estimates of inertial impaction.

Table 3.2.3. Correlations of inertial impaction.

CIEMAT-ARISG-I (Herranz et al., 2007): $Stk \geq 0.1$	
$\eta_{ST}^{imp} = \frac{0.75}{1 + 29.31 \cdot \exp(-3.85 \cdot Stk^{0.5})}$	
Wessel and Righi (1988): $\frac{Re_p^2}{Stk} \leq 50000$	
$Stk_e \geq 0.125$	
$\eta_{ST}^{imp} = 0.01978749 \cdot \ln(8 \cdot Stk_e) + 0.5136545 \cdot (Stk_e - 0.125) - 0.0482858 \cdot (Stk_e - 0.125)^2$	
$Stk_e > 0.5$	$\eta_{ST}^{imp} = \left(1 + \frac{1.54424}{Stk_e - 0.125} - \frac{0.538013}{(Stk_e - 0.125)^2} + \frac{0.2020116}{(Stk_e - 0.125)^3} \right)$
Ilias and Douglas (1989): $30 < Re_g < 40000$; $0.07 < Stk < 5.0$	
$\eta_{ST}^{imp} = \frac{Stk^3 + \frac{1.622 \cdot 10^{-4}}{Stk}}{1.031 \cdot Stk^3 + (1.140 + 4.044 \cdot 10^{-2} \ln(Re_T)) \cdot Stk^2 + 1.479 \cdot 10^{-2} \ln(Re_g) + 0.2013}$	
Zhu et al. (2000): Unrestricted	
$\eta_{ST}^{imp+int} = \frac{1 + \lambda}{2 \cdot Ku} \left[2 \cdot \ln(1 + \lambda) - 1 + \alpha_T + \frac{1 - 0.5\alpha_T}{(1 + \lambda)^2} - \frac{1}{2} \alpha_T (1 + \lambda)^2 \right]$	
$\lambda = \frac{d_p}{d_t} + Stk \cdot \sqrt{\alpha_T} \cdot \left(1 + \frac{\eta_{ST}^{imp+int}}{\lambda} \right) \cdot (1 + \lambda - \eta_{ST}^{imp+int}) \cdot \left\{ 1 - \exp \left[- \frac{1}{Stk \cdot \sqrt{\alpha_T}} \left(1 + \frac{\eta_{ST}^{imp+int}}{\lambda} \right)^{-1} \right] \right\}$	
$Ku = \alpha_T - \frac{\alpha_T^2}{4} - \frac{3}{4} - \frac{1}{2} \ln \alpha_T$	

3.2.4. Resuspension

As stated in section 3.1.2 (Eq. (3.1.9)), resuspension is considered through the inclusion in the single tube efficiency of the resuspension efficiency (i.e. mass fraction of the deposit getting back into the flowing gas):

$$\eta_{rs}(i) = \frac{m_{rs}(i)}{m_{dp}(i)} = 1 - \exp(-\Lambda \cdot \Delta t) \quad (3.2.12)$$

As noted, the resuspension efficiency is estimated from the resuspension rate (Λ) prevailing during the time interval being calculated (Δt).

ARI3SG expression for Λ is based on the approach followed by Parozzi (2000):

$$\Lambda(F_{rs}) = \begin{cases} 0.4037 \cdot (F_{rs} \cdot 10^6)^{0.6005} & 0 < F_{rs} < 3.065 \cdot 10^{-10} \text{ N} \\ 90.28 \cdot (F_{rs} \cdot 10^6)^{1.269} & F_{rs} \geq 3.065 \cdot 10^{-10} \text{ N} \end{cases} \quad (3.2.13)$$

Where F_{rs} is the net force resulting from the balance between “detaching” and “attaching” forces acting on the deposited particles:

$$F_{rs} = F_d + F_l - F_c - F_f \quad (3.2.14)$$

Where F_d and F_l are the drag and the lift forces (i.e. detaching forces), respectively, and F_c and F_f are the cohesive and friction forces (i.e. attaching forces), respectively. Other attaching forces, like those resulting from particle surface tension and gravitational and/or electrical fields have not been considered due to different reasons: dryness of the scenario under study, vertical orientation of tubes and large uncertainties concerning particle and tube charging. The resuspension force has been maximized by reducing the cohesive force as if the deposit consisted of just a single layer. Note that this simplification is conservative.

Once the individual expressions (Appendix C) are embedded in Eq. (3.2.14), the final expression for F_{rs} is:

$$F_{rs} = \frac{\mu_g^2}{\rho_g} \cdot (Re_p^*)^2 \cdot \left[\frac{\pi}{4} + 4.21 \cdot (Re_p^*)^{0.31} \right] - 4.644 \cdot 10^{-7} \cdot d_p \quad (3.2.15)$$

Where Re_p^* is the particle Reynolds number with the friction velocity U^* .

The expression Eq. (3.2.13) has been derived by fitting the estimates to an extensive database on resuspension (Fig. 3.2.5): Oak ridge, PSI Würenligen and STORM (Parozzi et al., 1995; Parozzi, 2000).

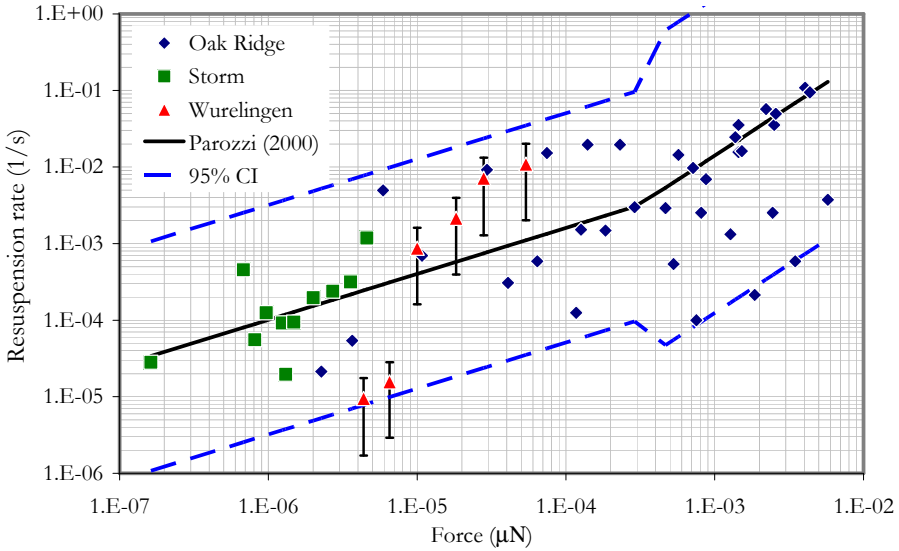


Fig. 3.2.5. Resuspension rate vs resuspension force.

Finally, by substituting Eq. (3.2.12) into the equation of the single tube collection efficiency (Eq. (3.1.13)) results:

$$\eta_{ST}^{(n)}(i) = \eta_{dp}(i) \cdot [1 - \eta_{rs}(i)] \cdot \frac{1 - \exp(-\Lambda \cdot n \cdot \Delta t)}{n \cdot [1 - \exp(-\Lambda \cdot \Delta t)]} \quad (3.2.16)$$

Eq. (3.2.16) shows that the decreasing multiplicative factor, which accounts for the cumulative effect of the resuspension (section 3.1.2), is the ratio between the resuspension efficiency that would take place in a time step of duration $n \cdot \Delta t$ and n -times the resuspension efficiency in a time step Δt .

It must be noticed that in ARI3SG modeling, collision and particle shape factors are assumed to be 1. On other side, the friction velocity (U^* , Eq. (3.2.6)) of the resuspension is obtained from the maximum between radial and axial velocities (hereafter called resuspension velocity, U_{rs}), in order to maintain conservative hypothesis:

$$U_{rs}(i) = \max[U_{rd}(i); U_{ax}(i)] \quad (3.2.17)$$

3.3. DEVELOPMENT OF ARICODE

The ARI3SG model has been implemented in highly modular Compaq Fortran code (Compaq visual Fortran version 6.6). It is the main subroutine of a Fortran platform called ARICODE that allows two running modes depending on the analysis to be performed. The “database” mode allows the execution of a whole set of cases producing a theoretical database with the tube bundle collection efficiency of each case. The single case mode (“singlcas”) provides, in addition to the bundle collection efficiency, a detailed description of the intermediate model results.

Fig. 3.3.1 depicts the flowchart of ARICODE platform. It consists of three main subroutines:

- ARI3DB is an interface that handles the input data file. It opens the input file reading the running mode (database/singlcas). Then, a loop reads the inlet and/or boundary conditions and calls the subroutine ARI3SG. Finally, the loop collects the model result, the tube bundle collection efficiency and writes a global output file (OutBundle).
- ARI3SG is the main subroutine of the program where the model ARI3SG is implemented. It executes the model and returns the tube bundle collection efficiency and in case of being in singlcas mode, it also calls WSCARI3 subroutine, which writes the intermediate model results.
- ARI3WSC is a subroutine interconnected to ARI3SG one that is called when the singlcas mode is run. It writes three output files with three levels of detailed information of the model: “OUTube” with results of each tube of the bundle; “OUTPSize” with results of each particle bin size at each tube; “OUTime” with the time history of the tube bundle collection efficiency.

External to ARICODE although closely linked is the so called Input_builder (Fig. 3.3.1) implemented in Mathematica 4.0. It generates the input data file from the inlet AMMD, GSD, aerosol density and integral mass injected by discretizing the inlet aerosol size distribution that is assumed to be log-normal. In addition, Input_builder adds to the input data file the remaining boundary conditions as initial velocity and geometry of the bundle. In case of generating a whole set of cases, it also selects randomly the initial and/or boundary conditions from the ranges that are given to the program. Further details are found in Appendix D with the source code of some of the programs used.

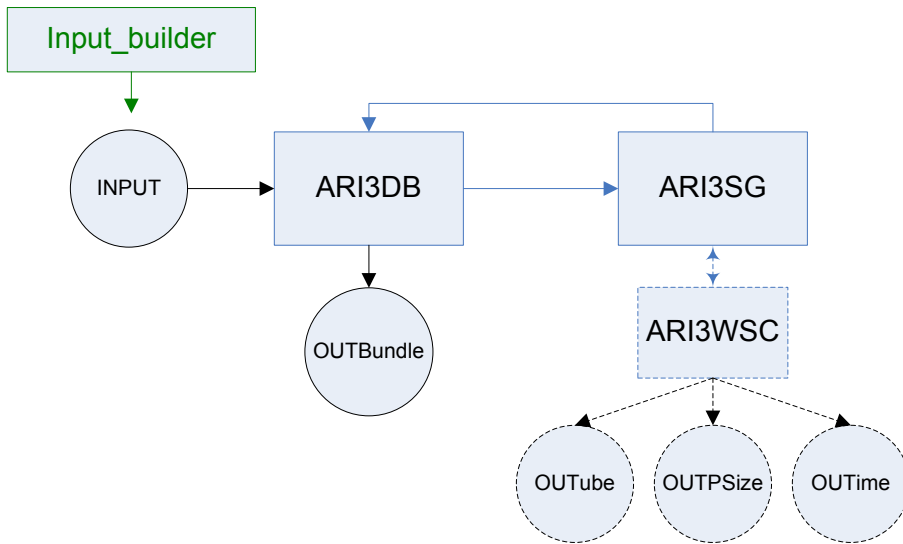


Fig. 3.3.1. ARICODE platform flowchart.

3.3.1. ARI3SG structure

The ARI3SG subroutine contains the coding of the model. It is highly modular because all the input variables and those generated through the model have been packed in 9 independent modules (Table 3.3.1). Each of them includes specific functions related with the nature of the variables.

Table 3.3.1. ARI3SG modules.

Module name	Description
BndlData	Geometrical information of the bundle of tubes and time conditions of the scenario: $d_t, s, L_t, N_t, n_{time,t}$ Function: ComputeNtubesMaxF
GasTHData	Gas properties and thermal conditions: P, T, ρ_g, μ Function: ComputeGasDensityF
SizeData	Particle size distribution and related variables: $q_p, AMMD, CMD, GSD, AMMD_{In}, GSD_{In}, N_{bins}, d_{par}(j), InletbinMass0(j), N_{parin0}(j), N_{parin}(i,j), InletbinMass0(i,j), MtotIntube(i,j), FracMinBin(i,j)$ Function: BinMassF, BinNbrPartF, CcF, StkF, ReparF, Compute_cmdF, Compute_gsdF, Compute_ammdF

Module name	Description
VData	Velocity related data: Radialvelocity, Axialvelocity, vinit, MssFlwRate Function: NewRadVeloGuillotF, RegasF, NewAxiVeloGuillotF, MassFlowInletF
BndEffData	Deposition and resuspension efficiencies: TubBinEffRad(i,j), TubBinEffAx(i,j), TubBinEffInit(i,j), ResusBinEff(i,j), MBinDepo(i,j), MDepoTube(i,j), TubEff(i,n), FinalBundleEff(i), TubBinEff(i,j,n), TubEff1, BundleDepoRad, BundleDepoAx
AxDpData	Variables related to the axial deposition: AxialDepoLength, AreaAxialDepoTube, UpwardFlowingArea, AxialVdepo, FactorAxialDepo Function: WallFricVeloF, WallShearStressF, RelaxTimeF, RelaxTimePlusF, DepVeloLiuAgarwPLUSF, DepVeloLiuAgarwF
FrcsData	Aerodynamic and adhesive forces: FGrav, FCohes, FFric, FDrag, FLift, FResul, FAdh, Nlayers Function: FGravitationalF, FCohesiveF, FFrictionalF, FDragF, FLiftF
RsspData	Resuspension variables: ResRateBinEcart(i,j), DELTA_t, VeloForResus Function: ResusRateEcartF
UncertData	Uncertainty variables: UncSDRad(j), UncEffAx(j), UncResusBinEff(j), UncAxTrm(j), UncResusTrm(j), UncResusRate(j), UncInitTubBinEff(j), UncFinalTubeBinEff(j), UncTubTrm(j), UncTubEff(j), UncTuBndle(j), UncSDUdepPlus, UncSumAllTubs, UncCmTrm

The flowchart of ARI3SG subroutine is shown in Fig. 3.3.2. It consists of three nested loops dependent on time, tube and particle bin size. For a given time (loop time), it computes the collection efficiency of each tube (loop tube) that is obtained through an average of the collection efficiency of each particle bin size (loop bin size). Fig. 3.3.2 shows that when the database mode is run, the model ARI3SG computes the last time step of the case ($n=t/\Delta t$) skipping the time-variations, this way a large database can be run within an optimized execution time. In case of singlcas mode, it computes the time variations (from $n=1$ to $t/\Delta t$) of the collection efficiency. The ARICODE platform including ARI3SG subroutine is written in around 1300 FORTRAN sentences. The source code is presented at the end of this document.

3. Development of the aerosol modeling

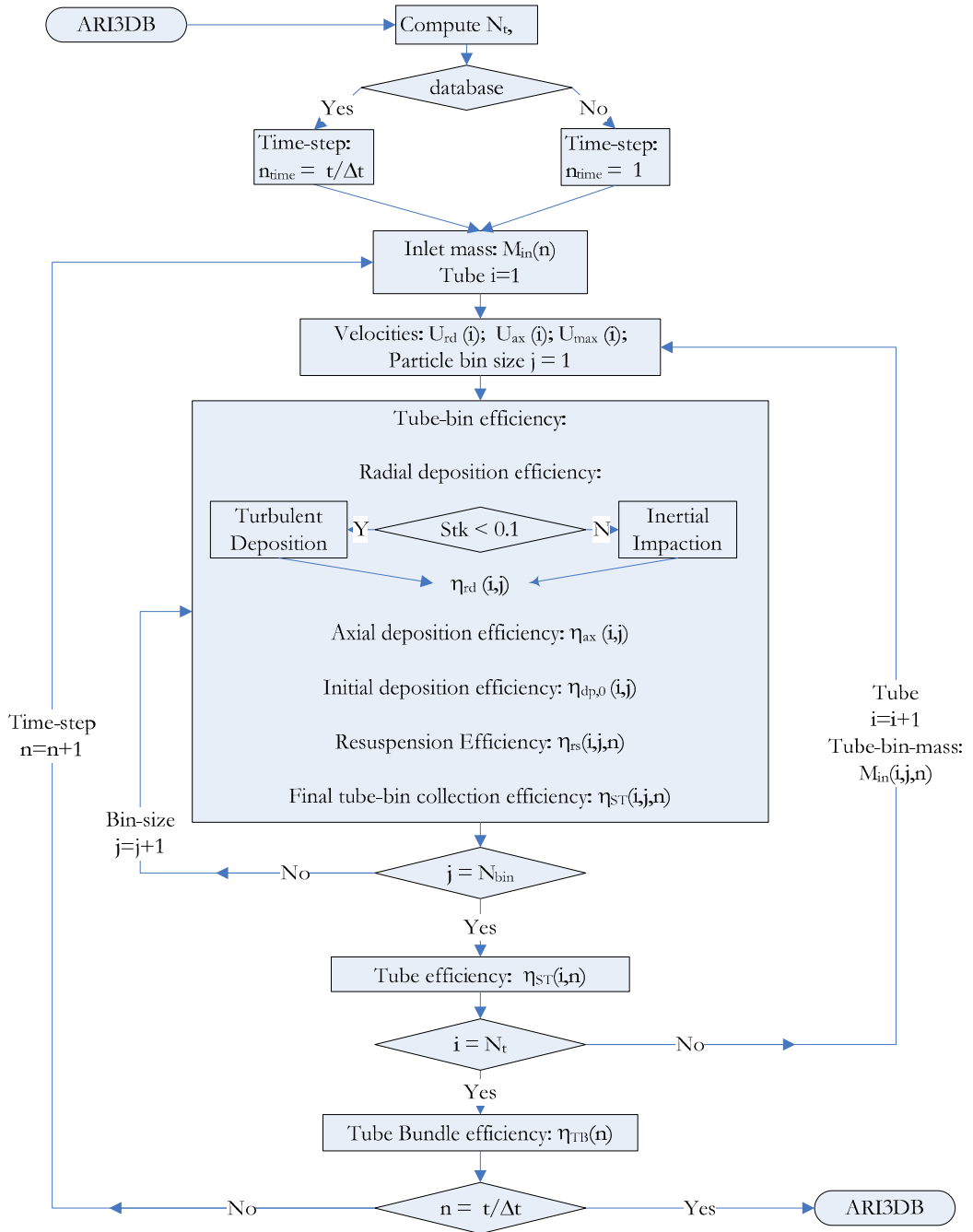


Fig. 3.3.2. ARI3SG flowchart.

3.3.2. Input description

The input deck of the code is set up by four types of data:

- Type of running mode: database/singlcas
- Geometrical variables: d_t , s , L_t
- Thermal and aerodynamics: P , T , U_0 , t , Δt
- Aerosol description:
 - Q_p , N_{bins}
 - $d_p(1), n_p(1), \dots, d_p(N_{bins}), n_p(N_{bins})$

An example of input deck is given in Appendix E.1.

3.3.3. Output description

The code generates a global output file called OutBundle.dat and in case of being in singlcas mode, it generates three more files: OuTube.dat, OutPSize.dat, OuTime.dat.

- OutBundle.dat file contains the boundary conditions of the case (tube diameter, duration, initial velocity, pressure, temperature, etc), the non-dimensional numbers characterizing the scenario (Re_g , Stk , Re_p), inlet particle size (AMMD, GSD) and the tube bundle efficiency.
- OuTube.dat file details at each tube the non-dimensional numbers, radial and axial velocities and AMMD and GSD of the size distribution, as well as the tube collection efficiency for all the time duration of the sequence.
- OutPSize.dat file details each bin of the particle size distribution at each tube. It includes bin diameter, inlet number of particles, mass, non-dimensional number of each bin size, radial and axial collection efficiencies, resuspension efficiency and the total collection efficiency for each bin at each tube.
- OuTime.dat file collects the time-varying of the collection efficiency of the tube bundle.

It must be mentioned that output files also provide the uncertainties of the models that are implemented in ARI3SG, which are introduced later on in section 3.6.1. An example of each output file is given in Appendix E.

3.4. VERIFICATION OF THE ARI3SG MODEL

ARI3SG has been verified through the analysis of asymptotic and solution-known cases. The intention is to check the right coding of the model and to demonstrate its physical response. This assessment has been performed in three steps: examination of major model elements (i.e., mass conservation and efficiency equations) to guarantee their consistency; checking of ARICODE coding and interfaces performance; and, finally, simulation of a set of well-known parametric cases (Table 3.4.1). Most cases were run on the basis of a set of default values for the scenario: $s=0.01$ m $d_t=0.02$ m, $N_t=11$, $d_p=1$ μm , $U_0=100$ m/s (these values are within the foreseen ranges in a SGTR scenario).

Table 3.4.1. Verification cases.

Asymptote	ARI3SG	ARICODE	
$s \rightarrow 0$ or $d_t \rightarrow \infty$	$\eta_{ST(i)}=0 \forall i$ tube	$\eta_{TB} \rightarrow 0$	\sqrt
	$\eta_{ST(i)}=1 \forall i$ tube	$\eta_{TB} \rightarrow 1$	\sqrt
	$N_t \rightarrow \infty$	$\eta_{TB} \rightarrow 1$	\sqrt
$s \rightarrow \infty$ or $d_t \rightarrow 0$		$\eta_{TB} \rightarrow 0$	\sqrt
$s=0.01$ $d_t=0.02$	$\eta_{ST(i)}=0 \forall i$ tube	$\eta_{TB}=0$	\sqrt
	$N_t \rightarrow \infty$	$\eta_{TB}=0.78$	\sqrt
	$t \rightarrow 0$	$\eta_{ST} \rightarrow \eta_{dp}$	\sqrt
	$t \rightarrow \infty$	$\eta_{ST} \rightarrow 0$	\sqrt
	$\eta_{dp} \rightarrow 0$	$\eta_{ST} \rightarrow 0$	\sqrt
	$\eta_{rs} \rightarrow 0$	$\eta_{ST} \rightarrow \eta_{dp}$	\sqrt
	$\eta_{rs} \rightarrow 1$	$\eta_{ST} \rightarrow 0$	\sqrt
	$N_{t,Max}=11$ and $\eta_{ST(i)}=1 \forall i$ tube	$\eta_{TB}=0.78$	\sqrt
	$N_t=1$ and $\eta_{ST(1)}=1$	$\eta_{TB}=0.64$	\sqrt
	$d_p=0$	$\eta_{TB}=0$	\sqrt
	$d_p \gg 10 \mu\text{m}$	$\eta_{TB}=0$	\sqrt
	0 particles	$\eta_{TB}=0$	\sqrt
	$U_0 \rightarrow 0$	$\eta_{TB}=0$	\sqrt

As expected, the highest collection efficiency is reached for an infinite number of tubes or a huge tube diameter. In addition, the table shows that given the tube packing density of the scenario ($\alpha=35\%$), the maximum collection efficiency that the model can predict is 78%. This value can also be reached with the maximum penetration ($N_{t,Max}=11$) if each single tube efficiency is maximum. Finally, the table also shows the decreasing trend of the collection efficiency with time, as a result of resuspension.

3.5. VALIDATION OF THE ARI3SG MODEL

Validation of the ARI3SG model was performed by comparing its predictions with the experimental SGTR and CAAT databases (Herranz et al., 2006; Sanchez-Velasco et al., 2010) obtained in the PECA facility of CIEMAT. They were devoted to investigate the aerosol retention in the break stage of a steam generator under dry conditions. These data sets allow analyzing the influence of the gas mass flow rates and the particle nature.

3.5.1. Experimental Set-up

The experimental set-up basically consisted of a gas supply system, an aerosol generation device, a tube bundle and a measurement system (i.e., sampling and instrumentation). Fig. 3.5.1 shows a sketch of the facility and a top view of the tube bundle within the 8.3 m³ vessel where it stood.

The bundle (330 × 300 mm) was a mock-up of the break stage of the secondary side of a steam generator. The tubes were 1.5 m high and 19.05 mm in diameter with a pitch to diameter ratio in the bundle of $p/d_t = 1.4$. They were arranged in a squared assembly of 11 × 11 (121 tubes), where the broken one was placed at the centre or displaced two positions depending on the breach configuration. Such configurations were based on CFD simulations (Quarini, 1999; Lopez del Pra et al., 2010a), which indicated that tubes beyond the fifth or seventh row from the breach should not affect substantially aerosol deposition. In other words, the size of the bundle is considered large enough to reproduce most of momentum dissipation of the incoming gas jet when moving through the system. The breach was placed at 0.24 m from the base.

The flow was injected into the broken tube through the base. Since the top end of the tube was closed, the flow was forced to exit through the breach and to expand across the bundle. Materials and dimensions of tubes (except for tube height) and support plates were identical to those used in a

3. Development of the aerosol modeling

real SG (Güntay et al., 2004). The whole structure was housed in a methacrylate frame and ended up with an upper plate simulating the separation between the break stage and the rest of the SG.

A fluidized bed generator (FBG) was used to produce the aerosol. In case of the CAAT experiments, a Venturi cone placed at the exit of the FBG partially de-agglomerated the particles reducing the injected aerosol diameter. Characterization of particles incoming and outgoing the bundle was done by online measurements devices based on different fundamentals: optical particle counter (OPC), aerodynamic particle sizer (APS), electrical low pressure impactor (ELPI) as well as by integral gravimetric systems: cascade impactors, membrane filters.

The aerosol deposits on tube surfaces were also collected and weighed to characterize the deposition pattern. Due to the symmetry of the bundle and the breach shape, $\frac{1}{4}$ of the tubes was weight. It was performed by means of U-rings set around the tubes, followed by wet paper which trapped the remaining attached particles.

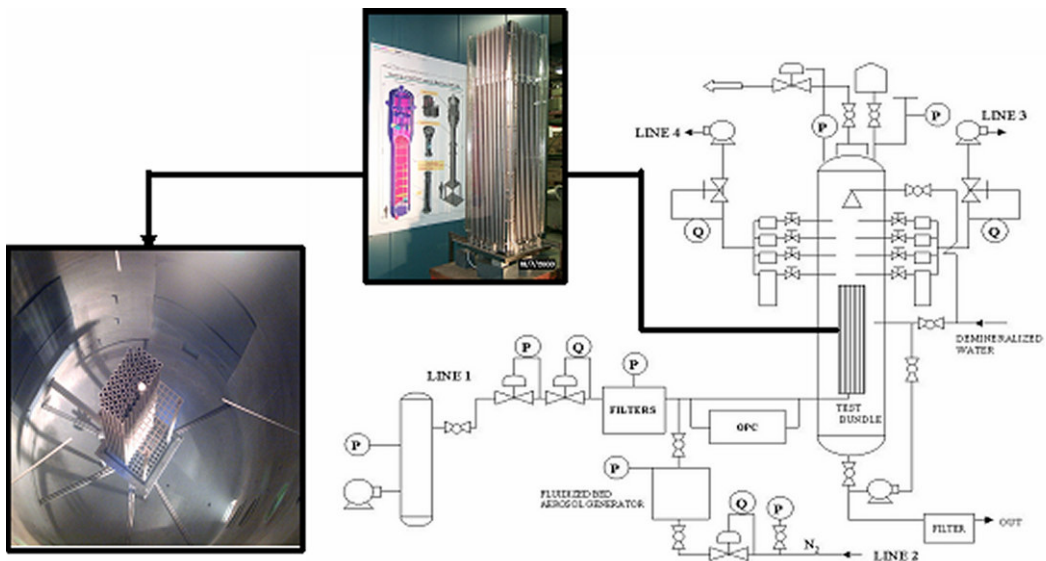


Fig. 3.5.1. Scheme of the PECA-SGTR facility.

The designs of the experimental matrixes were based on the analysis of the expected boundary conditions during the rupture of a tube in a SG and the LASS capabilities and limitations. According to simulations of SGTR scenarios carried out with the MELCOR and SCDAP/RELAP5 codes (Allison, 1995; Güntay et al., 2002; Dehbi et al., 2001), thermal and steam concentration gradients were not anticipated to play any role in the aerosol

deposition. This made it feasible to focus attention on achieving aerodynamic scenarios as close as possible to the actual scenarios and to use air as the carrier gas. The non-dimensional numbers characterizing both sets of experiments were $Re_g = 10^4-10^6$, $Stk = 10^{-2}-10$, $Rep = 0.1-300$, $Re_p^2/Stk = 10^2-10^3$. The tests were executed at room temperature and atmospheric pressure.

3.5.2. Database

The experimental boundary conditions and results of both databases are summarized in the following tables:

Table 3.5.1. SGTR experimental conditions and results (Herranz et al., 2006).

	Material	Time (s)	Φ (kg/h)	U_0^* (m/s)	Mass _{In} (g)	AMMD (μm)	GSD	η (%)
SGTR-1	TiO ₂	1860	249.7	252.24	96.61	7.42	1.8	3.96
SGTR-2	TiO ₂	1740	100.4	116.38	108.55	-	-	16
SGTR-3	TiO ₂	1620	149.3	160.86	113.47	6.72	1.67	8.65
SGTR-4	TiO ₂	1680	251.2	253.59	133.53	6.69	1.66	3.98
SGTR-5	TiO ₂	1740	103.1	118.85	74.87	-	-	18.8
SGTR-6	TiO ₂	1800	78.6	96.53	62.12	-	-	8.93
SGTR-7	TiO ₂	1800	71.8	90.34	56.6	3.37	1.49	14.98
SGTR-8	TiO ₂	1800	156.9	167.82	182.73	6.95	1.78	6.77
SGTR-9	TiO ₂	1800	245.2	248.11	186.35	7.13	1.78	4.08
SGTR-10	TiO ₂	1620	72.1	90.61	49.52	5.16	1.56	6.45
SGTR-11	TiO ₂	1620	150.2	161.74	120.36	6.7	1.67	7.24
SGTR-12	TiO ₂	1740	243.8	246.89	133.52	4.87	1.51	2.4

*Estimate

Table 3.5.2. CAAT experimental conditions and results(López del Prá et al., 2010c).

	Material	Time (s)	Φ (kg/h)	U_0^* (m/s)	Mass _{In} (g)	AMMD (μm)	GSD	η (%)
CAAT-1	TiO ₂	2208	93.4	109.99	20	3	2.9	27.5
CAAT-2	TiO ₂	1980	223	227.93	10	1.8	2.9	13.5
CAAT-3	TiO ₂	2760	99.7	115.73	128	1.1	5.3	15.8
CAAT-4	TiO ₂	3180	169	178.79	92	0.9	4	13.6
CAAT-5	TiO ₂	1860	125	138.75	55	1.1	3.8	15.8
CAAT-12	TiO ₂	2220	147	158.77	28	1.3	2.8	14
CAAT-8	SiO ₂	3180	183	191.53	34.5	1.2	3.3	84.1
CAAT-9	SiO ₂	3180	125	138.75	76.5	1.5	4.2	94.1
CAAT-10	SiO ₂	2340	176	185.16	33.15	1.3	6.1	92.9
CAAT-11	SiO ₂	3120	240	243.40	12.6	1.3	4.8	80.9
CAAT-13	SiO ₂	2820	81.4	99	41.3	1.3	2.8	81.2

*Estimate

3. Development of the aerosol modeling

Experimentally, two seeding materials were used to generate aerosols: TiO₂ and SiO₂. The former was used in the SGTR experiments whereas both of them were used in the CAAT ones. Table 3.5.3 collects their specifications (Degussa, 2005; Nanophase, 2002; Nagase, 2006).

Table 3.5.3. Manufacturer aerosol specifications.

Experiment	SGTR & CAAT	CAAT
Material	TiO ₂	SiO ₂
Aerosol size distribution	Polydisperse	Monodisperse
Average primary particle diameter (μm)	21.8·10 ⁻³	1.02
Material Density (kg/m ³)	3950	2000

3.5.3. Hypotheses and approximations performed

The inlet gas velocity (U_0) shown in Table 3.5.1 and Table 3.5.2 has been theoretically estimated according to Eq. (2.3.10).

The SiO₂ particles are spherical and monodisperse, so the derivation of the inlet count size distribution is straightforward. On the other hand, the TiO₂ material enters the facility in form of aggregates. It has been assumed that the aggregates are spherical and lognormally distributed with the AMMD and GSD obtained experimentally. It must be noted that there were no size measurements in tests SGTR-2, 5 and 6 and their sizes have been approximated with those of the closest gas mass flow rate tests (SGTR-3 and SGTR-10).

Regarding the TiO₂ particles density, it is an experimental unknown. However, the range of possible values was bounded theoretically. The aerosol density has to be lower than the material density due to the aggregate void fraction. The upper limit has been obtained assuming that primary particles forming the aerosol are solids spheres randomly packed with the highest configuration. Some researchers (Scott and Kilgour, 1969; Jaeger et al., 1992; Torquato et al., 2000) found out that the maximum density of such an arrangement was a 64% of the TiO₂ nominal one:

$$\rho_{\text{part,max}} = 0.64 \cdot \rho_{\text{TiO}_2} \quad (3.5.1)$$

Therefore, the upper bound of the aerosol density range has been taken as 2528 kg/m³.

Given the relevant role played by water density (1000 kg/m^3) in the characterization of aerodynamic aerosol motion (Hinds, 1999) it has been taken as the density reference in this study. As an approximation, the density interval has been distributed evenly at both sides of the reference density, so that the lower bound has been defined as:

$$\rho_{\text{part,min}} = \frac{1000}{2528} \cdot \rho_{\text{water}} \quad (3.5.2)$$

This results in a lower bound of 395.5 kg/m^3 , which agrees with the experimental lowest bound obtained by Leskinen et al. (2010) for TiO_2 aggregates.

In short, a reference density of 1000 kg/m^3 has been adopted and a density range has been estimated to be $400\text{-}2500 \text{ kg/m}^3$.

The inlet aerosol mass size distributions of SGTR and TiO_2 -CAAT simulations are shown in Fig. 3.5.2.

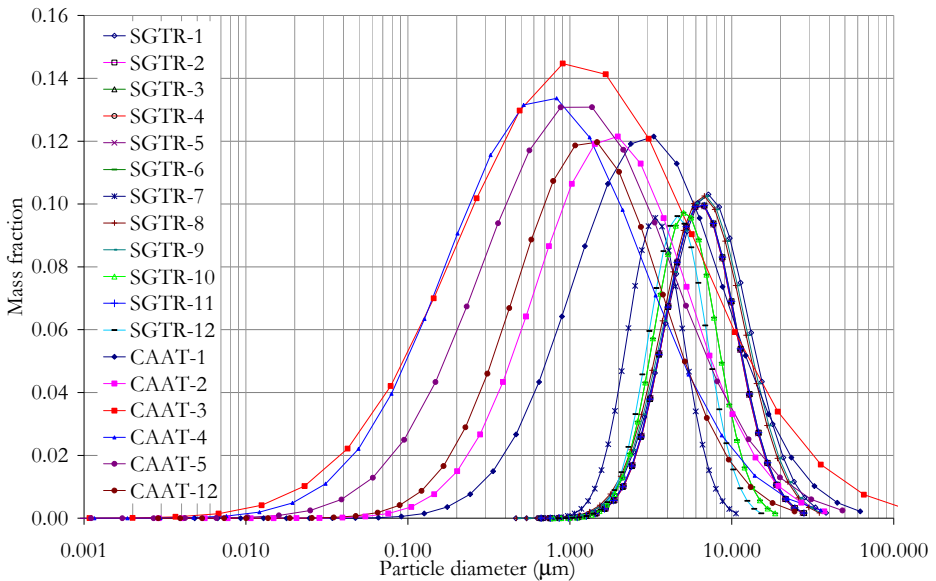


Fig. 3.5.2. Inlet aerosol mass distributions of TiO_2 simulations ($\rho=1000 \text{ kg/m}^3$).

3.5.4. Results obtained

3.5.4.1. TiO₂ simulations

This section compares SGTR and CAAT simulations of TiO₂ particles with the experimental data.

Fig. 3.5.3 shows the bundle collection efficiency versus the inlet gas mass flow rate of the SGTR simulations. Along with the experimental data, ARI3SG predictions of the reference and the minimum aerosol density cases are included. As for the reference density, the results of both cases indicate consistency with respect to data:

- Data and predictions lay within the “low range” of collection efficiency ($\leq 20\%$).
- ARI3SG results follow the experimental trend at gas mass flow rates higher than 100 kg/h: as gas mass flow rate increases, collection efficiency decreases. However, whereas the experimental trend decreases inversely proportional to the square of the inlet mass flow rate for $\Phi \geq 100$ kg/h (Herranz et al. 2006), predictions seem to decrease more slowly with the mass flow rate. That is, data decreased faster than estimates.

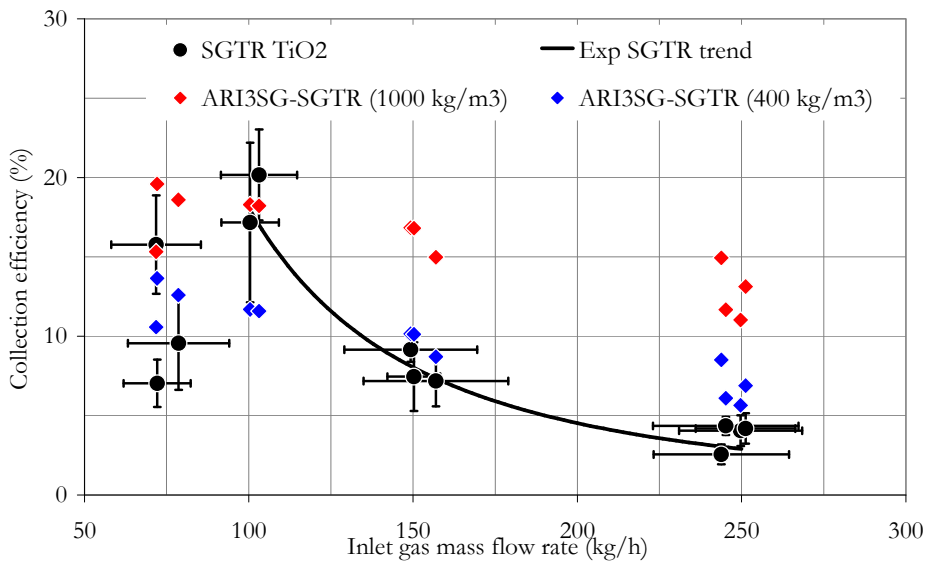


Fig. 3.5.3. TiO₂ SGTR, ARI3SG efficiency vs inlet gas mass flow rate (I).

As observed, the ARI3SG reference case overestimates predictions. By adopting the lowest bound of the density range new estimates resulted in a

notably better agreement with data. So, according to ARI3SG predictions SGTR-TiO₂ aerosols might have densities lower than 1000 kg/m³.

Experimental observations showed evidences of particle fragmentation in the scenario (Herranz et al., 2006). By assuming the experimental outlet size distribution (Table 3.5.4) and imposing a lower aerosol density, the results are closer to data (Fig. 3.5.4). The figure shows that, as expected, the smaller the particles the lower the integral collection efficiency.

Therefore, the above analyses show that most probably SGTR particles were less dense than 1000 kg/m³ and could have had sizes between inlet and outlet measurements.

Table 3.5.4. SGTR experimental outlet aerosol diameter.

Outlet	AMMD (μm)	GSD
SGTR-1	2.43	2.76
SGTR-2	2.31	2.68
SGTR-3	3.62	2.47
SGTR-4	3.62	2.20
SGTR-5	2.51	2.4
SGTR-6	3.14	2.55
SGTR-7	3.04	2.51
SGTR-8	3.85	2.22
SGTR-9	3.89	2.27
SGTR-10	3.11	2.59
SGTR-11	3.34	3.09
SGTR-12	2.48	2.65

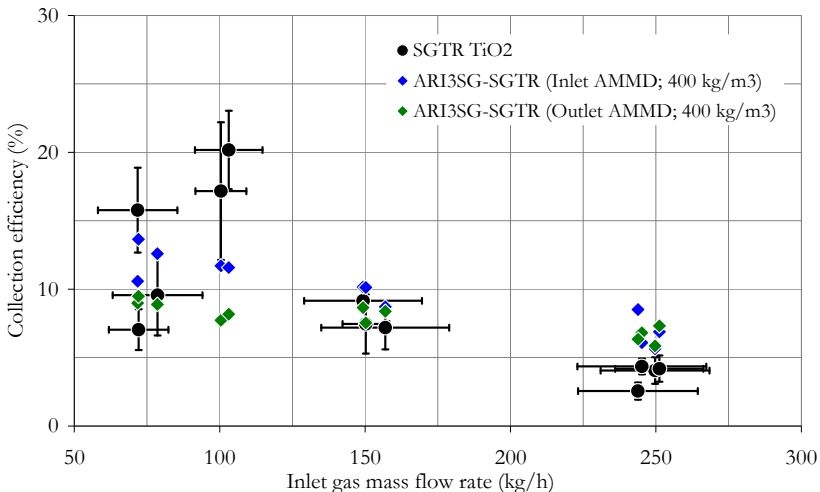


Fig. 3.5.4. TiO₂ SGTR, ARI3SG efficiency vs inlet gas mass flow rate (II).

Fig. 3.5.5 shows ARI3SG predictions of the TiO₂-CAAT tests. Consistently with TiO₂-SGTR, both data and estimates lay at the low range of collection efficiencies. Further than the quantitative agreement, it is also noticeable the fact that, neither data nor ARI3SG predictions change with the inlet gas mass flow rate. The slight fluctuations of ARI3SG estimates respond to variations in the initial and boundary conditions.

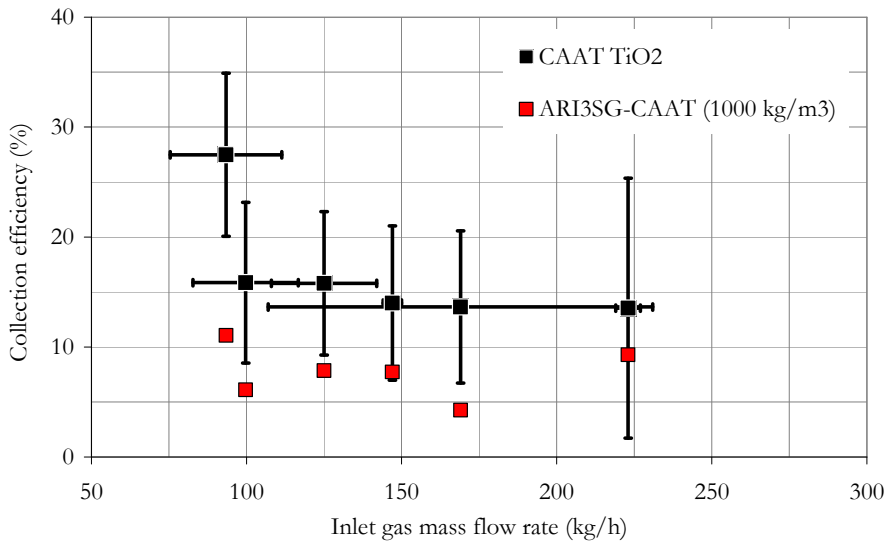


Fig. 3.5.5. TiO₂ CAAT, ARI3SG efficiency vs inlet gas mass flow rate.

In addition to previous ARI3SG-data analysis, a cross comparison of SGTR and CAAT data sets has been performed. It shows that whereas experimentally the CAAT tests reached slightly higher collection efficiencies than SGTR ones (Fig. 3.5.6(a)), the ARI3SG estimates indicate the opposite trend (Fig. 3.5.6(b)). In order to understand this discrepancy a set of studies have been carried out on the basis of the existing size and density uncertainties. As said above, particles density was not measured and there is no guarantee that TiO₂ particles in the SGTR and CAAT tests were equally dense, since even their generation was not fully equivalent (i.e., a venturi pipe was implemented in the CAAT tests to split up TiO₂ aggregates). In addition, particle size is affected by uncertainties too. On one side, there are evidences of particle fragmentation; on the other, even though the AMMDs given in Table 3.5.2 (measured with a Mark-III impactor) were given credit in the experimental analysis (Sánchez-Velasco

et al., 2010), other measurements (obtained with an APS) seemed to indicate particle diameters greater than those of Mark-III (although Mark-III measures looked more reliable).

Fig. 3.5.6(b) to Fig. 3.5.6(e) summarize the results of the analyses carried out with ARI3SG, the reference case included (Fig. 3.5.6(b)). In short, the results indicate that the CAAT particles might have been denser than the SGTR ones (and, even, the water) and bigger than measured by Mark-III.

According to the reference case results (Fig. 3.5.6(b)): the smaller the particle size (ARI3SG-CAAT), the lower the collection efficiency. By assuming a lower density for the SGTR particles, differences between both sets of predictions is diminished (Fig. 3.5.6(c)), but still opposite to experimental results. This opposite trend is reversed when assuming a higher density for the CAAT particles (Fig. 3.5.6(d)). Therefore, CAAT particles that had smaller sizes could have had higher densities than SGTR ones. This seems consistent with the fact that larger agglomerates of the same material usually have larger void fractions (Leskinen et al., 2011). In addition, the agreement between Fig. 3.5.6 (d) and (a) supports the experimental observation of SGTR particle fragmentation.

On the other side, by doubling the particle size of the CAAT particles, which results in AMMDs around 2 μm , the opposite trend between CAAT and SGTR predictions is almost reversed (Fig. 3.5.6(e)).

3. Development of the aerosol modeling

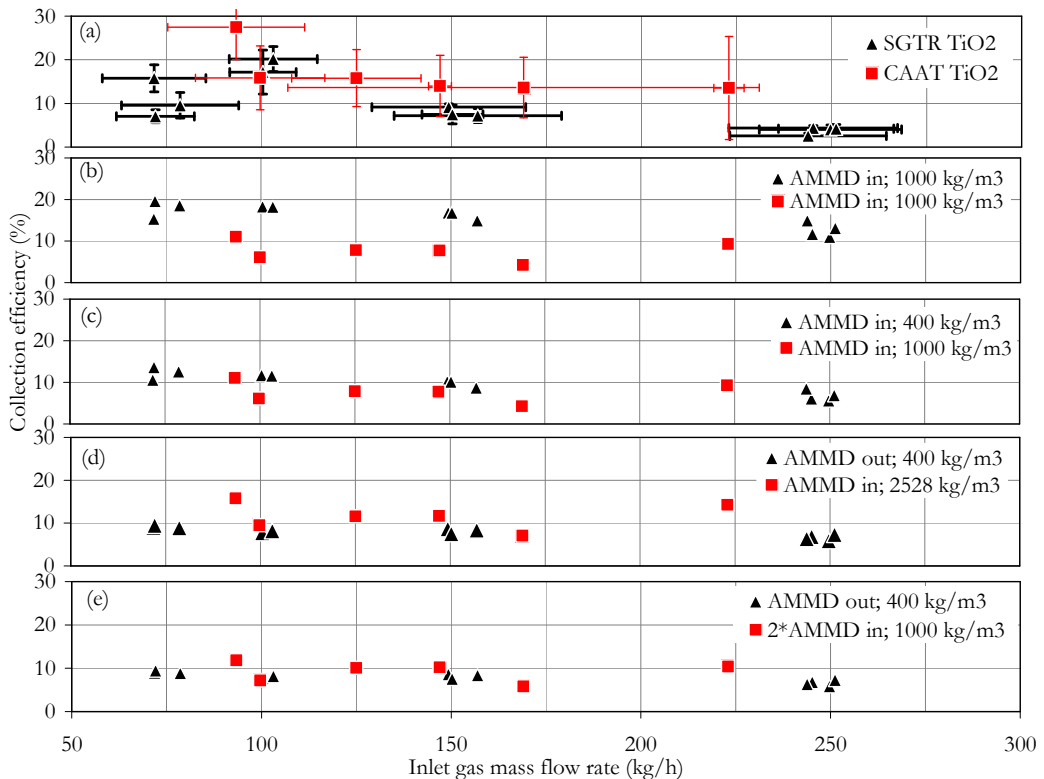


Fig. 3.5.6. TiO₂ SGTR, CAAT, ARI3SG efficiency vs inlet gas mass flow rate.

Father validation was performed with the experimental data obtained in the laboratory of the Paul Scherrer Institute (PSI). One of their experimental facilities is geometrically similar to the CIEMAT one (both manufactured by PSI), the main difference being that PSI one doubles the size of the CIEMAT's in terms of number of tubes. The test was performed with particles of a similar size of CAAT ones but with higher inlet gas mass flow rates (Lind et al., 2008). The comparison showed that prediction and data are in the same range with a slight ARI3SG underprediction (difference of 8%), although the estimate is within the experimental uncertainty band.

3.5.4.2. SiO₂ simulations

In the case of the SiO₂-CAAT tests, there was much less uncertainty in the inlet particle characterization, since they were spherical, nearly

monodisperse around 1 μm diameter. Nevertheless, given that these tests were conducted after TiO_2 ones some potential contamination was feasible, even once the injection lines had been flushed. As a result, Table 3.5.2 shows that Mark-III impactor measured sizes of around 1.2 μm of AMMD with a big GSD (from 3 to 6).

Fig. 3.5.7 shows that ARI3SG estimates a 10% of collection efficiency whereas retention was measured to be 80%. The discrepancy is outstanding. Even when only deposition mechanisms are taken into account in the modeling (i.e. no resuspension effect), estimates are still far from measurements. In addition, by neglecting resuspension predictions show a trend opposite to the data.

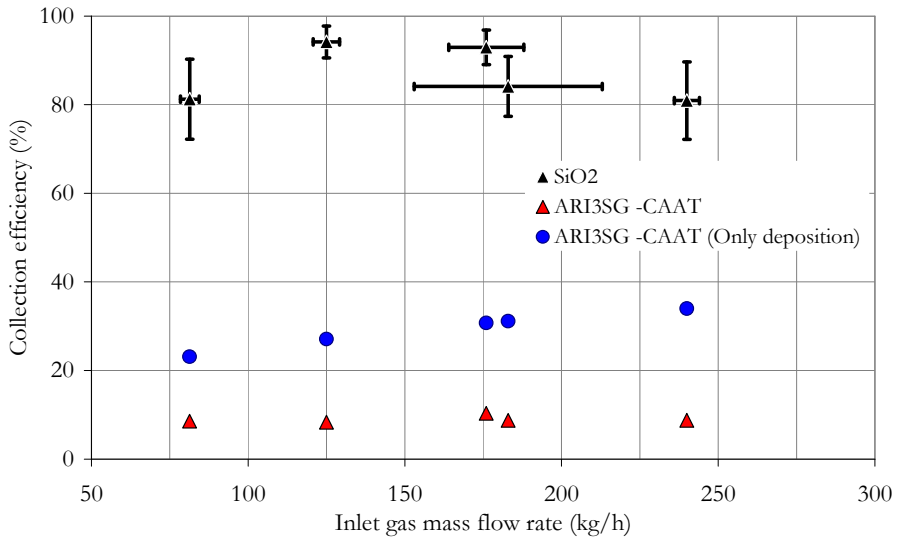


Fig. 3.5.7. SiO_2 CAAT, ARI3SG efficiency vs inlet gas mass flow rate (I).

SiO_2 efficiencies are much higher than TiO_2 ones. The reason behind could have been the different electrostatic behavior of both particle types. If electrical effects had come into play, they would have affected both to the deposition (since electrophoresis could have become a working mechanism for SiO_2) and by inhibiting resuspension to some extent (since electrical forces would have added to the attaching forces in the force balance).

Particles may become electrostatically charged by frictional contact with other materials. This phenomenon, called triboelectric charging, seems to happen often when generating particles by Fluidized Bed Generator (FBG; Yeh et al., 1988). The reason postulated for this phenomenon to affect

3. Development of the aerosol modeling

more strongly SiO₂ particles than TiO₂ ones, lies in their different electronegativity, which is higher for SiO₂ than for TiO₂. Given the correlation between specific charging and electronegativity (Matsusaka et al., 2010), it results that under the same conditions the specific charging of SiO₂ would nearly double TiO₂ one. This sensitivity to get charged by contact is further enhanced owing to the postulated lower density of TiO₂ agglomerates than SiO₂ particles one. In other words, if a SiO₂/TiO₂ density ratio around 2 is assumed ($\rho_{TiO_2}=1000 \text{ kg/m}^3$), SiO₂ particles would build up nearly 4 times more electrical charge than similar size TiO₂ particles. Lind et al. (2010) confirmed that fluidization of SiO₂ particles in a FBG increases their charge.

The analysis of the experimental results (Sanchez-Velasco et al., 2010), provided an ad-hoc numerical factor accounting for the difference in deposition of the SiO₂ particles with respect to TiO₂ ones. Accordingly, this factor was introduced into ARI3SG:

$$\eta_{SiO_2} = \eta_{ARI3SG} + 0.77 \quad (3.5.3)$$

The result is shown in Fig. 3.5.8. As expected, data and the adjusted estimates are in the higher range of collection efficiency. In addition, the experimental fluctuations of the collection efficiency are maintained by ARI3SG.

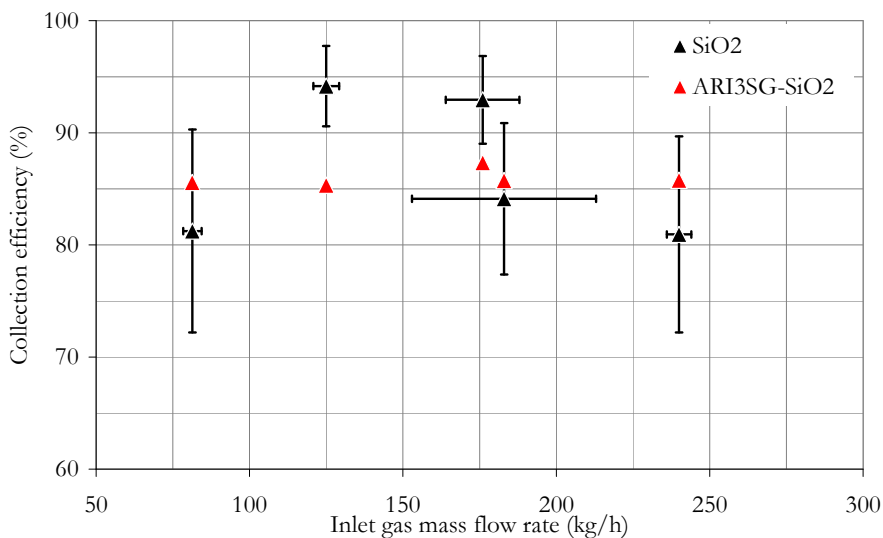


Fig. 3.5.8. SiO₂ CAAT, ARI3SG efficiency vs inlet gas mass flow rate (II).

3.6. UNCERTAINTY ANALYSES PERFORMED TO ARI3SG

The ARI3SG model provides the aerosol retention in the break stage of a steam generator under “dry” SGTR severe accident conditions. In the previous section its estimates have been compared to data and have shown a reasonable consistency; even further, parametric calculations have explored potential reasons for the experimental variations observed. So that ARI3SG has been used as an interpretation tool. However, given the ARI3SG approach, the empirical nature of the equations embedded and the requested input parameters, the ARI3SG estimates are forcefully affected by uncertainties of different kinds. Here two categories are distinguished: epistemic and stochastic uncertainties. The former comes from an incomplete knowledge of the system, not from its nature but from the limitation of our ability to model it (i.e. wrong modeling, measurement errors, etc), therefore they can be reduced. The later arise from the natural random variability inherent to the system itself, they can be more accurately characterized but not reduced (Chojnacki and Baccou, 2009).

In the case of ARI3SG, the epistemic uncertainty includes both those linked to the equations used to assess the effect of each individual aerosol mechanism considered, and the own filter approximation in which the whole model relies on. In this work those coming from the ARI3SG basic correlations have been considered (model uncertainties). The stochastic uncertainties have also been analyzed through the so called input uncertainties. As a result, those single points shown in the figures of previous sections under the ARI3SG heading will now turn into a band that encompasses the 95% of the confidence interval.

3.6.1. Model uncertainty applied to ARI3SG

Model uncertainty refers to those uncertainties associated to the modeling of deposition and resuspension mechanisms involved in the scenario. As seen above, each phenomenon was described through experimental correlations, which forcefully entail an uncertainty due to the scattering of the experimental data. Once those uncertainties were estimated, they have been propagated according to the law of uncertainties propagation (ISO Norm, 1995). This procedure leads to the combined standard uncertainty of the predicted efficiency ($u_c(\eta)$). As each of the experimental correlations is independent in the sense that they come from different experiments, this law can be expressed as (ISO Norm, 1995):

$$\boldsymbol{\eta} = f(x_1, \dots, x_N)$$

$$u_c(\boldsymbol{\eta}) = \left(\sum_{i=1}^N \left(\frac{\partial f}{\partial x_i} \right)^2 \cdot u^2(x_i) \right)^{1/2} \quad (3.6.1)$$

Where x_i are the independent variables and $u(x_i)$ their standard uncertainties.

Following previous formulation the combined standard uncertainty of each of the fundamental equations of ARI3SG has been derived. They are shown in Table 3.6.1 as functions of the uncertainties of their corresponding independent variables. As observed, the last three rows of the table show the dependence with the uncertainties of the experimental correlations used to model the deposition and resuspension phenomena: $u(\eta_{rd})$, $u(U^+)$ and $u(\Lambda)$.

Table 3.6.1. ARI3SG fundamental equations and uncertainties.

<p>Tube bundle efficiency</p> $\eta_{TB}(\eta_{ST}(1), \dots, \eta_{ST}(N_t)) = 1 - \exp \left\{ \frac{-1}{1-\alpha} \cdot \left[1 - \prod_{i=1}^{N_t} \left(1 - \frac{d_t \cdot \eta_{ST}(i)}{d_t + s} \right) \right] \right\}$ $u_c^2(\eta_{TB}) = \left[\frac{d_t}{d_t + s} \cdot \frac{(1-\eta_{TB})}{1-\alpha} \prod_{i=1}^{N_t} \left(1 - \frac{d_t \cdot \eta_{ST}(i)}{d_t + s} \right) \right]^2 \cdot \sum_{i=1}^{N_t} \left[\left(1 - \frac{d_t \cdot \eta_{ST}(i)}{d_t + s} \right)^{-1} \right]^2 \cdot u_c^2(\eta_{ST}(i))$
<p>Single tube efficiency</p> $\eta_{ST}(i) = \sum_{k=1}^{N_{bins}} Y(i, k) \cdot \eta_{dp}(i, k)$ $u_c^2(\eta_{ST}(i)) = \sum_{k=1}^{N_{bins}} Y^2(i, k) \cdot u_c^2(\eta_{dp}(i, k))$
<p>Tube-bin final efficiency</p> $\eta_{dp}(i, k) = \eta_{dp,0}(i, k) \cdot (1 - \eta_{rs}(i, k)) \cdot \frac{1 - (1 - \eta_{rs}(i, k))^n}{n \cdot \eta_{rs}(i, k)}$ $u_c^2(\eta_{dp}) = \left((1 - \eta_{rs}) \cdot \frac{1 - (1 - \eta_{rs})^n}{n \cdot \eta_{rs}} \right)^2 \cdot u_c^2(\eta_{dp,0}) + \left(\eta_{dp,0} \cdot \frac{(1 - \eta_{rs})^n \cdot (1 + n \cdot \eta_{rs}) - 1}{n \cdot (\eta_{rs})^2} \right)^2 \cdot u_c^2(\eta_{rs})$

<p>Tube-bin initial efficiency</p> $\eta_{dp,0}(\eta_{rd}, \eta_{ax}) = \eta_{rd} + \eta_{ax} - \eta_{rd} \cdot \eta_{ax}$ $u_c^2(\eta_{dp,0}) = (1 - \eta_{ax})^2 \cdot u^2(\eta_{rd}) + (1 - \eta_{rd})^2 \cdot u_c^2(\eta_{ax})$
<p>Tube-bin axial efficiency</p> $\eta_{ax}(U^+) = 1 - \exp\left(\frac{-U^* \cdot U^+ \cdot A_{dp}}{U_{ax} \cdot A_{crs}}\right)$ $u_c^2(\eta_{ax}) = \left[\frac{U^* \cdot A_{dp}}{U_{ax} \cdot A_{crs}} \cdot (1 - \eta_{ax})\right]^2 \cdot u^2(U^+)$
<p>Tube-bin resuspension efficiency</p> $\eta_{rs}(\Lambda) = 1 - \exp(-\Lambda \cdot \Delta t)$ $u_c^2(\eta_{rs}) = (\Delta t \cdot (1 - \eta_{rs}))^2 \cdot u^2(\Lambda)$

The standard uncertainties (u(f)) also called standard errors (SE) of the experimental correlations have been derived as follows (Coleman and Steele, 2009):

$$u(f) = SE = \left[\frac{1}{N-2} \sum_N (y_i - f(x_i))^2 \right]^{1/2} \quad (3.6.2)$$

Where f is the correlation and y_i and x_i are the dependent and independent experimental data, respectively.

The results are collected in Table 3.6.2 together with the averages of the 95% confidence intervals ($\overline{CI}_{95\%}$) and the deviations of the correlation from the experimental data (\overline{D}). For comparison purposes, the last two terms have been expressed in relative terms with respect to the correlation results. As expected, the average relative deviations are lower than the average of the confidence intervals, which extend the reach of predictions more than a 50%. The correlation that provides a better agreement with data is the inertial impaction one with a 19% of relative deviation, and the most improvable one is the resuspension rate with the highest CI (472%). Table 3.6.2 also includes the correlation coefficient (R^2).

Table 3.6.2. Uncertainties of correlations within ARI3SG.

Eq.	Range	u(f)	$\overline{CI}_{95\%}$	\overline{D}	R ²
Turbulent Deposition Efficiency:					
$\eta_{rd} = 0.438 + 0.071 \cdot \ln(\text{Stk})$	Stk < 0.1	0.0566	130%	35%	0.51
Inertial Impaction Efficiency:					
$\eta_{rd} = \frac{1}{1 + 4.87 \cdot 10^{-5} \cdot e^{10 \cdot \text{Stk}^{-1/8}}}$	Stk ≥ 0.1	0.0739	68%	19%	0.91
Dimensionless Axial Deposition Velocity:					
$U^+ = \text{Min}(6 \cdot 10^{-4} \cdot \tau_+^2, 0.1)$	$\tau_+ < 13$	0.437 · U ⁺	87.4%	30%	0.96
	$\tau_+ \geq 13$	0.03	60%	25%	
Resuspension Rate (1/s):					
$\Lambda(F) = \begin{cases} 0.4037 \cdot F^{0.6003} \\ 90.28 \cdot F^{1.269} \end{cases}$	$F < 3.065 \cdot 10^{-4} \mu\text{N}$	1.725 · Λ	344%	290%	0.6
	$F \geq 3.065 \cdot 10^{-4} \mu\text{N}$	2.367 · Λ	472%	57%	

It must be noted that standard uncertainties of the dimensionless axial deposition velocity (U^+ , $\tau_+ < 13$) and resuspension rate (Λ) correlations, given in Table 3.2.3, have been derived from their linear log-transformed functions through the first order Taylor series approximation. More details can be found in Appendix F.

Finally, the 95% of the CI of the correlations given in Table 3.6.2 and those of ARI3SG prediction (Table 3.6.1) are determined through the standard and combined uncertainties by $f(x) \pm 2 \cdot u(f)$ and $\eta_{TB} \pm 2 \cdot u_c(\eta_{TB})$, respectively.

Fig. 3.6.1 displays the propagation of the model uncertainty for the SGTR and CAAT simulations. It corresponds to the 95% of the confidence interval taking as the reference case the one established in previous section, so to say inlet values from Table 3.5.1 and Table 3.5.2 and densities of 1000 and 2000 kg/m³ for TiO₂ and SiO₂, respectively.

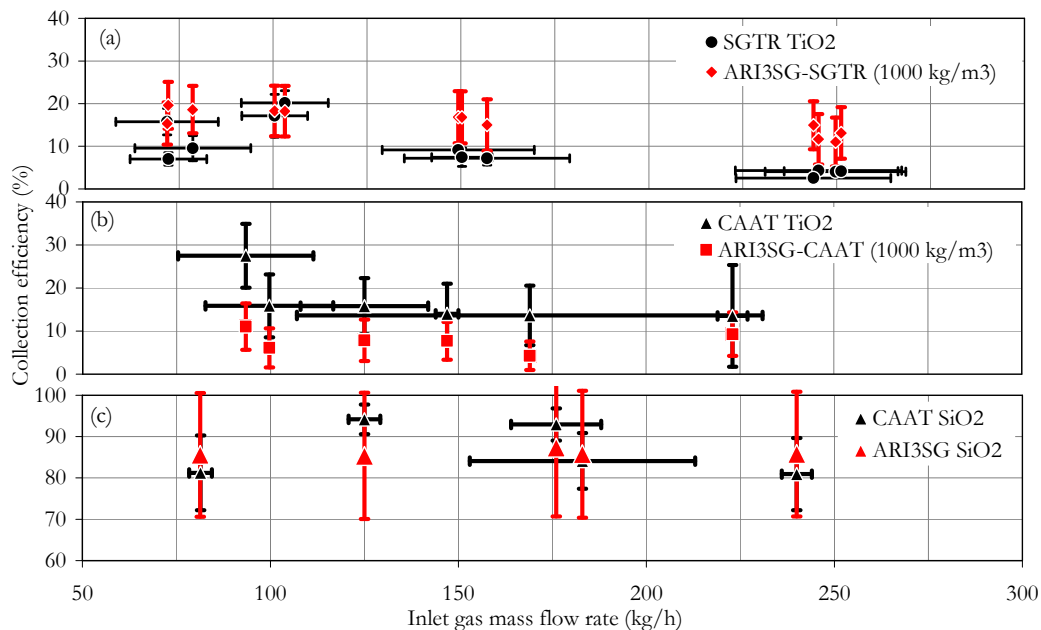


Fig. 3.6.1. Model uncertainty of SGTR and CAAT simulations.

Fig. 3.6.1 shows that consideration of the model uncertainty in ARI3SG brings most of predictions and data within the resulting uncertainty band. These bands that increase/decrease predictions an average of 38% and 62% of SGTR and TiO_2 -CAAT simulations respectively, overlap half of the experimental uncertainty range (Fig. 3.6.1(a)-(b)). The SiO_2 -CAAT case, they envelope the experimental results completely (Fig. 3.6.1(c)).

The comparison of both TiO_2 tests predictions (Fig. 3.6.1(a) and (b)) shows different lengths in the uncertainty bands. This is due to the different weight that each phenomenon involved has on each scenario, which in turn is due to the slight differences of the modeling of the initial and boundary conditions.

3.6.2. Input parameters uncertainty applied to ARI3SG

Input deck parameters in ARI3SG are far from being exact values. They come either from test measurements (i.e. particle diameter) or from derivations based on different kinds of hypotheses and approximations (i.e., density). Therefore, each attributed input value has an associated

uncertainty. This section assesses how these input parameter uncertainties affect the output of ARI3SG within a prescribed confidence range.

The procedure for determining output uncertainties followed the BEMUSE project guidelines (CSNI, 2007). It consists of 5 main steps:

- i. Choice of the most influencing variables of the scenario with their corresponding uncertainty ranges.
- ii. Proposal of a frequency function (probability density function, PDF) to each variable, with a mean (the reference value of the variable) and a standard deviation (its uncertainty). This way, the probability of having a particular value of that variable is given by the pdf.
- iii. Random sampling for each variable and for all the variables.
- iv. Code running.
- v. Repetition of iii and iv N_s times. This way all the sample inputs will provide outputs that will bound the uncertainty.

The number of samples N_s necessary for obtaining these bounds is derived from the Wilks theory (CSNI, 2007; Wilks, 1941, 1942). It uses the order statistics and says that when there is an N -sample of a random variable ordered (as the collection efficiency):

$$\eta: \eta_1(x_k, y_k, w_k, \dots) \leq \eta_2(x_i, y_i, w_i, \dots) \leq \dots \leq \eta_N(x_j, y_j, w_j, \dots)$$

Then, the probability β that the interval $[\eta_2, \eta_{N-1}]$ limits the α -percent of the total frequency of occurrence of the random variable η is given by (CSNI, 2007; Wilks 1941, 1942):

$$\beta = 1 - \alpha^{N_s} - N_s \cdot (1 - \alpha) \cdot \alpha^{N_s - 1} \quad (3.6.3)$$

That is, to get a 95% (α) of the variable η represented by $[\eta_2, \eta_{N_s-1}]$ with a confidence of 95% (β), it is necessary to conduct 93 (N_s) runs of ARI3SG.

This way, upper and lower limits of the collection efficiency ($\eta_2 = \eta_{LB}$; $\eta_{N_s-1} = \eta_{UB}$) determine the upper and lower uncertainty ranges. Their lengths Eq. (3.6.4) and Eq. (3.6.5) are given with respect to the reference case (η_{ref}), which is determined by the prediction of the mean values of each probability density function.

$$u_{UB}(\eta_{ref}) = \eta_{UB} - \eta_{ref} \quad (3.6.4)$$

$$u_{LB}(\eta_{ref}) = \eta_{ref} - \eta_{LB} \quad (3.6.5)$$

In the present formulation of ARI3SG, the input deck variables affected by uncertainties are:

- **Velocity.** The velocities of SGTR and CAAT tests are given in section 3.5.2 and their uncertainties are collected in Table 3.6.3.

Table 3.6.3. SGTR, CAAT inlet velocity uncertainty.

	$\delta\Phi$ (kg/h)	δU_0^* (m/s)		$\delta\Phi$ (kg/h)	δU_0^* (m/s)
SGTR-1	18.72	17.04	CAAT-1	18	16.38
SGTR-2	8.74	7.95	CAAT-2	4	3.64
SGTR-3	20.24	18.42	CAAT-3	17	15.47
SGTR-4	15.16	13.80	CAAT-4	62	56.42
SGTR-5	11.89	10.82	CAAT-5	17	15.47
SGTR-6	15.41	14.02	CAAT-12	3	2.73
SGTR-7	13.62	12.39			
SGTR-8	22.01	20.03	CAAT-8	30	27.30
SGTR-9	22.16	20.17	CAAT-9	4.2	3.82
SGTR-10	10.22	9.30	CAAT-10	12	10.92
SGTR-11	8.04	7.32	CAAT-11	4	3.64
SGTR-12	20.59	18.74	CAAT-13	3	2.73

*Estimate (section 2.3.3)

Velocities are assumed to follow a normal distribution as it seems more probable to have velocities close to the mean measured value than near the interval ends.

- **Aerosol size.** The aerosol size was also experimentally determined for TiO_2 particles. In this case, it is assumed that particles follow a lognormal distribution with its corresponding GSD (Table 3.5.1 and Table 3.5.2).
- **Aerosol density.** Regarding the aerosol density, it was an experimental unknown for TiO_2 aerosols. In section 0, density of the aggregates has been discussed and theoretically bounded. It falls within the range 400-2528 kg/m^3 (1000 kg/m^3 taken as the reference density). There is no clue about its frequency function, so that a uniform distribution has been assumed.

3. Development of the aerosol modeling

Following the procedure, 93 random samplings and computations were performed for each of the SGTR and CAAT experiments. As an example Fig. 3.6.2 and Fig. 3.6.3 show the histograms of the test SGTR-1 and SGTR-7 input samplings, respectively. In both cases, velocities follow a normal distribution. The former test is executed at higher velocities (252 ± 17 m/s) than the second one (90 ± 12 m/s). The AMMDs are lognormally distributed also with higher diameters for SGTR-1 test than SGTR-7 (Table 2).

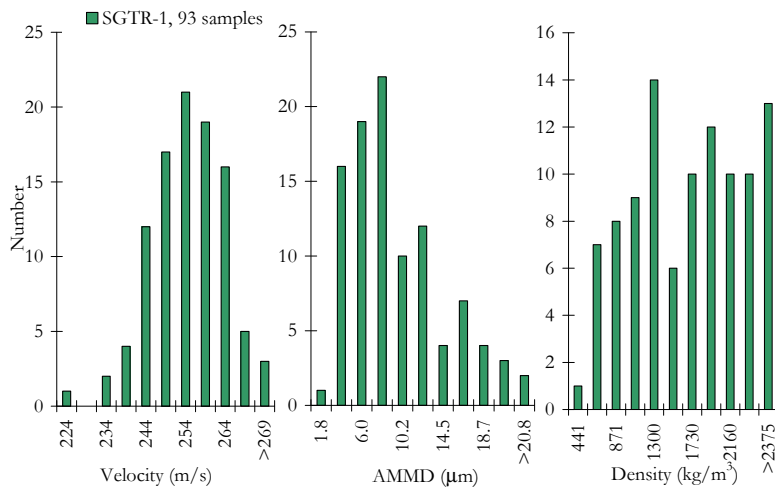


Fig. 3.6.2. Histogram of SGTR-1 input samplings.

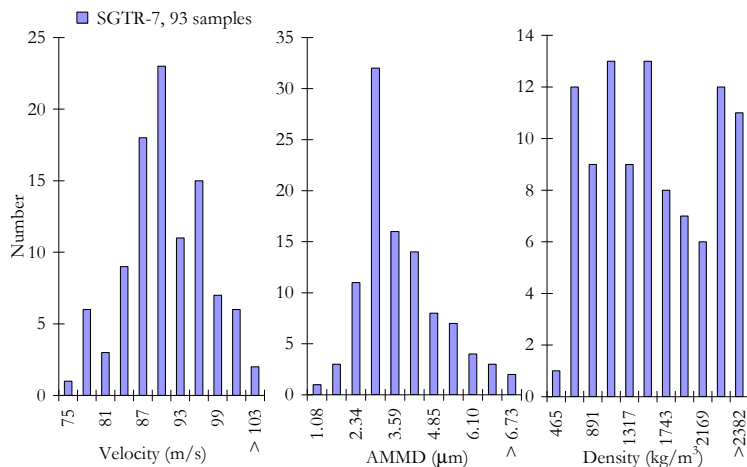


Fig. 3.6.3. Histogram of SGTR-7 input samplings.

3. Development of the aerosol modeling

Fig. 3.6.6 shows the lower and upper uncertainty bounds for the SGTR simulations. As observed, in most of the cases they envelop the experimental results so that the uncertainty in the input parameters account for the discrepancies between the reference prediction and data. The best estimate found in section 3.5.4 for SGTR simulations which assumed lower particle densities and sizes lay within this confidence interval.

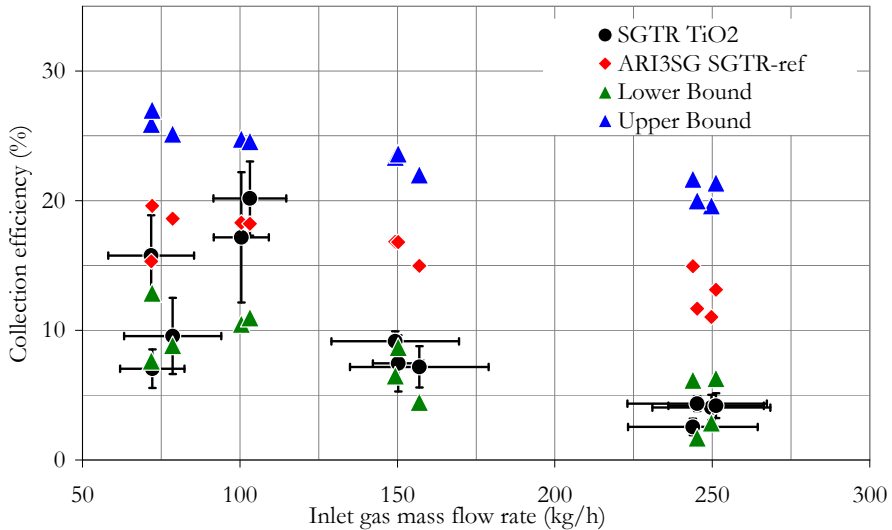


Fig. 3.6.6. Results of input uncertainty of SGTR simulations.

In case of TiO_2 -CAAT analysis, the upper bound obtained through Wilks envelops 50% of the experimental data (Fig. 3.6.7). However, they overlap with the experimental uncertainty band. As this bound takes into account variations of aerosol density and particle size, it underlines the previous discussion in section 3.5.4: the CAAT aerosols had either higher density than SGTR ones and/or were bigger than assumed.

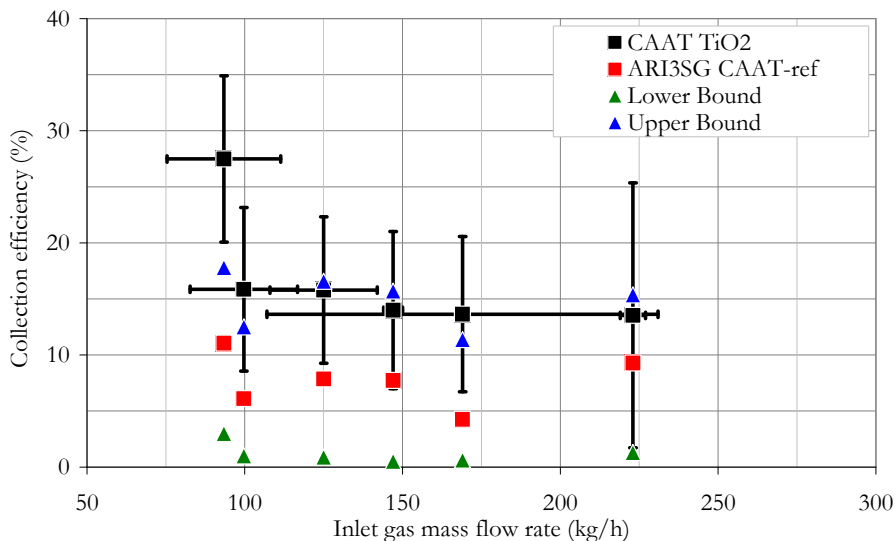


Fig. 3.6.7. Results of input uncertainty of TiO_2 -CAAT simulations.

The particles of the SiO_2 -CAAT experiments were monodisperse with a density of 2000 kg/m^3 . Therefore, velocity was the only variable submitted to uncertainty. The analysis performed, showed that nearly no influence on the collection efficiency (Eq. (3.5.3)), as both upper and lower bounds meant a difference less than a 1% of the prediction.

3.6.3. Sensitivity analysis performed

The influence of the uncertainty of each input parameter (velocity, AMMD and density) on the output has been individually analyzed. These analyses were performed through the SGTR-1 and SGTR-7 simulations by sampling the input parameter of interest while keeping the remaining ones with the reference value. Major observations are summarized as follows (Fig. 3.6.8 and Fig. 3.6.9):

Velocity variations (7-12%) have a low influence on the estimates as estimates vary from 1 to 6% of the prediction of the reference case.

The lower bound of the collection efficiency (full sensitivity column) seems to be determined by the uncertainty of the input AMMD, as sensitivity to AMMD is similar to the full one.

The upper bound of the full collection efficiency seems to result from the combination of the AMMD and the density variations. These joint

3. Development of the aerosol modeling

variations increase this upper bound as deposition phenomena dependent on the particle inertia.

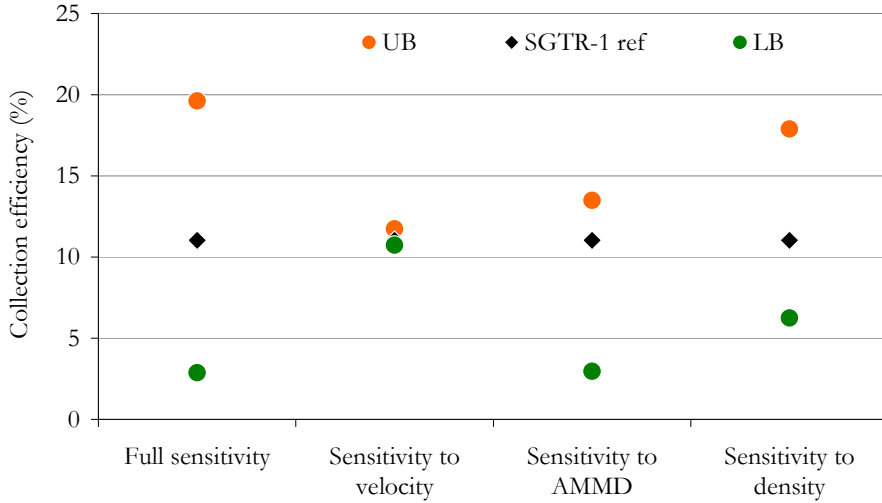


Fig. 3.6.8. Sensitivity results of SGTR-1 simulation.

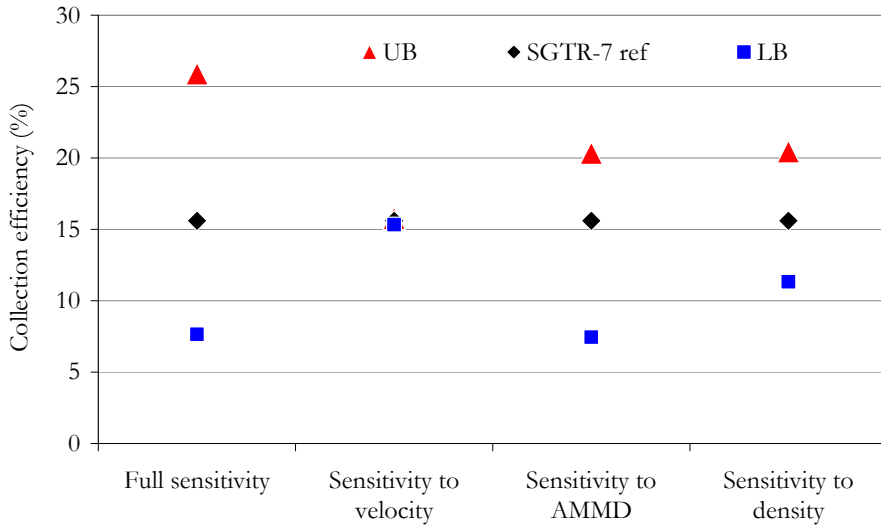


Fig. 3.6.9. Sensitivity results of SGTR-7 simulation.

These sensitivity analyses indicate that ARI3SG estimates are much less affected by gas velocity uncertainty than by those related to the particle characterization (i.e., size and density).

3.6.4. Total uncertainty performed

Finally, model uncertainties (u_c) and those resulting from the input parameter ones ($u_{UB, LB}$) are combined to yield the total uncertainty (u_T):

$$u_T(\eta_{ref}) = \begin{cases} +[u_{UB}(\eta_{ref}) + u_c(\eta_{UB})] \\ -[u_{LB}(\eta_{ref}) + u_c(\eta_{LB})] \end{cases} \quad (3.6.6)$$

Where u_{UB} and u_{LB} are given by Eqs. (3.6.4) and (3.6.5), respectively; $u_c(\eta_{UB})$ and $u_c(\eta_{LB})$ stand for the model uncertainties of the upper and lower collection efficiencies, respectively.

Fig. 3.6.10 shows the results of the reference case with the total uncertainty of ARI3SG simulations SGTR and CAAT experiments. In all cases except for one, the total uncertainties of predictions envelop data and even they overlap the experimental uncertainties.

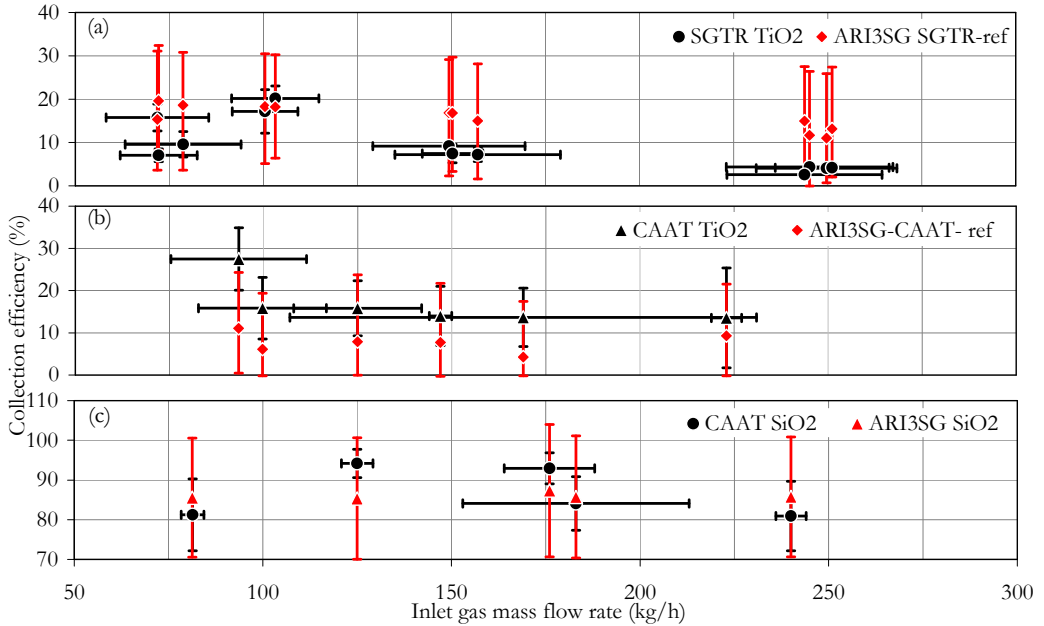


Fig. 3.6.10. Total uncertainty of SGTR and CAAT simulations.

Table 3.6.4 summarizes the uncertainty analysis in terms of averages. The variables included are: deviation between data and predictions, upper/lower bound uncertainties and model uncertainties. For comparison purposes, all of them are given in relative terms with respect to predictions of the reference case.

Table 3.6.4. Uncertainty ranges of ARI3SG simulations (SGTR, CAAT).

	\bar{D}	$\bar{u}_{UB,LB}$	$\bar{2 \cdot u_c(\eta_{UB,LB})}$	\bar{u}_T
TiO ₂ -SGTR	$\pm 0.48 \cdot \eta_{ref}$	$\pm 0.52 \cdot \eta_{ref}$	$+ 0.25 \cdot \eta_{UB}$ $- 0.6 \cdot \eta_{LB}$	$\pm 0.85 \cdot \eta_{ref}$
TiO ₂ -CAAT	$\pm 1.25 \cdot \eta_{ref}$	$+ 1.0 \cdot \eta_{ref}$ $- 0.85 \cdot \eta_{ref}$	$+ 0.4 \cdot \eta_{UB}$ $- 1.2 \cdot \eta_{LB}$	$+ 1.9 \cdot \eta_{ref}$ $- 1.0 \cdot \eta_{ref}$
SiO ₂ -CAAT	$\pm 0.06 \cdot \eta_{ref}$	$\pm 0.001 \cdot \eta_{ref}$	$\pm 0.18 \cdot \eta_{UB,LB}$	$\pm 0.18 \cdot \eta_{ref}$

It must be noticed that SiO₂ uncertainties are given with respect to the modified ARI3SG model which takes into account the deposition factor related to the particle charge (section 3.5.4.2).

The table shows the magnitude and scope of the uncertainty analysis. The deviations are in most of the cases smaller than the uncertainty band associated to ARI3SG estimates, in other words, data-predictions discrepancy are not such when one takes into account input and modeling uncertainties. As for the effect of input uncertainties, it is noticeable that whereas for SiO₂ particles they have been found negligible, this is not the case for the TiO₂ particles, particularly those of the CAAT tests. In most of the cases, input uncertainties introduce higher uncertainties in the results than those of the modeling itself. This discussion highlights the importance of achieving a good particle characterization in terms of density and size. Whenever those two parameters are highly uncertain, ARI3SG estimates should be given in terms of intervals rather than as a single collection efficiency value.

3.7. DERIVED CORRELATION OF ARI3SG

The final outcome of the work is the development of a theoretical correlation capable of estimating the aerosol retention within the break stage of a dry steam generator under SGTR conditions. The aim is to derive a simple expression dependent as much as feasible on non-dimensional numbers characterizing the scenario and encapsulating the ARI3SG behavior as accurately as possible. This way, its implementation in nuclear safety codes will be straightforward.

In order to do so, a theoretical tests matrix was set up based on characteristic intervals of the main scenario variables: initial velocity, aerosol density and size. The variables intervals sampled were those corresponding to the ARI3SG validation (Table 3.7.1). Sampling has been randomly conducted by assuming uniform distributions of the variables in their respective ranges and a lognormal size distributions for each (AMMD, GSD) pair. The results constitute a theoretical database consisting of more than 1000 cases. Specifically, the tube bundle has been described according to the CIEMAT mock-up (representative of a real steam generator): $d_t=1.9 \cdot 10^{-2}$ m; $s=10^{-2}$ m. A consistency checking was carried out to confirm that the corresponding non-dimensional numbers of all the cases were within the SGTR interesting ranges (Table 3.2.2).

Table 3.7.1. Characteristic SGTR & CAAT tests ranges.

Initial velocity:	78-270 m/s
AMMD:	0.1-8 μm
GSD:	1.5-3
Aerosol density:	400-3000 kg/m ³

Fig. 3.7.1 shows the ARI3SG collection efficiencies of the random theoretical database versus the Stokes number. As expected, it is seen that collection efficiency increases when increasing Stokes number. However, there is a wide scattering of results for a single Stokes.

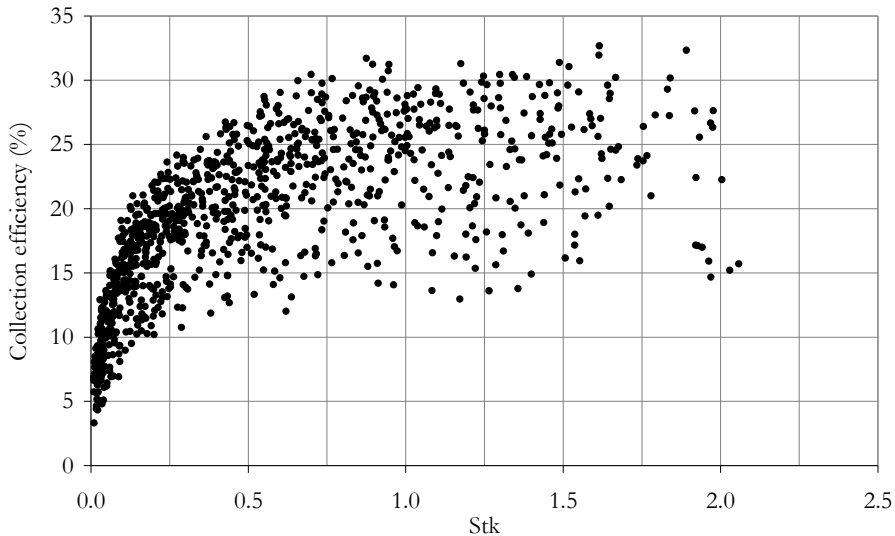


Fig. 3.7.1. ARI3SG results vs Stokes number.

As already seen in previous sections, phenomena involved in the scenario depend primarily on the Stokes number and particle diameter. Therefore, the final equation form of the collection efficiency was assumed to depend on the Stokes number. However, Brun et al. (1955) demonstrated theoretically that collection efficiency also depends on particle Reynolds number (Re_p). They introduced this dependence through the dimensionless parameter Re_p^2/Stk that together with Stk is sufficient to define the conditions of an impinging particle. Note that Re_p^2/Stk is independent of particle diameter.

A set of generic type equations were tried out (i.e., exponential, potential, sigmoid, etc), and in the end, the one that got the best fitting to the ARI3SG results has been:

$$\eta_{TB} = 0.47 \cdot \exp \left[-0.009 \cdot \left(\frac{Re_p^2}{Stk} \right)^{\frac{1}{2}} \right] \cdot Stk^{\frac{1}{4}} \quad (3.7.1)$$

The correlation coefficient of Eq. (3.7.1) is 0.98 with a standard uncertainty of 0.012. In relative terms the average deviation of the correlation with respect to the ARI3SG model predictions is 6.8% which seems reasonable.

By plotting this equation versus ARI3SG predictions, a remarkable agreement has been found (Fig. 3.7.2). At the lower range of collection efficiency (<10%), the correlation experiences a bias to over predict ARI3SG. Anyway, as it has been shown in the preceding sections, the uncertainty bands will for sure envelope this discrepancy.

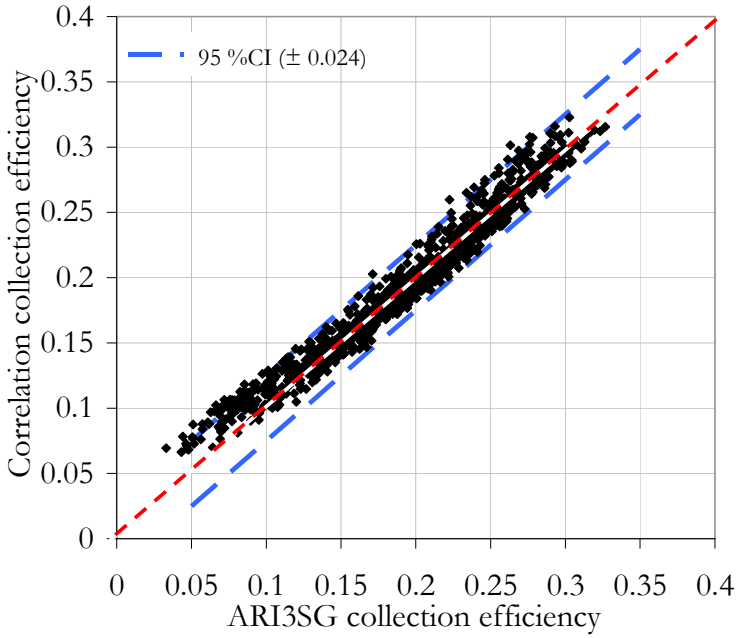


Fig. 3.7.2. Correlation vs ARI3SG collection efficiency.

Eq. (3.7.1) indicates that the total collection efficiency predicted by ARI3SG under the conditions of interest in dry-SGTR scenarios is dependent not only on the particle inertia around the tube (through the Stk number) but also on the gas flow influence over the particle as Re_p^2/Stk results a function of the Re_g .

3.8. CONCLUSIONS OF THE AEROSOL MODELING

- **The predictive capability of aerosol retention at the break stage of a dry steam generator has been extended.** Despite the intrinsic complexity of the scenario, by adopting the filter approach and accounting for most of the working mechanisms in the scenario, a semi-empirical model called ARI3SG has been developed. The main model output is the bundle efficiency, although additional information regarding the time evolution of the bundle efficiency as well as individual tube contributions to the overall retention may also be provided. The aerosol mechanisms equations encapsulated within ARI3SG have an empiric nature. Some of them have been derived through compiling and correlating extensive databases from tests with certain similarities to the scenario under study (inertial and turbulent radial deposition). Some others have been taken from the available literature (turbulent axial deposition). And, finally, some have been adopted and then adapted to the ARI3SG context, always with a conservative character (resuspension).

- **A computational platform has been built up, ARICODE, as a driver of the analyses.** ARICODE consists of a set of elements, which provide a sound structure to the analysis conduction. The main element is, of course, the ARI3SG model, whose programming has been given a highly modular structure. All the elements of this platform are written in FORTRAN, except for the so called “input_builder”, which has been developed in the Mathematica environment.

- **The ARI3SG model predictions have been compared with the available database of the scenario under analysis.** Data from the SGTR and ARTIST projects have been used for this purpose. Through such comparisons two major tasks have been conducted: ARI3SG validation and test interpretation.

As for the ARI3SG validation, the model has shown a great consistency when compared to TiO_2 data, predicting bundle efficiency at the lower range (i.e., 5-30%) and following the trends measured at gas flow rates over 100 kg/h. The SiO_2 simulation is a different matter; according to the data discussions an ad-hoc factor (0.77) has been introduced, possibly to take into account electrical effects in particle behavior.

As for the test interpretation, by analyzing the major uncertainties regarding TiO_2 particle characterization, the ARI3SG model has pointed that data-estimates discrepancies found could come from

density and size particle uncertainties. Generally speaking, TiO_2 aggregates would be smaller than measured and their density is likely to have been far from the nominal TiO_2 density.

Even more important, by discussing data through ARI3SG calculations and analyses of TiO_2 and SiO_2 properties, a potential explanation of the substantial difference observed in retention efficiency has been postulated. It would have been the greater susceptibility of SiO_2 to get electrically charged (triboelectric effect) the main reason behind the larger SiO_2 retention, by enhancing electrophoresis and decreasing resuspension. This assumption needs further tests to be validated.

- **A comprehensive uncertainty treatment has been developed to fully capture the predictive capability of ARI3SG.** Both model and input uncertainties have been considered and, as a result, it has been realized that data-estimates differences lose any significance when uncertainty bands have been considered. In all the cases, input uncertainties impact dominates over the modeling ones.

- **The ARI3SG model predictive capability has been encapsulated in a theoretical correlation based on Stk and Rep non-dimensional numbers.** A large number of cases have been randomly created by sampling the ranges of the main variables (i.e., density, AMMD, U_g), and their corresponding bundle efficiency has been showed to follow a decreasing exponential function with the Re_p^2/Stk multiplied by an increasing function of the Stk number. The R^2 of the correlation found is 0.98 which is high, and the standard uncertainty is 0.012. In relative terms the average deviation of the correlation with respect to the ARI3SG model is 6.8% which seems reasonable.

4. CONCLUSIONS AND FINAL REMARKS

This work thesis presents a theoretical model (ARI3SG) for the aerosol retention efficiency of the break stage of a dry steam generator under hypothetical severe accident SGTR conditions.

The theoretical research has been developed following two research lines. The first one, an investigation through 3D simulations has been devoted to characterize gas aerodynamics across the tube bundle. The second one, the most influential aerosol phenomena for the aerosol retention in the SGTR scenario have been modeled following a filter approach. The approximate nature of the model is balanced through an uncertainty analysis that provides a range of estimates of the modeled retention efficiency.

In both research lines, the theoretical results have been compared to experimental data allowing the validation of the models and strengthening its reliability. As a result, a Fortran code implementing the model for the Aerosol Retention In the Secondary Side of the Steam Generator (ARI3SG) has been built up. The ARI3SG estimates of the retention in dry SGTR scenarios have been encapsulated in a correlation that is available for use in severe accident nuclear safety codes like MELCOR or ASTEC.

4.1. CONCLUSIONS AND FINAL REMARKS ON FLUID FLOW MODELING

A thorough characterization of the gas flow coming out from a broken tube under SGTR conditions was carried out with 3D simulations performed with FLUENT 6.2 code. The bundle of tubes of the break stage of the SG was modeled for two breach shapes: guillotine and fish-mouth. The results were qualified and validated against representative experimental data and provided valuable information to understand the jet behavior across the bundle. From such an understanding, useful aerodynamic laws and approaches for aerosol retention modeling have been derived. The major insights obtained may be summarized as follows:

- The jet behaves quite differently depending of the breach type. In the case of guillotine breaks, the jet flows through the bundle describing a pseudo-parabolic trajectory. Due to azimuthal symmetry of jet topology as well as dominance of radial and axial velocity components at different regions of the bundle, the jet development may be described in two stages: an initial radial expansion and a subsequent

axial development. Fish-mouth jets, unlike guillotine ones, develop radially and axially at the same time, which prevents from a simplistic splitting of jet evolution in stages.

In addition to the qualitative differences referred above, quantitative differences are set out in key variables, like jet penetration and velocity. At the same initial mass flow rate, jets from fish-mouth breaches reach further radial distances than those from guillotine breaches. Additionally, maximum gas velocities (near the breach) are higher in fish-mouth configurations; however, radial and axial velocity decay is sharper in the case of guillotine breaches. The higher “fish-mouth velocities” seems to be caused by a smaller exit cross-section whereas the fast velocity decrease of “guillotine jets” might be a consequence of the large exchange surface area exposed.

- The tubes act as turbulence and upward motion enhancers. By comparing experimental and analytically free and “in-bundle” jets, it has been demonstrated that the tubes increase turbulence and force a gas mass fraction to flow upwards. The turbulence augmentation seems to be caused by the acceleration of the flow due to the cross-section restriction in the presence of tubes. The accentuation of the vertical orientation may be due to the so called Coanda Effect.
- The mass flow rate affects quantitatively some important features of the jet. By increasing the gas mass flow rate, the momentum exchange between the jet exiting the breach and the initially quiescent gas in the bundle is intensified; in other words, the so called suction effect (i.e., some quiescent gas is eventually entrained in the jet) is fostered. In addition, high mass flow rates result in deeper jet penetrations in the bundle.

4.2. CONCLUSIONS AND FINAL REMARKS ON AEROSOL MODELING

The aerosol retention in the break stage of a failed, water-empty steam generator under the anticipated conditions of a core meltdown SGTR sequence has been modeled extending the predictability capability of current nuclear safety codes. The model ARI3SG has been validated with the available experimental data. The semi-empiric analytical tool developed on the basis of the tube bundle filter performance, has been encapsulated in a FORTRAN code from which a theoretical correlation relying on non-dimensional numbers has been derived. No less important, an uncertainty

analysis accounting for both input deck and models, has allowed assessing the true ARI3SG predictability.

Among the final remarks derived from this work, one may highlight the following ones:

- The break-stage of a failed steam generator has a non-null capability of retaining particles. Even in the adverse case of loose agglomerates, a fraction of the mass could be retained, although one should not anticipate retention mass fractions higher than 30%. The actual retention will be strongly dependent on particle nature and it will change with the inlet gas flow rate.
- Turbulent and inertial mechanisms will be the main source of aerosol mass depletion; however, their efficiency will be lowered to some extent by particle resuspension. In addition to these, always working mechanisms, there are some others which will take place depending on particle nature, like fragmentation or electrophoresis.
- Suitable account of phenomena fostering and hindering deposition within a calculation structure based on the filter performance of the break stage can approximate in-bundle aerosol retention. Nonetheless, some working phenomena might require information not available in current safety codes, like particle charge.
- Scenario modeling is feasible. Given the intrinsic complexity of the scenario (i.e., geometry, boundary conditions) and the inherent uncertainties associated to key variables (i.e., gas velocity, particle nature and size), any intended theoretical approach should be accompanied by an uncertainty analysis that results in a range of retention efficiency more than in a single value.
- The net aerosol deposition within the bundle can be encapsulated in a correlation based on non-dimensional numbers such as Stk and Re_p . Far from pursuing accuracy, predictions from this type of equations should be taken as indicating an efficiency range. In case that electric particle charge enhances deposition, predictions would be conservative.

4.3. MODELING DRAWBACKS AND FUTURE WORK

This research has meant a significant progress in the SGTR issue research. However, there are still gaps to fill in terms of the full scenario understanding and maturity of predictive tools. Factors such as breach shape or tube vibration are assumed to have an effect, but there are not reliable data on the

matter. These two aspects are being addressed in the current CIEMAT experimental program within ARTIST II.

In addition to the shortcomings of the ARI3SG modeling scope (i.e., only the near-field is modeled), the simplicity associated to the filter approach necessarily involves a loss of detail: no distinction was made between guillotine and fish-mouth breach type, despite showing a low influence in the integral retention efficiency of the SGTR tests.

Concerning the aerosol phenomena, some missing and other improvable mechanisms should be considered:

- Particle agglomeration and fragmentation of aggregates that may be present in the scenario are not taken into account in the modeling and should be included in future versions.
- Turbulent deposition in a cross-flow configuration that has been modeled by an empirical correlation is highly uncertain due to the scattering and the few data available and should be improved.
- Resuspension was modeled through an empirical correlation that was seen to be highly uncertain and should be improved, either by increasing the database or by developing new mechanistic models.

Although ARI3SG has been an improvement of the predictive capability in the scenarios investigated, it requires to be strengthened by extending its validation and by updating its formulation to better accommodate the scenario features whenever further insights into the scenario are gained.

The next step of the modeling will be the comparison with the experimental CAAT2 data that are currently being performed as part of ARTIST II project. These tests will further assess the influence of breach shape on the aerosol retention by using a fish-mouth configuration.

Regarding current version, it is foreseen to implement the correlation derived from ARI3SG estimates into the severe accident code MELCOR. The predictability of the source term retention in a calculation of a SGTR sequence of a Spanish NPP will be checked through the comparison of the results obtained from the extended and non-extended code versions.

5. PUBLISHED PAPERS

This section collects the publications in journals and/or conferences that have been performed from the work presented in this thesis.

5.1. INTERNATIONAL JOURNALS

Luis E. Herranz, F.J.S. Velasco, Claudia L. del Prá, 2006, “*Aerosol Retention near the Tube Breach During Steam Generator Tube Rupture Sequences*”. Nucl Tech 154(1), 85-94.

Luis E. Herranz, C.L. del Prá , A. Dehbi, 2007. “*Major Challenges to Model Aerosol Retention in the Nearby of a Tube Breach During SGTR Sequences*”. Nucl Tech 158, pp.83-93.

L.E. Herranz, C. López del Prá, F.J. Sánchez Velasco, 2008. “*Preliminary Steps towards Assessing Aerosol Retention in the Break Stage of a Dry Steam Generator during SGTR Sequences*”. Nucl. Eng. and Des. 238, pp 1392–1399.

Velasco FJS, López del Prá C, Herranz L.E., 2008. “*Expansion of a radial jet from a guillotine tube breach in a shell-and-tube heat exchanger*”. Exp Ther & Fluid Sci 32. pp 947-961.

Velasco FJS, López del Prá C, Herranz L.E., 2010. “*Aerosol Retention in the Vicinity of a Breach in a Tube Bundle: An Experimental Investigation*”. Aer. Sci. and Tech., 44:349–361, 2010.

López del Prá C, Velasco FJS, Herranz L.E., 2010. “*Aerodynamics of a gas jet entering the secondary side of a vertical shell-and-tube heat exchanger: numerical analysis of anticipated severe accident SGTR conditions*”. Eng Appli of Comp Fluid Mech, 4-1 pp. 91-105.

López del Prá C, Velasco FJS, Herranz L.E., 2010. “*Simulation of a gas jet entering the secondary side of a steam generator during a SGTR sequence: Validation of a Fluent 6.2 Model*”. Nuc. Eng. Des. Vol 240, n9, pp 2206-2214.

Luis E. Herranz, Claudia Lopez, 2011. “*ARI3SG: Aerosol Retention in the Secondary Side of a Steam Generator. Part I: Model essentials, verification and correlation*”. Accepted for publication in Nucl. Eng. and Des. (2012).

Claudia Lopez, Luis E. Herranz. 2011. “*ARI3SG: Aerosol Retention in the Secondary Side of a Steam Generator. Part II: Model validation and uncertainty analysis*”. Accepted for publication in Nucl. Eng. and Des. (2012).

5.2. NATIONAL JOURNALS

Luis E. Herranz, Claudia López del Prá, F. J. Sanchez Velasco (2006). “*Investigación del CIEMAT en secuencias SGTR de Accidente Severo*”. Award “Nuclear España 2006”. Nuclear España, pag. 22-28, feb 2006.

5.3. INTERNATIONAL CONFERENCES

Luis E. Herranz, Claudia López del Prá, J.L Muñoz-Cobo, 2004. “*A Theoretical Correlation to Estimate Aerosol Retention within the Secondary Side of a Nuclear Power Plant Steam Generator under Accident Conditions*”. EAC 2004. Budapest, 6-10 Sep.

Luis E. Herranz, Claudia L. del Prá, F. J. S. Velasco, J.L. Muñoz-Cobo, A. Escrivá, 2005. “*Insights into Aerosol Depletion from a high velocity flow across a tube bank: A key Scenario for nuclear Safety*”. 6th World Conf on Expl Heat Transfer, Fluid Mech & Therm. Matsushima, Miyagi, Japón. 17-21 April

F. J. Sánchez-Velasco, C. López del Prá, Luis E. Herranz, 2006. “*Aerodynamics of a Radial Jet from a Tube Breach in a Shell-and-Tube Heat Exchanger*”. 13th Symp on Applications of Laser Techniques to Fluid Mechanics, Paper 1070, Lisboa, Portugal, 26-29 Jun.

F.J.S. Velasco, C. López del Prá, Luis E. Herranz, 2007. “*Jet Expansion from a Fish-Mouth Tube Breach in a Shell and Tube Heat Exchanger*”. 7th Int. Symp. On Particle Image Velocimetry, Rome (Italy), 11-14th Sep.

C. López del Prá, F. J. Sánchez Velasco, Luis E. Herranz, 2007. “*CFD Modeling of a Gas Jet in the Nearby of a Broken Tube in a Shell-and-Tube Heat Exchanger: Application to a Risk-Dominant Scenario in Nuclear Power Plants*”. 5th International Conference on Heat Transfer, Fluid Mechanics and Thermodynamics, Sun City, South Africa, 2-4 July.

F.J.S. Velasco, C. López del Prá, Luis E. Herranz, 2007. “*Uncertainty on experimental aerosol characterization: Calibration tests supporting aerosol studies under severe accident SGTR conditions*”. EAC 2007, Salzburg, Austria , 9-14 Sep.

Luis E. Herranz, C. López del Prá, F.J. Sánchez-Velasco, 2008. “*Aerodynamics of a Particle-laden Gas Jet in the Break Stage of a Steam Generator during Severe SGTR Sequences*”. Anaheim, CA, 8-11 June. American Nuclear Society ANS-2008.

F.J.S. Velasco, C. López del Prá, Luis E. Herranz, 2008. “*Experimental study of aerosol removal from a gas jet moving through a tube bank*”. EAC 2008 Thessaloniki, Greece. 24-29 Aug.

López del Prá C., F. J. Sánchez Velasco, Luis E. Herranz, 2008. *“Jet Aerodynamics in the breach nearby of a failed shell-and-tube heat exchanger: application to a risk dominant scenario in nuclear power plants”*. XCFD4NRS, Grenoble, France, 10-12 Sep 2008.

López del Prá C., Luis E. Herranz, 2010. *“Modeling Aerosol Retention in the Break Stage of a Failed SG during a Core Meltdown Sequence”*. IAC 2010, Aug. 29- Sep. 3 Helsinki (Finland).

C. López del Prá, L.E. Herranz, 2010. *“Application of the filter model approach to particle trapping in the break stage of a steam generator: The ARI3SG model.”*. ANS 2010, Nov 7-11, 2010. Las Vegas (Nevada).

Claudia López, Luis E. Herranz, 2011. *“SG retention predictability during “dry” severe accident SGTR sequences: An assessment of uncertainties”*. ICAPP 2011. Nice, France, May 2-5.

Lopez del Prá C., Luis E. Herranz, 2011. *“Uncertainty Analysis of Aerosol Retention in the Break Stage of a Vertical Steam Generator under SGTR Accident Conditions”*. EAC 2011. Manchester, England, Sep 5-9.

5.4. NATIONAL CONFERENCES

Claudia López del Prá, L. E. Herranz, 2003. *“Modelling Aerosol Retention in the Secondary Side of a Steam Generator during a SGTR Sequence: Fundamentals and Limitations.”*. 29 Reunión Anual de la SNE, Zaragoza, Octubre 1-3.

Claudia L. del Prá, Luis E. Herranz, José L. Muñoz-Cobo, Alberto Escrivá, 2004. *“ARISG-MCNP: Modelo Probabilista de la Eficiencia de Retención en el Secundario de un Generador de Vapor durante Secuencias SGTR”*. 30 Reunión Anual de la SNE, Alicante, 29 Sep- 1 Oct, 2004.

C. L. del Prá, F. J. Velasco, Luis E. Herranz, J. L. Muñoz-Cobo, A. Escrivá, 2005. *“Comportamiento de Aerosoles en secuencias SGTR: Lecciones Aprendidas a través del Análisis Aerodinámico”*. 31 Reunión Anual de la SNE, Logroño, 19 -21 Oct, 2005.

Escrivá, A. Geraldo, J. L. Muñoz-Cobo, C. L. Del Prá, Luis E. Herranz, 2005. *“Estudio con CFX de la Hidrodinámica de Chorros Producidos en la Rotura de Tubos del Generador de Vapor”*. 31 Reunión Anual de la SNE, Logroño, 19-21 Oct, 2005.

C. López del Prá, F. J. Sánchez-Velasco, L. E. Herranz, 2006. *“Estudios Fluidodinámicos en Secuencias SGTR de Accidente Severo (II): Validación de los Análisis 3D de la Etapa de Rotura”*. 32 Reunión Anual de la SNE, Tarragona, 4-6 Oct, 2006.

5. Published papers

F.J. Sánchez-Velasco, C. López del Prá, L. E. Herranz, 2006. *“Fluid Dynamic Investigation in Severe Accident SGTR sequences (I): Results of the CAHT Experimental Program”*. 32 Reunión Anual de la SNE, Tarragona, 4-6 Oct, 2006.

F.J.S. Velasco, C. López del Prá, Luis E. Herranz, 2007. *“Aerosol studies under severe accident SGTR conditions: Measurements and uncertainties”*. RECTA 2007, Madrid, 5 -6 de jul, 2007.

C. López del Prá, F.J. Sánchez-Velasco, L. E. Herranz, 2007. *“Modelo unidimensional de la aerodinámica de chorros en el secundario de un generador de vapor durante secuencias SGTR con Fusión de núcleo”*. 33 Reunión Anual de la SNE, Segovia, 26-28 Sep, 2007.

F.J. Sánchez-Velasco, C. López del Prá, Luis E. Herranz, 2007. *“Aerodinámica de chorros en el secundario de un generador de vapor durante secuencias SGTR con Fusión de núcleo”*. 33 Reunión Anual de la SNE, Segovia, 26-28 Sep, 2007.

C. López del Prá, F.J.S. Velasco, Luis E. Herranz, 2008. *“ARI3SG: Modelo de retención de partículas en el secundario de un generador de vapor seco durante secuencias SGTR de accidente severo”*. 34 Reunión Anual de la SNE. Murcia, 29-31 Oct, 2008.

F.J. Sánchez-Velasco, C. López del Prá, Luis E. Herranz, 2008. *“Caracterización experimental de la retención de aerosoles en el secundario de un generador de vapor durante secuencias SGTR con fusión de núcleo”*. 34 Reunión Anual de la SNE. Murcia, 29-31 Oct, 2008.

C. López del Prá, Luis E. Herranz, 2010, Validation of the ARI3SG model of the retention of aerosols within the break stage of secondary side of a SG during a SGTR sequence.,36 Reunión Anual de la SNE,Santiago de Compostela, 6-8 Octubre, 2010

Claudia López, Luis E. Herranz, 2011. *“Modelización de la retención de aerosoles nucleares en un escenario SGTR de accidente en un reactor PWR”*. V Reunión Española de Ciencia y Tecnología de Aerosoles – RECTA 2011.

6. NOMENCLATURE

A	Area
ACMD	Aerodynamic count median diameter
AMMD	Aerodynamic mass median diameter
APS	Aerosol particle sizer
ARCI	Average relative confidence interval
ARD	Average relative deviation
CAAT	Cimat artist aerosol test
CAHT	Cimat artist hydrodynamic test
C	Aerosol mass concentration
C_c	Cunningham slip correction factor.
C_D	Drag coefficient
CI	Confidence interval
d	Diameter
DF	Decontamination factor
Deg	deggusa
ELPI	Electrical low pressure impactor
F	Force
FBG	Fluidized bed generator
f_w	Wall friction factor
g	Gravity
GSD	Geometric standard deviation
H_c	coefficient dependent on material and system properties (N/m)
i	Tube position
k	Turbulent kinetic energy
k_1	Pressure loss coefficient
L	Length
LB	Lower bound
M	Million
m	Mass
N, n	Number
Nph	Nanophase
P	Pressure
p	Pitch distance, spacing between tubes
PIV	Particle image velocimeter
r	Radial distance to the axis of the broken tube
RANS	Reynolds average navier stokes
Re	Reynolds number
RSM	Reynolds stress model

6. Nomenclature

s	Spacing between tubes
Sc	Schmidt number
SE	Standard error
SG	Steam generator
SGTR	Steam generator tube rupture
Stk	Stokes number
SST	Shear-stress transport
T	Temperature
t	Time
TU	Turbulent intensity
U	Velocity
u	Uncertainty
U*	Friction velocity
UB	Upper bound
u _c	Combined uncertainty
y	Mass fraction
y ⁺	Non dimensional distance to the wall

Greek symbols

α	Tube-bundle packing density
ϵ	Turbulent or eddy diffusion coefficient
η	Efficiency
Λ	Resuspension rate
μ	Dynamic viscosity
ν	Kinematic viscosity
τ	Relaxation time
τ_w	Wall shear stress
ρ	Density
Φ	Gas mass flow rate
ω	Specific turbulent dissipation rate

Subscripts/Superscripts

0	Initial, inlet
+	Dimensionless
ae, aero	Aerodynamic
adh	adhesive
ax	Axial
b	Burst or lift
c	Cohesive
d	Drag

dp	Deposition
e	electrostatic
f	Frictional
g	Gas
h	hydraulic
imp	Impaction
in	Inlet
L	Layers
LB	Lower bound
p	Particle
rd	Radial
ref	Reference
ret	Retained
rs	Resuspension
s	Sample
ST	Single Tube
t	Tube
TB	Tube bundle
tbt	Turbulent
TS	Terminal settling
UB	Upper bound
w	Wall

7. REFERENCES

- Allison C. M., 1995. “*SCDAP/RELAP5/MOD3.1 Code Manual*”, NUREG/CR-6150 (Jun. 1995).
- Allelein, Auvinen, Ball, Guntay, Herranz, Hidaka, Jones, Kissane, Powers, Webber, 2009. *State of the art report on nuclear aerosols*. NEA/CSNI/R(2009)5.
- Angioletti M., Nino E., Rouocco G., 2005. *CFD turbulent modelling of jet impingement and its validation by particle image velocimetry and mass transfer measurements*. Int. J. of Thermal Science 44, pp 349-356.
- Auvinen, A., Jokiniemi, J.K., Lähde, A., Routamo, T., Lundström, P., Tuomisto, H., Dienstbier, J., Guntay, S., Suckow, D., Dehbi, A., Slooman, M., Herranz, L.E., Peyres, V., Polo, J., 2005. *Steam generator tube rupture (SGTR) scenarios*. Nucl. Eng. Des. Vol.235, pp. 457-472.
- Bakker, P., 2001a. *Important Accident Scenarios and Conditions*, SAM-SGTR-D001.
- Bakker, P.J.T., 2001b. *Steam Generator Tube ruptures: experimental boundary conditions*, SAM-SGTR-D005.
- Bakker P., Slooman M., Dienstbier J., Guntay S., Herranz L., Jokiniemi J., Routamo T., 2001. *Accident Management Aspects of EU-SGTR Project*, NEA/CSNI/R(2001)20 Proc of the Workshop on Implementation of Severe Accident Management Measures., Villigen, Switzerland.
- Bardina J.E., Huang P.G., Coakley T.J., 1997. *Turbulence Modeling Validation, Testing and Development*. NASA Technical Memorandum 110446.
- Benhamadouche S, Laurence D., 2003. *LES, coarse LES and transient RANS comparisons on the flow across a tube bundle*. Int. J. of Heat and Fluid Flow 24. pp 470-479.
- Braaten, D.A., Paw U., Shaw, R.H. , 1990. Particle Resuspension in a Turbulent Boundary layer –Observed and Modelled-, Journal of Aerosol Science, 21(5), 613-628.
- Brun, R. J., Lewis, W., Perkins, P. J. and Serafini, J. S., 1955. *Impingement of Cloud Droplets on a Cylinder and Procedure for Measuring Liquid-Water Content and Droplet Sizes in Supercooled Clouds by Rotating Multicylinder Method*. Report 1215, U.S. National Advisory Committee for Aeronautics.

7. References

- Chen Y.K., Yu C.P. 1993. *Particle deposition from duct flows by combined mechanisms*. Aer. Sci. Tech. 19: 389-395.
- Chojnacki E., Baccou J. *Sunset_V_2007_20: Theory manual and user guide*. DPAM/SEMIC-2009-328 IRSN (2009)
- Cnat, 2010. www.cnat.es. Spanish NPP Almaraz-Trillo.
- Coleman, HW., Steele, G., 2009. *Experimentation, Validation, and uncertainty analysis for engineers*. John Wiley & Sons Inc. 3rd edition.
- Craft T.J. Graham L.J.W., Launder B. E., 1993. *Impinging jet studies for turbulence model assessment-II. An examination of the performance of four turbulence models*. Int. J. Heat Mass Transfer. Vol 36, No 10. pp 2685-2697.
- CSNI: Committee on the safety of nuclear installations (NEA, OECD), 2007. *BEMUSE Phase III Report*. NEA/CSNI R(2007)4.
- Degussa Inc., 2005. Aeroxide P25 product specifications data sheet. Frankfurt, Germany.
- Dehbi A., Güntay S., Suckow D. 2001. "Test Matrix for the ARTIST Consortium Experiments", Draft, TM-42-01-01, Paul Scherrer Institut (2001).
- Dorman, R.G., Filtration, Chapter VIII in "*Aerosol Science*" edited by C.N. Davies, Academic Press, Oxford, 1966.
- Douglas P.L., Ilias S., 1988. *On the Deposition of Aerosol Particles on Cylinders in Turbulent Cross Flow*, J. Aerosol Sci., 19, 4,451-462.
- Douglas, 1980. See Douglas P.L., Ilias S., 1988.
- FLUENT, 2005. *FLUENT 6.2 Users Guide*. Lebanon, USA.
- Fox, R. W., McDonald, A. T., Pritchard P. J., 2004. *Introduction to Fluid Mechanics*. 6th edition. Ed. John Wiley and Sons.
- Fuchs, N.A., 1964. *Mechanics of Aerosols*, Pergamon, New York.
- Glasstone S., Sesonske A., 1963. *Nuclear Reactor Engineering*. D. Van Nostrand, New York (1963).
- Güntay, S., Dehbi A., Suckow, D., Birchley, J., 2001. *Accident management issues within the ARTIST project*. NEA/CSNI/R(2001)20, Nuclear Energy Agency

-
- Güntay S, Dehbi A, Suckow D, Birchley J, 2002. *ARTIST: an international project investigating aerosol retention in a ruptured steam generator*. Int congress on advanced nuclear power plants ICAPP'02, June 9-13, Hollywood, Florida.
- Güntay S., Suckow D., Dehbi A., Kapulla R., 2004. *ARTIST: introduction and first results*. Nucl Eng Des Vol.231, pp.109-120.
- Herranz L., Del Prá C.L., Velasco F.J.S., Muñoz-Cobo J.L., Escrivá A, 2005. *Insights into aerosol depletion from a high velocity flow across a tube bank: a key scenario for nuclear safety*. Proc of 6th World conf on experimental heat transfer, fluid mechanics and thermodynamics. April 17-21, Miyagi, Japan.
- Herranz L., Sánchez-Velasco F.J., Del Prá C.L., 2006. *Aerosol retention near the tube breach during steam generator tube rupture sequences*. Nucl Tech Vol.154, pp.85-94.
- Herranz L.E., Del Prá C.L., Dehbi A., 2007. *Major Challenges to modeling aerosol retention near a tube breach during steam generator tube rupture sequences*. Nucl Tech Vol.158, pp.83-93.
- Herranz L.E., López del Prá C., Sánchez Velasco F.J., 2008. *Preliminary steps toward assessing aerosol retention in the break stage of a dry steam generator during severe accident SGTR sequences*", Nucl. Eng. Des. 238 pp 1392-1399.
- Hinds, W.C., 1999. *Aerosol Technology: Properties, Behaviour, and Measurement of Airborne Particles*, 2nd ed. Wiley-Interscience.
- Ilias, S., Douglas, P.L., 1989. *Inertial impaction of aerosol articles on cylinders at intermediate and high Reynolds numbers*, Chem. Eng. Sci., 44, 1, 81.
- ISO NORM, 1995. *Guide to expression of uncertainty in measurement*. Corrected and Reprinted. ISBN 92-67-10188-9. International Organization for Standardization, Geneva, Switzerland.
- Jaeger, H.M., Sidney, R., Nagel, 1992. *Physics of the granular state*. Science Vol 255 no 5051 pp 1523-1531.
- Kissane, M., 2008. *On the nature of aerosols produced during severe accident of a water-cooled nuclear reactor*. Nuc. Eng. Des., 238. pp 2792-2800.
- Leskinen J., Lyyrinen J., Ruusunen J., Joutsensaari J., Auvinen A., Jokiniemi J., 2010. *"Comparison of nanoparticle density measurements using APM and impactor-classifier"*. International Aerosol Conference 2010. Helsinki (Finland).
- Leaver D.E., Li J., Sher R., 1998. *New Design Applications of Natural Aerosol Deposition*
-

7. References

in Nuclear Plant Accident Analyses, NEA/CSNI/R(98)4.

Liao, Y., Guentay, S. 2009. *Potential steam generator tube rupture in the presence of severe accident thermal challenge and tube flaws due to foreign object wear*. Nuc. Eng. Des. 239. pp 1128-1135.

Lind, T., Suckow, D., Dehbi. A., 2008. *Summary report on ARTIST Phase II tests for retention in the break stage*. Artist 72-08. TM-42-08-04. Paul Scherrer Institut. Switzerland.

Lind, T., Danner S., Güntay, S., 2010. *Monodisperse fine aerosol generation using fluidized bed*. Powder Technology 199. pp 232-237.

Liu, H.Y.B., Agarwal, J. IK. 1974. *Experimental observation of aerosol deposition in turbulent flow*. Aer. Sci. Vol 5 pp. 145-155.

López del Prá, C., Velasco, F.J.S., Herranz, L.E., 2010a. *Simulation of a gas jet entering the secondary side of a steam generator during a SGTR sequence: Validation of a FLUENT 6.2 Model*. Nuc. Eng. Des. Vol 240, n9, pp 2206-2214.

López del Prá, C., Velasco, F.J.S., Herranz, L.E., 2010b. *Aerodynamics of a gas entering the secondary side of a vertical shell-and-tube heat exchanger: Numerical analysis of anticipated severe accident SGTR conditions*. Eng. Appl. Comp. Fl. Mech. Vol 4-1. pp 91-105.

López del Prá, C., Sánchez, F.J., Delgado, R, Herranz, L.E., 2010c. *Experiments and modeling of aerosol retention in the break stage of a failed steam generator during severe accident SGTR sequences*. Technical report, CIEMAT, DFN/SN-01/OP-10.

Macdonald, P.E., Shah V.N., Ward L.W., Ellison PG. 1996. *Steam Generator Tube Ruptures*. NUREG/CR-6365.

Mahaffy J., Chung B., Dubois F., Ducros F., Graffard E., Heitsch M., Henriksson M., Komen E., Moretti F., Morii T., Muhlbauer P., Rohde U., Scheuerer M., Smith B. L., Song C., Watanabe T., Zigh G., 2007. *Best Practice Guidelines for the use of CFD in Nuclear Reactor Safety Applications*. NEA/CSNI/R(2007)5.

Matsusaka, S., Maruyama, H., Matsuyama, T., Ghadiri, M., 2010. *Triboelectric charging of powders: A review*. Chemical Engineering Science 65, pp. 5781-5807.

May, K.R., Clifford, R., 1967. *The impaction of Aerosol Particles on cylinders, spheres ribbons and discs*. Ann. Occup. Hyg. Vol 10, pp 83-95. Pergamon Press Ltd.

Menter F.R., 1994. *Two-Equation Eddy-Viscosity Turbulence Models for Engineering Applications*. AIAA Journal, Vol 32, pp.1598-1605.

Menter F., Hemstrom B., Henriksson M., Karlsson R., Latrobe A., Martin A., Muhlbauer P., Mscheuerer, Smith B., Takacs T., Willemsen S., 2002. *CFD Best Practice Guidelines for CFD Code Validation for Reactor-Safety Applications*. ECORA, Contract FICKS-CT-2001-00154.

Meyer K.E., 1994. *Experimental and numerical investigation of turbulent flow and heat transfer in staggered tube bundles*. PhD. Thesis, Technical University of Denmark.

Murray, R. I., 2001. *Nuclear Energy. An introduction to the concepts, systems, and applications of nuclear processes*. Fifth edition. Ed. Butterworth Heinemann.

Nagase Inc., 2006. Seahostar product specifications data sheet. Japan.

Nanophase Inc., 2002. NANOTEK product specifications data sheet. Romeoville, IL, USA.

NEA, 1979. Nuclear aerosols in reactor safety: a state of the art report / by a group of experts of the NEA Committee on the Safety of Nuclear Installations by OECD Nuclear Energy Agency, 1979.

Parozzi, F., Alonso, A., Bolado, R., Hontanon, E., Capitão, J.A., Drossinos, Y., 1995. *Nuclear Science and Technology: Aerosol Physical Resuspension under LWR Severe Accident Conditions*. State of the Art Review, European Commission Final Report, EUR 16505, Brussels, 1995.

Parozzi, F., 2000. *A fast-running model for physical aerosol resuspension accounting for STORM experimental results*. Int. Mtg. "Best-Estimate" Methods in Nuclear Installation Safety Analysis (BE-2000), Washington Dc, USA, November 2000.

Paul S.S., Ormiston S.J., Tachie M.F., 2008. *Experimental and numerical investigation of turbulent cross-flow in a staggered tube bundle*. Int J. Heat Mass Transfer Vol.29, pp.387-414.

Polat S., Huang B., Mujumdar A. S., Douglas W. J. M., 1989. *Numerical flow and heat transfer under impinging jets: a review. Volume 2 of Annual Review of Numerical Fluid Mechanics and Heat Transfer*, Hemisphere Publishing Corporation, New York, NY, Chapter 4, pp.157-197.

Quarini, J., 1999. *CFD model of the PSI steam generator*. Report submitted to Paul Scherrer Institut.

Ranz, W.E., Wong, J.B., 1952. *Impaction of dust and smoke particles on surface body and body collectors*, Ind. & Eng. Chem., 44, 6, 1371.

7. References

- Rollet-Miet P., Laurence D., Ferziger J., 1999. *LES and RANS turbulent flow in tube bundles*. Int. J. of Heat and Fluid Flow 20. pp 241-254.
- Sagot, B., Antonini G., Christgen A., Buron F., 2008. *Jet impingement heat transfer on a flat plate at a constant wall temperature*. Int. J. of Thermal Sciences, doi:10.1016/j.ijthermalsci.200710.020.
- Sanchez-Velasco F.J., López del Prá C., Herranz L.E., 2007. *Aerodynamic characterization of jets within the break stage during severe accident SGTR sequences*. Technical report, CIEMAT, DFN/SN-04/OP-07.
- Sanchez-Velasco F.J., López del Prá C., Herranz L.E., 2010. *Aerosol retention in the vicinity of a breach in a tube bundle: an experimental investigation*. Aer. Sci. and Tech., vol 44, pp. 349-361.
- Schlichting H., Gersten K., 2000. *Boundary Layer Theory*. Chap. 12.2.3. Ed Springer.
- Schuh H., Persson B., 1964. *Heat transfer on circular cylinders exposed to free-jet flow*. Int J Heat Mass Transfer Vol.7, pp.1257-1271.
- Scott, G.D., Kilgour, D.M., 1969. *The density of random close packing of spheres*. Bti.J. Appl. Phys. Ser2 Vol 2 pp 863-866.
- Sippola, M. R., and Nazararoff W., 2002. *Particle deposition from turbulent flow: review of published research and its applicability to ventilation ducts in commercial buildings*. Lawrence Berkeley National Laboratory Report LBNL-51432, June 2002.
- Theerachaisupakij, W. , Matsusaka, S., Akashi, Y., Masuda, H., 2003. *Reentrainment of deposited particles by drag and aerosol collision*, Journal of Aerosol Science 34, 261-273.
- Torquato, S., Truskett, TM., Debenedetti, PG., 2000. *Is random close packing of spheres well defined?*. Phys. Rev Lett. Vol 84 no 10 pp 2064-2067.
- USNRC, 1990. *Severe accident risks: an assessment of five U.S. nuclear power plants*, Vol.2. Sandia National Laboratory Report NUREG-1150.
- Velasco, F.J.S., López del Prá, C., Herranz, L.E., 2008. *Expansion of a radial jet from a guillotine tube breach in a shell-and-tube heat exchanger*. Exp Ther & Fluid Sci 32. pp 947-961.
- Wessel, R.A., Righi, J., 1988. *Generalized Correlations for Inertial Impaction of Particles in a Cylinder*, Aerosol Sci. Tech, 9, 29-60.

- White F., 2003. Fluid Mechanics. Fifth edition, international edition. McGraw Hill.
- Wilks, SS., 1941. *Determination of sample sizes for setting tolerance limits*. Ann. Math. Statis. Vol 12 no1 pp91-96
- Wilks, SS., 1942. *Statistical prediction with special reference to the problem of tolerance limits*. Ann. Math. Statis. Vol 13 no 4, pp 400-409.
- Wong, J.B., Johnstone, H. F., 1953. Engineering Experimental Station, University of Illinois, Tech. Rep. N 11.
- Wong, J.B., Ranz, W.E., Johnstone, H. F., 1955. *Inertial Impaction of aerosol particles on cylinders*. Jour. Appl. Phys. Vol 26-2. 244-249
- Wood, N.B., 1981. *A simple method for the calculation of turbulent deposition to smooth and rough surfaces*. J. Aerosol Sci. Vol 12 no 3 pp 275-290.
- Yeh, H.C., Carpenter, R.L., Cheng, Y.S. 1988. *Electrostatic charge of aerosol particles from a fluidized bed aerosol generator*. J. Aerosol Sci., Vol. 19 No 1, pp 147-151.
- Zhu, CH., Lin, CH., Cheung, CH., 2000. *Inertial Impaction-Dominated Fibrous Filtration with Rectangular or Cylindrical Fiber*", Powder Technology 112, 149-162.

APPENDIXES

APPENDIXES:

A. PRELIMINARY HYDRODYNAMIC SIMULATIONS.....	A-1
A.1.SIMPLIFIED BUNDLE.....	A-1
A.1.1. AERODYNAMIC RESULTS.....	A-2
A.1.2. DISCUSSION OF AEROSOL EXPERIMENTS.....	A-5
A.2. SUPPORT PLATE AS A POROUS MEDIA	A-7
A.3. PROCEDURE FOR CFD SIMULATIONS.....	A-9
A.4. INITIAL SIMULATIONS: STANDARD κ - ϵ MODEL.....	A-13
A.5. TURBULENCE ASSESSMENT: RSM MODEL.....	A-17
B. POSTPROCESS OF FLUENT FILES.....	B-1
C. RESUSPENSION.....	C-1
D. ARI3SG INPUT GENERATION.....	D-1
D.1. LOGNORMAL PARTICLE DISCRETIZATION.....	D-1
D.2. SOURCE CODE OF INPUT GENERATION OF ARICODE.....	D-4
E. INPUT AND OUTPUT FILES OF ARICODE.....	E-1
E.1. ARICODE INPUT.....	E-1
E.2. ARICODE OUTPUT.....	E-4
E.2.1. OUTBUNDLE.DAT.....	E-4
E.2.2. OUTUBE.DAT.....	E-5
E.2.3. OUTPSIZE.DAT.....	E-7
E.2.4. OUTIME.DAT.....	E-13
F. UNCERTAINTY OF THE DIMENSIONLESS AXIAL DEPOSITION VELOCITY AND RESUSPENSION RATE CORRELATIONS.....	F-1
 ARICODE.....	ARICODE.f-1
ARI3SG.....	ARI3SG.f-1
ARI3WSC.....	ARI3WSC.f-1

A. PRELIMINARY HYDRODYNAMIC SIMULATIONS

This appendix summarizes the initial simulations of the break stage of the SGTR scenario with the FLUENT 6.1, 6.2 and Gambit 2, 2.2 codes. They were the base of the final simulations presented in Chapter 2 and provided: the first insights in the interpretation of the flow behavior and the aerosol retention experiments SGTR (Herranz et al., 2006) and the main approximations and modeling used in the final simulations. No less important was learning the procedure for performing CFD simulations with rigor and goodness. It was learnt during a placement at the laboratory of Severe Accident Research of the Paul Scherrer Institut (PSI, Switzerland). Part of the following section resulted from this placement. The author wants to express the gratitude to this group for this opportunity and to offer a word of thanks to Abdel Dehbi for teaching the author to perform 3D simulations. In addition, the author wants to thank Salih Guntay and Luis Enrique Herranz for doing it possible.

A.1. SIMPLIFIED BUNDLE

The first 3D simulations were performed by reducing the experimental mock-up (section 2.1.5) to 3 tubes of 1.5 m height. The domain was vertically bounded by walls and the single broken tube of a guillotine breach type was placed at the centre, whose upper part was simplified assuming a solid rod (Fig. A.1).

By using the FLUENT 6.1 code, one half of this arrangement was meshed in a total of around 400000 hexahedral cells (the smallest ones of $7.23 \cdot 10^{-10} \text{ m}^3$ were located close to the breach). Through a sensitivity study it was found that this nodalization scheme was simple and good enough. The outlet conditions at the top and bottom of the volume were modeled imposing a constant pressure condition of 1 atm.

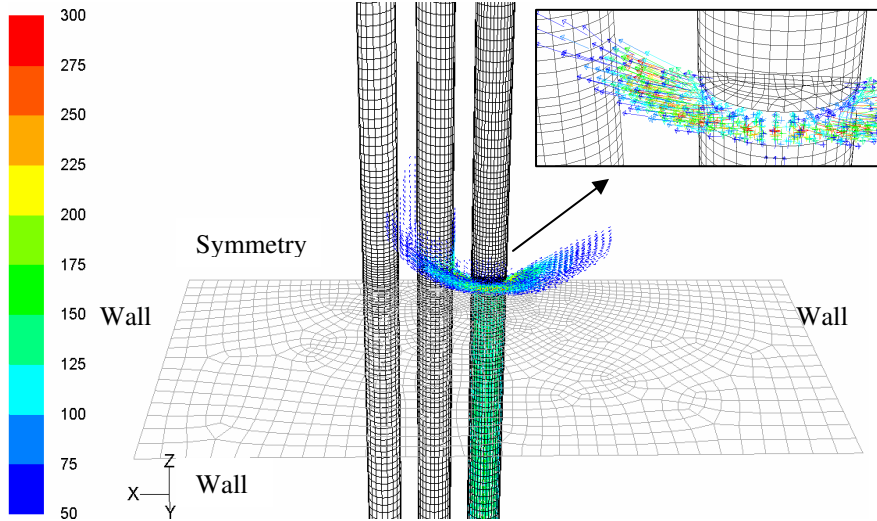


Fig. A.1. Detailed mesh of the simplified bundle (250 kg/h).

Two inlet gas mass flow rates placed at the base of the broken tube were investigated: 150 kg/h and 250 kg/h. The air flow exiting the breach was assumed to behave as a compressible flow. According to the anticipated boundary conditions, thermal equilibrium has been imposed in the secondary side. Turbulence was approximated through the standard κ - ϵ model.

A.1.1. Aerodynamic results

In order to illustrate the aerodynamic results obtained, a comparative analysis is set below between both inlet gas mass flow rates (150 kg/h and 250 kg/h). The jet variables considered of greater interest in the scenario under study from the point of view of aerosol deposition are: local velocity (U), penetration (L), deflection (α , angle of maximum velocity vector) and turbulence. A synthesis of the results obtained is gathered in Table A.1. Turbulence is described in terms of intensity (Tu , referred to the local flow velocity). In the discussion below a cylindrical coordinate system located at the center of the breach was used.

Table A.1. Variables characterizing the flow across the simplified bundle.

Variable	Location	Cases	
Φ (kg/h)	Inlet	250	150
	Break	300	203
	Facing tube 1	170	108
U_{\max} (m/s)	Over tube 1	170	108
	Facing tube 2	52	26
	Over tube 2	48	26
α	Break	18	19
	Facing tube 1	32	36
	Over tube 1	40	45
L (m)		$\sim 3.16 \cdot d_t$	$\sim 2.68 \cdot d_t$
TU_{\max} (%)	Over tube 1	145	145

Fig. A.2 shows the velocity field of the 250 kg/h and 150 kg/h cases, respectively. At the outlet of the breach, the jet velocity ranges from about 100 m/s to 300 m/s in the former case, and it hardly gets to 200 m/s (maximum velocity) in the latter. This quantitative difference in velocity is held over the surface of the closest tube. As in the case of velocity, the penetration is different. In both cases the jet reaches the second tube surface. However, in the 250 kg/h case the gas penetrates further whereas it hardly touches the tube surface in the 150 kg/h one. Despite its longer penetration, even the 250 kg/h case does not get into the gap between the second and the third tubes.

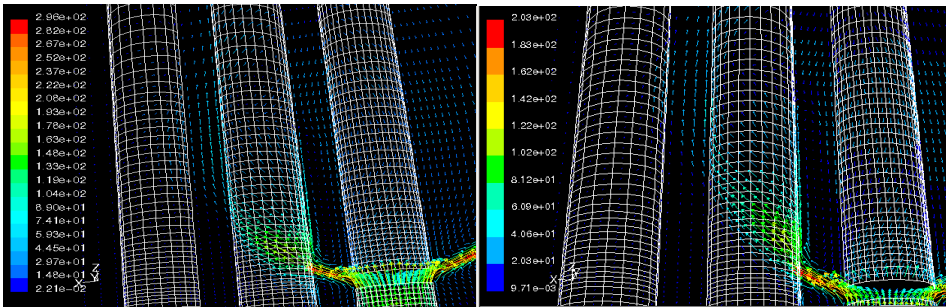


Fig. A.2. Velocity fields of the 250 kg/h case (left) and 150 kg/h case (right).

The presence of tubes enhances the upwards deflection of the jet with respect to the one of a free jet. Even though the direction of the emerging jets (α) is similar in both cases, it seems that the higher the flow rate, the smaller the enhancing deflection effect of the tubes.

Apart from quantitative considerations, three major observations closely related to the aerosol deposits distribution on tube surfaces are noted:

- The jet splits into three fluid streams upon contacting the first tube. Two of them are characterized by a substantial radial component of the velocity, whereas the other has a velocity dominated by the axial component. The former ones cross the tube flowing over its surface. They reach a maximum velocity located at a radial distance that is dependent on the gas mass flow rate (i.e., the higher mass flow rate, the deeper location). The latter gets stuck to the tube surface and it essentially flows upwards. This splitting results in a “maple-leaf” like distribution of the gas flow over the closest tubes to the breach.

- The wake region downstream the closest tubes facing the breach collect the two lateral fluid streams flowing over the tubes. Due to their ascending component they meet each other a few centimeters above the stagnation point.

- In both cases a vortex is set up a few centimeters over the breach in between the broken tube and the closest neighbor one. It results in a descending gas flow towards the breach next to the broken tube surface.

Finally, in order to prove the consistency of the aerodynamic simulations and the actual conditions anticipated in a postulated SGTR sequence, Fig. A.3 shows the evolution of the gas Reynolds number, Re_g , versus the radial coordinate along the streamline of maximum flow velocity over the surface of the first neighbor tube. In both cases, Re_g lays between 10^4 and 10^6 . It may be noted that despite the similarity of both curves, in the 250 kg/h case the Re_g is over 10^5 along most of the surface, whereas it is not so for the 150 kg/h one.

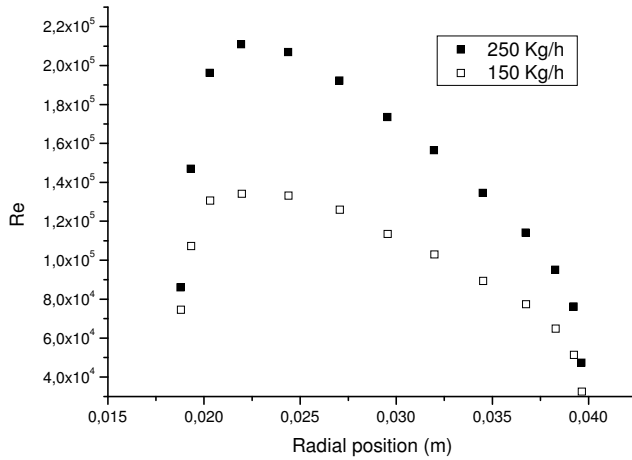


Fig. A.3. Re_g number around the surface of the first tube.

A.1.2. Discussion of aerosol experiments

From the 3-D simulations some insights were got into the aerosol deposition pattern observed in the experiments. As for the generic deposition profiles:

- “Hill-shaped” deposits located on the tubes adjacent to the breach at the height of the upper end of the breach are related to a gas approaching tube surfaces at very high velocities with a quite significant component perpendicular to the those surfaces. It is considered that under those conditions inertial impaction will probably be the dominant mechanism of aerosol depletion (Fig. A.4 (left)).

- At higher and lower locations, more spread aerosol deposits were observed. Rather lower velocities with substantially less pronounced normal-to-surface components are predicted there. Thus, at those locations inertial impaction should be rather less intense whereas turbulent deposition could become the dominant deposition mechanism.

- Deposition on the wake region of the flow was substantial and looked consistent with the aerodynamic predictions (Fig. A.4 (right)).

Over the tube breach at the broken tube some deposits were also noted. This is consistent with the prediction of a vortex slightly above the breach in the gap between the broken tube and the adjacent ones.

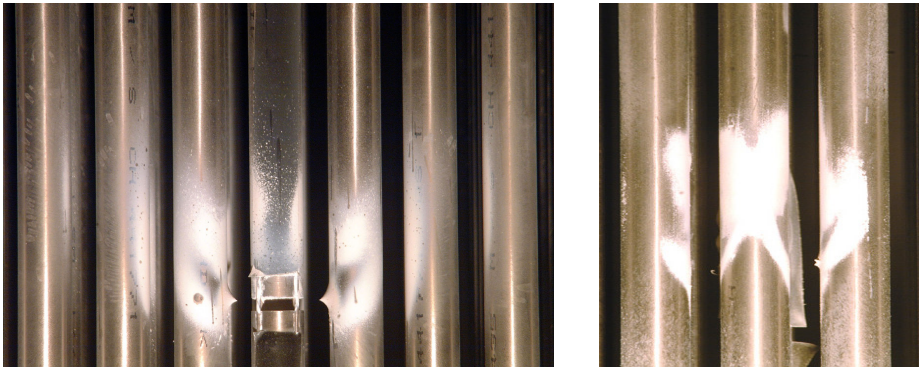


Fig. A.4. Aerosol deposition patterns: facing (left), rear (right).

At farther tubes, lower velocities mostly directed parallel to tube surfaces seem to indicate that turbulent deposition could dominate deposition.

In order to underline the effect of the gas flow on the aerosol deposition, a comparison between the 250 kg/h case and the 150 kg/h one has been set. Experimentally (Herranz et al., 2006), it was observed that the mass deposited on the tubes facing the breach in the case of the highest gas flow rate was about half the one measured at 150 kg/h. This difference was even bigger on the tubes behind the “breach-facing” ones. This resulted in a decaying trend of the retention efficiency when the gas flow was raised (Fig. 1.3.3). This is contrary to the tendency expected from the deposition mechanisms (i.e., inertial impaction and turbulent deposition) that are proportional to the particle velocity. Hence, other phenomena driving to less aerosol deposition at high flow rates should be present in the scenario.

Particle resuspension is a candidate process. The high flow rates could make particles detach from surfaces by two mechanisms. On one side, they would yield drag forces on deposited particles that in the presence of “burst-sweep” events in the laminar sub-layer of turbulent flows could remove particles from the surface (Braaten et al., 1990). On the other, the already deposited material can undergo some erosion: the impaction of particles can cause detachments from a previously deposited material (Theerachaisupakij et al., 2003).

Particle fragmentation could also play a role. In the experiments, TiO₂ micron particles were injected. Their characterization showed that they were loose aggregates of TiO₂ seeds bonded by weak forces. Under these conditions, high gas velocities could yield tangential stresses over the particle surface that makes them break up. In addition, particle disintegration could also be a consequence of a particle collision against tube surfaces. Both dis-aggregation mechanisms, even though not very well characterized, have been reported elsewhere (Fuch, 1964).

There are evidences that both resuspension and fragmentation could have been present in the aerosol retention experiments (Herranz et al., 2006). The particle size distribution at the outlet of the bundle showed a good fraction of particles with sizes smaller than the injected ones (fragmentation), but there also existed a significant fraction of mass linked to particles which size was well above the upper bound of the inlet size distribution (resuspension).

In sight of the observations presented above concerning aerosol deposits and taking into account the aerodynamic predictions, a tentative explanation could be at least partially based on the magnitude of the Re_g number. Assuming that other conditions were kept identical in the experiments, the higher Re_g in the 250 kg/h test would have caused a net enhancement of the degrading mechanisms with respect to their effect in the 150 kg/h test. In other words, the higher Re_g number would not necessarily mean higher retention efficiency, since mechanisms degrading retention efficiency can be enhanced even further than the deposition ones.

A.2. SUPPORT PLATE AS A POROUS MEDIA

One of the components of the bundle of tubes is the upper support plate (chapter 2; Fig. 2.1.1). It consists of a solid plate of 0.006 m thick placed at 1.1 m from the bottom which maintains the tubes in their positions within the bundle. Fig. A.5 shows the shape of the plate (grey color) and the open areas around the tubes and close to the wall where the flow passes through (blue color).

There are two options for modeling this component: a detailed geometrical description as shown in Fig. A.5, or a porous medium approximation. The former would be more rigorous but it would increase the complexity of the scenario which would be costly in terms of computation time. The latter is an approximation which results in substantial computing time savings.

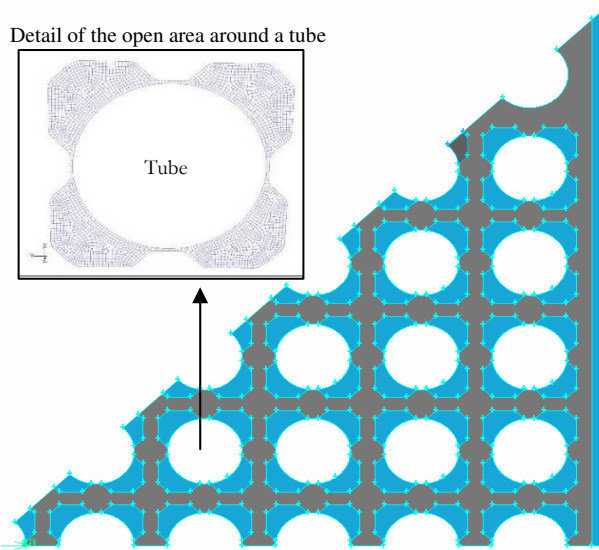


Fig. A.5. Horizontal cross-section of the support plate.

Fluent 6.1 has two possibilities for doing this approximation: a porous media and a porous jump. The porous media is applied to a volume defining pressure losses in the 3 directions of flow, whereas the porous jump is a 1D simplification applied to a face zone, a membrane, etc. The porous jump is more robust and yields better convergence (FLUENT, 2005) and it will be used in the simulations given that the support plate thickness is little (0.006 m) compared to the whole height of the break stage (1.5 m).

Two pressure losses take place through the porous jump: viscous and inertial losses. The first one is approximated by the Darcy's law, in which the pressure gradient is directly proportional to the fluid velocity as,

$$\nabla P = -\frac{\mu}{\alpha} U \quad (\text{A.1})$$

where α is the permeability (input for fluent), and the velocity (U) is taken at the inlet face of the porous. In these simulations, this term is neglected due to the thinness of the plate.

The second one is related to the changes in the flow area of the plate. It can be expressed as (White, 2003; FLUENT, 2005),

$$\Delta P = k_1 \cdot \frac{\rho_g \cdot U^2}{2}$$

where k_1 is the loss coefficient.

In the case that is being analyzed, k_1 has been taken in the range 3.2-4, which correspond to the pressure drop in a perforated plate with an open area of 0.46% of the total open area before the plate. This value comes from empirical tabular functions obtained from the literature (Fox et al., 2004).

A.3. PROCEDURE FOR CFD SIMULATIONS

This section presents the procedure followed to perform the 3D simulations with rigor and goodness. The steps followed are summarized in the following diagram and explained below. Chapter 2 was performed following this process. Further information of the procedure can be found in Mahaffy et al. (2007) and Menter (2002). Worth to note that section A.4 presents the initial simulations of the whole bundle together with an example of grid dependent, grid independent and a wrong capturing of the turbulent cases.

- 1. Preliminary analysis:** flow regime, expected velocities, characteristic lengths, expected y^+ values, initial sizes of BL, symmetries...

- 2. Geometry:**
 - Geometry generation
 - Meshing:
 - Grid quality
- 3. FLUENT case:**
 - Models
 - Momentum
 - Energy
 - Turbulence
 - Compressibility
 - Further approx.: porous media, etc
....
 - Numerics
 - Solver
 - Segregated: Implicit
 - Coupled: Implicit/Explicit
 - Discretization
 - 1st order, 2nd order, PRESTO, ...
 - Relaxation factors
 - Time dependence: Steady/ Unsteady
 - Boundary Conditions: P_{in} , V_{in} , \dot{m}_{in} , TU_{in} , P_{out} , ...
 - Initialization of Solution

4. **FLUENT result:** 

- Convergence
- Model assessment: Conservative equations, y^+ values,...
- Grid optimization: mesh refinement

5. **Grid independent:** 

- Coarse mesh
- Fine mesh

6. Validation

1. Preliminary analysis of the scenario.

It consisted on the analysis of the expected flow performance. The characteristic variables of the scenario were estimated at different regions: velocity at the inlet, outlet, support plate and the breach; flow rates at these regions, the Re_g numbers, characteristic lengths, etc. On this basis, the flow regime was determined, a turbulent model was chosen and the initial and boundary conditions were set. Depending on the turbulent model and boundary layer treatment, it is determined the size of the mesh close to the walls (see section A.4).

2. Grid generation.

Grid generation is designed according to the flow characteristics and turbulence modeling. The mesh was chosen structured composed by hexahedral cells. They were arranged trying to follow the direction of the flow.

Once the sizes of the cells of the boundary layer were created, according to the sizes estimated from wall treatment theory (see section A.4), the mesh was generated applying a growing factor lower than 1.4 to the subsequent cells. Growing was applied starting from the breach so that this region was having a higher grid density where higher velocity gradients were expected.

The quality of the mesh was assessed checking that the following parameters were within acceptable ranges:

- Aspect ratio: ratio between the maximum and minimum averaged edges length. From 10 to 50 is seen acceptable.
- Angle skewness or equiangle skew (Q_{EAS}): a measure of cells deviation from perfect equilateral cells. Table A.2 outlines the overall relationship between the equiangle skewness (Q_{EAS}) and the cell quality (FLUENT, 2005).

Table A.2. Equiangle skew vs mesh quality (FLUENT, 2005).

Q_{EAS}	Quality
$Q_{EAS}=0$	Equilateral (perfect)
$0 < Q_{EAS} \leq 0.25$	Excellent
$0.25 < Q_{EAS} \leq 0.5$	Good
$0.5 < Q_{EAS} \leq 0.75$	Fair
$0.75 < Q_{EAS} \leq 0.9$	Poor
$0.9 < Q_{EAS} < 1$	Very poor (sliver)
$Q_{EAS}=1$	Degenerate

- Size skewness: a measure of cells deviation from perfect equilateral cells.
- Growing factors: ratio between the sizes of consecutive cells. Growing factors below 2 are seen acceptable.

3. Fluent case

Once the grid is read by FLUENT, the models, solver, discretization scheme, operating initial and boundary conditions are determined. Initially, a simplest case is chosen and once it provides an initial solution the complexity of the scenario is increased and optimized as seen in the following point 4. This is performed by including energy equation, turbulence, compressibility, by increasing the order of discretization.

4. Fluent results

Two criteria were used to stop the iterative solution of FLUENT calculations. On one side, the scaled residuals of the continuity, energy and each of the momentum and turbulent equations (in this case of the RANS approximation) were controlled and monitored. It was considered satisfactory when they reached low and steady values (below 10^{-3} except for the energy one that should drop below 10^{-6}). On other side, some target variables at some specific regions of the domain were monitored until they reached steady values.

Once the case is steady and has converged, the results are assessed by checking the conservative equations and the expected velocities on specific surfaces as the inlet or outlet among others. On other side, y^+ values are also checked in order to estimate if the grid is adequate to the problem. So to say, if a wall function is applied to the flow close to the wall then the y^+ values should be between 30 and 500.

When these results are assessed, the mesh is “optimized” by refining the cells (splitting the cells) in those regions with higher velocity gradients and the iterative calculations start again.

This process is finished when the results of these cases converge to the same value. It can be verified by comparing the velocity components of different cases along imaginary lines of the domain (Fig. A.6).

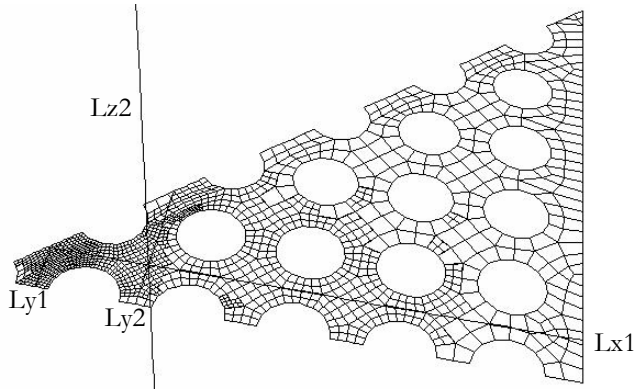


Fig. A.6. Imaginary lines and horizontal cut of meshed domain.

5. Grid independent

Finally, the grid independent analysis ensures that the results obtained are independent from the mesh. This analysis is performed by comparing the results of the case obtained with a mesh (called coarse) with those obtained with a higher grid density one (called fine mesh). The fine mesh is obtained by splitting by two each edge of the coarse mesh so that the resulting grid size is eight times the initial one:

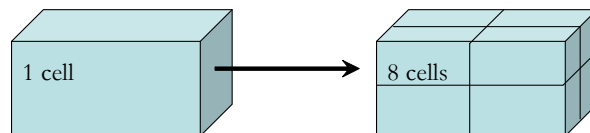


Fig. A.7. Splitting criteria for grid independent.

An example of grid-dependent, grid independent result is given in the following section A.4.

6. Validation

Finally, the results are compared with the available experimental data. Attention must be paid to the results extracted from FLUENT as it provides the computed cell-center values or values that have been interpolated to the nodes of the mesh.

Further information of this process can be found in the Best practices guidelines for the use of CFD in nuclear reactor safety applications of the Nuclear Energy Agency (NEA, Mahaffy et al., 2007). Annex I of NEA's report provides a checklist for the CFD calculations.

A.4. INITIAL SIMULATIONS: STANDARD k - ϵ MODEL

In the simulations performed of the SGTR scenario described in chapter 2, the turbulent model initially chosen was the standard k - ϵ with a boundary layer treatment of standard wall functions. The reasoning behind this choosing was the robustness of this model; it is the most widely known and extensively used in many industrial applications with a low cost of computational time (FLUENT, 2005; Mahaffy et al., 2007). As will be seen in this section, these simulations finally turned out not to be good in the sense that this model was not the appropriate for the SGTR scenario under discussion. The results presented in this section show the complexity of the scenario and the complexity of the procedure of performing CFD simulations.

K - ϵ turbulent model belongs to the two-equation approximation of the RANS approach, k being the turbulent kinetic energy and ϵ its dissipation rate. As introduced in section 2.1.1, turbulent effects are obtained from two separate transport equations (Eq. (2.1.4)) which allows the turbulent velocity and length scales to be independently determined.

$$\frac{\partial}{\partial x_i}(\rho \cdot \phi \cdot U_i) = \frac{\partial}{\partial x_j}(\Gamma_\phi \cdot \frac{\partial \phi}{\partial x_j}) + G_\phi - Y_\phi \quad (2.1.4)$$

Where ϕ denotes the independent variable (k and/or ϵ) and G , Y and Γ represent generation, dissipation and effective diffusivity of the given quantity, respectively. Description of these expressions can be found in literature (Menter, 1994; Bardina et al., 1997; Fluent, 2005).

Regarding the boundary layer treatment, the wall-functions apply semi-empirical functions to the flow behavior close to the walls instead of solving the flow in the boundary layer (called by FLUENT near-wall treatment). These functions provide economical, robust and reasonable accuracy (FLUENT, 2005). They can be written as (White, 2003; Fox et al., 2004):

$$\begin{cases} \frac{U}{u^*} = y^+; & y^+ < 5 \quad (\text{viscous sublayer}) \\ \frac{U}{u^*} = 2.5 \cdot \ln(y^+) + 5; & 30 < y^+ < 300 \quad (\text{logarithmic sublayer}) \end{cases} \quad (\text{A.2})$$

where u^* is the friction velocity ($u^* = \sqrt{\tau_w / \rho_g}$), τ_w is the wall shear stress and y^+ is the non dimensional wall distance characterizing the boundary layer,

$$y^+ = \frac{\rho_g \cdot u^* \cdot y}{\mu} \quad (\text{A.3})$$

where y is the distance to the wall.

FLUENT applies the “law of the wall” if the first cell of the mesh is within the viscosity sublayer ($y^+ < 5$) and the “logarithmic law” if the cell is within the logarithmic layer ($30 < y^+ < 300$) or within the transition region ($5 < y^+ < 30$). It is highly recommended to place the first cell of the boundary layer within the logarithmic sublayer because the log-law is valid for this region (White, 2003; Fox et al., 2004).

Fig. A.8 shows an example of Coarse and Fine meshes that were constructed in order to capture the logarithmic sublayer. They were generated placing a row of cells around each of the tubes with a depth of around 0.004 and 0.0025 m for the Coarse and Fine meshes, respectively. The length “ y ” of cell was estimated from the expected y^+ value of this layer and substituting the remaining variables in Eq. (A.3).

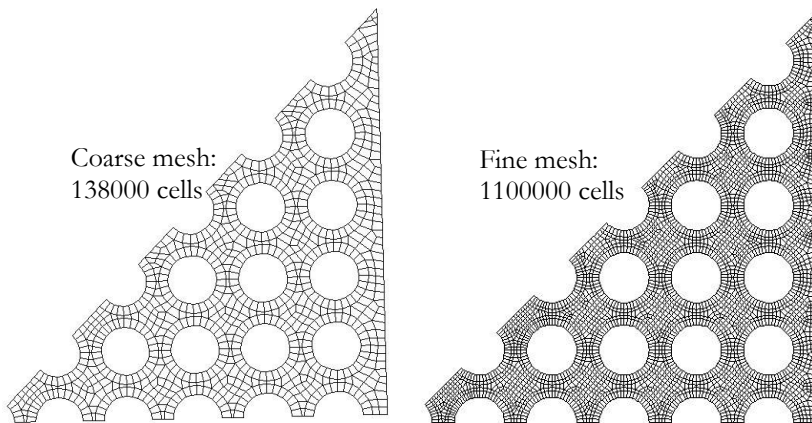


Fig. A.8. Horizontal cut sections of the CIEMAT mock-up.

Following the procedure presented in previous section, the size of the Fine mesh shown in Fig. A.8 is around 8 times the Coarse one ($140 \cdot 10^3$ cells). A total of 6 grids with their corresponding converged FLUENT cases were performed in order to find an optimum mesh size to ensure the grid independent result. The following figures just illustrate the weakest points of these initial simulations through a grid dependent result, a grid independent one and a failed capture of the turbulence. Worth to note that each of the results presented had a grid quality had converged and the result was optimized as explained in previous section.

- **Grid dependent result**

Fig. A.9 shows the Y velocity component along line ly2 (Fig. A.6) for two sets of meshes composed by a coarse and a fine one. This figure shows how the result depends on the grid since the fine mesh provides velocity results up to 60% higher than the coarse one.

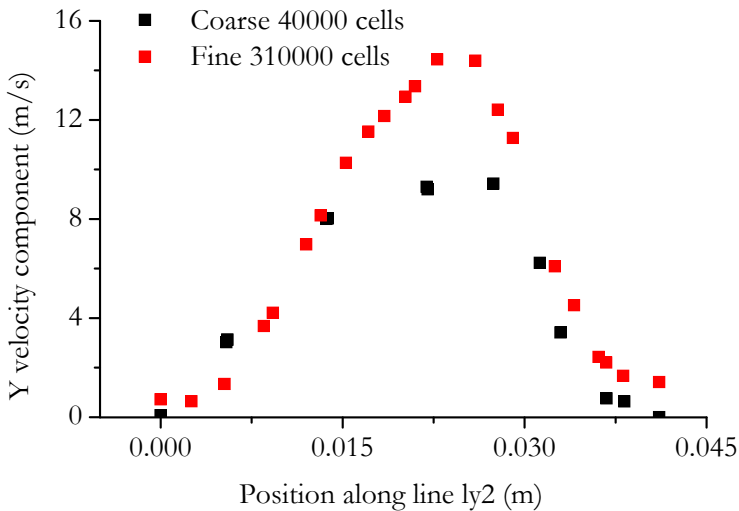


Fig. A.9. Grid dependent profiles.

- **Grid independent result**

Fig. A.10 shows a grid independent result. The velocities along line ly2 of the coarse (0.14 million cells) and the fine (1million cells) meshes display similar profiles with small differences lower than the 20%. However, these did not capture turbulence as will be seen next.

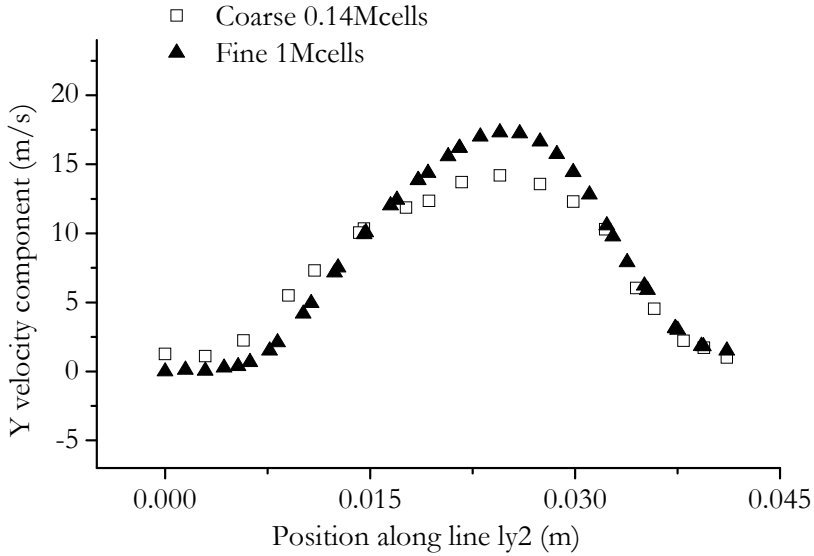


Fig. A.10. Grid independent profiles.

- ***Wrong capture of turbulence***

According to the optimization process, the simulations presented in Fig. A.10 were further refined at those regions with higher velocity gradients. The results can be seen in Fig. A.11 through the Coarse/Fine-Optimized cases. As observed, the velocity profiles of these optimized cases show again a similar profile with smaller discrepancies, which indicates that the result is independent of the grid. However, the comparison of the non-optimized and optimized profiles shows a change in the behavior: close to 0 m velocities become negative and the maximum velocity has been displaced along ly_2 . This change arises because during the mesh optimization the cells close to the walls were split, so that the new sizes got out of the logarithmic sublayer (i.e. y^+ values were found to be much lower than 30).

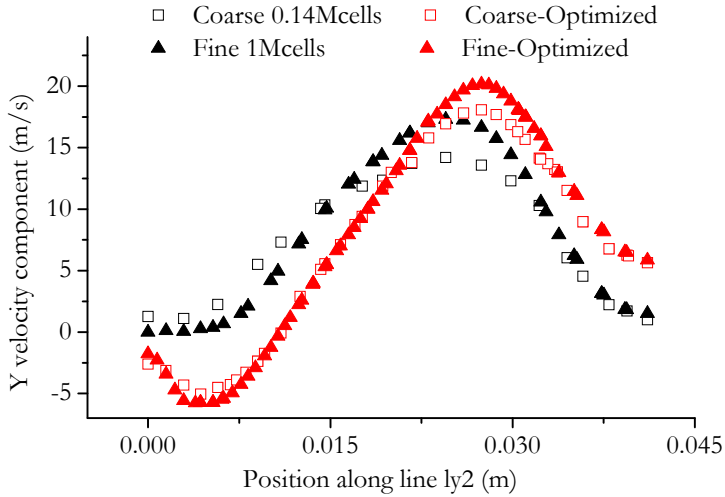


Fig. A.11. Wrong capture of turbulence.

A detailed analysis of these simulations showed that there was a wide range of flow regimes along the bundle of tubes. Close to the breach the flow was highly turbulent whereas in the upper regions (close to the outlet) turbulence had decreased. For this reason it was not possible to maintain the cells close to the wall within the logarithmic boundary layer all along the tube in order to apply the wall-functions. It was found that SST k-w was more appropriate for this application as it models adverse pressure gradients with flow separation, among other reasons (see chapter 2). It applies the near wall treatment that solves the flow all the way to the wall. The grid requirement is to have y^+ values below 5 and to have around 10 cells within the viscosity-affected near-wall region ($Re_y < 200$) to be able to resolve the mean velocity and turbulent quantities in that region (FLUENT, 2005).

A.5. TURBULENCE ASSESSMENT: RSM MODEL

An assessment of the turbulent model was performed by running the case of 250 kg/h with the turbulent Reynolds Stress Model (RSM). This model solves the transport equations individually for each component of the turbulent Reynolds Stress ($\overline{\rho U'_i U'_j}$). The inherent modeling of stress anisotropies theoretically make Reynolds Stress models more suited to complex flows than the two equation models. For this reason it was assessed the SST k-w through the comparison with the RSM one. The RSM model adds six transport equations that together with an equation

for the dissipation rate close the RANS system (FLUENT, 2005; Mahaffy et al., 2007). This increase means a high computational expense so that only one case was performed.

Fig. A.12 compares FLUENT predictions of SST k-w and RSM models obtained in the space between the broken tube and the first neighbor and the equivalent PIV measurements of velocity fields acquired in the CAHT campaign (Herranz et al., 2008).

Overall the experimental description and both theoretical one are consistent: once impacting the neighbor tube, the gas exiting the breach in form of a jet splits in upwards, downwards and sideways streams (just the two former can be observed in the plot). The jet causes a noticeable entrainment of the fluid around, both at the upper and at the lower region. Nonetheless, again consistently with data, FLUENT anticipates a more substantial suction above than below the jet. In addition, it seems that theoretically both regions are wider than the experimental ones. It seems that the RSM would agree more with the experimental results than SST k-w as it has a smaller suction region. All in all, SST k-w and RSM show similar predictions with minor differences: there is a wider RSM initial jet than SST k-w and a shorter RSM impinging region.

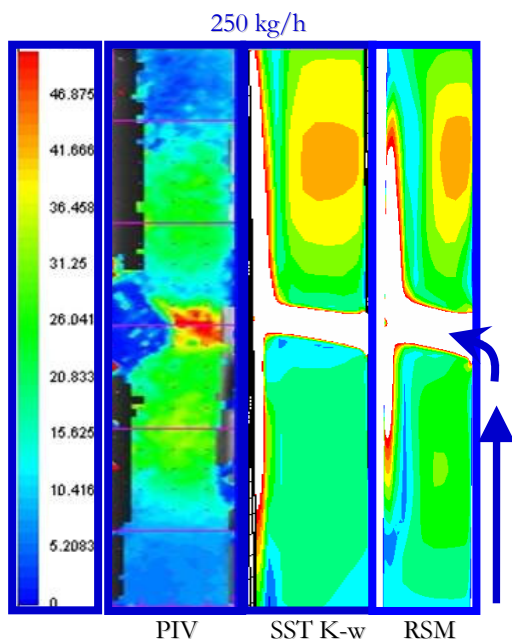


Fig. A.12. PIV SST-kw and RSM results (250 kg/h).

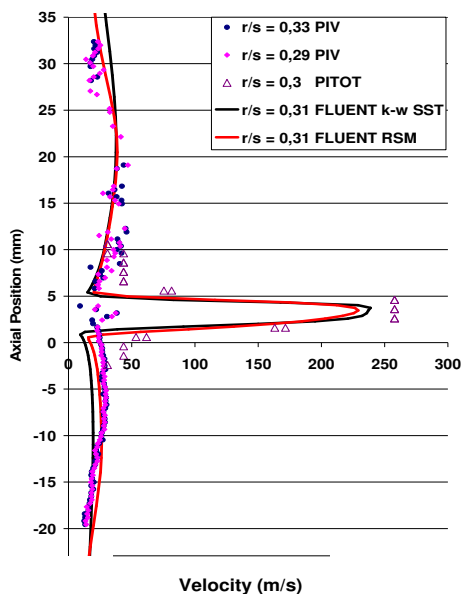


Fig. A.13. PIV, PITOT, SST-kw and RSM profiles (250 kg/h).

Fig. A.13 allows a quantitative comparison between predictions and data along a line located at 1/3 of the tube spacing (see section 2.1.5). Both FLUENT results captured the experimental profile and its accuracy can be considered reasonable. As observed there are very slight differences between both SST k-w and RSM results. At the core region the RSM velocity is a 5% lower than the SST k-w one. In agreement to Fig. A.12 below the jet core region, the RSM velocities are higher than the SST k-w and closer to data.

Table A.3 gathers some meaningful velocities of the simulations. As noted, RSM predicts slightly lower velocities than SST k-w, being the highest difference an 8%.

Table A.3. Velocities of SST k-w and RSM simulations

250 kg/h	SST k-w	RSM
U_{\max} (m/s)	250	231
U_{breach} (m/s)	175	173
U_{outlet} (m/s)	0.69	0.69

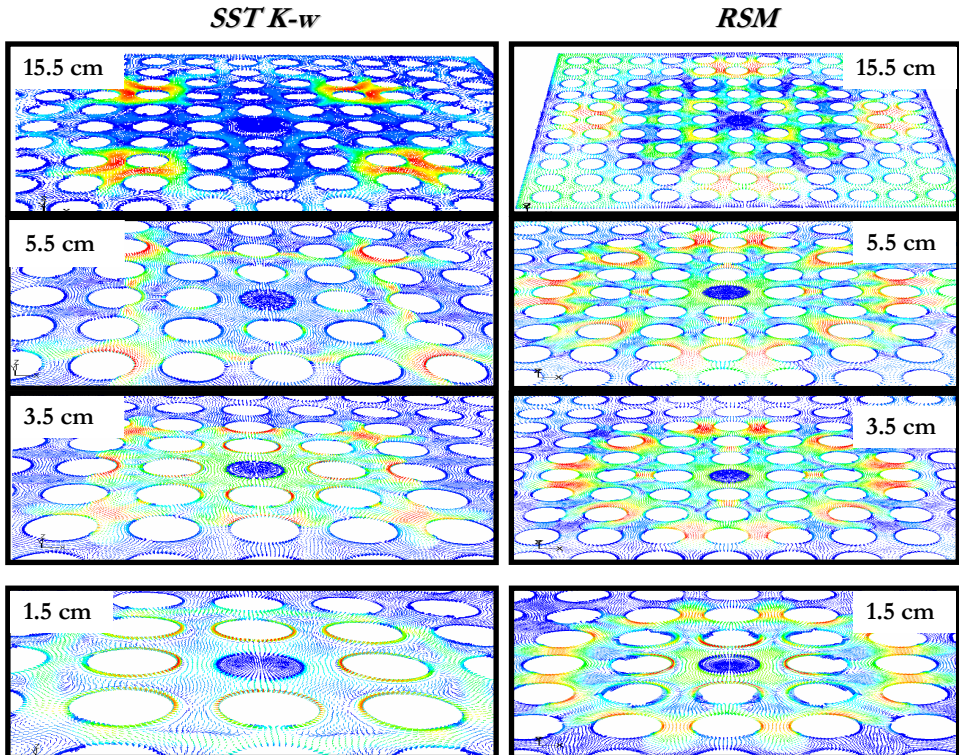


Fig. A.14. SST k-w and RSM velocity vectors (250 kg/h).

Jet evolution across the bundle can be observed in Fig. A.14 which shows the velocity fields at different heights for the SST k-w and RSM cases. Similar to chapter 2, colors of the figure have a different meaning in each plot, since the scales are different. The figure shows several differences between both jets:

- The initial expansion of the RSM jet seems more symmetric and circular than the SST k-w that looks more squared.
- A faster penetration is found in the RSM jet as for the same height the jet reaches a deeper penetration than the SST k-w one (at least 1 tube).
- It seems that the wake region is promoted in the RSM case, whereas it seems vanished in the SST k-w one.
- At a height of 15.5 cm the RSM jet evolves in a crossed direction whereas the SST k-w flows mainly in the diagonal direction.

Radial and axial velocity components have been analyzed along four different azimuthal directions (i.e., 0° , 15° , 30° and 45°). Fig. A.15 and Fig. A.16 shows the normalized maximum radial/axial velocity as a function of the radial/axial distance from the breach. Both figures show that both maxima velocities of both turbulent models follow similar trends, even at some azimuthal directions the profiles are almost the same. That is the case of the radial velocity decrease between the first and second along the direction 30° (Fig. A.15) or the axial evolution in most directions (Fig. A.16). However, the RSM normalized radial velocity profile decreases slower than the SST k-w as observed in the direction 15° .

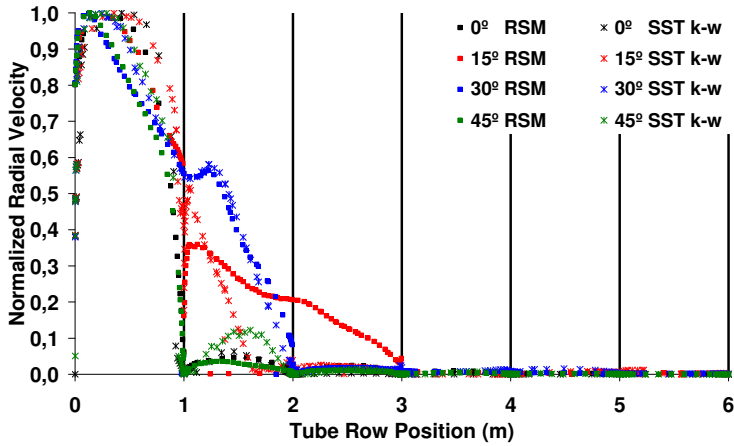


Fig. A.15. Normalized maximum radial velocities vs tube row position.

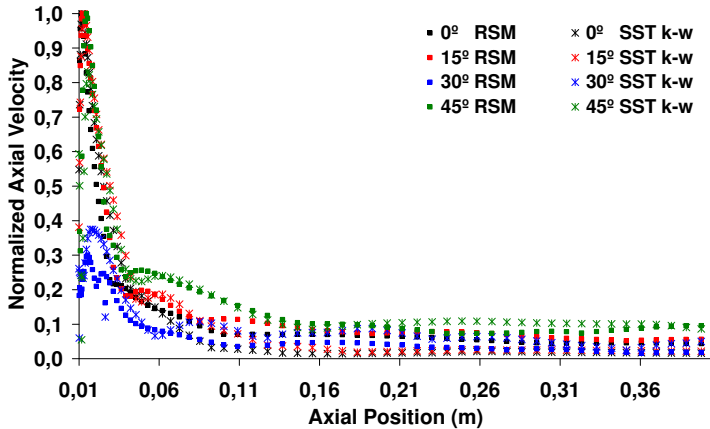


Fig. A.16. Normalized maximum axial velocities vs tube row position.

Finally, and even when there was simulated only the case of 250 kg/h with the RSM turbulent model, it has been derived a correlation for the maximum radial velocity depletion as a function of the tube row position Eq.(A.4).

$$U_{rd,RSM}(i) = \frac{3}{2i^3} U_g(0) \quad (A.4)$$

Eq.(A.4) is compared with the correlation derived for the SST k-w case (section 2.3) and with the profile of Leaver et al. (1998) in Fig. A.17. Worth to note that profiles are normalized with respect to their initial velocities.

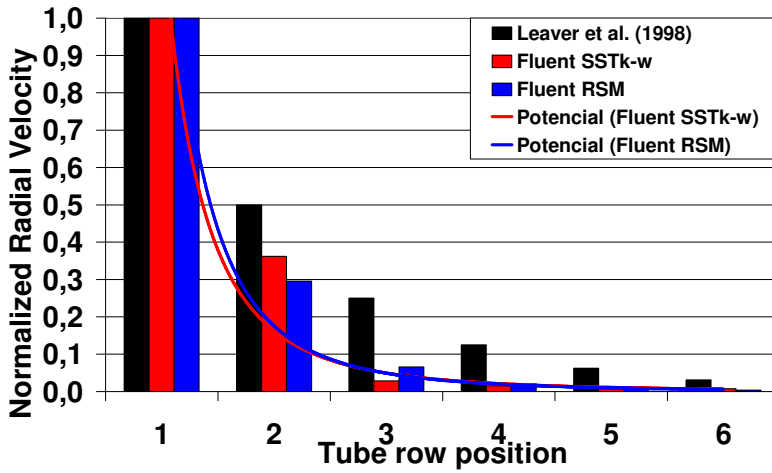


Fig. A.17. Normalized radial velocity vs tube row position.

As observed in Fig. A.17, velocity trends for RSM and SST k-w cases are similar. SST k-w profile decays fast within the first three tubes, whereas the RSM one do it within the first four, however differences between both velocities are around a 5%.

Finally, this analysis has shown that the RSM turbulent model provides similar results than the SST k-w one for the purpose pursued of a 1D approximation. This result support the use of the SST k-w turbulent model in the simulations and the final correlation derived.

B. POSTPROCESS OF FLUENT FILES

This appendix collects three of the several FORTRAN codes developed to postprocess the data files obtained from FLUENT simulations. These files consisted on columns with spatial coordinates and their corresponding velocity components. They were generated within FLUENT at different azimuthal planes.

The first postprocess program extracts the maximum velocity and its spatial position as a function of the radial coordinate for different azimuthal planes. The second one extracts the maximum axial velocity and its spatial position as a function of the axial component. The third one extracts the maximum total, radial and axial velocities (with their corresponding spatial positions) in each of the spacings between tubes.

```
Program FLUAZIMRADMAXVEL
C
C 22-01-2007
C Author: Claudia López del Prá.
C Affiliation: Project of Nuclear Safety Technology
C              Department of Nuclear Fission (CIEMAT)
C
C This program reads fluent ascii file of data and
C returns maximum velocity positions as a function of
C the radial distance
C Input File: columns x y x V Vaxial, Vradial, Vtang
C
C
C DEFINITION OF VARIABLES
C
C
C
C call abrextraeRad('250InputAzim5grad.dat', '250OutAzimRad5.dat')
C print *, 'caso 0'
C call abrextraeRad('250InputAzim10grad.dat', '250OutAzimRad10.dat')
C print *, 'caso 15'
C call abrextraeRad('250InputAzim20grad.dat', '250OutAzimRad20.dat')
C call abrextraeRad('250InputAzim25grad.dat', '250OutAzimRad25.dat')
C call abrextraeRad('250InputAzim35grad.dat', '250OutAzimRad35.dat')
C call abrextraeRad('250InputAzim40grad.dat', '250OutAzimRad40.dat')
C print *, 'caso ultimo'
C
C end program FLUAZIMRADMAXVEL
```

Program FLUAZIMRADMAXVEL

```
C
C 22-01-2007
C Author: Claudia López del Prá.
C Affiliation: Project of Nuclear Safety Technology
C              Department of Nuclear Fission (CIEMAT)
C
C This program reads fluent ascii file of data and
C returns maximum velocity positions as a function of
C the radial distance
C Input File: columns x y x V Vaxial, Vradial, Vtang
C
C
C DEFINITION OF VARIABLES
C
C
C call abrextraeRad('250InputAzim5grad.dat', '250OutAzimRad5.dat')
C print *, 'caso 0'
C call abrextraeRad('250InputAzim10grad.dat', '250OutAzimRad10.dat')
C print *, 'caso 15'
C call abrextraeRad('250InputAzim20grad.dat', '250OutAzimRad20.dat')
C call abrextraeRad('250InputAzim25grad.dat', '250OutAzimRad25.dat')
C call abrextraeRad('250InputAzim35grad.dat', '250OutAzimRad35.dat')
C call abrextraeRad('250InputAzim40grad.dat', '250OutAzimRad40.dat')
C print *, 'caso ultimo'
C
C end program FLUAZIMRADMAXVEL
C
C subroutine abrextraeRad(archivoentrada,archivosalida)
C
C character*50::variabls,w,ww,www,www,wwwww,wwwww,wwwww
C character*30::archivoentrada,archivosalida
C integer::i=0,nodenbr=0,count=0,st=0
C logical::var_control
C double precision::xcoor,ycoor,zcoor,rad
C double precision::vtot,vaxial,vrad,vtag
C Integer::xcoorInt,ycoorInt,zcoorInt,radInt
C Integer::vtotInt,vaxialInt,vradInt,vtagInt
C Integer,dimension(10000)::MaxX=(/(0.0,j=1,10000)/),
C                               MaxY=(/(0.0,j=1,10000)/),
C                               MaxZ=(/(0.0,j=1,10000)/),
C                               MaxR=(/(0.0,j=1,10000)/),
C                               MaxAx=(/(0.0,j=1,10000)/),
C                               MaxV=(/(0.0,j=1,10000)/),
C                               MaxVaxial=(/(0.0,j=1,10000)/),
C                               MaxVrad=(/(0.0,j=1,10000)/),
C                               MaxVtag=(/(0.0,j=1,10000)/)
```

```

MaxX=(/(0.0,j=1,10000)/)
MaxY=(/(0.0,j=1,10000)/)
MaxZ=(/(0.0,j=1,10000)/)
MaxR=(/(0.0,j=1,10000)/)
MaxAx=(/(0.0,j=1,10000)/)
MaxV=(/(0.0,j=1,10000)/)
MaxVaxial=(/(0.0,j=1,10000)/)
MaxVrad=(/(0.0,j=1,10000)/)
MaxVtag=(/(0.0,j=1,10000)/)

open(55,file=archivoentrada)
read(55,*) variables,w,ww,www,wwww,wwwww,wwwww

read(55,*,IOSTAT=st)nodenbr,xcoor,ycoor,zcoor,vtot,vaxial,vrad,
& vtag
rad=sqrt(xcoor**2+ycoor**2)-(0.01905/2.0)

xcoorInt = xcoor*1e+5
ycoorInt = ycoor*1e+5
zcoorInt = zcoor*1e+5
vtotInt = vtot*1e+5
vaxialInt=vaxial*1e+5
vradInt = vrad*1e+5
vtagInt = vtag*1e+5
radInt = rad*1e+5

i=1
count=1
var_control=.true.

Bucle_Leer:Do while (st==0)

Bucle_Seleccion:Do While (var_control)
var_control=.false.

If (MaxR(i)==radInt) then
if (MaxV(i) < vtotInt) then
MaxX(i)=xcoorInt
MaxY(i)=ycoorInt
MaxZ(i)=zcoorInt
MaxR(i)=radInt
MaxAx(i)=zcoorInt
MaxV(i)=vtotInt
MaxVaxial(i)=vaxialInt
MaxVrad(i)=vradInt
MaxVtag(i)=vtagInt
end if

```

```

else if (MaxR(i)==0) then
  if (vtotInt > 0) then
    MaxX(i)=xcoorInt
    MaxY(i)=ycoorInt
    MaxZ(i)=zcoorInt
    MaxR(i)=radInt
    MaxAx(i)=zcoorInt
    MaxV(i)=vtotInt
    MaxVaxial(i)=vaxialInt
    MaxVrad(i)=vradInt
    MaxVtag(i)=vtagInt
    count=count+1
  end if

else
  var_control=.true.
  i=i+1
end if

end do Bucle_Seleccion

read(55,*,IOSTAT=st)nodenbr,xcoor,ycoor,zcoor,vtot,vaxial,
vrad,vtag
rad=sqrt(xcoor**2+ycoor**2)-(0.01905/2.0)

xcoorInt = xcoor*1e+5
ycoorInt = ycoor*1e+5
zcoorInt = zcoor*1e+5
vtotInt = vtot*1e+5
vaxialInt= vaxial*1e+5
vradInt = vrad*1e+5
vtagInt = vtag*1e+5
radInt = rad*1e+5

i=1
var_control=.true.

end do Bucle_Leer

close(55)

open(77,file=archivosalida)
write(77,1010)
1010 format(3x,'radPos',9x,'AxPos',9x,'xcoor',9x,'ycoor',9x,'vtot',9x
,'vaxial',9x,'vradial',9x,'vtag')

writting: do i=1,count-1
write(77,1011) MaxR(i)*1e-5,(MaxAx(i)-24170)*1e-5,MaxX(i)*1e-5,
MaxY(i)*1e-5, MaxV(i)*1e-5,MaxVaxial(i)*1e-5,MaxVrad(i)*1e-5,
MaxVtag(i)*1e-5
1011 format(8(e13.5,1x))
end do writting

close(77)

end subroutine abreextraeRad

```



```

MaxX=(/(0.0,j=1,10000)/)
MaxY=(/(0.0,j=1,10000)/)
MaxZ=(/(0.0,j=1,10000)/)
MaxR=(/(0.0,j=1,10000)/)
MaxAx=(/(0.0,j=1,10000)/)
MaxV=(/(0.0,j=1,10000)/)
MaxVaxial=(/(0.0,j=1,10000)/)
MaxVrad=(/(0.0,j=1,10000)/)
MaxVtag=(/(0.0,j=1,10000)/)

open(55,file=archivoentrada)
read(55,*) variables,w,ww,www,www,wwwww,wwwww,wwwww

read(55,*,IOSTAT=st)nodenbr,xcoor,ycoor,zcoor,vtot,vaxial,vrad,
& vtag
rad=sqrt(xcoor**2+ycoor**2)-(0.01905/2.0)

xcoorInt = xcoor*1e+5
ycoorInt = ycoor*1e+5
zcoorInt = zcoor*1e+5
vtotInt = vtot*1e+5
vaxialInt=vaxial*1e+5
vradInt = vrad*1e+5
vtagInt = vtag*1e+5
radInt = rad*1e+5

i=1
count=1
var_control=.true.

Bucle_Leer:Do while (st==0)

Bucle_Seleccion:Do While (var_control)
var_control=.false.

If (MaxAx(i)==zcoorInt) then
if (abs(MaxVaxial(i)) < abs(vaxialInt)) then
MaxX(i)=xcoorInt
MaxY(i)=ycoorInt
MaxZ(i)=zcoorInt
MaxR(i)=radInt
MaxAx(i)=zcoorInt
MaxV(i)=vtotInt
MaxVaxial(i)=vaxialInt
MaxVrad(i)=vradInt
MaxVtag(i)=vtagInt
end if

```

```

else if (MaxAx(i)==0) then
  if (abs(vaxialInt) > 0) then
    MaxX(i)=xcoorInt
    MaxY(i)=ycoorInt
    MaxZ(i)=zcoorInt
    MaxR(i)=radInt
    MaxAx(i)=zcoorInt
    MaxV(i)=vtotInt
    MaxVaxial(i)=vaxialInt
    MaxVrad(i)=vradInt
    MaxVtag(i)=vtagInt
    count=count+1
  end if

else
  var_control=.true.
  i=i+1
end if

end do Bucle_Seleccion

read(55,*, IOSTAT=st) nodenbr, xcoor, ycoor, zcoor, vtot, vaxial,
vrad, vtag
rad=sqrt(xcoor**2+ycoor**2)-(0.01905/2.0)

xcoorInt = xcoor*1e+5
ycoorInt = ycoor*1e+5
zcoorInt = zcoor*1e+5
vtotInt = vtot*1e+5
vaxialInt= vaxial*1e+5
vradInt = vrad*1e+5
vtagInt = vtag*1e+5
radInt = rad*1e+5

i=1
var_control=.true.

end do Bucle_Leer

close(55)

open(77,file=archivosalida)
write(77,1010)
1010 format(3x,'radPos',9x,'AxPos',9x,'xcoor',9x,'ycoor',9x,'vtot',9x
& , 'vaxial',9x,'vradial',9x,'vtag')
writting: do i=1,count-1
write(77,1011) MaxR(i)*1e-5, (MaxAx(i)-24170)*1e-5, MaxX(i)*1e-5,
& MaxY(i)*1e-5, MaxV(i)*1e-5, MaxVaxial(i)*1e-5, MaxVrad(i)*1e-5,
& MaxVtag(i)*1e-5
1011 format(8(e13.5,1x))
end do writting

close(77)

end subroutine abreextraeRad

```

Program FLUAZIMAXMAXVEL

```
C
C 22-01-2007
C Author: Claudia López del Prá.
C Affiliation: Project of Nuclear Safety Technology
C              Department of Nuclear Fission (CIEMAT)
C
C This program reads fluent ascii file of data:
C (node number, xcoordi, ycoor, zcoordi, vmag, vaxial, vradial, vtag)
C It subtracts maximum velocities(tot,radial,axial) at each space between tubes.
C There are 6 spaces between tubes.
C
C
C
C Note: 1. There were problems when reading the variables,
C        so all of them are converted into Integer being multiplied by 1e5
C        2. Input files come directly from fluent
C
C
C DEFINITION OF VARIABLES
C
C Integer, dimension(6,9)::MaxVtotInt=(/((0,j=1,9),k=1,6)/)
C Integer, dimension(6,9)::MaxVradInt=(/((0,j=1,9),k=1,6)/)
C Integer, dimension(6,9)::MaxVaxInt=(/((0,j=1,9),k=1,6)/)
C
C common/varmax/MaxVtotInt,MaxVradInt,MaxVaxInt
C
C open(77,file='250MaxVSpacing')
C write(77,1010)
1010 format(3x,'angle',9x,'S1Vtot',9x,'S2Vtot',9x,'S3Vtot',9x
&  , 'S4Vtot',9x,'S5Vtot',9x,'S6Vtot',9x,
&  'S1Vrad',9x,'S2Vrad',9x,'S3rad',9x,'S4Vrad',9x,'S5Vrad',
&  9x,'S6Vrad',9x,
&  'S1Vax',9x,'S2Vax',9x,'S3ax',9x,'S4Vax',9x,'S5Vax',
&  9x,'S6Vax')
C
C call abre_lee_extrae('250InputAzim0grad.dat')
C call writtingdata(0,'250Maxmax0.dat')
C
C call abre_lee_extrae('250InputAzim5grad.dat')
C call writtingdata(5,'250Maxmax5.dat')
C
C call abre_lee_extrae('250InputAzim10grad.dat')
C call writtingdata(10,'250Maxmax10.dat')
C
C call abre_lee_extrae('250InputAzim15grad.dat')
C call writtingdata(15,'250Maxmax15.dat')
C
C call abre_lee_extrae('250InputAzim20grad.dat')
C call writtingdata(20,'250Maxmax20.dat')
```

```

call abre_lee_extrae('250InputAzim25grad.dat')
call writtingdata(25,'250Maxmax25.dat')

call abre_lee_extrae('250InputAzim30grad.dat')
call writtingdata(30,'250Maxmax30.dat')

call abre_lee_extrae('250InputAzim35grad.dat')
call writtingdata(35,'250Maxmax35.dat')

call abre_lee_extrae('250InputAzim40grad.dat')
call writtingdata(40,'250Maxmax40.dat')

call abre_lee_extrae('250InputAzim45grad.dat')
call writtingdata(45,'250Maxmax45.dat')

close(77)

end program FLUAZIMAXMAXVEL

subroutine writtingdata(alfa,archivosalida)
character*30::archivosalida
Integer, dimension(6,9)::MaxVtotInt=(/((0,j=1,9),k=1,6)/)
Integer, dimension(6,9)::MaxVradInt=(/((0,j=1,9),k=1,6)/)
Integer, dimension(6,9)::MaxVaxInt=(/((0,j=1,9),k=1,6)/)
integer:: alfa

common/varmax/MaxVtotInt,MaxVradInt,MaxVaxInt

write(77,1011)alfa,(MaxVtotInt(j,5)*1e-5,j=1,6),
& (MaxVradInt(j,7)*1e-5,j=1,6),(MaxVaxInt(j,6)*1e-5,j=1,6)
1011 format(i2,18(e13.5,1x))

open(55,file=archivosalida)
write(55,1012)
1012 format(3x,'radPos',9x,'AxPos',9x,'xcoor',9x,'ycoor',9x,'vtot',9x
& , 'vaxial',9x,'vradial',9x,'vtag')

writting: do k=1,6
write(55,1013)MaxVtotInt(k,9)*1e-5,
& (MaxVtotInt(k,4)-24170)*1e-5,MaxVtotInt(k,2)*1e-5,
& MaxVtotInt(k,3)*1e-5,MaxVtotInt(k,5)*1e-5,
& MaxVtotInt(k,6)*1e-5,MaxVtotInt(k,7)*1e-5,MaxVtotInt(k,8)*1e-5
write(55,1013)MaxVradInt(k,9)*1e-5,
& (MaxVradInt(k,4)-24170)*1e-5,MaxVradInt(k,2)*1e-5,
& MaxVradInt(k,3)*1e-5,MaxVradInt(k,5)*1e-5,
& MaxVradInt(k,6)*1e-5,MaxVradInt(k,7)*1e-5,MaxVradInt(k,8)*1e-5

```

```

write(55,1013)MaxVaxInt(k,9)*1e-5,
&      (MaxVaxInt(k,4)-24170)*1e-5,MaxVaxInt(k,2)*1e-5,
&      MaxVaxInt(k,3)*1e-5,MaxVaxInt(k,5)*1e-5,
&      MaxVaxInt(k,6)*1e-5,MaxVaxInt(k,7)*1e-5,MaxVaxInt(k,8)*1e-5
1013 format(8(e13.5,1x))
      end do writting
close(55)
end subroutine writtingdata

subroutine abre_lee_extrae(archivoentrada)

character*50::variables,w,ww,www,wwww,wwwww,wwwww,wwwww
character*30::archivoentrada
integer::i,j,k,st
logical::var_control

double precision, dimension(9)::VecIn=(/(0.0,j=1,9)/)
Integer, dimension(9)::VecInInt=(/(0,j=1,9)/)

Integer, dimension(6,9)::MaxVtotInt=(/((0,j=1,9),k=1,6)/)
Integer, dimension(6,9)::MaxVradInt=(/((0,j=1,9),k=1,6)/)
Integer, dimension(6,9)::MaxVaxInt=(/((0,j=1,9),k=1,6)/)

common/varmax/MaxVtotInt,MaxVradInt,MaxVaxInt

open(66,file=archivoentrada)
read(66,*) variables,w,ww,www,wwww,wwwww,wwwww,wwwww
read(66,*,IOSTAT=st)VecIn(1),VecIn(2),VecIn(3),VecIn(4),VecIn(5),
& VecIn(6),VecIn(7),VecIn(8)
!Vector positions correspond to the following values:
! nodenbr,xcoor,ycoor,zcoor,vtot,vaxial,vrad, vtag

VecIn(9)=sqrt(VecIn(2)**2+VecIn(3)**2)-(0.01905/2.0) !Radial position
BucleInteger: Do i=1,9
  VecInInt(i)=VecIn(i)*1e+5
End Do BucleInteger

BucleInitVar: Do i=1,6
  Do j=1,9
    MaxVtotInt(i,j)=0
    MaxVradInt(i,j)=0
    MaxVaxInt(i,j)=0
  end do
End Do BucleInitVar

```

```

Bucle_Leer:Do while (st==0)

  If      (VecInInt(2) <= 2743) then
  i=1
  else if (VecInInt(2) <= 5486) then
  i=2
  else if (VecInInt(2) <= 8229) then
  i=3
  else if (VecInInt(2) <= 10972) then
  i=4
  else if (VecInInt(2) <= 13715) then
  i=5
  else
  i=6
  end if

  If (MaxVtotInt(i,5)< VecInInt(5)) then
  do k=1,9
    MaxVtotInt(i,k)= VecInInt(k)
  end do
  end if

  If (abs(MaxVradInt(i,7))< abs(VecInInt(7))) then
  do k=1,9
    MaxVradInt(i,k)= VecInInt(k)
  end do
  end if

  If (abs(MaxVaxInt(i,6))< abs(VecInInt(6))) then
  do k=1,9
    MaxVaxInt(i,k)= VecInInt(k)
  end do
  end if

  read(66,*,IOSTAT=st)VecIn(1),VecIn(2),VecIn(3),VecIn(4),VecIn(5),
& VecIn(6),VecIn(7),VecIn(8)

  VecIn(9)=sqrt(VecIn(2)**2+VecIn(3)**2)-(0.01905/2.0) !Radial position

Do i=1,9
  VecInInt(i)=VecIn(i)*1e+5
End Do

end do Bucle_Leer

close(66)

end subroutine abre_lee_extrae

```


C. RESUSPENSION

The resuspension efficiency defined as the fraction of the resuspended mass from the deposited one (Eq. (3.1.9)) during a time-step of duration Δt , can be written as:

$$\eta_{rs} = 1 - \exp(-\Lambda \cdot \Delta t) \quad (C.1)$$

Where Λ is the resuspension rate.

ARI3SG models Λ similarly to the severe accident code ECART (Parozzi, 2000). ECART's model is semi-empirical and has been developed on the bases of lab-scale and large-scale tests close to LWR severe accident conditions (Oak ridge, PSI Würenligen and STORM; Parozzi et al., 1995; Parozzi, 2000). It is based on a force balance (F_{rs}) set onto deposited particles in which a particle is detached from a surface at a given rate (Λ) when the aerodynamic force acting onto the particle exceeds its adhesion to the surface. It is given by:

$$\Lambda(F_{rs}) = \begin{cases} 0.4037 \cdot (F_{rs} \cdot 10^6)^{0.6003} & 0 < F_{rs} < 3.065 \cdot 10^{-10} \text{ N} \\ 90.28 \cdot (F_{rs} \cdot 10^6)^{1.269} & F_{rs} \geq 3.065 \cdot 10^{-10} \text{ N} \end{cases} \quad (C.2)$$

Fig. B.1 shows the experimental resuspension rate together with previous correlation and its 95% confidence interval. As expected, as the force balance increases, the resuspension rate increases. The length of the confidence interval means in average a 300 to 400% of the prediction, whereas the average relative error of the correlation is 2090% and 280% for the high and low forces, respectively. It must be noticed that the differences between the averages of the relative confidence intervals and errors are due to that the former are relative to predictions and the later to the experimental data.

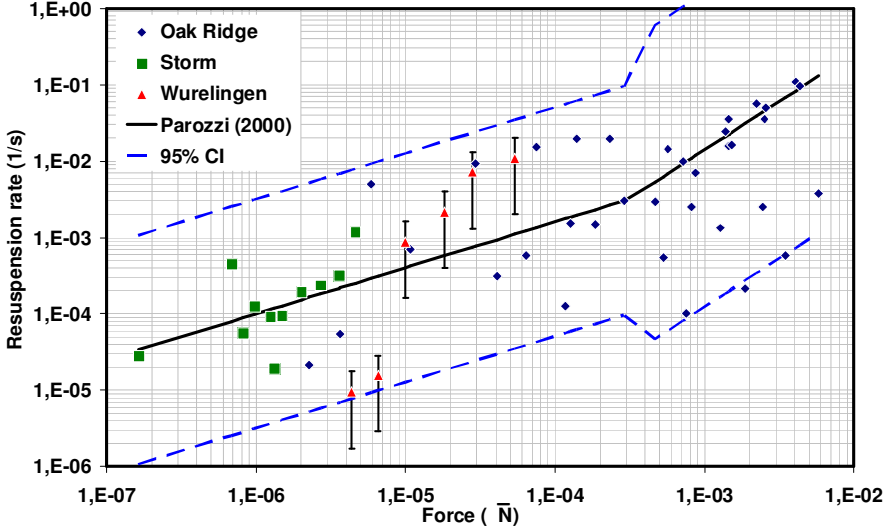


Fig. C.1 Resuspension rate vs resuspension force.

The aerodynamic forces responsible for the resuspension of the deposited particles are divided in drag (F_d) and lift force (F_l). The former is due to the particle resistance to the flow and is modeled accounting for the force that the wall shear stress ($\tau_w = \rho_g \cdot (U^*)^2$) exerts to the projected surface of the deposited particle (Parozzi, 2000):

$$F_d = \tau_w \cdot \frac{\pi \cdot d_p^2}{4} \quad (C.3)$$

The later also called burst force results from turbulent eddies which crashes the boundary layer resuspending particles. It has a fluctuating nature and is considered the main mechanism responsible for resuspension (Parozzi et al., 1995; Parozzi, 2000):

$$F_l = 4.21 \cdot \rho_g \cdot \left(\frac{\mu_g}{\rho_g} \right)^2 \cdot \left(\frac{\rho_g \cdot U^* \cdot d_p}{\mu_g} \right)^{2.31} \quad (C.4)$$

The adhesive forces that keep the particle attached to the surface are gravitational, electrostatic, surface tension adhesion, cohesive and frictional. From these forces, only the last two ones are relevant in the scenario. The gravitational force is neglected due to the verticality of the tube surfaces; The electrostatic one is also neglected as the possible particle charge is unlikely to

be important (NEA, 1979); and finally, the surface tension adhesion is not taken into account due to the dryness condition of the SGTR scenario.

The cohesive force (F_c) of the deposits increases as its depth increases. It is modeled taking into account the number of deposited layers (N_L) of particles of diameter d_p with the following relationship (Parozzi, 2000):

$$F_c = (2.87 \cdot 10^{-7} \sqrt{\min(N_L, 10)} + 10^{-7}) \cdot d_p \quad (C.5)$$

This relationship was found to be bounded to a maximum of 10 layers, value at which the cohesive force remains constant for deepest deposits (Parozzi, 2000).

The frictional force (F_f) that maintains the particle sliding and/or rolling on the surface is due to the cohesive force and therefore it is modeled as a fraction (20%) of it (Parozzi et al., 1995):

$$F_f = 0.2 * (F_c) \quad (C.6)$$

The balance of previous forces gives rise to the resuspension force (F_{rs}):

$$\begin{aligned} F_{rs} &= (F_d + F_f) - (F_c + F_f) \\ &= \rho_g \cdot (U^*)^2 \cdot d_p^2 \cdot \left[\frac{\pi}{4} + 4.21 \cdot \left(\frac{\rho_g \cdot U^* \cdot d_p}{\mu_g} \right)^{0.31} \right] \\ &\quad - 1.2 \cdot (2.87 \cdot \sqrt{\min(N_L, 10)} + 1.0) \cdot 10^{-7} \cdot d_p \end{aligned} \quad (C.7)$$

The influence of the time in the resuspension efficiency is clear in Eq. (C.7), as the interval of time (Δt) increases the efficiency increases. In the case of the resuspension rate, this influence is taken into account through the cumulative deposits, so to say through the number of layers (N_L) of deposited particles that as mentioned, in terms of the cohesive force it reaches a maximum from 10 layers on.

In order to be conservative, ARI3SG assumes a maximum resuspension efficiency (or resuspension rate) for all the time intervals Δt . It is obtained maximizing with time the resuspension force which implies a minimum cohesive force equivalent to the cohesion of 1 layer. Therefore, the resuspension force results:

$$F_{rs} = \rho_g \cdot (U^*)^2 \cdot d_p^2 \cdot \left[\frac{\pi}{4} + 4.21 \cdot \left(\frac{\rho_g \cdot U^* \cdot d_p}{\mu_g} \right)^{0.31} \right] - 4.644 \cdot 10^{-7} \cdot d_p \quad (C.8)$$

A parametric study showed a low sensitivity of the ARI3SG model with respect to the cohesive force. The case analyzed displayed differences around

a 2% in the final collection efficiency when assuming maximum and minimum cohesion forces.

Finally, by substituting Eq. (C.1) into the equation of the single tube collection efficiency results:

$$\eta_{ST}^{(n)}(i) = \eta_{dp}(i) \cdot [1 - \eta_{rs}(i)] \cdot \frac{1 - [1 - \eta_{rs}(i)]^n}{n \cdot \eta_{rs}(i)} \quad (C.9)$$

$$\eta_{ST}^{(n)}(i) = \eta_{dp}(i) \cdot [1 - \eta_{rs}(i)] \cdot \frac{1 - \exp(-\Lambda \cdot n \cdot \Delta t)}{n \cdot [1 - \exp(-\Lambda \cdot \Delta t)]} \quad (C.10)$$

Eq. (C.10) shows that the decreasing multiplicative factor, which accounts for the cumulative effect of the resuspension (section 3.1.2), is the ratio between the resuspension efficiency that would take place in a time step of duration $n \cdot \Delta t$ and n -times the resuspension efficiency in a time step Δt .

It must be noticed that in ARI3SG modeling, collision and particle shape factors are assumed to be 1. On other side, the friction velocity (U^*) of the resuspension is obtained from the maximum between radial and axial velocities (hereafter called resuspension velocity, U_{rs}), in order to maintain conservative hypothesis:

$$U_{rs}(i) = \max(U_{rd}(i); U_{ax}(i)) \quad (C.11)$$

D. ARI3SG INPUT GENERATION

Input of ARI3SG is performed through a Mathematica 4.0 program. It collects boundary and initial conditions of the scenario and generates the following input deck.

```
database/singlcas
dt, s, Lt
P, T, U0, t, Δt
ρp, Nbins
dp(1), np(1),....., dp(Nbins), np(Nbins)
P, T, U0, t, Δt
ρp, Nbins
dp(1), np(1),....., dp(Nbins), np(Nbins)
P, T, U0, t, Δt
ρp, Nbins
dp(1), np(1),....., dp(Nbins), np(Nbins)
```

As observed in the last row, aerosol size distribution is characterized through N_{bins} sections of n_p number of particles of diameter d_p . This description in number and diameters is independent of the aerosol size distribution.

D.1. LOGNORMAL PARTICLE DISCRETIZATION

It is assumed that in the SGTR scenario particle size follow a lognormal distribution. Description in number of particles and diameters has been performed discretizing the lognormal particle mass distribution in N_{bins} sections. Each bin is characterized by having n_p number of particles of diameter d_p .

In order to do so, it is required to know the integral aerosol mass injected (M_{in}), the aerosol density (ρ_p) and one of the characteristic diameters of the aerosol distribution. The latest could be given as AMMD, ACMD, MMD, CMD or d_m^- as Hatch-Choate equations (Hinds, 1999) allow the conversion into MMD. These relationships are summarized in Fig. D.1.

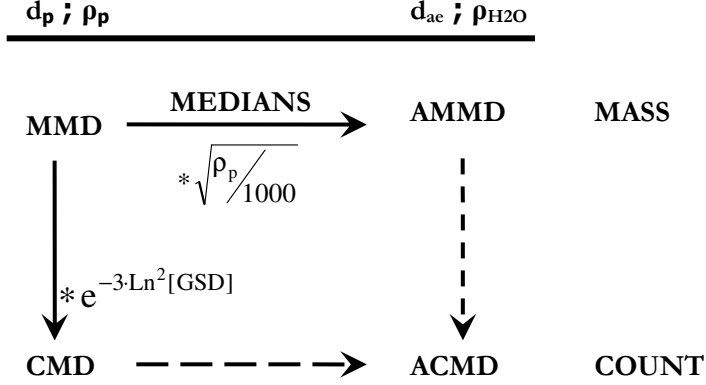


Fig. D.1. Conversion diagram of count and mass medians.

The 99% of the lognormal particle count and mass distributions lie within the intervals: $[\text{CMD} \cdot \text{GSD}^{-3}, \text{CMD} \cdot \text{GSD}^{+3}]$ and $[\text{MMD} \cdot \text{GSD}^{-3}, \text{MMD} \cdot \text{GSD}^{+3}]$ respectively. Both ranges have been joined in order to ensure that a 99% of count and mass descriptions are included in the discretization. This range is $[\text{CMD} \cdot \text{GSD}^{-3}, \text{MMD} \cdot \text{GSD}^{+3}]$.

By splitting this range in $N_{\text{bins}}=30$ sections, it is obtained the following limiting particle bins sizes:

$$d_p(i) = \left\{ \text{CMD} \cdot \text{GSD}^{\frac{6i}{N_{\text{bins}}}-3} \cdot \exp\left(\frac{3 \cdot i \cdot [\ln(\text{GSD})]^2}{N_{\text{bins}}}\right); i = 0..N_{\text{bins}} \right\} \quad (\text{D.1})$$

Then, the mass fraction between two consecutive particle sizes ($d_p(i)$ and $d_p(i+1)$) is obtained by integrating the lognormal mass frequency function in the interval $d_p(i)$ - $d_p(i+1)$. This step is performed automatically by Mathematica 4.0:

$$\text{MFraction}(i) = \int_{d_p(i)}^{d_p(i+1)} \frac{1}{\sqrt{2\pi} \cdot d_p \cdot \ln(\text{GSD})} \exp\left[-\left(\frac{\ln(d_p) - \ln(\text{MMD})}{\sqrt{2} \cdot \ln(\text{GSD})}\right)^2\right] dd_p \quad (\text{D.2})$$

By multiplying by the integral aerosol mass injected (M_{in}) it is obtained the total mass at each bin size ($M_{\text{Bin}}(i)$):

$$M_{\text{bin}}(i) = \text{MFraction}(i) * M_{\text{in}} \quad (\text{D.3})$$

On other side, the particle diameter that has been chosen to characterize each bin size is the geometric average of the bin, so to say:

$$d_{\text{bin}}(i) = \sqrt{d_p(i) \cdot d_p(i+1)}; \quad i = 0, \dots, N_{\text{bins}} - 1 \quad (\text{D.4})$$

Then, the number of particles ($n_p(i)$) of size $d_{\text{bin}}(i)$ that the mass $M_{\text{bin}}(i)$ contain is:

$$n_p(i) = \frac{M_{\text{bin}}(i)}{\rho_p \cdot \pi/6 \cdot d_{\text{bin}}^3(i)} \quad (\text{D.5})$$

This way, all the mass of the distribution is characterized obtaining the discretization: $\{d_p(1), n_p(1), \dots, d_p(N_{\text{bins}}), n_p(N_{\text{bins}})\}$. **Fig. D.2** show an example of the count size distribution.

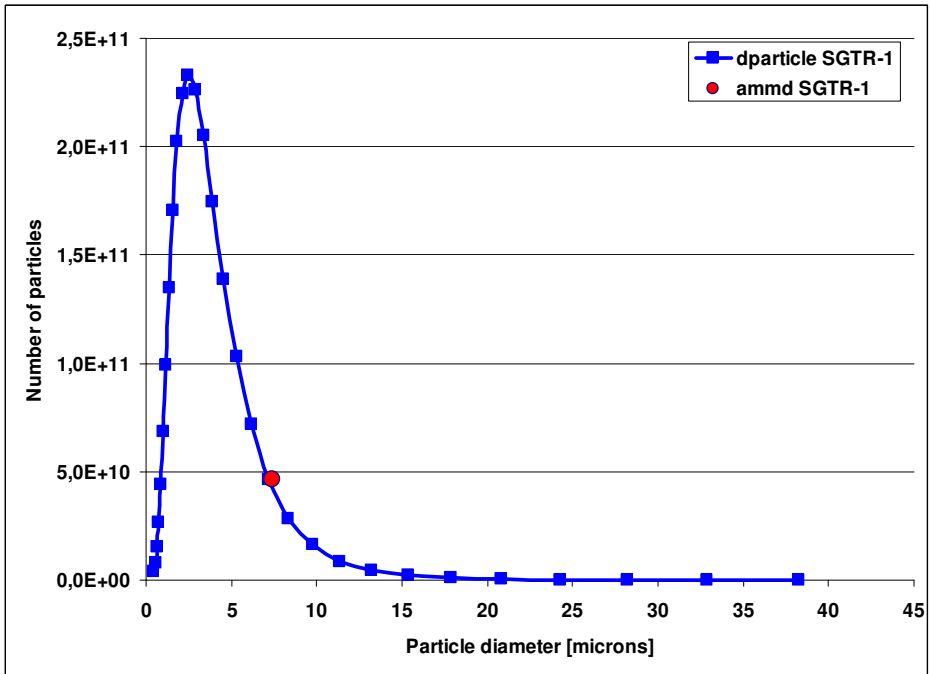


Fig. D.2. Count size distribution of the source term.

The source code of the mathematica program that generates the input deck of ARICODE is given in the following section.

D.2. SOURCE CODE OF INPUT GENERATION OF ARICODE

The source code in Mathematica 4.0 of the input generation of ARICODE is given as follows. The first one correspond to the input performed for the simulation of the reference case SGTR experiments, whereas the second one presents the input generation for the uncertainty analysis of the same experiments.

- ***SGTR reference case:***

```
ClearAll[]
<<Statistics`ContinuousDistributions`
<<Graphics`Graphics`
<<LinearAlgebra`MatrixManipulation`
$Path;
SetDirectory["c:\Privada\SGTR"];
ddtube=0.019;
stube=0.01;
P=120000.0;
T=293.0;
TubeTotLength=0.9;
Caso={{guillotine,database}}};
Caso=Append[Caso,{{ddtube,stube,TubeTotLength,P,T}}];

Experimental data:
TimeExper1=Table[{31.,29.,27.,28.,29.,30.,30.,27.,29.,30.,30.,27.}];
MasstotIn1=Table[{96.61,108.55,113.47,133.53,74.87,182.73,186.35,120.36,133.
52,62.12,56.6,49.52}];
v=Table[{252.24,116.38,160.86,253.59,118.85,167.82,248.11,161.74,246.89,96.5
3,90.34,90.61}];
ammd=Table[{7.42,6.72,6.72,6.69,6.72,6.95,7.13,6.7,4.87,5.16,3.37,5.16}];
gsd=Table[{1.8,1.67,1.67,1.66,1.67,1.78,1.78,1.67,1.51,1.56,1.49,1.56}];
ρ=Sort[Table[{1000.*10^-3}]]
deltat=1.0
TimeExperRef=TimeExper1*60.
MasstotIn=MasstotIn1/1000
{1860.,1740.,1620.,1680.,1740.,1800.,1800.,1620.,1740.,1800.,1800.,1620.}
{0.09661,0.10855,0.11347,0.13353,0.07487,0.18273,0.18635,0.12036,0.13352,0.0
6212,0.0566,0.04952}
VRef=v;
AmmRef=ammd;
GsdRef=gsd;
ρRef=ρ;
```

```

For[i = 0, i < Dimensions[AmmdRef][[1]], i ++;
  mmd = AmmdRef[[i]] /  $\sqrt{\rho\text{Ref}[[1]}}$ ;
  cmd = mmd *  $e^{-3 * \text{Log}[\text{GsdRef}[[i]]]^2}$ ;
  nbins = 30;
  PtosUnionCmdMmd = Table[cmd *  $\text{GsdRef}[[i]]^{\frac{6 * n}{\text{nbins}} - 3}$ 
    * Exp[ $\frac{n}{\text{nbins}} * 3 * \text{Log}[\text{GsdRef}[[i]]]^2$ ], {n, 0, nbins}];
  distribMmd = LogNormalDistribution[Log[mmd],
    Log[GsdRef[[i]]];
  frecMmd = PDF[distribMmd, x];
  fraction = Table[Integrate[frecMmd,
    {x, PtosUnionCmdMmd[[i]], PtosUnionCmdMmd[[i + 1]]}],
    {i, Dimensions[PtosUnionCmdMmd][[1]] - 1}];
  NuevosDiamUnionCmdMmd = Table[
     $\sqrt{\text{PtosUnionCmdMmd}[[kk]] * \text{PtosUnionCmdMmd}[[kk + 1]]}$ ,
    {kk, 1, Dimensions[PtosUnionCmdMmd][[1]] - 1}];

  MParticlesMass = fraction * MasstotIn[[i]];
  NParticlesCount = Table[ $\left\{ \frac{\text{MParticlesMass}[[i]]}{\rho\text{Ref}[[1]] * 10^3 * \frac{\pi}{6} * (\text{NuevosDiamUnionCmdMmd}[[i]] * 10^{-6})^3} \right\}$ ,
    {i, Dimensions[NuevosDiamUnionCmdMmd][[1]]}];
  ParesPtos = Table[ $\{\text{NuevosDiamUnionCmdMmd}[[i]] * 10^{-6}, \text{NParticlesCount}[[i]]\}$ ,
    {i, Dimensions[NuevosDiamUnionCmdMmd][[1]]}];
  Caso = Append[Caso,  $\{\{\text{AmmdRef}[[i]] * 10^{-6}, \text{GsdRef}[[i]],$ 
    Dimensions[NuevosDiamUnionCmdMmd][[1]],  $\rho\text{Ref}[[1]] * 10^3,$ 
    VRef[[i]], deltat, TimeExperRef[[i]]\}];
  Caso = Append[Caso, {Flatten[ParesPtos]};
]

Export["InputArg1.dat",Caso]

```

- ***SGTR uncertainty analysis:***

```

ClearAll[]
<< Statistics`ContinuousDistributions`
<< Graphics`Graphics`
<< LinearAlgebra`MatrixManipulation`
$Path;
SetDirectory["c:\Privada\SGTR"];

ntubes = 5;
ddtube = 0.019;
stube = 0.01;
P = 120000.0;
T = 293.0;
TubeTotLength = 1.1;
Caso = {{{guillotine}}};
Caso = Append[Caso, {{database}}];
Caso = Append[Caso, {{ntubes, ddtube, stube, TubeTotLength, P, T}}];

Experimental data:
TimeResus1 =
  Table[{31., 29., 27., 28., 29., 30., 30., 27., 29., 30., 30., 27.}];
MasstotIn1 =
  Table[{96.61, 108.55, 113.47, 133.53, 74.87, 182.73, 186.35, 120.36,
    133.52, 62.12, 56.6, 49.52}];
v = Table[{252.24, 116.38, 160.86, 253.59, 118.85, 167.82, 248.11, 161.74,
  246.89, 96.53, 90.34, 90.61}];
ammd = Table[{7.42, 6.72, 6.72, 6.69, 6.72, 6.95, 7.13, 6.7, 4.87, 5.16, 3.37,
  5.16}];
gsd = Table[{1.8, 1.67, 1.67, 1.66, 1.67, 1.78, 1.78, 1.67, 1.51, 1.56, 1.49,
  1.56}];

UncertV =
  Table[{18.72, 8.74, 20.24, 15.16, 11.89, 22.01, 22.16, 8.04, 20.59, 15.41,
  13.62, 10.22}];
ρ = Sort[Table[{{1000. * 10^-3}]]
TimeResusRef = TimeResus1 * 60.
MasstotIn = MasstotIn1 / 1000
VRef = v;
AmmdRef = ammd;
GsdRef = gsd;
ρRef = ρ;
SeedingNbr = 0;

```

```

For[i = 0, i < Dimensions[AmmdRef][[1]], i++;
  mmd = AmmdRef[[i]] /  $\sqrt{\rho\text{Ref}[[1] ]}$ ;
  cmd = mmd *  $e^{-3 * \text{Log}[\text{GsdRef}[[i]]^2]}$ ;
  nbins = 30;
  PtosUnionCmdMmd = Table[cmd * GsdRef[[i]] $\frac{6 * n}{\text{nbins}}^{-3}$ 
    * Exp[ $\frac{n}{\text{nbins}} * 3 * \text{Log}[\text{GsdRef}[[i]]^2]$ , {n, 0, nbins}];
  distribMmd = LogNormalDistribution[Log[mmd], Log[GsdRef[[i]]];
  frecMmd = PDF[distribMmd, x];
  fraction = Table[Integrate[frecMmd,
    {x, PtosUnionCmdMmd[[i]], PtosUnionCmdMmd[[i + 1]]},
    {1, Dimensions[PtosUnionCmdMmd][[1] - 1}];
  NuevosDiamUnionCmdMmd = Table[
     $\sqrt{\text{PtosUnionCmdMmd}[[kk]] * \text{PtosUnionCmdMmd}[[kk + 1] ]}$ ,
    {kk, 1, Dimensions[PtosUnionCmdMmd][[1] - 1}];
  MParticlesMass = fraction * MasstotIn[[i];
  NParticlesCount = Table[
    { $\frac{\text{MParticlesMass}[[i]]}{\rho\text{Ref}[[1]] * 10^3 * \frac{\pi}{6} * (\text{NuevosDiamUnionCmdMmd}[[i]] * 10^{-6})^3}$ },
    {1, Dimensions[NuevosDiamUnionCmdMmd][[1]]};
  ParesPtos = Table[{NuevosDiamUnionCmdMmd[[i]] * 10-6,
    NParticlesCount[[i]]}, {1, Dimensions[NuevosDiamUnionCmdMmd][[1]]};
  Caso = Append[Caso, {{AmmdRef[[i]] * 10-6, GsdRef[[i]],
    Dimensions[NuevosDiamUnionCmdMmd][[1]],  $\rho\text{Ref}[[1]] * 10^3$ , VRef[[i]], TimeResusRef[[i]]}}];
  Caso = Append[Caso, {Flatten[ParesPtos]};

VDist = NormalDistribution[VRef[[i]], UncertV[[i]] / 2.0];
AmmdDist = LogNormalDistribution[Log[AmmdRef[[i]]], Log[GsdRef[[i]]];
 $\rho\text{Dist} = \text{UniformDistribution}[\rho\text{Ref}[[1]] / 2.6, \rho\text{Ref}[[1]] * 2.6];

SeedingNbr = SeedingNbr + 1; SeedRandom[SeedingNbr];
UncAmmdNbrs = Table[Random[AmmdDist], {100}];
SeedingNbr = SeedingNbr + 1; SeedRandom[SeedingNbr];
UncVNbrs = Table[Random[VDist], {100}];
SeedingNbr = SeedingNbr + 1; SeedRandom[SeedingNbr];
Unc $\rho$ Nbrs = Table[Random[ $\rho\text{Dist}$ ], {100}];$ 
```

```

For[j = 0, j < Dimensions[UncAmmdNbrs][[1]], j ++;
  Unmmd = UncAmmdNbrs[[j]] /  $\sqrt{\text{Unc}\rho\text{Nbrs}[[j]]}$ ;
  Uncmd = Unmmd *  $e^{-3 * \text{Log}[\text{GsdRef}[[i]]^2]}$ ;
  nbins = 30;
  UnPtos = Table[Uncmd *  $\text{GsdRef}[[i]]^{\frac{6 * n}{\text{nbins}} - 3} * \text{Exp}\left[\frac{n}{\text{nbins}} * 3 * \text{Log}[\text{GsdRef}[[i]]^2]\right]$ , {n, 0, nbins}];
  UndistMmd = LogNormalDistribution[Log[Unmmd], Log[GsdRef[[i]]];
  UnPdfMmd = PDF[UndistMmd, x];
  fraction = Table[Integrate[UnPdfMmd, {x, UnPtos[[1]], UnPtos[[1 + 1]]}],
    {1, Dimensions[UnPtos][[1]] - 1}];
  Und = Table[ $\sqrt{\text{UnPtos}[[kk]] * \text{UnPtos}[[kk + 1]]}$ , {kk, 1, Dimensions[UnPtos][[1]] - 1}];
  UnPMass = fraction * MasstotIn[[i]];
  UnPCount = Table[ $\left\{\frac{\text{UnPMass}[[1]]}{\text{Unc}\rho\text{Nbrs}[[j]] * 10^3 * \frac{\pi}{6} * (\text{Und}[[1]] * 10^{-6})^3}\right\}$ ,
    {1, Dimensions[Und][[1]]}];
  UnParesPtos = Table[{Und[[1]] *  $10^{-6}$ , UnPCount[[1]]}, {1, Dimensions[Und][[1]]};
  Caso = Append[Caso, {{UncAmmdNbrs[[j]] *  $10^{-6}$ , GsdRef[[i]], Dimensions[Und][[1]],
    Unc\rhoNbrs[[j]] *  $10^3$ , UncVNbrs[[j]], TimeResusRef[[i]]}}];
  Caso = Append[Caso, {Flatten[UnParesPtos]}];
  Clear[Unmmd, Uncmd, nbins, UnPtos, UndistMmd, UnPdfMmd, fraction,
    Und, UnPMass, UnPCount, UnParesPtos]
]
]

Export["InputArg1.dat", Caso]

```

E. INPUT AND OUTPUT FILES OF ARICODE

E.1. ARICODE INPUT

This section contains the input file of three cases to be run in database mode. The first line of each case has been highlighted in order to distinguish them, and the first two lines are common to the three cases.

This section contains the input file of three cases to be run in database mode. The first line of each case has been highlighted in order to distinguish them, and the first two lines are common to the three cases.

```
database
0.019, 0.01, 0.9
120000., 293., 109.99, 2280., 1.0
2528.,30
6.07385175635607e-9,    1.123042467463833e11,    8.417358004322864e-9,    2.5298424590827454e11,    1.1665071624244725e-8,
5.191282250426098e11,    1.616586771394024e-8,    9.7038426996869e11,    2.2403229689687924e-8,    1.6523602069293816e12,
3.104718592346944e-8,    2.563075308975562e12,    4.30262853668e-8,    3.621740198816487e12,    5.96273439089978e-8,
4.662039650455503e12,    8.263367639878422e-8,    5.466893919115025e12,    1.1451666345561622e-7,    5.840021172927757e12,
1.5870123151388452e-7,    5.683294441672217e12,    2.199337644323271e-7,    5.038491190839199e12,    3.0479196837954234e-7,
4.069282926549137e12,    4.2239146057657926e-7,    2.994018581379527e12,    5.853649848996189e-7,    2.006837739630542e12,
8.112194434016227e-7,    1.2254423307242803e12,    1.1242165184610224e-6,    6.817070320739009e11,    1.5579789052897522e-6,
3.454841337651502e11,    2.1591021208714e-6,    1.5950884411834763e11,    2.992159876185482e-6,    6.709163420840071e10,    4.14664069758819e-6,
2.570864886401244e10,    5.746560941394288e-6,    8.974649018584478e9,    7.96378684856046e-6,    2.8541895529114785e9,
0.000011036496717968593,    8.269414698427255e8,    0.000015294766437370048,    2.1826926086110616e8,    0.00002119602681463571,
5.24849978632247e7,    0.000029374201598073484,    1.1497443258856509e7,    0.00004070780467820862,    2.294506398382888e6,
0.00005641431159197422,    417154.8946086665,    0.00007818094288194387,    69091.30613184093
```

120000., 293., 148.35065553835767, 1800, 1.0
1587.5239089263382,30
2.2468483563565157e-8, 2.6912000972132817e12, 2.7605780136075977e-8, 5.645133625847787e12, 3.391769163082963e-8,
1.098427186253721e13, 4.167278736168241e-8, 1.9826172912820355e13, 5.120104355549621e-8, 3.3195464960549656e13,
6.290788370883727e-8, 5.1557573616167875e13, 7.729142919587587e-8, 7.42816503192109e13, 9.496369413396553e-8,
9.927671466237305e13, 1.166766263399687e-7, 1.2308109623334447e14, 1.4335410240962376e-7, 1.4155155681182912e14,
1.7613123829780426e-7, 1.510144166548527e14, 2.1640268804916533e-7, 1.4945266345054762e14, 2.6588198577088055e-7,
1.372054364330542e14, 3.2667445582471544e-7, 1.1684824728132014e14, 4.0136679353799797e-7, 9.231175525696131e13,
4.931371280569708e-7, 6.76513283147195e13, 6.058902504729868e-7, 4.599182420903021e13, 7.444237611243261e-7,
2.900482778787188e13, 9.146322055749848e-7, 1.6968581513182924e13, 1.123757885174824e-6, 9.208873480888104e12,
1.3806990140902723e-6, 4.6361043578960205e12, 1.696388334764193e-6, 2.1651377045511326e12, 2.084258301741555e-6,
9.380008714451472e11, 2.560812627246962e-6, 3.7696933176292017e11, 3.1463285075501365e-6, 1.4053788111580368e11,
3.865719409570836e-6, 4.8603194816584e10, 4.749595128948742e-6, 1.5592637632666943e10, 5.835564224625923e-6, 4.640415990090969e9,
7.169834248013325e-6, 1.2810789689827712e9, 8.809177855853365e-6, 3.2807681444666181e8
120000., 293., 251.5912807600054, 1800, 1.0
1172.0810569189334,30
1.8981025472474725e-7, 6.211076482843911e10, 2.204935794622516e-7, 1.252417615198081e11, 2.561369439948261e-7,
2.3635195653156738e11, 2.975421517443343e-7, 4.174438201365651e11, 3.456406197554881e-7, 6.900279339505736e11,
4.0151433107740435e-7, 1.067495509602294e12, 4.664201741525077e-7, 1.5455998914571821e12, 5.418182167313888e-7,
2.094404524189786e12, 6.294045503400396e-7, 2.6561787149643535e12, 7.311494441412304e-7, 3.152738570093964e12,
8.493416664674895e-7, 3.502298945542216e12, 9.866399710459584e-7, 3.641276268395847e12, 1.1461329061063215e-6,
3.54315150805633e12, 1.3314082917876557e-6, 3.2267248698623374e12, 1.5466339287500426e-6, 2.7502403254443506e12,
1.7966513535445972e-6, 2.193896617480727e12, 2.087084749784586e-6, 1.6379427305585532e12, 2.4244674650925602e-6,
1.1445070608427764e12, 2.8163889798433126e-6, 7.48471978909078e11, 3.2716656337889973e-6, 4.581101860632831e11,
3.8005389510902927e-6, 2.6242284494098508e11, 4.414906025108207e-6, 1.4069235659604034e11, 5.128587145500792e-6,
7.059539253710864e10, 5.957636687940897e-6, 3.315270308027049e10, 6.92070425997091e-6, 1.4571287910647074e10,
8.039454227030677e-6, 5.9939477112677e9, 9.339053055966462e-6, 2.307615856580092e9, 0.000010848735438894329,
8.314748251392517e8, 0.000012602461932468582, 2.803942643041363e8, 0.000014639682906260126, 8.8495852783076e7

E.2. ARICODE OUTPUT

This section contains the output files of ARICODE: OutBundle.dat, OuTube.dat, OutPSize.dat and OuTime.dat. They correspond to previous input. The last three files given in this section correspond to the files generated for the first case of previous input when it is run in singlcas mode. They are shown as columns of data and in some cases columns have been splitted due to the length of the files.

E.2.1. OutBundle.dat

dtube	stube	P	T	Time	DELTA_T	Ntime Step	Tube Length	vinit	mssflowrate
0,019	0,01	1,20E+05	293	2,28E+03	1,00	2280	9,00E-01	1,10E+02	9,34E+01
0,019	0,01	1,20E+05	293	1,80E+03	1,00	1800	9,00E-01	1,48E+02	1,36E+02
0,019	0,01	1,20E+05	293	1,80E+03	1,00	1800	9,00E-01	2,52E+02	2,49E+02

Regas	rhopar	Ammdd In	gsdIn	RepIn	StkIn	Nt	VRadOut
1,68E+05	2,53E+03	5,74	2,89	5,08E+01	6,03E-01	9	1,89E-01
2,27E+05	1,59E+03	1,27	2,11	1,52E+01	4,35E-02	9	2,54E-01
3,85E+05	1,17E+03	2,96	1,78	5,99E+01	3,75E-01	9	4,31E-01

RegasOut	ammddOut	gsdOut	RepAMMDOut	StkAMMDOut	BundleEff	UncBundle(95%CI)
2,88E+02	4,98	2,84	7,55E-02	7,81E-04	2,72E+01	5,89
3,89E+02	1,22	2,10	2,49E-02	6,81E-05	1,11E+01	4,73
6,60E+02	2,81	1,77	9,76E-02	5,82E-04	1,77E+01	5,47

E.2.2. OutTube.dat

The following table shows only the first 44 lines of results of OutTube.dat file.

Tube	V-Rad	V-Ax	V-Resus	Regas	ammd	gsd	rhopar	StkIn	RepIn	Δ_t	TubEff	Uncer
1	1,10E+02	8,80E+01	1,10E+02	1,68E+05	5,74E-06	2,89	2,53E+03	6,03E-01	5,08E+01	1	25,03	16,47
2	1,72E+01	2,20E+01	2,20E+01	2,63E+04	4,73E-06	2,82	2,53E+03	6,42E-02	6,53	1	24,28	5,32
3	5,09	9,78	9,78	7,79E+03	4,34E-06	2,79	2,53E+03	1,61E-02	1,78	1	14,54	3,50
4	2,15	5,50	5,50	3,28E+03	4,22E-06	2,78	2,53E+03	6,43E-03	7,30E-01	1	8,36	3,19
5	1,10	3,52	3,52	1,68E+03	4,19E-06	2,78	2,53E+03	3,24E-03	3,71E-01	1	5,39	2,69
6	6,37E-01	2,44	2,44	9,73E+02	4,18E-06	2,78	2,53E+03	1,87E-03	2,14E-01	1	3,62	2,04
7	4,01E-01	1,80	1,80	6,13E+02	4,17E-06	2,78	2,53E+03	1,17E-03	1,35E-01	1	2,33	1,45
8	2,69E-01	1,37	1,37	4,11E+02	4,17E-06	2,78	2,53E+03	7,85E-04	9,02E-02	1	1,44	0,83
9	1,89E-01	1,09	1,09	2,88E+02	4,17E-06	2,78	2,53E+03	5,51E-04	6,33E-02	1	0,92	0,78
1	1,10E+02	8,80E+01	1,10E+02	1,68E+05	5,74E-06	2,89	2,53E+03	6,03E-01	5,08E+01	1	22,70	16,49
2	1,72E+01	2,20E+01	2,20E+01	2,63E+04	4,73E-06	2,82	2,53E+03	6,44E-02	6,54	1	23,72	5,78
3	5,09	9,78	9,78	7,79E+03	4,34E-06	2,79	2,53E+03	1,61E-02	1,78	1	14,78	3,57
4	2,15	5,50	5,50	3,28E+03	4,23E-06	2,78	2,53E+03	6,44E-03	7,31E-01	1	8,81	3,18
5	1,10	3,52	3,52	1,68E+03	4,19E-06	2,78	2,53E+03	3,25E-03	3,71E-01	1	5,80	2,69
6	6,37E-01	2,44	2,44	9,73E+02	4,18E-06	2,78	2,53E+03	1,87E-03	2,14E-01	1	3,90	2,07
7	4,01E-01	1,80	1,80	6,13E+02	4,18E-06	2,78	2,53E+03	1,17E-03	1,35E-01	1	2,55	1,50
8	2,69E-01	1,37	1,37	4,11E+02	4,18E-06	2,78	2,53E+03	7,86E-04	9,02E-02	1	1,60	0,91
9	1,89E-01	1,09	1,09	2,88E+02	4,17E-06	2,78	2,53E+03	5,52E-04	6,34E-02	1	1,02	0,86
1	1,10E+02	8,80E+01	1,10E+02	1,68E+05	5,74E-06	2,89	2,53E+03	6,03E-01	5,08E+01	1	21,03	16,30
2	1,72E+01	2,20E+01	2,20E+01	2,63E+04	4,74E-06	2,83	2,53E+03	6,45E-02	6,55	1	23,19	6,12
3	5,09	9,78	9,78	7,79E+03	4,35E-06	2,79	2,53E+03	1,61E-02	1,78	1	14,92	3,64
4	2,15	5,50	5,50	3,28E+03	4,23E-06	2,78	2,53E+03	6,45E-03	7,31E-01	1	9,15	3,18

5	1,10	3,52	3,52	1,68E+03	4,20E-06	2,78	2,53E+03	3,25E-03	3,71E-01	1	6,08	2,70
6	6,37E-01	2,44	2,44	9,73E+02	4,18E-06	2,78	2,53E+03	1,87E-03	2,14E-01	1	4,11	2,09
7	4,01E-01	1,80	1,80	6,13E+02	4,18E-06	2,78	2,53E+03	1,18E-03	1,35E-01	1	2,70	1,55
8	2,69E-01	1,37	1,37	4,11E+02	4,18E-06	2,78	2,53E+03	7,87E-04	9,03E-02	1	1,71	0,97
9	1,89E-01	1,09	1,09	2,88E+02	4,18E-06	2,78	2,53E+03	5,53E-04	6,34E-02	1	1,10	0,92
1	1,10E+02	8,80E+01	1,10E+02	1,68E+05	5,74E-06	2,89	2,53E+03	6,03E-01	5,08E+01	1	19,73	16,06
2	1,72E+01	2,20E+01	2,20E+01	2,63E+04	4,74E-06	2,83	2,53E+03	6,47E-02	6,56	1	22,71	6,40
3	5,09	9,78	9,78	7,79E+03	4,35E-06	2,79	2,53E+03	1,62E-02	1,78	1	15,01	3,70
4	2,15	5,50	5,50	3,28E+03	4,23E-06	2,78	2,53E+03	6,46E-03	7,32E-01	1	9,40	3,19
5	1,10	3,52	3,52	1,68E+03	4,20E-06	2,78	2,53E+03	3,26E-03	3,72E-01	1	6,30	2,71
6	6,37E-01	2,44	2,44	9,73E+02	4,19E-06	2,78	2,53E+03	1,87E-03	2,14E-01	1	4,26	2,12
7	4,01E-01	1,80	1,80	6,13E+02	4,18E-06	2,78	2,53E+03	1,18E-03	1,35E-01	1	2,82	1,59
8	2,69E-01	1,37	1,37	4,11E+02	4,18E-06	2,78	2,53E+03	7,88E-04	9,03E-02	1	1,80	1,02
9	1,89E-01	1,09	1,09	2,88E+02	4,18E-06	2,78	2,53E+03	5,53E-04	6,34E-02	1	1,15	0,96
1	1,10E+02	8,80E+01	1,10E+02	1,68E+05	5,74E-06	2,89	2,53E+03	6,03E-01	5,08E+01	1	18,68	15,78
2	1,72E+01	2,20E+01	2,20E+01	2,63E+04	4,75E-06	2,83	2,53E+03	6,48E-02	6,57	1	22,28	6,63
3	5,09	9,78	9,78	7,79E+03	4,35E-06	2,79	2,53E+03	1,62E-02	1,78	1	15,08	3,77
4	2,15	5,50	5,50	3,28E+03	4,24E-06	2,78	2,53E+03	6,47E-03	7,32E-01	1	9,61	3,19
5	1,10	3,52	3,52	1,68E+03	4,20E-06	2,78	2,53E+03	3,26E-03	3,72E-01	1	6,47	2,71
6	6,37E-01	2,44	2,44	9,73E+02	4,19E-06	2,78	2,53E+03	1,88E-03	2,15E-01	1	4,39	2,14
7	4,01E-01	1,80	1,80	6,13E+02	4,18E-06	2,78	2,53E+03	1,18E-03	1,35E-01	1	2,92	1,62

E.2.3. OutPSize.dat

The following table shows the first 42 rows of the output file. It has been splitted in three tables.

tube	dpar(k)	npin(k)	BinMass(k)	RePar	CcF	StkF	EffRad	UncEffRad (95%CI)	RelTime Plus	LiuAgar VPlus	UncSDLiu (95%CI)
1	6,07E-03	1,12E+11	3,33E-11	5,38E-02	31	5,17E-05	0,00	0,00	1,18E-02	8,42E-08	7,36E-08
1	8,42E-03	2,53E+11	2,00E-10	7,45E-02	22,6	7,22E-05	0,00	0,00	1,65E-02	1,64E-07	1,43E-07
1	1,17E-02	5,19E+11	1,09E-09	1,03E-01	16.5	1,01E-04	0,00	0,00	2,32E-02	3,22E-07	2,81E-07
1	1,62E-02	9,70E+11	5,43E-09	1,43E-01	12	1,42E-04	0,00	0,00	3,26E-02	6,36E-07	5,56E-07
1	2,24E-02	1,65E+12	2,46E-08	1,98E-01	8,87	2,01E-04	0,00	0,00	4,60E-02	1,27E-06	1,11E-06
1	3,10E-02	2,56E+12	1,02E-07	2,75E-01	6,58	2,87E-04	0,00	0,00	6,56E-02	2,58E-06	2,26E-06
1	4,30E-02	3,62E+12	3,82E-07	3,81E-01	4,94	4,13E-04	0,00	0,00	9,47E-02	5,38E-06	4,70E-06
1	5,96E-02	4,66E+12	1,31E-06	5,28E-01	3,77	6,06E-04	0,00	0,00	1,39E-01	1,15E-05	1,01E-05
1	8,26E-02	5,47E+12	4,08E-06	7,31E-01	2,94	9,06E-04	0,00	0,00	2,08E-01	2,59E-05	2,26E-05
1	1,15E-01	5,84E+12	1,16E-05	1,01	2,35	1,39E-03	0,00	0,00	3,19E-01	6,11E-05	5,34E-05
1	1,59E-01	5,68E+12	3,01E-05	1,40	1,94	2,21E-03	2,31E-03	1,13E-01	5,06E-01	1,54E-04	1,34E-04
1	2,20E-01	5,04E+12	7,09E-05	1,95	1,66	3,63E-03	3,77E-02	1,13E-01	8,31E-01	4,15E-04	3,63E-04
1	3,05E-01	4,07E+12	1,53E-04	2,70	1,47	6,16E-03	7,54E-02	1,13E-01	1,41	1,19E-03	1,04E-03
1	4,22E-01	2,99E+12	2,99E-04	3,74	1,33	1,08E-02	1,15E-01	1,13E-01	2,46	3,64E-03	3,18E-03
1	5,85E-01	2,01E+12	5,33E-04	5,18	1,24	1,92E-02	1,56E-01	1,13E-01	4,40	1,16E-02	1,01E-02
1	8,11E-01	1,23E+12	8,66E-04	7,18	1,17	3,49E-02	1,99E-01	1,13E-01	7,99	3,83E-02	3,34E-02
1	1,12	6,82E+11	1,28E-03	9,95	1,12	6,42E-02	2,43E-01	1,13E-01	1,47E+01	1,00E-01	8,74E-02
1	1,56	3,45E+11	1,73E-03	1,38E+01	1,09	1,20E-01	4,26E-02	1,48E-01	2,74E+01	1,00E-01	8,74E-02
1	2,16	1,60E+11	2,13E-03	1,91E+01	1,07	2,24E-01	1,07E-01	1,48E-01	5,14E+01	1,00E-01	8,74E-02
1	2,99	6,71E+10	2,38E-03	2,65E+01	1,05	4,23E-01	2,31E-01	1,48E-01	9,70E+01	1,00E-01	8,74E-02
1	4,15	2,57E+10	2,43E-03	3,67E+01	1,03	8,03E-01	4,14E-01	1,48E-01	1,84E+02	1,00E-01	8,74E-02
1	5,75	8,97E+09	2,25E-03	5,09E+01	1,02	1,53	6,10E-01	1,48E-01	3,50E+02	1,00E-01	8,74E-02

1	7,96	2,85E+09	1,91E-03	7,05E+01	1,02	2,92	7,65E-01	1,48E-01	6,68E+02	1,00E-01	8,74E-02
1	1,10E+01	8,27E+08	1,47E-03	9,77E+01	1,01	5,57	8,66E-01	1,48E-01	1,28E+03	1,00E-01	8,74E-02
1	1,53E+01	2,18E+08	1,03E-03	1,35E+02	1,01	1,07E+01	9,23E-01	1,48E-01	2,44E+03	1,00E-01	8,74E-02
1	2,12E+01	5,25E+07	6,62E-04	1,88E+02	1,01	2,04E+01	9,56E-01	1,48E-01	4,68E+03	1,00E-01	8,74E-02
1	2,94E+01	1,15E+07	3,86E-04	2,60E+02	1,00	3,92E+01	9,74E-01	1,48E-01	8,97E+03	1,00E-01	8,74E-02
1	4,07E+01	2,29E+06	2,05E-04	3,60E+02	1,00	7,51E+01	9,84E-01	1,48E-01	1,72E+04	1,00E-01	8,74E-02
1	5,64E+01	4,17E+05	9,91E-05	4,99E+02	1,00	1,44E+02	9,90E-01	1,48E-01	3,30E+04	1,00E-01	8,74E-02
1	7,82E+01	6,91E+04	4,37E-05	6,92E+02	1,00	2,77E+02	9,93E-01	1,48E-01	6,33E+04	1,00E-01	8,74E-02
2	6,07E-03	1,12E+11	3,33E-11	8,40E-03	31	8,08E-06	0,00	0,00	1,02E-03	6,22E-10	5,43E-10
2	8,42E-03	2,53E+11	2,00E-10	1,16E-02	22,6	1,13E-05	0,00	0,00	1,42E-03	1,21E-09	1,06E-09
2	1,17E-02	5,19E+11	1,09E-09	1,61E-02	16,5	1,58E-05	0,00	0,00	1,99E-03	2,38E-09	2,08E-09
2	1,62E-02	9,70E+11	5,43E-09	2,24E-02	12	2,22E-05	0,00	0,00	2,80E-03	4,69E-09	4,10E-09
2	2,24E-02	1,65E+12	2,46E-08	3,10E-02	8,87	3,14E-05	0,00	0,00	3,96E-03	9,39E-09	8,20E-09
2	3,10E-02	2,56E+12	1,02E-07	4,29E-02	6,58	4,48E-05	0,00	0,00	5,64E-03	1,91E-08	1,67E-08
2	4,30E-02	3,62E+12	3,82E-07	5,95E-02	4,94	6,46E-05	0,00	0,00	8,13E-03	3,97E-08	3,47E-08
2	5,96E-02	4,66E+12	1,31E-06	8,25E-02	3,77	9,46E-05	0,00	0,00	1,19E-02	8,52E-08	7,45E-08
2	8,26E-02	5,47E+12	4,08E-06	1,14E-01	2,94	1,42E-04	0,00	0,00	1,78E-02	1,91E-07	1,67E-07
2	1,15E-01	5,84E+12	1,16E-05	1,58E-01	2,35	2,18E-04	0,00	0,00	2,74E-02	4,51E-07	3,94E-07
2	1,59E-01	5,67E+12	3,00E-05	2,19E-01	1,94	3,46E-04	0,00	0,00	4,35E-02	1,14E-06	9,93E-07

EffAx	UncEffAx (95%CI)	EffDepO	UncDep0 (95%CI)	FCohes	FFric	FDrag	FLift	FAdh	FResult	Nlys	ResRate
7,72E-09	6,75E-09	7,72E-09	6,75E-09	2,34E-09	4,68E-10	1,03E-09	8,54E-10	2,81E-09	-9,22E-10	1	0,00
1,50E-08	1,32E-08	1,50E-08	1,32E-08	3,24E-09	6,48E-10	1,98E-09	1,81E-09	3,89E-09	-9,61E-11	1	0,00
2,95E-08	2,58E-08	2,95E-08	2,58E-08	4,49E-09	8,98E-10	3,80E-09	3,85E-09	5,39E-09	2,27E-09	1	2,61E-06
5,83E-08	5,09E-08	5,83E-08	5,09E-08	6,22E-09	1,24E-09	7,30E-09	8,19E-09	7,47E-09	8,02E-09	1	5,57E-06
1,17E-07	1,02E-07	1,17E-07	1,02E-07	8,63E-09	1,73E-09	1,40E-08	1,74E-08	1,04E-08	2,11E-08	1	9,95E-06
2,37E-07	2,07E-07	2,37E-07	2,07E-07	1,20E-08	2,39E-09	2,69E-08	3,70E-08	1,43E-08	4,96E-08	1	1,66E-05
4,93E-07	4,31E-07	4,93E-07	4,31E-07	1,66E-08	3,31E-09	5,17E-08	7,86E-08	1,99E-08	1,10E-07	1	2,69E-05
1,06E-06	9,25E-07	1,06E-06	9,25E-07	2,30E-08	4,59E-09	9,93E-08	1,67E-07	2,75E-08	2,39E-07	1	4,27E-05
2,37E-06	2,07E-06	2,37E-06	2,07E-06	3,18E-08	6,36E-09	1,91E-07	3,55E-07	3,82E-08	5,07E-07	1	6,72E-05
5,60E-06	4,90E-06	5,60E-06	4,90E-06	4,41E-08	8,82E-09	3,66E-07	7,54E-07	5,29E-08	1,07E-06	1	1,05E-04
1,41E-05	1,23E-05	2,33E-03	1,13E-01	6,11E-08	1,22E-08	7,03E-07	1,60E-06	7,33E-08	2,23E-06	1	1,64E-04
3,80E-05	3,32E-05	3,77E-02	1,13E-01	8,47E-08	1,69E-08	1,35E-06	3,41E-06	1,02E-07	4,65E-06	1	2,54E-04
1,09E-04	9,56E-05	7,55E-02	1,13E-01	1,17E-07	2,35E-08	2,59E-06	7,24E-06	1,41E-07	9,69E-06	1	3,95E-04
3,33E-04	2,91E-04	1,15E-01	1,13E-01	1,63E-07	3,25E-08	4,98E-06	1,54E-05	1,95E-07	2,02E-05	1	6,13E-04
1,06E-03	9,28E-04	1,57E-01	1,13E-01	2,25E-07	4,51E-08	9,57E-06	3,27E-05	2,70E-07	4,20E-05	1	9,52E-04
3,50E-03	3,05E-03	2,02E-01	1,13E-01	3,12E-07	6,25E-08	1,84E-05	6,94E-05	3,75E-07	8,74E-05	1	1,48E-03
9,12E-03	7,94E-03	2,49E-01	1,12E-01	4,33E-07	8,66E-08	3,53E-05	1,48E-04	5,19E-07	1,82E-04	1	2,30E-03
9,12E-03	7,94E-03	5,14E-02	1,47E-01	6,00E-07	1,20E-07	6,78E-05	3,14E-04	7,20E-07	3,81E-04	1	4,13E-03
9,12E-03	7,94E-03	1,15E-01	1,47E-01	8,31E-07	1,66E-07	1,30E-04	6,66E-04	9,98E-07	7,95E-04	1	1,05E-02
9,12E-03	7,94E-03	2,38E-01	1,47E-01	1,15E-06	2,30E-07	2,50E-04	1,42E-03	1,38E-06	1,66E-03	1	2,69E-02
9,12E-03	7,94E-03	4,19E-01	1,47E-01	1,60E-06	3,19E-07	4,80E-04	3,01E-03	1,92E-06	3,49E-03	1	6,87E-02
9,12E-03	7,94E-03	6,13E-01	1,46E-01	2,21E-06	4,42E-07	9,22E-04	6,39E-03	2,65E-06	7,31E-03	1	1,76E-01
9,12E-03	7,94E-03	7,67E-01	1,46E-01	3,07E-06	6,13E-07	1,77E-03	1,36E-02	3,68E-06	1,54E-02	1	4,51E-01
9,12E-03	7,94E-03	8,67E-01	1,46E-01	4,25E-06	8,50E-07	3,40E-03	2,89E-02	5,10E-06	3,23E-02	1	1,16
9,12E-03	7,94E-03	9,24E-01	1,46E-01	5,89E-06	1,18E-06	6,53E-03	6,13E-02	7,07E-06	6,79E-02	1	2,97

9,12E-03	7,94E-03	9,56E-01	1,46E-01	8,16E-06	1,63E-06	1,25E-02	1,30E-01	9,79E-06	1,43E-01	1	7,64
9,12E-03	7,94E-03	9,74E-01	1,46E-01	1,13E-05	2,26E-06	2,41E-02	2,77E-01	1,36E-05	3,01E-01	1	1,97E+01
9,12E-03	7,94E-03	9,84E-01	1,46E-01	1,57E-05	3,13E-06	4,63E-02	5,89E-01	1,88E-05	6,35E-01	1	5,07E+01
9,12E-03	7,94E-03	9,90E-01	1,46E-01	2,17E-05	4,34E-06	8,89E-02	1,25	2,61E-05	1,34	1	1,31E+02
9,12E-03	7,94E-03	9,93E-01	1,46E-01	3,01E-05	6,02E-06	1,71E-01	2,66	3,61E-05	2,83	1	3,38E+02
1,34E-10	1,17E-10	1,34E-10	1,17E-10	2,34E-09	4,68E-10	5,94E-11	3,16E-11	2,81E-09	-2,72E-09	1	0,00
2,60E-10	2,28E-10	2,60E-10	2,28E-10	3,24E-09	6,48E-10	1,14E-10	6,72E-11	3,89E-09	-3,71E-09	1	0,00
5,11E-10	4,46E-10	5,11E-10	4,46E-10	4,49E-09	8,98E-10	2,19E-10	1,43E-10	5,39E-09	-5,03E-09	1	0,00
1,01E-09	8,82E-10	1,01E-09	8,82E-10	6,22E-09	1,24E-09	4,21E-10	3,03E-10	7,47E-09	-6,74E-09	1	0,00
2,02E-09	1,76E-09	2,02E-09	1,76E-09	8,63E-09	1,73E-09	8,08E-10	6,45E-10	1,04E-08	-8,90E-09	1	0,00
4,10E-09	3,58E-09	4,10E-09	3,58E-09	1,20E-08	2,39E-09	1,55E-09	1,37E-09	1,43E-08	-1,14E-08	1	0,00
8,53E-09	7,46E-09	8,53E-09	7,46E-09	1,66E-08	3,31E-09	2,98E-09	2,91E-09	1,99E-08	-1,40E-08	1	0,00
1,83E-08	1,60E-08	1,83E-08	1,60E-08	2,30E-08	4,59E-09	5,72E-09	6,19E-09	2,75E-08	-1,56E-08	1	0,00
4,10E-08	3,59E-08	4,10E-08	3,59E-08	3,18E-08	6,36E-09	1,10E-08	1,31E-08	3,82E-08	-1,40E-08	1	0,00
9,69E-08	8,47E-08	9,69E-08	8,47E-08	4,41E-08	8,82E-09	2,11E-08	2,79E-08	5,29E-08	-3,85E-09	1	0,00
2,44E-07	2,13E-07	2,44E-07	2,13E-07	6,11E-08	1,22E-08	4,06E-08	5,94E-08	7,33E-08	2,66E-08	1	1,14E-05

UncResRate(95%CI)	EffResus	UncEffResus(95%CI)	EffFinal	UncEffFinal(95%CI)
0,00	0,00	0,00	7,72E-09	6,75E-09
0,00	0,00	0,00	1,50E-08	1,32E-08
9,00E-06	2,61E-06	9,00E-06	2,94E-08	2,57E-08
1,92E-05	5,57E-06	1,92E-05	5,79E-08	5,06E-08
3,43E-05	9,95E-06	3,43E-05	1,15E-07	1,01E-07
5,74E-05	1,66E-05	5,74E-05	2,33E-07	2,04E-07
9,28E-05	2,69E-05	9,28E-05	4,78E-07	4,21E-07
1,47E-04	4,27E-05	1,47E-04	1,01E-06	8,97E-07
2,32E-04	6,72E-05	2,32E-04	2,20E-06	2,00E-06
3,62E-04	1,05E-04	3,62E-04	4,98E-06	4,78E-06
5,64E-04	1,64E-04	5,64E-04	1,94E-03	9,45E-02
8,77E-04	2,54E-04	8,77E-04	2,86E-02	8,97E-02
1,36E-03	3,95E-04	1,36E-03	4,97E-02	9,95E-02
2,11E-03	6,13E-04	2,11E-03	6,21E-02	1,31E-01
3,28E-03	9,51E-04	3,28E-03	6,42E-02	1,66E-01
5,10E-03	1,48E-03	5,09E-03	5,78E-02	1,78E-01
7,93E-03	2,30E-03	7,91E-03	4,73E-02	1,60E-01
1,96E-02	4,12E-03	1,95E-02	5,44E-03	3,01E-02
4,99E-02	1,05E-02	4,93E-02	4,76E-03	2,34E-02
1,27E-01	2,65E-02	1,24E-01	3,83E-03	1,85E-02
3,25E-01	6,64E-02	3,04E-01	2,59E-03	1,27E-02
8,32E-01	1,61E-01	6,98E-01	1,40E-03	7,23E-03
2,13	3,63E-01	1,36	5,91E-04	3,48E-03
5,47	6,85E-01	1,72	1,74E-04	1,39E-03
1,41E+01	9,49E-01	7,21E-01	2,19E-05	3,25E-04
3,62E+01	1,00	1,73E-02	2,01E-07	7,28E-06

9,32E+01	1,00	2,65E-07	1,21E-12	1,13E-10
2,40E+02	1,00	2,25E-20	0,00	9,73E-24
6,19E+02	1,00	9,38E-55	0,00	4,07E-58
0,00	0,00	0,00	1,34E-10	1,17E-10
0,00	0,00	0,00	2,60E-10	2,28E-10
0,00	0,00	0,00	5,11E-10	4,46E-10
0,00	0,00	0,00	1,01E-09	8,82E-10
0,00	0,00	0,00	2,02E-09	1,76E-09
0,00	0,00	0,00	4,10E-09	3,58E-09
0,00	0,00	0,00	8,53E-09	7,46E-09
0,00	0,00	0,00	1,83E-08	1,60E-08
0,00	0,00	0,00	4,10E-08	3,59E-08
0,00	0,00	0,00	9,69E-08	8,47E-08
3,95E-05	1,14E-05	3,95E-05	2,41E-07	2,11E-07

E.2.4. OuTime.dat

The following figures show the first and last 44 rows of the OuTime.dat file.

timestep	time	FinalbundleEff	Uncert (95%CI)	timestep	time	FinalbundleEff	Uncert(95%CI)
1	1,00	4,94E+01	5,96	2238	2,24E+03	2,73E+01	5,88
2	2,00	4,89E+01	6,03	2239	2,24E+03	2,73E+01	5,88
3	3,00	4,86E+01	6,05	2240	2,24E+03	2,73E+01	5,88
4	4,00	4,83E+01	6,04	2241	2,24E+03	2,73E+01	5,88
5	5,00	4,81E+01	6,03	2242	2,24E+03	2,73E+01	5,88
6	6,00	4,78E+01	6,00	2243	2,24E+03	2,73E+01	5,88
7	7,00	4,76E+01	5,97	2244	2,24E+03	2,73E+01	5,88
8	8,00	4,74E+01	5,94	2245	2,25E+03	2,73E+01	5,88
9	9,00	4,73E+01	5,91	2246	2,25E+03	2,73E+01	5,88
10	1,00E+01	4,71E+01	5,88	2247	2,25E+03	2,73E+01	5,88
11	1,10E+01	4,69E+01	5,85	2248	2,25E+03	2,73E+01	5,88
12	1,20E+01	4,68E+01	5,82	2249	2,25E+03	2,73E+01	5,88
13	1,30E+01	4,67E+01	5,79	2250	2,25E+03	2,73E+01	5,88
14	1,40E+01	4,65E+01	5,76	2251	2,25E+03	2,73E+01	5,88
15	1,50E+01	4,64E+01	5,73	2252	2,25E+03	2,73E+01	5,88
16	1,60E+01	4,63E+01	5,71	2253	2,25E+03	2,73E+01	5,88
17	1,70E+01	4,62E+01	5,68	2254	2,25E+03	2,73E+01	5,88
18	1,80E+01	4,61E+01	5,65	2255	2,26E+03	2,73E+01	5,88
19	1,90E+01	4,60E+01	5,63	2256	2,26E+03	2,73E+01	5,89
20	2,00E+01	4,59E+01	5,60	2257	2,26E+03	2,73E+01	5,89
21	2,10E+01	4,58E+01	5,58	2258	2,26E+03	2,73E+01	5,89
22	2,20E+01	4,57E+01	5,56	2259	2,26E+03	2,73E+01	5,89

23	2,30E+01	4,56E+01	5,54	2260	2,26E+03	2,73E+01	5,89
24	2,40E+01	4,55E+01	5,52	2261	2,26E+03	2,73E+01	5,89
25	2,50E+01	4,55E+01	5,50	2262	2,26E+03	2,73E+01	5,89
26	2,60E+01	4,54E+01	5,48	2263	2,26E+03	2,73E+01	5,89
27	2,70E+01	4,53E+01	5,46	2264	2,26E+03	2,72E+01	5,89
28	2,80E+01	4,52E+01	5,44	2265	2,27E+03	2,72E+01	5,89
29	2,90E+01	4,52E+01	5,42	2266	2,27E+03	2,72E+01	5,89
30	3,00E+01	4,51E+01	5,41	2267	2,27E+03	2,72E+01	5,89
31	3,10E+01	4,50E+01	5,39	2268	2,27E+03	2,72E+01	5,89
32	3,20E+01	4,49E+01	5,37	2269	2,27E+03	2,72E+01	5,89
33	3,30E+01	4,49E+01	5,36	2270	2,27E+03	2,72E+01	5,89
34	3,40E+01	4,48E+01	5,34	2271	2,27E+03	2,72E+01	5,89
35	3,50E+01	4,48E+01	5,33	2272	2,27E+03	2,72E+01	5,89
36	3,60E+01	4,47E+01	5,32	2273	2,27E+03	2,72E+01	5,89
37	3,70E+01	4,46E+01	5,30	2274	2,27E+03	2,72E+01	5,89
38	3,80E+01	4,46E+01	5,29	2275	2,28E+03	2,72E+01	5,89
39	3,90E+01	4,45E+01	5,27	2276	2,28E+03	2,72E+01	5,89
40	4,00E+01	4,45E+01	5,26	2277	2,28E+03	2,72E+01	5,89
41	4,10E+01	4,44E+01	5,25	2278	2,28E+03	2,72E+01	5,89
42	4,20E+01	4,44E+01	5,24	2279	2,28E+03	2,72E+01	5,89
43	4,30E+01	4,43E+01	5,22	2280	2,28E+03	2,72E+01	5,89

F. UNCERTAINTY OF THE DIMENSIONLESS AXIAL DEPOSITION VELOCITY AND RESUSPENSION RATE CORRELATIONS

It must be noted that in case of the dimensionless axial deposition velocity (U^+) and resuspension rate (Λ) correlations, standard uncertainties have been obtained from the linear log-transformed functions from where they come from. So to say, in the first case

$$\begin{aligned}
 U^+ &= \text{Min}(6 \cdot 10^{-4} \cdot (\tau_+)^2, 0.1) \\
 \left\{ \begin{array}{l} \text{Ln}(U^+) = \text{Ln}(6 \cdot 10^{-4}) + 2 \cdot \text{Ln}(\tau_+) \quad \tau_+ < 13 \\ U^+ = 0.1 \quad \tau_+ \geq 13 \end{array} \right. \\
 \Rightarrow \left\{ \begin{array}{l} u(\text{Ln}(U^+)) = 0.437 \quad \tau_+ < 13 \\ u(U^+) = 0.03 \quad \tau_+ \geq 13 \end{array} \right. \quad (\text{F-1})
 \end{aligned}$$

This way and after transforming back the natural logarithm, it is obtained the following uncertainty range with a 95% of confidence level:

$$U^+ = \begin{cases} 6 \cdot 10^{-4} \cdot (\tau_+)^2 \cdot e^{\pm 2 \cdot 0.437} & \tau_+ < 13 \\ 0.1 \pm 2 \cdot 0.03 & \tau_+ \geq 13 \end{cases} \quad (\text{F-2})$$

Similarly, the uncertainty range of the resuspension rate correlation is:

$$\Lambda(F) [1/s] = \begin{cases} 0.4037 \cdot F^{0.6003} \cdot e^{\pm 2 \cdot 1.725} & F < 3.065 \cdot 10^{-4} \mu\text{N} \\ 90.28 \cdot F^{1.269} \cdot e^{\pm 2 \cdot 2.367} & F \geq 3.065 \cdot 10^{-4} \mu\text{N} \end{cases} \quad (\text{F-3})$$

Both uncertainty ranges were shown in Fig. 25 (section 3.2.3.1) and Fig. 28 (section 3.2.4). However, due to the complexity of propagating the log-transformed standard uncertainties through the model, it has been applied the first order Taylor series approximation, obtaining:

$$\begin{aligned}
 u(\text{Ln}(U^+)) &= \frac{1}{U^+} \cdot u(U^+) \Rightarrow \\
 \left\{ \begin{array}{l} u(U^+) = U^+ \cdot u(\text{Ln}(U^+)) = U^+ \cdot 0.437 \quad \tau_+ < 13 \\ u(U^+) = 0.03 \quad \tau_+ \geq 13 \end{array} \right. \quad (\text{F-4})
 \end{aligned}$$

$$u(\ln(\Lambda)) = \frac{1}{\Lambda} \cdot u(\Lambda) \quad \Rightarrow$$

$$u(\Lambda) = \begin{cases} \Lambda \cdot 1.725 & F < 3.065 \cdot 10^{-4} \mu\text{N} \\ \Lambda \cdot 2.367 & F \geq 3.065 \cdot 10^{-4} \mu\text{N} \end{cases}$$

(F-5)

```

C= *****
C= *****
C= **
C= **          This program opens reads and writes a          **
C= **          database which uses Ari3sg procedure          **
C= **
C= *****
C= *****
C= *****
C= **          INPUT FILE: "AR3SGINPUT.dat"          **
C= **          The input of this program has this format:          **
C= **
C= ** inputmode {database,singlcas}          **
C= ** dtube,stube, tubtotlenght          **
C= ** BucleLeerl: DO until end of file          **
C= ** P,T, vinit, TimeExper, DELTA_t          **
C= ** rhopar, nbins          **
C= ** BucleLeerDatosDistribucion: DO kk=1,nbins          **
C= ** (dpar(jj),nparin(jj,1),jj=1,nbins)          **
C= **
C= **          * * * * *
C= ** typeout=singlcas is used for writing a detailed output **
C= ** it can only be used for 1 input case (not more) **
C= *****
C= **          OUTPUT FILE: "OutputArg1.dat"          **
C= **          The output has this format:          **
C= **          (in one line)          **
C= **
C= ** dtube stube P T vgas(1) rhopar ammd gsd          **
C= ** RepAmmd StkAmmd StkeAmmd bankeff          **
C= **
C= *****
C= *****
C=
C= DB=data base
C= rho=density

```

Program ARICODE

```

USE GasTherHyCondDATA
USE BundleDATA
USE VelocityDATA
USE PartDistribDATA
USE BundleEfficiencyDATA
USE Resuspension
USE Uncertainty

implicit none

integer:: st=0
integer(8):: jj
double precision:: densammd

cldp

densammd=1000.0

open(55,file='ARI3SGINPUT.dat')
read(55,*,IOSTAT=st)inputmode
read(55,*,IOSTAT=st)dtube,stube,TubTotLength

open(66,file='Output-Bundle.dat')

write(66,1010)
1010 format(' dt          st          P          T          Time
&delta_T          NStep          Lt          U0          mssflowrate
& Reg          rhop          AMMDIn          GSDIn
&          RepAMMDIn          StkIn          Nt

```

```

&      Urdout      Regout      AMMDOut      GSDout      RepAMMDout
&      Stkout
&      BundleEff  Unc(95%CI)')

      read(55,*,IOSTAT=st)P,T, vinit, TimeExper, DELTA_t
      read(55,*,IOSTAT=st)rhopar, nbins

BucleFicheroAbiertoConDatos:DO WHILE (st==0)

      NTimeStep=Int(TimeExper/DELTA_t)

      allocate (dpar(nbins))
      allocate (nparin0(nbins))
      allocate (FinalBundleEff(NTimeStep))
      allocate (UncTuBndle(NTimeStep))

      CALL  InitVar

      read(55,*,IOSTAT=st) (dpar(jj),nparin0(jj),jj=1,nbins)

Cldp  Pruebas para las simulaciones SGTR así la masa que metemos no hay que cambiarla
      !antes metíamos el total y en el siguiente loop se divide por el NtimeStep que sea

      Loop_Nro_part_SGTRtimestep: DO jj=1,nbins
          nparin0(jj)=nparin0(jj)/NTimeStep
      END DO Loop_Nro_part_SGTRtimestep

Cldp  Fin Pruebas

      Print *, 'case= ', vinit

      CALL  ARI3SG

      write(66,1011)dtube,
&stube,
& P,
& T,
& TimeExper,
& DELTA_t,
& NTimeStep,
& TubTotLength,
& vinit,
& mssflwrate,
& RegasF(vinit,dtube),
& rhopar,
& ammdIn*1e6,
& gsdIn,
& ReparF(vinit,ammdIn),
& StkF(ammdIn,densammd,vinit),
& NtubesMax,
& Radialvelocity,
& RegasF(Radialvelocity,dtube),
& ammd*1e6,
& gsd,
& ReparF(Radialvelocity,ammd),
& StkF(ammd,densammd,Radialvelocity),
& FinalBundleEff(NTimeStep)*100,
& 2.0*UncTuBndle(NTimeStep)*100

1011  format(x,2(e11.5,2x),x,e11.5,x,f5.1,x,2(e11.5,x),I8,4x,9(e11.5,x),
& I4,7x,6(e11.5,x),3x, 2(e11.5,x))

      deallocate (dpar)
      deallocate (nparin0)

```

```

deallocate (FinalBundleEff)
deallocate (UncTuBndle)

read(55,*,IOSTAT=st)P,T, vinit, TimeExper, DELTA_t
read(55,*,IOSTAT=st)rhopar, nbins

END DO BucleFicheroAbiertoConDatos

  close(55)
  close(66)

Print *,'final'
STOP  ' Stop ARICODE'

  END PROGRAM ARICODE

  Subroutine InitVar

USE GasTherHyCondDATA
USE BundleDATA
USE PartDistribDATA
USE BundleEfficiencyDATA
USE VelocityDATA
USE AxialDeposition
USE Forces
USE Resuspension
USE Uncertainty
implicit none

integer(8)::k,s
k=0
s=0

Loop_InitBins3: DO k=1,nbins
  dpar(k)=0.0
  nparin0(k)=0.0
END DO Loop_InitBins3

Loop_Init_TimeStep: Do s=1,NTimeStep
  FinalBundleEff(s)=0.0
  UncTuBndle(s)=0.0
END DO Loop_Init_TimeStep

End Subroutine InitVar

```



```

MODULE BundleDATA
implicit none
character(8)::inputmode  !={database,singlcas}
double precision:: dtube,stube
double precision:: TubTotLength,TimeExper
integer(8)::NtubesMax
integer(8)::NTimeStep,N_init

contains
  function ComputeNtubesMaxF(Length) result(Nrotubos)
  implicit none
  double precision:: realx,Rntubes,Length
  integer(8):: Nrotubos

      realx=12.5*Length/(dtube+stube)+1.0
      Rntubes=(Sqrt(realx)-1.0)/2.0
      Nrotubos= nint(Rntubes)
  end function ComputeNtubesMaxF

END MODULE BundleDATA

MODULE GasTherHyCondDATA
implicit none
double precision:: Mgas,mugas,rhogas,RR,pi
double precision:: P,T
data RR/0.082/,pi/3.14159/
data Mgas/29./,mugas/1.8e-5/

  contains

      function ComputeGasDensityF() result (GasDensity)
  implicit none
  double precision::GasDensity
      GasDensity=P*1e-5*Mgas/RR/T
  end function ComputeGasDensityF

end module GasTherHyCondDATA

MODULE PartDistribDATA

Use GasTherHyCondDATA
Use BundleDATA
implicit none
double precision:: rhopar, ammd, cmd, gsd, ammdIn,gsdIn,NparinTot
integer(8):: nbins
double precision, allocatable, dimension (: ) :: dpar,
& InletBinMass0, nparin0
double precision, allocatable, dimension (:,:) :: nparin,
& InletBinMass,MtotInTube, FracMinBin
contains

Function BinMassF(numberBin,Nstep) result (BinMass)
double precision:: BinMass
integer(8)::numberBin,Nstep

BinMass=(nparin(numberBin,Nstep)*rhopar*pi*dpar(numberBin)**3)/6.

  end function BinMassF

Function BinNbrPartF(numberBin,Nstep) result (BinNro)
double precision:: BinNro
integer(8)::numberBin,Nstep

BinNro=InletBinMass(numberBin,Nstep)*6.0/
& (rhopar*pi*(dpar(numberBin))**3)

  end function BinNbrPartF

function CcF(diam) result (Cc)
double precision, intent(in):: diam

```

```

        double precision:: Cc
Cc=1.+2.*(6.32+2.01*exp(-0.1095*(P*7.5e-4)*(diam*1.e6)))
& /(P*7.5e-4)/(diam*1.e6)
end function CcF

function StkF(diam,denspar,velo) result (Stk)
    double precision, intent(in):: velo, diam, denspar
    double precision:: Stk

Stk=CcF(diam)*denspar*diam*diam*velo/18/mugas/dtube
end function StkF

function ReParF(velo,diam) result (Repart)
    double precision:: velo, diam
    double precision:: Repart

    Repart=rhogas*velo*diam/mugas
end function ReParF

function Compute_cmdF(Nstep) result (value)
    double precision:: Cumul_lncmd,divisln cmd
    double precision::value
    integer(8)::k,Nstep

    Cumul_lncmd=0.0
    divisln cmd=0.0
    Loop_sumatorio: DO k=1,nbins
        Cumul_lncmd=nparin(k,Nstep)*log(dpar(k))+Cumul_lncmd
        divisln cmd=nparin(k,Nstep)+divisln cmd
    End do Loop_sumatorio
    value=exp(Cumul_lncmd/divisln cmd)
end function Compute_cmdF

function Compute_gsdF(Nstep) result (value)
    double precision::Cumul_lngsd,divisln cmd
    double precision::value
    integer(8)::k,Nstep

    Cumul_lngsd=0.0
    divisln cmd=0.0
    Loop_sumatorio: DO k=1,nbins
        Cumul_lngsd=nparin(k,Nstep)*(log(dpar(k))-log(cmd))**2 +
&         Cumul_lngsd
        divisln cmd=nparin(k,Nstep)+divisln cmd
    End do Loop_sumatorio
    value=exp(sqrt(Cumul_lngsd/(divisln cmd-1)))
end function Compute_gsdF

function Compute_ammdF() result (value)
    double precision::value

    value=cmd*exp(3*(log(gsd)**2))*sqrt(rhopar/1000.0)
End function Compute_ammdF

END MODULE PartDistribDATA

MODULE VelocityDATA
USE BundleDATA
USE GasTherHyCondData
implicit none
double precision:: Radialvelocity,Axialvelocity
double precision:: vinit,MssFlwRate

contains

function NewRadVeloGuillotF(tube) result (newVelo)
    integer(8):: tube
    double precision:: newVelo

    if (tube==1) then

```

```

        newVelo=vinit
    else
        newVelo=(5.0/4.0)*vinit/(tube**3)
    end if

end function NewRadVeloGuillotF

function RegasF(velo,length) result (Renumber)
    double precision:: velo,length,Renumber

    Renumber=rhogas*velo*length/mugas

end function RegasF

function NewAxiVeloGuillotF(tube) result (newVelo)
    integer(8):: tube
    double precision:: newVelo

    NewVelo=(4.0/5.0)*vinit/(tube**2)

end function NewAxiVeloGuillotF

function MassFlowInletF() result (massflowrate)
    double precision:: massflowrate
    massflowrate=(vinit-25.)/0.91

end function MassFlowInletF

END MODULE VelocityDATA

MODULE BundleEfficiencyDATA
implicit none

    double precision, allocatable, dimension (:,:) :: TubBinEffRad,
    & TubBinEffAx, TubBinEffInit,ResusBinEff ! (i,k)
    double precision, allocatable, dimension (:,:,) :: TubBinEff ! (i,k,s)
    double precision, allocatable, dimension (:,:) :: MBinDepo ! (k,s)
    double precision, allocatable, dimension (:,:) :: MDepoTube ! (i,s)
    double precision, allocatable, dimension (:,:) :: TubEff ! (i,s)
    double precision, allocatable, dimension (:) :: FinalBundleEff

    double precision:: TubEff1
    double precision:: BundleDepoRad,BundleDepoAx
END MODULE BundleEfficiencyDATA

MODULE AxialDeposition
    USE PartDistribData
    USE velocityData
implicit none
double precision:: AxialDepoLength
double precision:: AreaAxialDepoTube, UpwardFlowingArea
double precision:: AxialVdepo, FactorAxialDepo

contains

FUNCTION WallFricVeloF(Velo) result (WallFricVelo)
    double precision:: Velo,WallFricVelo,fw

    fw=0.0014+0.125/(RegasF(Velo,dtube)**0.32) !wall friction
    !factor of Astec
    ! fw=0.316/(4*(Regas**0.25)) !wall friction factor Agarwal paper

    WallFricVelo=Velo*((fw/2)**0.5)

END FUNCTION WallFricVeloF

FUNCTION WallShearStressF(Velo) result (value)
    double precision:: Velo,value

    value=rhogas*(WallFricVeloF(Velo))**2

```

```

END FUNCTION WallShearStressF

FUNCTION RelaxTimeF(diam) result (relaxTime)
  double precision::diam,relaxTime

  relaxTime=CcF(diam)*rhopar*diam**2/(18*mugas)
END FUNCTION RelaxTimeF

FUNCTION RelaxTimePlusF(Velo,diam) result (RelTimPlus)
  double precision:: Velo,RelTimPlus,diam

  RelTimPlus=WallFricVeloF(Velo)**2*RelaxTimeF(diam)
&      *rhogas/mugas
END FUNCTION RelaxTimePlusF

FUNCTION DepVeloLiuAgarwPLUSF(Velo,diam) result (Uplus)
  double precision:: Velo,diam,Uplus

  Uplus=Min(0.0006*(RelaxTimePlusF(Velo,diam)**2),0.1)
END FUNCTION DepVeloLiuAgarwPLUSF

FUNCTION DepVeloLiuAgarwF(Velo,diam) result (depvelo)
  double precision:: Velo,diam,depvelo

  depvelo=WallFricVeloF(Velo)*DepVeloLiuAgarwPLUSF(Velo,diam)
END FUNCTION DepVeloLiuAgarwF

END MODULE AxialDeposition

MODULE Forces
USE PartDistribDATA
USE AxialDeposition
implicit none
double precision:: FGrav,FCohes,FFric,FDrag,FLift
double precision:: FResul,FAdh
integer(8)::Nlayers

contains

Function FGravitationalF(diam) result (value)
  double precision::velo,diam,value

  value=4.0*Pi*diam**3*rhopar*9.8/6.0
End Function FGravitationalF

Function FCohesiveF(Number,diam) result (value)
  double precision::value,diam,Hfactor
  integer(8)::Number,number2
  Number2=Min(10,Number)
  Hfactor=2.85e-7*sqrt(Real(number2))+1.0e-7
  value=diam*Hfactor
End Function FCohesiveF

Function FFriictionalF(Number,diam) result (value)
  double precision::value,diam
  integer(8)::number

  value=0.2*FCohesiveF(Number,diam)
End Function FFriictionalF

Function FDragF(velo,diam) result (value)
  double precision:: velo,diam,value

  value=WallShearStressF(velo)*pi*diam**2/4.0
End Function FDragF

```

```
Function FLiftF(velo,diam) result (value)
double precision:: velo,diam,value
double precision:: velo2
```

```
    velo2=WallFricVeloF(velo)
    value=4.21*rhogas*((mugas/rhogas)**2)*
&      (ReparF(velo2,diam))**2.31
```

```
End Function FLiftF
```

```
End MODULE Forces
```

```
MODULE Resuspension
```

```
implicit none
double precision, allocatable, dimension (:,:) :: ResRateBinEcart
double precision:: DELTA_t, VeloForResus
contains
```

```
Function ResusRateEcartF(force) result (value)
double precision::force,value
```

```
    If(force<3.065e-4)then
        value=0.4037*(force**0.6003)
    else
        value=90.28*(force**1.269)
    end if
```

```
End Function ResusRateEcartF
```

```
END MODULE Resuspension
```

```
Module Uncertainty
```

```
implicit none
double precision, allocatable, dimension (:) :: UncSDRad,
&    UncEffAx, UncResusBinEff,UncAxTrm,UncResusTrm, UncResusRate
```

```
double precision, allocatable, dimension (:) ::
&    UncInitTubBinEff,UncFinalTubeBinEff
```

```
double precision, allocatable, dimension (:) :: UncTubTrm,
&    UncTubEff,UncTuBndle
double precision::UncSDUdepPlus,UncSumAllTubs, UncCmTrm
```

```
End Module Uncertainty
```

```
C= *****
C= *****
C= **
C= **          Program computing Bundle Efficiency ARIS3G          **
C= **
C= *****
C= *****
C=
```

```
Subroutine ARI3SG
```

```
USE GasTherHyCondDATA
USE BundleDATA
USE PartDistribDATA
USE BundleEfficiencyDATA
USE VelocityDATA
USE AxialDeposition
USE Forces
USE Resuspension
USE Uncertainty
```

```
implicit none
```

```
!Temporal and/or local variables used in the program
integer(8):: i,k,s
```

```

double precision:: Stks
double precision::Radialcoleff,Axialcoleff
double precision::prod
double precision::MtotDepoInit
double precision::UncLoc_1
      double precision::Locall,UncTub_Loc,UncSumAllTubs_Loc

rhogas=ComputeGasDensityF()
NtubesMax= ComputeNtubesMaxF(TubTotLength)

cldp for SGTR experiments Ntubes=5
! NtubesMax=1
cldp fine

CALL ALLOCATING
Call Initializing

CALL ARI3WSC(1,i,k,s)

s=1
Loop_Cte_Bin_Mass: DO k=1,nbins      !This variable controls the total bin
      nparin(k,s)=nparin0(k)        !mass that enters at each tube stage
      InletBinMass0(k)=BinMassF(k,s)
END DO Loop_Cte_Bin_Mass

IF (inputmode=="singlcas") THEN
      N_init=1
ELSE
      N_init=NTimeStep
END IF

!*****
!*****
!*****
Loop_Time_Step: DO s=N_init,NTimeStep !*****
!*****
NparinTot=0
Loop_Inlet_Bin_Mass_TimeStep_s: DO k=1,nbins
      InletBinMass(k,s)=s*InletBinMass0(k)
      nparin(k,s)= BinNbrPartF(k,s)
      NparinTot=nparin(k,s)+NparinTot
END DO Loop_Inlet_Bin_Mass_TimeStep_s

!*****
!*****
i=0
Loop_Tubes_Efficiency: DO WHILE ((i<NtubesMax).AND.(NparinTot>2.)) !*****
!*****
      i=i+1
      cmd=Compute_cmdF(s)
      qsd=Compute_qsdF(s)
      ammd=Compute_ammdF()
      If (i==1)Then
            ammdIn=ammd
            gsdIn=gsd
      end if

      Radialvelocity=NewRadVeloGuillotF(i)
      Axialvelocity=NewAxiVeloGuillotF(i)
      VeloForResus=DMax1(Radialvelocity,Axialvelocity)

!*****
Loop_Tube_Bin_Efficiency: DO k=1,nbins !*****

!*****
!***** Radial Bin Efficiency *****
!*****
Stks= StkF(dpar(k),rhopar,Radialvelocity) !Radial Tube-Bin

IF(Stks.lt.0.0021)then
      Radialcoleff=0.0

```

```

        UncSDRad(k)=0.0
    ELSE IF (Stks.lt.0.1)then
        Radialcoleff=0.438269+0.0713031*LOG(Stks)
        UncSDRad(k)=0.0566
    ELSE
        Radialcoleff=1.0/(1.0+4.87e-5*exp(10.0/(Stks**0.125)))
        UncSDRad(k)=0.0739
    END IF

```

```

    TubBinEffRad(i,k)=Radialcoleff

```

```

!*****
!***** Axial Bin Efficiency *****
!*****

```

```

    AxialDepoLength=(4.0/5.0)*(4.0/5.0)*(dtube+stube)*i

```

```

    AreaAxialDepoTube= pi*dtube*AxialDepoLength

```

```

    AxialVdepo=DepVeloLiuAgarwF(Axialvelocity,dpar(k))

```

```

    UpwardFlowingArea=(dtube+stube)**2-pi*(dtube**2)/4.0

```

```

    FactorAxialDepo=AxialVdepo*AreaAxialDepoTube/
    (Axialvelocity*UpwardFlowingArea)

```

```

&

```

```

    Axialcoleff=1.0-exp(-FactorAxialDepo)
    TubBinEffAx(i,k)=Axialcoleff

```

```

!*****
!***Uncertainty**
!*****

```

```

    Local1=WallFricVeloF(Axialvelocity)*0.1

```

```

IF(AxialVdepo<Local1) then

```

```

    UncSDUdepPlus=0.437*DepVeloLiuAgarwPLUSF(Axialvelocity,dpar(k))

```

```

    ELSE

```

```

    UncSDUdepPlus=0.03

```

```

END IF

```

```

    UncAxTrm(k)=(WallFricVeloF(Axialvelocity)*AreaAxialDepoTube/
    (Axialvelocity*UpwardFlowingArea))
    *exp(-FactorAxialDepo)

```

```

&

```

```

&

```

```

    UncEffAx(k)=UncAxTrm(k)*UncSDUdepPlus

```

```

!*****
!***** Initial Deposition Bin Efficiency *****
!*****

```

```

    TubBinEffInit(i,k)=Radialcoleff+Axialcoleff

```

```

&

```

```

    -Radialcoleff*Axialcoleff

```

```

!*****
!***Uncertainty**
!*****

```

```

    UncInitTubBinEff(k)=sqrt(
    ((1-TubBinEffAx(i,k))*UncSDRad(k))**2
    +((1-TubBinEffRad(i,k))*UncEffAx(k))**2)

```

```

&

```

```

&

```

```

!*****
!***** Resuspension *****
!*****

```

```

    MBinDepo(k,s)=InletBinMass(k,s)*TubBinEffInit(i,k)

```

```

    Nlayers=0

```

```

    Nlayers=Int(MBinDepo(k,s)/rhopar/AreaAxialDepoTube/dpar(k))

```

```

cldp19042010 Modificación maxima resuspensión

```

```

    Nlayers=1

```

```

cldp19042010 FIN Modificación maxima resuspensión

```

```

    FCohes=FCohesiveF(Nlayers,dpar(k))*1.0e6

```

```

    FFric=0.2*FCohes

```

```

    FDrag=FDragF(VeloForResus,dpar(k))*1.0e6

```

```

    FLift=FLiftF(VeloForResus,dpar(k))*1.0e6

```

```

    FAdh=FCohes+FFric

```

```

    FResult=FDrag+FLift-FAdh

```

```

cldp02022010 Modificación eliminando la resuspensión y tener soloDepo
!FResul=0.0
cldp02022010 FIN Modificación eliminando la resuspensión y tener soloDepo

```

```

ResRateBinEcart(i,k)=0.0
IF(FResul>0.0) THEN
    ResRateBinEcart(i,k)=ResusRateEcartF(FResul)
End IF

ResusBinEff(i,k)=1.0-exp(-ResRateBinEcart(i,k)*DELTA_t)

```

```

!*****
!***Uncertainty**
!*****

```

```

If(FResul>3.065e-4)then
    UncResusRate(k)=2.367*ResRateBinEcart(i,k)
else if(FResul>0.0)then
    UncResusRate(k)=1.725*ResRateBinEcart(i,k)
else
    UncResusRate(k)=0.0
end if

```

```

UncResusTrm(k)=DELTA_t*exp(-ResRateBinEcart(i,k)*DELTA_t)
UncResusBinEff(k)=UncResusTrm(k)*UncResusRate(k)

```

```

!*****
!***** FINAL TUBE BIN EFFICIENCY *****
!*****

```

```

If(ResusBinEff(i,k)>0.0) then
    TubBinEff(i,k,s)=TubBinEffInit(i,k)*(1.0-ResusBinEff(i,k))*
& (1.0-(1.0-ResusBinEff(i,k)**s)/s/ResusBinEff(i,k)
else
    TubBinEff(i,k,s)=TubBinEffInit(i,k)
end if

```

```

!*****
!***Uncertainty**
!*****

```

```

If(ResusBinEff(i,k)>0.0) then
    UncFinalTubeBinEff(k)=sqrt(
& ((1.-ResusBinEff(i,k))*(1.-(1.-ResusBinEff(i,k)**s)/
& (s*ResusBinEff(i,k))*UncInitTubBinEff(k) )**2
& + ( TubBinEffInit(i,k)*(1.-ResusBinEff(i,k)**s*
& (1.+s*ResusBinEff(i,k)-1.)/(s*(ResusBinEff(i,k)**2.))
& *UncResusBinEff(k) )**2)
else
    UncFinalTubeBinEff(k)=UncInitTubBinEff(k)
end if

```

```

CALL ARI3WSC(2,i,k,s)

```

```

END DO Loop_Tube_Bin_Efficiency !*****
!*****

```

```

!***** Mass computations*****

```

```

    MtotInTube(i,s)=0.0
    MdepoTube(i,s)=0.0
Loop_MassComputations: DO k=1,nbins
    MtotInTube(i,s)=InletBinMass(k,s)+MtotInTube(i,s)
    MBinDepo(k,s)=InletBinMass(k,s)*TubBinEff(i,k,s)
    MdepoTube(i,s)=MBinDepo(k,s)+MdepoTube(i,s)
END DO Loop_MassComputations

```

```

    TubEff(i,s)=MdepoTube(i,s)/MtotInTube(i,s)

```

```

cldp prueba

```

```

! TubEff(i,s)=1.
cldp fin prueba

Loop_MassFractions: do k=1,nbins
  FracMinBin(k,s)=InletBinMass(k,s)/MtotInTube(i,s)
End do Loop_MassFractions

!*****
!***Uncertainty**
!*****
UncTub_Loc=0.0
Loop_UncertnTube: Do k=1,nbins
  UncTub_Loc=(FracMinBin(k,s)*UncFinalTubeBinEff(k))**2+
& UncTub_Loc
End Do Loop_UncertnTube

UncTubEff(i)=sqrt(UncTub_Loc)
!*****

NparinTot=0
Loop_UpdateInletBinMasstoNextTubeStage: Do k=1,nbins
  InletBinMass(k,s)=(1-TubBinEff(i,k,s))*InletBinMass(k,s)
  nparin(k,s)= BinNbrPartF(k,s)
  NparinTot=nparin(k,s)+NparinTot
END DO Loop_UpdateInletBinMasstoNextTubeStage

CALL ARI3WSC(3,i,k,s)

END DO Loop_Tubes_Efficiency !*****
!*****

!***** Bundle Efficiency *****
1013 prod=1.

Loop_BundleDepoRad_Product: Do i=1,NtubesMax
  prod= prod*(1-(dtube*TubEff(i,s)/(stube+dtube)))
END DO Loop_BundleDeporad_Product

FinalBundleEff(s)=1.-exp(-4*(1-prod)*(dtube+stube)**2/
& (4*(dtube+stube)**2-pi*dtube**2))

!*****
!***Uncertainty**
!*****

UncSumAllTubs_Loc=0.0
Loop_Sum_Uncer:Do i=1,NtubesMax
  UncTubTrm(i)=(stube+dtube)/(stube+dtube-dtube*TubEff(i,s))
  UncSumAllTubs_Loc=(UncTubTrm(i)*UncTubEff(i))**2
& +UncSumAllTubs_Loc
End do Loop_Sum_Uncer

UncSumAllTubs=sqrt(UncSumAllTubs_Loc)
UncLoc_1=4*dtube*(dtube+stube)/(4*((dtube+stube)**2)-pi*dtube**2)
UncCmTrm=(UncLoc_1*prod*(1-FinalBundleEff(s)))

UncTuBndle(s)=UncCmTrm*UncSumAllTubs

End Do Loop_Time_Step !*****
!*****

MssFlwRate=MassFlowInletF()

i=1
k=1
Loop_write3: Do s=1,NTimeStep
  CALL ARI3WSC(4,i,k,s)
end do Loop_write3

CALL ARI3WSC(7,i,k,s)

```

CALL DeALLOCATING

END Subroutine ARI3SG

Subroutine ALLOCATING

```
USE GasTherHyCondDATA
USE BundleDATA
USE PartDistribDATA
USE BundleEfficiencyDATA
USE VelocityDATA
USE AxialDeposition
USE Forces
USE Resuspension
USE Uncertainty
implicit none

allocate (InletBinMass0 (nbins))
allocate (InletBinMass (nbins, NTimeStep))
allocate (MtotInTube (NtubesMax, NTimeStep))
allocate (FracMinBin (nbins, NTimeStep))
allocate (nparin (nbins, NTimeStep))

allocate (TubBinEffRad (NtubesMax, nbins))
allocate (TubBinEffAx (NtubesMax, nbins))
allocate (TubBinEffInit (NtubesMax, nbins))
allocate (ResusBinEff (NtubesMax, nbins))

allocate (TubBinEff (NtubesMax, nbins, NTimeStep))

allocate (MdepoTube (NtubesMax, NTimeStep))
allocate (MbinDepo (nbins, NTimeStep))

allocate (TubEff (NtubesMax, NTimeStep))

allocate (ResRateBinEcart (NtubesMax, nbins))

allocate (UncSDRad (nbins))
allocate (UncEffAx (nbins))
allocate (UncAxTrm (nbins))
allocate (UncResusRate (nbins))
allocate (UncResusBinEff (nbins))
allocate (UncResusTrm (nbins))

allocate (UncInitTubBinEff (nbins))
allocate (UncFinalTubeBinEff (nbins))
allocate (UncTubTrm (ntubesMax))
allocate (UncTubEff (ntubesMax))
```

End Subroutine ALLOCATING

Subroutine Initializing

```
USE GasTherHyCondDATA
USE BundleDATA
USE PartDistribDATA
USE BundleEfficiencyDATA
USE VelocityDATA
USE AxialDeposition
USE Forces
USE Resuspension
USE Uncertainty
```

```

implicit none
integer(8):: i,k,s

i=0
k=0
s=0

Loop_Init_TimeStep: Do s=1,NTimeStep

    Loop_InitBins1: DO k=1,nbins
        InletBinMass(k,s)=0.0
        nparin(k,s)=0.0
        FracMinBin(k,s)=0.0
        MBinDepo(k,s)=0.0
    END DO Loop_InitBins1

    Loop_InitTubes: DO i=1,NtubesMax
        MtotInTube(i,s)=0.0
        MdepoTube(i,s)=0.0
        TubEff(i,s)=0.0
        Loop_InitBins: DO k=1,nbins
            TubBinEff(i,k,s)=0.0
        END DO Loop_InitBins
    END DO Loop_InitTubes
END DO Loop_Init_TimeStep

Loop_InitTubes2: DO i=1,NtubesMax
    Loop_InitBins21: DO k=1,nbins
        TubBinEffAx(i,k)=0.0
        TubBinEffInit(i,k)=0.0
        ResusBin_Eff(i,k)=0.0
        TubBinEffRad(i,k)=0.0
        ResRateBinEcart(i,k)=0.0
    END DO Loop_InitBins21
END DO Loop_InitTubes2

Loop_InitBins3: DO k=1,nbins
    InletBinMass0(k)=0.0
END DO Loop_InitBins3

End Subroutine Initializing

Subroutine DeALLOCATING

USE GasTherHyCondDATA
USE BundleDATA
USE PartDistribDATA
USE BundleEfficiencyDATA
USE VelocityDATA
USE AxialDeposition
USE Forces
USE Resuspension
USE Uncertainty
implicit none

deallocate (InletBinMass0)
deallocate (InletBinMass)
deallocate (nparin)

deallocate (MtotInTube)
deallocate (FracMinBin)

deallocate (TubBinEffRad)
deallocate (TubBinEffAx)
deallocate (TubBinEffInit)
deallocate (ResusBinEff)

deallocate (TubBinEff)

deallocate (MdepoTube)
deallocate (MBinDepo)

```

```
deallocate (TubEff)
deallocate (ResRateBinEcart)
deallocate (UncResusRate)
deallocate (UncSDRad)
deallocate (UncEffAx)
deallocate (UncResusBinEff)

deallocate (UncInitTubBinEff)
deallocate (UncFinalTubeBinEff)
deallocate (UncTubTrm)
deallocate (UncTubEff)
deallocate (UncAxTrm)
deallocate (UncResusTrm)
```

End Subroutine DeALLOCATING

```

Subroutine ARI3WSC(m,ii,kk,ss)

USE GasTherHyCondDATA
USE BundleDATA
USE PartDistribDATA
USE BundleEfficiencyDATA
USE VelocityDATA
USE AxialDeposition
USE Forces
USE Resuspension
USE Uncertainty

implicit none

integer(8):: m,ii,kk,ss

double precision:: densammd

densammd=1000.0

IF (inputmode=="singlcas") THEN    !1

IF(m==1) THEN

open (77,file="Output-Particle.dat")
write(77,10)
10  format(' time      tube      dpar(k)
& nparin(k)      InBinMass(kg)      RePar      Cc      Stk
&      EffRd      UncEffRd(95%CI) RelTimePlus
&LiuAgarVPlus  UncSDLiu(95%CI) EffAx      UncEffAx(95%CI)
&EffDep0  UncEffDep0(95%CI) FCohes
&      FFric
&      FDrag
&      FLift
&      FAdh      FResult
&
&Nlayers  ResusRate  UncRsRate(95%CI) EffResus
& UncEffRs(95%CI)  EffFinal  UncEffFinal(95%CI)')

open (78,file="Output-Tube.dat")
write(78,11)
11  format(' time      tube      V-Rad      V-Ax      V-Resus      Regas
&      ammd      gsd      rhopar
&      StkAmmd      RepairAmmd  DELTA_t
&      TubEff      UncertTubEff(95%CI)')

open (79,file="Output-Timel.dat")
write(79,12)
12  format(' tstep      time      FinalTBEff  Uncert(95%CI)')

ELSE IF (m==2) THEN
IF (ss==NTimeStep) THEN

write(77,17)
&  ss*DELTA_t,
&  ii,
&  dpar(kk)*1e6,
&  nparin(kk,ss),
&  InletBinMass(kk,ss),
&  RepairF(Radialvelocity,dpar(kk)),
&  CcF(dpar(kk)),
&  StkF(dpar(kk),rhopar,Radialvelocity),
&  TubBinEffRad(ii,kk),
&  2.*UncSDRad(kk),
&  RelaxTimePlusF(Axialvelocity,dpar(kk)),
&  DepVeloLiuAgarwPLUSF(Axialvelocity,dpar(kk)),
&  2.0*UncSDUdepPlus,
&  TubBinEffAx(ii,kk),
&  2.0*UncEffAx(kk),
&  TubBinEffInit(ii,kk),

```

```

& 2.0*UncInitTubBinEff(kk),
& FCohes,
& FFric,
& FDrag,
& FLift,
& FAdh,
& FResult,
& Nlayers,
& ResRateBinEcart(ii,kk),
& 2.0*UncResusRate(kk),
& ResusBinEff(ii,kk),
& 2.0*UncResusBinEff(kk),
& TubBinEff(ii,kk,ss),
& 2.0*UncFinalTubeBinEff(kk)
17 format(e12.6,2x, I4,2x,21(e12.6,2x),2x,I4,2x,6(e12.6,2x))

```

```

END IF

```

```

ELSE IF (m==3) THEN

```

```

write(78,18)ss*DELTA_t,ii,
& Radialvelocity,
& Axialvelocity,
& VeloForResus,
& RegasF(RadialVelocity, dtube),
& ammd,
& gsd,
& rhopar,
& StkF(ammd,densammd,Radialvelocity),
& RepairF(Radialvelocity,ammd),
& DELTA_t,
& TubEff(ii,ss)*100.,
& 2.0*UncTubEff(ii)*100.
18 format(e12.6,2x,I4,x,12(e12.6,x))

```

```

ELSE IF (m==4) THEN

```

```

write(79,19) ss,ss*Delta_t, 100*FinalBundleEff(ss),
& 2.0*UncTuBndle(ss)*100
19 format(I6,2x,3(e12.6,2x))

```

```

ELSE IF (m==7) THEN

```

```

close(77)
close(78)
close(79)

```

```

END IF

```

```

END IF

```

```

END Subroutine ARI3WSC

```

